STATISTICALLY RELEVANT AND IRRELEVANT CONSERVED QUANTITIES FOR THE EQUILIBRIUM STATISTICAL DESCRIPTION OF THE TRUNCATED BURGERS-HOPF EQUATION AND THE EQUATIONS FOR BAROTROPIC FLOW

By

Rafail V. Abramov

A Thesis Submitted to the Graduate

Faculty of Rensselaer Polytechnic Institute

in Partial Fulfillment of the

Requirements for the Degree of

DOCTOR OF PHILOSOPHY

Major Subject: Mathematics

Approved by the
Examining Committee:

Gregor Kovačič, Thesis Adviser

Andrew J. Majda, Thesis Adviser

Joseph Flaherty, Member

Peter Kramer, Member

Victor Roytburd, Member

Rensselaer Polytechnic Institute
Troy, New York

June 2002
(For Graduation August 2002)

STATISTICALLY RELEVANT AND IRRELEVANT CONSERVED QUANTITIES FOR THE EQUILIBRIUM STATISTICAL DESCRIPTION OF THE TRUNCATED BURGERS-HOPF EQUATION AND THE EQUATIONS FOR BAROTROPIC FLOW

By

Rafail V. Abramov

An Abstract of a Thesis Submitted to the Graduate

Faculty of Rensselaer Polytechnic Institute

in Partial Fulfillment of the

Requirements for the Degree of

DOCTOR OF PHILOSOPHY

Major Subject: Mathematics

The original of the complete thesis is on file
in the Rensselaer Polytechnic Institute Library

Examining Committee:

Gregor Kovačič, Thesis Adviser

Andrew J. Majda, Thesis Adviser

Joseph Flaherty, Member

Peter Kramer, Member

Victor Roytburd, Member

Rensselaer Polytechnic Institute
Troy, New York

June 2002
(For Graduation August 2002)

CONTENTS

ACKNOWLEDGMENT

The author would like to thank the following people:

- Prof. Gregor Kovačič and Prof. Andy Majda for helping him out with producing the thesis, and for being the author's advisors during his PhD program at RPI and Courant;
- Dr. Ibrahim Fatkullin, Dr. Ilya Timofeyev, and Prof. Eric Vanden Eijnden for many helpful pieces of advice;
- Mrs. Victoria I. for providing the author with excellent food and drinks, wonderful company, lots of phone calls, and other scientific inspirations;
- Dr. Ildar Gabitov for various help;
- Prof. Joseph Flaherty, Prof. Victor Roytburd, and Prof. Peter Kramer for being in the author's examining committee;
- Dr. Ibrahim Fatkullin, Dr. Rinat Gabitov, Dr. Kartik Krishnan, Dr. Greg Pavliotis, and Mr. Vladislav Rogovoy for being good friends;
- Mr. Coffee, Mr. Samuel Adams, Mr. John Walker, and Mr. Marlboro for psychological support;
- RPI Office of the Bursar for limiting the author's commitment to Mr. Samuel Adams, Mr. John Walker, and Mr. Marlboro;
- The International Olympic Committee for the fair and unbiased judgement during the 2002 Winter Olympics;
- And, of course, You, the honorable reader of this thesis. Please turn the page, for there are many interesting things within, waiting for You to explore them.

ABSTRACT

The purpose of the current work is to study the statistical relevance and irrelevance of the additional conserved quantities in the simple models of actual weather systems. Here we consider the two models with the key features of statistical weather behavior: the truncated Burgers-Hopf (TBH) equation, which is, in fact, the Galerkin projection of the actual Burgers-Hopf equation on the finite Fourier basis; and the two different truncations of the equations for barotropic flow with topography – the traditional spectral truncation and the sine-bracket truncation. In the case with TBH the recently discovered Hamiltonian structure proposes the cubic Hamiltonian to be considered as an additional conserved quantity, since the equilibrium statistical theory developed for TBH is based on the conservation of energy. Thus, the question arises of the statistical significance of the Hamiltonian, beyond that of the energy. First, an appropriate statistical theory is developed which includes both the energy and the Hamiltonian. Then a convergent Monte-Carlo algorithm is developed for computing equilibrium statistical distributions. The probability distribution of the Hamiltonian on a microcanonical energy surface is studied through the Monte-Carlo algorithm and leads to the concept of statistically relevant and irrelevant values for the Hamiltonian. Empirical numerical estimates and simple analysis are combined to demonstrate that the set of statistically relevant values of the Hamiltonian has vanishingly small measure as the number of degrees of freedom increases with fixed mean energy. The predictions of the theory for relevant and irrelevant values for the Hamiltonian are confirmed through systematic numerical simulations. For statistically relevant values of the Hamiltonian, these simulations show a surprising spectral tilt rather than equipartition of energy. This spectral tilt is predicted and confirmed independently by Monte-Carlo simulations based on equilibrium statistical mechanics together with a heuristic formula for the tilt. For the equations for barotropic flow with topography, the two different spectral truncations are considered – the traditional truncation and the sine-bracket truncation. The main difference between the two is that, apart from the energy and the enstrophy, which are the conserved quantities for the traditional truncation, there is a vast number of additional invariants for the sine-bracket truncation, which, in fact, are the Casimir invariants for the Poisson bracket of the sine-bracket truncation. On the other hand, the suitable energy-enstrophy based statistical theory is developed for the traditional truncation. The natural question which arises is that are the additional

conserved quantities in the sine-bracket truncation statistically important and when? We answer this question by performing a series of direct numerical simulations for both truncations, three different geophysical situations, with varying third Casimir invariant. The special numerical symplectic time integrator has been employed in the direct simulations to preserved the additional Casimir invariants with machine precision, and the gradient descent optimization procedure was used to generate the initial conditions with predefined conserved quantities. The situation with the third Casimir invariant is very similar to the TBH case in the sense that additional conserved quantities are statistically irrelevant, if the third Casimir invariant is set to zero, and appropriate numerical simulations confirm that the statistical results for the sine-bracket truncation are essentially identical with those for the traditional truncation in this case. However, when the third Casimir invariant is shifted away from the origin, the statistical influence of the additional conserved quantity is observed in the mean flow, mean energy and pseudo-energy, time correlation functions and probability density functions. The statistical trends are observed and quantified through the series of direct numerical simulations with different values of the third Casimir invariant. The two important statistical trends we would like to emphasize are the systematic bending of the mean state scatterplots, and the accumulating skewness in the probability density functions for the potential vorticity. The results established here for the both models are a prototype for similar issues with significant practical importance in much more complex geophysical applications.

CHAPTER 1
INTRODUCTION

The classical statistical mechanics predictions for the complex systems require the substantial amount of knowledge about conserved quantities in the system. However in some important cases, like the equations for barotropic flow, the number of conserved quantities is infinite. Therefore the natural question arises: are all conserved quantities important for making a successful prediction or only some of them? Here in this work, we consider two dynamical systems which possess different conserved quantities: the truncated Burgers-Hopf equations and the truncated equations for barotropic flow.

The truncated Burgers-Hopf equations (TBH) were proposed by Majda and Timofeyev in [18, 19] as a good toy model which has all key properties of actual weather systems, like non-linearity (as an advection term), energy conservation, correlation scaling, and many others, but, unlike the actual weather system, is one-dimensional, which makes it easier to study and learn how to make the statistical predictions. For a long time it has been thought that the TBH possesses, apart from the mass conservation, only one conserved quantity, which is the energy. The statistical predictions made for the TBH were successful and confirmed by the direct numerical simulations. However, Kovačič, Majda, and the author discovered the Hamiltonian structure for the TBH in [2]. One would assume that the energy, which is the quadratic conserved quantity, turns out to be the Hamiltonian for the TBH. Well, that was not the case. The Hamiltonian turned out to be the cubic functional, and was never known before as the conserved quantity for the truncated Burgers-Hopf equations. That in some sense made the Hamiltonian an additional conserved quantity, which has not been taken into account for the statistical predictions. In the thesis we study the influence of the Hamiltonian on the statistical behavior of the system and compare the results to the canonical energy-based statistical predictions. It turns out that for some certain values of the Hamiltonian the system exhibits the statistical behavior that has not been observed before, such as energy spectrum tilt, and the slow decay of the time correlations. However, we show explicitly that those special values of the Hamiltonian are statistically rarely achievable for generic initial conditions, which makes the Hamiltonian for the truncated Burgers-Hopf equations statistically irrelevant in most of natural cases.

The equations for barotropic flow are the more sophisticated model of actual weather

systems. In the current work we consider the 2D Euler equations, which are the equations for barotropic flow without damping and forcing. The equations for barotropic flow possess the Hamiltonian structure on the periodic domain, and, as a consequence, an infinite number of the conserved quantities which are, in fact, the Casimir invariants for the corresponding Poisson bracket. And, of course, the equations for barotropic flow preserve the circulation and the kinetic energy of the flow. It has been thought for a long time, that the energy and the enstrophy (low-order convex Casimir invariant of the Poisson bracket) are the only conserved quantities which govern the statistical predictions. In addition, the most generic and straightforward traditional Fourier truncation of the equations for barotropic flow preserves exactly the circulation, energy, and the enstrophy, while the higher order conserved quantities are lost. As a consequence, the canonical energy-enstrophy based statistical theory was developed for the equations for barotropic flow (see [17], for example), and the predictions of the statistical theory were confirmed by the direct numerical simulations with the traditional truncation of the equations for barotropic flow. Well, no one can make the direct numerical simulations with the equations for barotropic flow themselves, and the traditional truncation preserves exactly those quantities which are taken into account by the statistical theory. Nonetheless, many people believe that the energy and enstrophy are crucial for the statistical predictions, and the rest of the conserved quantities is statistically irrelevant. In the thesis we employed, as well as the traditional truncation, the *sine-bracket truncation* of the equations for barotropic flow, which was independently proposed by Zeitlin in [25], and by Miller, Weichman, and Cross in [21]. Unlike the traditional truncation, the sine-bracket truncation retains the Hamiltonian structure and the vast amount of corresponding Casimir invariants, the number of which is proportional to the size of truncation. In order to preserve the additional conserved quantities with machine precision during numerical simulations, we used the special structure-preserving symplectic time integrator which was proposed by McLachlan in [20]. Through the direct numerical simulations with both the traditional and the sine-bracket truncations, we show and exactly quantify the conditions where the additional conserved quantities are statistically relevant, and where they are statistically irrelevant. The situation here is unlike the TBH case, because, as we will see, the regime where additional conserved quantities are statistically relevant is quite achievable. We observe and quantify the effects of the statistically relevant additional conserved quantities on the properties of the most probable statistical macrostate of the system, such as mean stream

functions and their moments, mean energy and pseudo-energy spectra, collinearity of the mean state, time correlation functions and probability density functions. Also for the variety of the natural initial conditions we show that the additional conserved quantities are statistically irrelevant, and the statistical results of the direct numerical simulations with the sine-bracket truncation coincide with those for the traditional truncation, and the energy-enstrophy based statistical predictions.

- In the remainder of the Chapter 1 we present the basic facts about Hamiltonian systems, and also the basic knowledge about statistical predictions, which we will need throughout the thesis.

- In the Chapter 2 we discuss the influence of the statistically relevant Hamiltonian on the truncated Burgers-Hopf equations. We explicitly show that for some special values the Hamiltonian is statistically relevant and quantify the effects of the Hamiltonian on the statistical properties of the TBH. We also show that those special values of the Hamiltonian are statistically rarely achievable, and for the most natural cases the Hamiltonian is statistically irrelevant.

- In the Chapter 3 we introduce the equations for barotropic flow, and the traditional spectral truncation of the equations for barotropic flow. We discuss the conserved quantities for the equations for barotropic flow, and also show which conserved quantities are retained after the truncation. Also in Chapter 3 we present the empirical statistical theory for the most probable statistical state of the equations for barotropic flow, and the complete statistical theory for the traditional truncation of the equations for barotropic flow.

- In the Chapter 4 we introduce the sine-bracket truncation of the equations for barotropic flow. We show that the sine-bracket truncation possesses the Hamiltonian structure, and that the corresponding Poisson bracket possesses the Casimir invariants, which are in some sense finite-dimensional approximations of the Casimir invariants of the equations for barotropic flow. Also in the Chapter 4 we describe the special structure-preserving symplectic numerical time integrator for the sine-bracket truncation, which allows us to preserve all Casimir invariants with machine precision. The optimization procedure for generating initial conditions with pre-defined Casimir invariants is also presented in the Chapter 4.

- In the Chapter 5 we present the basic numerical simulations with the traditional truncation for the three different geophysical situations. We show that in each case the direct numerical simulations confirm the statistical predictions made in the Chapter 3.

- In the Chapter 6 we present the direct numerical simulations with the sine-bracket truncation for the same three geophysical situations. We show that for the statistically irrelevant values of the additional conserved quantities the results of the simulations confirm the statistical predictions. For the statistically relevant values of additional conserved quantities we show and quantify the statistical trends in behavior of the mean state, energy, time correlations and probability density functions.

- Chapter 7 contains the summary of the work done in Chapters 5 and 6, and the concluding discussion. Also in the Chapter 7 we show a very interesting observation. In the particular geophysical case we consider, the statistical theory from the Chapter 3 predicts the zonal jet structure for the mean flow. We observe, however, that statistically relevant additional conserved quantities are responsible for creating vortices in the zonal jet, which the conventional statistical theory from Chapter 3 could not predict.

1.1 Basic facts on Hamiltonian systems

Our work in this thesis requires some basic understanding of Hamiltonian systems in general sense. In this section we present the fundamental facts about continuous and finite-dimensional Hamiltonian systems.

1.1.1 Finite-dimensional systems

Let us consider the equation of a finite-dimensional Hamiltonian system:

$$\frac{\mathrm{d}\mathbf{y}}{\mathrm{d}t} = \mathbf{J}(\mathbf{y})\nabla H(\mathbf{y}), \tag{1.1}$$

where $\mathbf{y}$ is the column vector of dynamical variables, H is a *hamiltonian* function and $\mathbf{J}$ is a *symplectic matrix* which is skew-symmetric and satisfies the Jacobi identity

$$\sum_l (J_{pl}\partial_l J_{qr} + J_{rl}\partial_l J_{pq} + J_{ql}\partial_l J_{rp}) = 0 \quad \forall p, q, r \leq N, \tag{1.2}$$

where N is the dimension of the system. The Jacobi identity essentially tells us that the system can be represented in its canonical action-angle variables (see [22] and references therein). We will be proving the Jacobi identity here for a few cases, however, as the reader will see, in this work we never really take any advantage of the Jacobi identity.

Let us denote the *Poisson bracket* for $F(\mathbf{y})$ and $G(\mathbf{y})$ by

$$\{F, G\} = (\nabla F, \mathbf{J}\nabla G), \tag{1.3}$$

where $(\cdot, \cdot)$ denotes the scalar product of two vectors. Due to skew-symmetry of $\mathbf{J}$ we have

$$\{F, G\} = -\{G, F\}. \tag{1.4}$$

In this notation the time evolution for any $F(\mathbf{y})$ can be written in the form

$$\frac{\mathrm{d}F}{\mathrm{d}t} = (\nabla F, \dot{\mathbf{y}}) = (\nabla F, \mathbf{J}\nabla H) = \{F, H\}, \tag{1.5}$$

thus from (1.4) and (1.5) we have

$$\frac{\mathrm{d}H}{\mathrm{d}t} = \{H, H\} = -\{H, H\} = 0, \tag{1.6}$$

i.e. H is the *conserved quantity* of the system.

Generally, the conserved quantities of the system (1.1) depend on both $\mathbf{J}$ and H. Let us take the basis of the kernel $\ker(\mathbf{J}) : \mathbf{K}_j(\mathbf{y}),\ \ 0 < j \leq \dim(\ker(\mathbf{J}))$. For some $\mathbf{K}_j(\mathbf{y})$ (let us denote it as $\mathbf{K}_{j_k}(\mathbf{y})$) we can find $C_k(\mathbf{y})$ such that

$$\mathbf{K}_{j_k}(\mathbf{y}) = \nabla C_k(\mathbf{y}). \tag{1.7}$$

The latter means that

$$\mathbf{J}\nabla C_k(\mathbf{y}) \equiv 0,$$

which, in turn, is followed by

$$\frac{\mathrm{d}C_k}{\mathrm{d}t} = \{C_k, H\} = -\{H, C_k\} = (\nabla H, \mathbf{J}\nabla C_k) = 0,$$

i.e. C_k is conserved in time regardless of Hamiltonian and, therefore is the property of $\mathbf{J}$ alone. These conserved quantities are called the *Casimir invariants*. For simple Poisson

brackets the Casimir invariants are easy to find, and if we are looking for the conserved quantities of the system, then the Casimir invariants are the best candidates to be found quickly.

1.1.2 Continuous systems

The continuous analogue of (1.1) can be written as

$$\frac{\partial}{\partial t}u(\mathbf{x},t) = \mathcal{J}\frac{\delta \mathcal{H}}{\delta u} \tag{1.8}$$

where $\mathcal{J}$ is a skew-adjoint operator, $\mathcal{H}$ is a functional. We assume that $\mathcal{H}$ is written as a functional scalar product and may depend on u, $\mathbf{x}$, and various derivatives and quadratures of u with respect to $\mathbf{x}$.

The Poisson bracket for the operator $\mathcal{J}$ is defined as

$$\{\mathcal{F},\mathcal{G}\} = \left[\frac{\delta \mathcal{F}}{\delta \mathbf{u}}, \mathcal{J}\frac{\delta \mathcal{G}}{\delta \mathbf{u}}\right], \tag{1.9}$$

where square brackets denote the functional scalar product. Due to $\mathcal{J} = -\mathcal{J}^\dagger$ we have

$$\{\mathcal{F},\mathcal{G}\} = -\{\mathcal{G},\mathcal{F}\}.$$

The Jacobi identity in this case has the form

$$\{\{\mathcal{A},\mathcal{B}\},\mathcal{C}\} + \{\{\mathcal{C},\mathcal{A}\},\mathcal{B}\} + \{\{\mathcal{B},\mathcal{C}\},\mathcal{A}\} = 0$$

for any $\mathcal{A},\mathcal{B},\mathcal{C}$.

Now, for any functional $\mathcal{F}$ we can write

$$\frac{\mathrm{d}\mathcal{F}}{\mathrm{d}t} = \left[\frac{\delta \mathcal{F}}{\delta u}, u_t\right] = \left[\frac{\delta \mathcal{F}}{\delta u}, \mathcal{J}\frac{\delta \mathcal{H}}{\delta u}\right] = \{\mathcal{F},\mathcal{H}\},$$

i.e. the evolution of $\mathcal{F}$ in time can be represented as the Poisson bracket. Note that

$$\frac{\mathrm{d}\mathcal{H}}{\mathrm{d}t} = \{\mathcal{H},\mathcal{H}\} = -\{\mathcal{H},\mathcal{H}\} = 0,$$

so that $\mathcal{H}$ is a conserved quantity for (1.8).

Corresponding Casimir invariants depend on $\mathcal{J}$ only, therefore they are defined by

$$\mathcal{J}\frac{\delta \mathcal{C}}{\delta \mathbf{u}} = \mathbf{0}. \tag{1.10}$$

Later we will see that the two-dimensional barotropic flow has many conserved quantities, most of which are the Casimir invariants of the corresponding Poisson bracket. The conserved quantities play the role of system constraints in a statistical-mechanical sense, preventing the system from evolving on a significant part of the phase space, and therefore will be of absolute importance in our studies.

1.2 Basic statistical mechanics

In this section we present the basic facts we need to know about equilibrium statistical mechanics. The statistical description of a dynamical system is the one given in terms of probabilities, or probability densities. Let us suppose that we have a dynamical system of the form

$$\frac{\mathrm{d}}{\mathrm{d}t}\vec{u} = \vec{F}(\vec{u}). \tag{1.11}$$

Thus, the solution to the general equation (1.11) is a vector $\vec{u}$ which satisfies the equation at any given time. If we are able to solve the system (1.11), then, for some initial $\vec{u}_0$, we know how it behaves as the time passes.

1.2.1 Probability density and the Liouville equation

The statistical description of the dynamical system (1.11) involves the object called the probability density:

Definition 1 *A probability density $\rho(\vec{u}, t)$, associated to the variable $\vec{u}(t)$ from (1.11) is a function defined on $\mathbb{R}^{N+1} \times \mathbb{R}$, where N is the dimension of $\vec{u}$, which satisfies the following properties:*

- *$\rho(\vec{u}, t)$ is non-negative with unit total mass, i.e.*

$$\rho \geq 0, \quad \int_{\mathbb{R}^N} \rho(\vec{\lambda}, t)\, \mathrm{d}\vec{\lambda} = 1 \ \forall t.$$

- *For almost any $\{S : S \subset \mathbb{R}^N\}$, the probability of the event $\{\vec{u} \in S\}$ at the time t is*

given by the measure $\mu(S)$, which is defined by

$$\text{Prob}\{\vec{u} \in S\} = \mu(S) = \int_S \rho(\vec{\lambda}, t)\, \mathrm{d}\lambda,$$

The measure μ associated to the probability density ρ is called the probability measure.

The expected value of a quantity $G(\vec{u})$ at a time t is given by

$$\bar{G} = \int_{\mathbb{R}^N} G(\vec{\lambda})\rho(\vec{\lambda}, t)\, \mathrm{d}\vec{\lambda}.$$

Thus knowing the probability density $\rho(\vec{u}, t)$ at a given time t, we possess some general information about the system (1.11).

Now, let us assume that instead of a given initial condition $\vec{u}_0$, we have an initial probability density $\rho_0(\vec{u})$. What we can do now, is to throw many initial vectors $\vec{u}_i(0)$ in $\mathbb{R}^N$ according to the given probability density $\rho_0(\vec{u})$. Now, we let some time t to pass, so that all $\vec{u}_i$ would evolve under (1.11). The following question arises: according to which probability density $\vec{u}_i(t)$ are distributed at the time t?

The answer to the question is given by the following *Liouville equation* for the probability density:

$$\frac{\partial}{\partial t}\rho(\vec{u}, t) + \text{div}_{\vec{u}} \left[\rho(\vec{u}, t)\vec{F}(\vec{u})\right] = 0. \tag{1.12}$$

Thus, if we have the dynamical system of the form (1.11) for evolution of a vector $\vec{u}(t)$, the corresponding evolution equation for the probability density $\rho(\vec{u}, t)$ for $\vec{u}(t)$, which is defined in the Definition 1, is given by the Liouville equation (1.12).

1.2.2 The Liouville property and the invariant probability measure

As we would see in the previous section, given the initial probability density $\rho_0(\vec{u})$, we can (in principle) find the probability density for $\vec{u}(t)$ at any moment of time by solving the corresponding Liouville equation. However, usually it is hard to do, and therefore we will make the following assumption: let us assume that for the majority of natural initial conditions for the Liouville equation, the solution eventually approaches one of the steady solutions of the Liouville equation. A steady solution of the Liouville equation is called the *invariant probability density*, and the probability measure, associated with this probability density, is called the *invariant probability measure*. With the above assumption we can

look for the steady solutions of the Liouville equation, which is much simpler than solving it directly.

To give the reader an example, let us assume that the dynamical system (1.11) conserves the convex functional, *energy*, of the form

$$E = \frac{1}{2}\sum_i u_i^2. \tag{1.13}$$

In other words, the energy (1.13) is a sphere in $\mathbb{R}^N$, centered at the origin. Since the energy is conserved, any trajectory for (1.11) lies in the sphere of constant energy (1.13).

We also require the additional property for the right-hand side of (1.11), which is called the *Liouville property*:

$$\mathrm{div}\vec{F} = 0. \tag{1.14}$$

Given the properties (1.13) and (1.12) of the dynamical system (1.11), we are now going to show that the uniform measure on the surface of constant energy is the invariant probability measure.

First of all, let us note that if the system (1.11) possesses the Liouville property (1.14), then the Liouville equation (1.12) for (1.11) becomes

$$\frac{\partial \rho}{\partial t} + \vec{F}\nabla\rho = 0,$$

which means that the following relation holds:

$$\rho(\vec{u}(t_1), t_1) = \rho(\vec{u}(t_2), t_2), \tag{1.15}$$

i.e. the probability density along *any* trajectory is constant (does not depend on time). This includes all trajectories that lie on the surface of constant energy. However, we are talking about the probability density *in the phase space*, and *not* the probability density *on the surface* (which is a set of measure zero).

In order to see that the uniform surface measure is the invariant probability measure on the surface of constant energy, let us think about the volume which is confined between the two nested surfaces of constant energy. Obviously this set is invariant under the equations (1.11), since any trajectory in this set will stay in this set forever, and therefore the measure of this set will not change in time. Then, the uniform probability measure of

any subset of the phase space between the two nested spheres of constant energy will also stay constant due to (1.15). Now we write

$$\mathrm{d}\mu = \mathrm{d}s \cdot \mathrm{d}h = \mathrm{const},$$

where $\mathrm{d}\mu$ is the uniform phase space probability measure (which is invariant), $\mathrm{d}s$ is the uniform surface measure, and $\mathrm{d}h$ is the "height" of the thin layer of phase space between our surfaces. In order to see that the surface measure $\mathrm{d}s$ is invariant probability measure, we will show that the "height" $\mathrm{d}h$ stays constant on the surface.

As we assume that the energy surfaces are close to each other, we can write

$$\mathrm{d}h = |\nabla E| \, \mathrm{d}E,$$

where E is the energy, and $\mathrm{d}E$ is the difference of energy between two surfaces. Now taking into account the formula for energy (1.13), we conclude that $|\nabla E|$ is the constant on the surface of constant energy. That means that the "height" of the layer is constant, too, and therefore the uniform constant energy surface measure is the invariant probability measure on the surface of constant energy.

1.2.3 The canonical Gibbs measure based on microcanonical uniform surface measure

In the previous section we have shown that the uniform constant energy surface measure is the invariant probability measure on the surface of constant energy for (1.11). The question is: what would the projection of probability measure on only one coordinate look like? We consider the $(N-1)$-dimensional sphere in N-dimensional space. Let us choose the coordinate u out of $\{u_1 \dots u_N\}$. If we choose the interval du on the coordinate u, then the area of the piece of the sphere which can be projected onto du is

$$\mathrm{d}S = \alpha(N)(R^2 - u^2)^{\frac{N-2}{2}} R \, \mathrm{d}u = \alpha(N) R^{N-1} \left(1 - \frac{u^2}{R^2}\right)^{\frac{N-2}{2}} \mathrm{d}u.$$

where $\alpha(N)$ is the coefficient for the sphere area and depends on N only (we do not need to know the precise formula for it). We now put $\alpha(N)R^{N-1}$ into the normalizing factor and write the projection of the surface probability measure:

$$\mathrm{d}P_{R,N} = \frac{1}{Z_{R,N}} \left(1 - \frac{u^2}{R^2}\right)^{\frac{N-2}{2}} \mathrm{d}u.$$

Taking into account the expression for energy (1.13), we note that

$$R^2 = 2E.$$

That means we can rewrite $\mathrm{d}P$ as

$$\mathrm{d}P_{E,N} = \frac{1}{Z_{E,N}} \left(1 - \frac{u^2}{2E}\right)^{\frac{N-2}{2}} \mathrm{d}u.$$

Now we will take the limit as $N \to \infty$ (we have many dimensions). Obviously, the limit as E stays fixed degenerates to the delta-function centered at zero. Let us scale energy with the number of dimensions, i.e. let us keep the *energy density* (energy per degree of freedom) fixed. In order to do it, we introduce the *variance*

$$\sigma^2 = \frac{2E}{N}.$$

Then we write

$$\mathrm{d}P_{\sigma^2,N} = \frac{1}{Z_{\sigma^2,N}} \left(1 - \frac{u^2}{\sigma^2 N}\right)^{\frac{N-2}{2}} = \frac{1}{Z_{\sigma^2,N'}} \left(1 - \frac{u^2}{2\sigma^2 N'}\right)^{N'-1} \mathrm{d}u.$$

(Here we substituted $2N' = N$). Now it is very easy to take limit as $N' \to \infty$:

$$\mathrm{d}P_{\sigma^2} = \lim_{N' \to \infty} \mathrm{d}P_{\sigma^2,N'} = \frac{1}{Z_{\sigma^2}} \exp\left(-\frac{u^2}{2\sigma^2}\right) \mathrm{d}u. \tag{1.16}$$

We can see that in case with many dimensions and energy density fixed the probability measure for one degree of freedom is Gaussian.

Strictly saying, the distributions along different directions are not independent from each other for the finite-dimensional sphere. However, for simplicity we can assume, that when we have a really large amount of degrees of freedom (how large – that's the question), then we could take a smaller set of degrees of freedom out of the whole system and say that since we have many dimensions overall, then the degrees of freedom in our set are almost independent. That means that the measure for this set is just a product of the

measures for the separate degrees of freedom in this set:

$$\mathrm{d}P_{\sigma^2,\mathrm{Gibbs}} = \frac{1}{Z_{\sigma^2}} \exp\left(-\frac{1}{2\sigma^2}\sum_j u_j^2\right) \mathrm{d}\vec{u} = \frac{1}{Z_{\sigma^2}} \exp\left(-\frac{E}{\sigma^2}\right) \mathrm{d}\vec{u}. \tag{1.17}$$

This is the *canonical Gibbs probability measure*. It is very convenient to use, unlike the uniform surface measure which we have started with. The only question is to which extent the canonical Gibbs measure is a valid approximation to the microcanonical surface measure.

1.2.4 The maximum entropy principle and the most probable probability measure

The maximum entropy principle presented here utilizes ideas from the information theory developed by Shannon [24] and Jaynes [8] in late forties – mid fifties of the last century. The more applicable for our purposes description of the maximum entropy principle can be found in [17] by Majda and Wang. This alternative approach to the statistical description of the system provides very efficient tool of determining the large-scale behavior of the system. Unlike conventional techniques, this method allows us to predict the most probable probability measure taking into account the prior information about the system. In order to employ this method, first we define the *entropy* as a functional on the space of probability densities:

$$S[\rho] = -\int \rho \ln(\rho). \tag{1.18}$$

We define the most probable probability measure ρ^* as the measure which maximizes the Shannon entropy subject to the constraint $\bar{E}[\rho] = \bar{E}$, where E is the energy (1.13):

$$\bar{E}[\rho] = \int E\rho.$$

Using the Lagrange multiplier rule, we write

$$\left.\frac{\delta S}{\delta \rho}\right|_{\rho=\rho^*} = \theta \left.\frac{\delta \bar{E}}{\delta \rho}\right|_{\rho=\rho^*}, \tag{1.19}$$

where θ is the Lagrange multiplier for energy. The above equation yields the following expression for the most probable probability measure

$$\rho^* = \frac{1}{Z}\exp(-\theta E) = \frac{1}{Z}\exp\left(-\frac{\theta}{2}\sum_j u_j^2\right). \tag{1.20}$$

As we can see, the most probable probability measure (1.20) coincides with the canonical Gibbs measure (1.17) derived in the previous section. Also from (1.20) follows that the most probable mean state for the equation (1.11) is zero.

1.3 Predictions of the most probable canonical measure under the constraint of known microcanonical measure

In this section we describe the method of the canonical measure prediction given already known microcanonical measure on a manifold of motion. Unlike the predictions with the least bias (in case we do not know anything about the system apart from some conserved quantities), this prediction has a bias, given by a microcanonical measure. The advantage of this method is that microcanonical measure (at least its projections) can be determined numerically from a single direct simulation of the system. We also show the real application of this method to the statistical study of the truncated system of barotropic flow equations with topography with many conserved quantities.

As we know, the statistical theory based on maximizing the entropy subject to the conserved quantities constraints gives the most probable statistical state provided that no prior knowledge about the system is given. Namely, for the entropy defined by

$$S(\rho) = -\int \rho \ln(\rho), \tag{1.21}$$

and the energy E, given by (1.13), the most probable statistical state is defined by

$$\left.\frac{\delta S}{\delta \rho}\right|_{\rho=\rho^*} = \left.\frac{\delta \bar{E}}{\delta \rho}\right|_{\rho=\rho^*}, \tag{1.22}$$

where θ is the Lagrange multiplier for the mean energy, and ρ^* is the probability density associated with the most probable statistical state. This method always yields the canonical Gibbs probability measure

$$\rho^* = \Gamma^{-1}\exp\left(-\theta E\right). \tag{1.23}$$

Let us note, that the above method formally works only when the conserved quantities are convex, in other words, when ρ^* is normalizable. However, it happens regularly that

interesting conserved quantities are not convex, and this method does not work.

Now let us assume that we already know the microcanonical distribution on some closed surface (can be measured directly). Given this constraint, we again ask the question: what would be the canonical Gibbs measure on that surface? Well, the answer is

$$\rho^*(\,\mathrm{d}\mu) = \Gamma^{-1} \exp\left(-\theta E\right)\,\mathrm{d}\mu, \tag{1.24}$$

where $\mathrm{d}\mu$ is the microcanonical surface measure (which is known). The way we do that is that we now think of a manifold as of the whole phase space (we can do that provided that the number of dimensions is big enough), and then do precisely the same thing as if no bias were given. This time, however, we have no problem with conserved quantities which are not convex, because the motion occurs on a finite manifold. Let us now choose the suitable coordinate system, such that we can project μ on the basis vectors:

$$\mathrm{d}\mu = \Pi(\lambda)\,\mathrm{d}\lambda. \tag{1.25}$$

The canonical Gibbs measure written in this notation is

$$\rho^*(\lambda) = \Gamma^{-1} \exp\left(-\theta E(\lambda)\right) \Pi(\lambda). \tag{1.26}$$

Thus, knowing the microcanonical measure on the surface in which the motion occurs, we can predict the canonical Gibbs measure.

1.3.1 Predictions of the most probable canonical measure via entropy maximization

In this section we consider the situation described above in terms of entropy theory. Given the initial bias, we would like to count that into the entropy theory. The entropy in this case will be written as

$$S(\rho, \Pi) = -\int \rho \ln\left(\frac{\rho}{\Pi}\right), \tag{1.27}$$

where Π is the initial bias (prior distribution). The predicted most probable statistical state is, as before, described by the equation

$$\left.\frac{\delta S}{\delta \rho}\right|_{\rho=\rho^*} = \theta \left.\frac{\delta \bar{E}}{\delta \rho}\right|_{\rho=\rho^*}. \tag{1.28}$$

However, this time the solution of the equation is

$$\rho^*(\lambda) = \Gamma^{-1} \exp\left(\theta E(\lambda)\right) \Pi(\lambda), \tag{1.29}$$

As we can see, we obtain the same result as in previous section just by maximizing the entropy under the initial bias.

As we will see later in this work, the maximum entropy principle is the powerful tool for the predictions of the most probable statistical state of the system. In Sections 1.2.2 and 1.2.3 we have shown the rigorous way of finding the invariant probability measure on the surface of constant energy and its projections on the individual coordinates, however that was done in the simplest case one can imagine, with a single spherical conserved quantity. In case with several conserved quantities it is very hard (maybe even impossible) to find the invariant probability measure rigorously. However, as the reader probably observed, several conserved quantities is not a problem for the maximum entropy principle, it just means that the equation (1.19) has more than one terms in the right-hand side. We will use the maximum entropy principle in determining the most probable statistical state in the truncated Burgers-Hopf equation, and in the truncated equations for the barotropic flow. As the reader will later see, the maximum entropy principle works just fine and the direct numerical simulations confirm the statistical predictions in most cases.

CHAPTER 2
HAMILTONIAN STRUCTURE AND STATISTICALLY RELEVANT CONSERVED QUANTITIES FOR THE TRUNCATED BURGERS-HOPF EQUATION

This chapter is based on the paper [2] by G. Kovačič, A. Majda and the author.

Recently, Majda and Timofeyev [18, 19] have introduced the Galerkin truncation of the Burgers-Hopf equation as an extremely simple one-dimensional model with complex features in common with vastly more complex and challenging problems in contemporary science ranging from short term climate prediction for the coupled atmosphere-ocean system to simulating protein folding through molecular dynamics. The model is defined through the finite Fourier series truncation of a real-valued 2π-periodic function f, $P_\Lambda f = f_\Lambda$, with

$$P_\Lambda f = f_\Lambda = \sum_{|k| \leq \Lambda} \hat{f}_k \, e^{ikx}, \quad \hat{f}_{-k} = \hat{f}_k^*.$$

This model is defined by the Galerkin truncation of the Burgers-Hopf equation,

$$(u_\Lambda)_t + \frac{1}{2} P_\Lambda (u_\Lambda^2)_x = 0.$$

Despite its simplicity, solutions of this model with a fairly large number of degrees of freedom, i.e. Λ ranging from 10 to 200, exhibit intrinsic chaos and more importantly as a model for complex applications, a wide range of scales for the correlations which can be predicted by a simple scaling theory and confirmed numerically (see [18, 19], and Sections 2.2 and 2.3 below). These properties make the truncated Burgers-Hopf equation an ideal simplified model for testing theories of predictability [9] and stochastic mode reduction [14, 15] designed for vastly more complex applications.

Solutions of the truncated Burgers-Hopf equations have the three conserved quantities

$$\int u_\Lambda dx = M, \quad \text{Momentum},$$

$$\int P(u_\Lambda^2)dx = E, \quad \text{Energy},$$

$$\int P(u_\Lambda^3)dx = H, \quad \text{Hamiltonian}.$$

In references [18] and [19], Majda and Timofeyev developed an equilibrium statistical theory for the truncated Burgers-Hopf equation based solely on the two conserved quantities defined by momentum and energy, M and E alone, with corresponding predictions of equipartition of energy which were verified with astonishing accuracy for a wide variety of deterministic and random initial data. See Sections 2.2 and 2.3 in this chapter for more discussion and amplification on the results from [18] and [19]. The first new contribution in the thesis is developed in Section 2.1 where the authors established that the TBH equation is a Hamiltonian system with Hamiltonian, $H(u_\Lambda)$, defined by the integral of the third power of u_Λ; in particular, $H(u_\Lambda)$ is a conserved quantity.

At the time of their initial investigations, Majda and Timofeyev [18, 19] were unaware of the additional conserved quantity, $H(u_\Lambda)$. Thus, the question naturally arises regarding whether and when this additional conserved quantity is statistically relevant for solutions of the truncated Burgers-Hopf dynamics? Quantifying and answering this question through the symbiotic interaction of mathematical theory, concise numerical algorithms for equilibrium statistical mechanics, and direct simulations is the objective of Sections 2.2, 2.3 and 2.4 in this chapter.

In Section 2.2, the authors discuss equilibrium statistical mechanics formulations for the truncated Burgers-Hopf equation which include the Hamiltonian, $H(u_\Lambda)$, as a conserved quantity. Also a convergent Monte-Carlo algorithm for computing integrals over large dimensional spheres, utilized here for Λ ranging from 10 to 100, is developed in Section 2.2. This algorithm is applied in Section 2.2 for calculating the probability density of the Hamiltonian on a microcanonical energy surface with fixed mean energy as the number of degrees of freedom, Λ, increases. This probability distribution is roughly self-similar and Gaussian and peaks sharply around the value $H(u_\Lambda) = 0$ as Λ increases. Since the Hamiltonian is clearly statistically irrelevant on the subsurface defined by $H(u_\Lambda) = 0$, these facts naturally lead to the concept of statistically relevant and irrelevant values of the Hamiltonian defined in Section 2.2. It is established in Section 2.2 through the above empirical facts and a simple small deviation argument that the statistically relevant values for the Hamiltonian occupy a set of vanishingly small probability as Λ increases for fixed mean energy. All of the initial data, both deterministic and random, utilized by

Majda and Timofeyev in references [18] and [19] lie in the statistically irrelevant regime for the Hamiltonian and this explains why the Hamiltonian played no role in the earlier studies. In Section 2.3, systematic numerical simulations are developed for the truncated Burgers-Hopf equation which confirm the role of statistically relevant and irrelevant values for the Hamiltonian. The correlation scaling law proposed in [18] and [19] is confirmed for both statistically relevant and irrelevant values of the Hamiltonian. Despite this fact, for statistically relevant values of the Hamiltonian, there is a tilt in the energy spectrum rather than equipartition of energy. In Section 2.4, this novel tilt in the spectrum for statistically relevant values of the Hamiltonian is predicted with surprising accuracy by a purely equilibrium statistical Monte-Carlo calculation. This agreement between the equilibrium statistical predictions and the direct numerical simulations for the spectral tilt verifies the accuracy of both complementary approaches and also sharply supports the ergodicity of the truncated Burgers-Hopf equation on the intersection of the hypersurfaces, $H = H_0$ and $E = E_0$.

Once again, the truncated Burgers-Hopf equation has a role as a simple model. The issues of statistically relevant and irrelevant conserved quantities discussed in the thesis for the truncated Burgers-Hopf equation serve as an elementary model for the same issues in much more complex geophysical applications where these issues have genuinely practical significance ([5, 7, 16, 17, 23], also see additional references in [16]). To simplify this discussion, we note that inviscid two-dimensional flow has the infinitely many conserved quantities involving vorticity,

$$\int |\omega|^p = Q_p(\omega),$$

besides the energy and the statistical relevance of these and related conserved quantities is a hotly debated topic in the applied literature ([5, 7, 16, 17, 23] and references therein).

2.1 Truncated Burgers-Hopf Equation as a Hamiltonian System

We begin with the Burgers-Hopf equation,

$$u_t + uu_x = 0, \qquad u(x,t) = u(x + 2\pi, t). \tag{2.1}$$

It is well known that for smooth solutions the Burgers-Hopf equation (2.1) is Hamiltonian, and can in fact be derived via two distinct Hamiltonian structures [22]. We begin this section by briefly reviewing the structure that we will use in the rest of the chapter.

To set the framework for our discussion, we first recall the definition of a Poisson bracket on the space of infinitely smooth periodic functions on the interval $[0, 2\pi]$; see [1, 3]. Given any two functionals $\mathcal{F}[u, u_x, u_{xx}, \ldots]$ and $\mathcal{G}[u, u_x, u_{xx}, \ldots]$ on this space, a Poisson bracket is defined by the formula

$$\{\mathcal{F}, \mathcal{G}\} \equiv \int_0^{2\pi} dx \, \frac{\delta \mathcal{F}}{\delta u} J \frac{\delta \mathcal{G}}{\delta u}, \tag{2.2}$$

where $\delta \cdot / \delta u$ denotes the variational derivative. The operator

$$J(u, u_x, u_{xx}, \ldots)$$

is called the symplectic operator, and must satisfy the following two properties:

- J must be skew-symmetric, so that $\{\mathcal{A}, \mathcal{B}\} = -\{\mathcal{B}, \mathcal{A}\}$ for any two functionals $\mathcal{A}[u, u_x, u_{xx}, \ldots]$ and $\mathcal{B}[u, u_x, u_{xx}, \ldots]$,
- J must induce the Jacobi identity

$$\{\{\mathcal{A}, \mathcal{B}\}, \mathcal{C}\} + \{\{\mathcal{C}, \mathcal{A}\}, \mathcal{B}\} + \{\{\mathcal{B}, \mathcal{C}\}, \mathcal{A}\} = 0$$

  in the Poisson bracket (2.2).

Given a Poisson bracket, an equation of the form

$$u_t = F(u, u_x, u_{xx}, \ldots) \tag{2.3}$$

is defined to be Hamiltonian if it can be written as

$$u_t = J(u, u_x, u_{xx}, \ldots) \frac{\delta \mathcal{H}[u, u_x, u_{xx}, \ldots]}{\delta u}. \tag{2.4}$$

The functional $\mathcal{H}$ is the corresponding Hamiltonian for this equation.

One can easily compute that the evolution of any quantity

$$\mathcal{F}[u, u_x, u_{xx}, \ldots]$$

under the dynamics of equation (2.4) obeys the equation

$$\mathcal{F}_t = \{\mathcal{F}, \mathcal{H}\}. \tag{2.5}$$

Two more properties are evident, namely,

- The Hamiltonian is conserved in time, i.e.

$$\mathcal{H}_t = \{\mathcal{H}, \mathcal{H}\} = -\{\mathcal{H}, \mathcal{H}\} = 0.$$

- Any functional $\mathcal{C}$ that satisfies

$$J\frac{\delta \mathcal{C}}{\delta u} \equiv 0 \tag{2.6}$$

  independently of the choice of the function u is conserved regardless of what the Hamiltonian $\mathcal{H}$ is. Such functionals are called Casimir invariants, and only depend on the operator J.

2.1.1 A Hamiltonian representation of the Burgers-Hopf equation

The Burgers-Hopf equation (2.1) belongs to the class of equations

$$u_t + [f(u)]_x = 0. \tag{2.7}$$

Restricted to smooth solutions, any such equation with periodic boundary conditions $u(x,t) = u(x+2\pi, t)$ is Hamiltonian, and can be written as

$$u_t = J\frac{\delta \mathcal{H}}{\delta u}, \tag{2.8a}$$

where the symplectic operator J and the Hamiltonian $\mathcal{H}$ are given by the formulas

$$J = -2\pi\frac{\partial}{\partial x} \tag{2.8b}$$

$$\mathcal{H} = \int_0^{2\pi} F(u)dx, \qquad F_u = f(u), \tag{2.8c}$$

respectively. For periodic u, the symplectic operator J is clearly skew-symmetric, and automatically satisfies the Jacobi identity because it does not depend on the function u or its derivatives. The corresponding Poisson bracket is

$$\{\mathcal{F}, \mathcal{G}\} = \int_0^{2\pi} \frac{\delta \mathcal{F}}{\delta u}\left(-2\pi\frac{\partial}{\partial x}\right)\frac{\delta \mathcal{G}}{\delta u}dx. \tag{2.9}$$

For the Burgers-Hopf equation (2.1) we set

$$f(u) = \frac{1}{2}u^2,$$

and therefore

$$\mathcal{H} = \frac{1}{12\pi}\int_0^{2\pi} u^3 dx. \tag{2.10}$$

In the context of the Korteweg-deVries equation, the Hamiltonian structure (2.8) and the Poisson bracket (2.9) were discovered in [6].

The symplectic operator (2.8b) possesses a single Casimir invariant. To show this, we note that the condition that this Casimir invariant must satisfy is

$$\frac{\partial}{\partial x}\frac{\delta \mathcal{C}}{\delta u} = 0,$$

that is,

$$\frac{\delta \mathcal{C}}{\delta u} = \text{const.}$$

Since this last equation must be valid for every smooth function u that is inserted in the functional $\mathcal{C}$, the only possible solution can be

$$\mathcal{C} = \text{const.}\int_0^{2\pi} u\, dx.$$

The particular choice of the constant, $1/2\pi$, yields

$$\mathcal{C} = \frac{1}{2\pi}\int_0^{2\pi} u\, dx, \tag{2.11}$$

which is the momentum of the solution $u(x,t)$.

The generalized equation (2.7) also has infinitely many conserved quantities of the form

$$\frac{\partial}{\partial t}\int_0^{2\pi} g(u)\, dx = 0. \tag{2.12}$$

This can be easily shown by the calculation

$$\frac{\partial}{\partial t}\int_0^{2\pi} g(u)\,dx = \int_0^{2\pi} g_t dx = \int_0^{2\pi} g_u u_t\,dx =$$
$$= -\int_0^{2\pi} g_u f_u u_x\,dx = -\int_0^{2\pi} G'(u)u_x\,dx =$$
$$= -\int_0^{2\pi}\Big[G(u)\Big]_x\,dx = 0,$$

with $G(u)$ chosen so that $G'(u) = g_u(u)f_u(u)$, with $u(x,t)$ real and periodic.

2.1.2 Hamiltonian representation of the truncated Burgers-Hopf equation

In this section we explain how the Hamiltonian structure of the Burgers-Hopf equation (2.1) that we discussed in the previous section induces a Hamiltonian structure on the finite Fourier truncation of this equation. In particular, we will see that both the Hamiltonian (2.10) and the momentum Casimir (2.11) that we find in the truncated system are natural truncations of their counterparts in the original Burgers-Hopf dynamics. We will show below that another conserved quantity, the energy, also survives under truncation.

We begin by denoting the projection operator P_Λ on a finite number, $(2\Lambda+1)$, of Fourier modes by

$$P_\Lambda f(x) = f_\Lambda(x) = \sum_{k=-\Lambda}^{\Lambda} \hat{f}_k e^{ikx}, \tag{2.13}$$

where

$$\hat{f}_k = \frac{1}{2\pi}\int_0^{2\pi} f(x)e^{-ikx}dx$$

is the k-th Fourier coefficient of the function $f(x)$. For real functions $f(x)$,

$$\hat{f}_{-k} = \hat{f}_k^*.$$

By using the projection operator (2.13), we write the truncated Burgers-Hopf equation as

$$(u_\Lambda)_t + \frac{1}{2}\frac{\partial}{\partial x}P_\Lambda\left(u_\Lambda^2\right) = 0. \tag{2.14}$$

This equation is Hamiltonian with the same symplectic structure (2.8) as the original Burgers-Hopf equation (2.1), and the corresponding Hamiltonian is the projection of the

original Hamiltonian (2.10) on the first $(2\Lambda + 1)$ Fourier modes,

$$H = \frac{1}{12\pi} \int_0^{2\pi} P_\Lambda(u_\Lambda^3) dx. \tag{2.15}$$

To show this, we first observe that the restriction of the Poisson bracket (2.9) to functionals of the form

$$\mathcal{F}_\Lambda \left[u_\Lambda, u_{\Lambda\, x}, u_{\Lambda\, xx}, \ldots\right] = \int_0^{2\pi} P_\Lambda F\left(u_\Lambda, u_{\Lambda\, x}, u_{\Lambda\, xx}, \ldots\right)\, dx. \tag{2.16}$$

is clearly still a Poisson bracket. Thus all we have to show is that the equation (2.14) has the form (2.8a) with the Hamiltonian (2.15). This is true because

$$\frac{\delta H(u_\Lambda)}{\delta u_\Lambda} = \frac{1}{12\pi} \frac{\partial P_\Lambda(u_\Lambda^3)}{\partial u_\Lambda} = \frac{1}{4\pi} P_\Lambda(u_\Lambda^2), \tag{2.17}$$

where the last equality is shown by a straightforward calculation.

Since the Poisson bracket for the truncated Burgers-Hopf equation (2.14) is the same as that for the original Burgers-Hopf equation (2.1), it possesses the same momentum Casimir invariant, which in the appropriate projected space reads

$$C = \frac{1}{2\pi} \int_0^{2\pi} u_\Lambda\, dx. \tag{2.18}$$

The projected Burgers-Hopf equation (2.14) possesses one more conserved quantity, namely, the *energy*

$$E = \frac{1}{4\pi} \int_0^{2\pi} P_\Lambda\left(u_\Lambda^2\right)\, dx. \tag{2.19}$$

In order to see that the energy is indeed conserved, we compute its Poisson bracket with the Hamiltonian (2.15) to obtain

$$\{E, H\} = -\int_0^{2\pi} \frac{1}{2\pi} u_\Lambda \frac{\partial}{\partial x} \frac{1}{2} P_\Lambda(u_\Lambda^2) dx =$$

$$= \int_0^{2\pi} \frac{1}{4\pi} P_\Lambda(u_\Lambda^2) \frac{\partial u_\Lambda}{\partial x} dx = \int_0^{2\pi} \frac{1}{12\pi} \frac{\partial P_\Lambda(u_\Lambda^3)}{\partial x} dx = 0,$$

where in the last formula we utilized (2.17).

Since no shocks can develop in a finite truncation, the Hamiltonian (2.15), the

momentum (2.18), and the energy (2.19) are conserved by the dynamics of the truncated Burgers-Hopf equations (2.14) for all times.

While, for smooth solution, the original Burgers-Hopf equation (2.1) possesses an infinite family of conserved quantities, this appears not to be the case for the projected Burgers-Hopf equation (2.14). In fact, we find that no projected powers of u except for the first three just described are conserved, that is,

$$\{P_\Lambda\left(u_\Lambda^n\right), H\} \neq 0, \qquad n > 3.$$

To show this, we follow the sequence of equalities that begins with the anti-symmetry of the Poisson bracket,

$$\int_0^{2\pi} \frac{\partial P_\Lambda\left(u_\Lambda^n\right)}{\partial u_\Lambda} \frac{\partial}{\partial x} \frac{\partial P_\Lambda\left(u_\Lambda^3\right)}{\partial u_\Lambda} dx = -\int_0^{2\pi} \frac{\partial P_\Lambda\left(u_\Lambda^3\right)}{\partial u_\Lambda} \frac{\partial}{\partial x} \frac{\partial P_\Lambda\left(u_\Lambda^n\right)}{\partial u_\Lambda} dx,$$

$$\int_0^{2\pi} P_\Lambda\left(u_\Lambda^{n-1}\right) \frac{\partial}{\partial x} P_\Lambda\left(u_\Lambda^2\right) dx = -\int_0^{2\pi} P_\Lambda\left(u_\Lambda^2\right) \frac{\partial}{\partial x} P_\Lambda\left(u_\Lambda^{n-1}\right) dx,$$

$$\begin{aligned} 2\int_0^{2\pi} P_\Lambda\left(u_\Lambda^{n-1}\right) P_\Lambda\left(u_\Lambda \frac{\partial u_\Lambda}{\partial x}\right) dx = \\ = -(n-1)\int_0^{2\pi} P_\Lambda\left(u_\Lambda^2\right) P_\Lambda\left(u_\Lambda^{n-2} \frac{\partial u_\Lambda}{\partial x}\right) dx. \end{aligned} \tag{2.20}$$

On the other hand, if the Poisson bracket of two quantities vanishes, it is symmetric, therefore

$$\begin{aligned} 2\int_0^{2\pi} P_\Lambda\left(u_\Lambda^{n-1}\right) P_\Lambda\left(u_\Lambda \frac{\partial u_\Lambda}{\partial x}\right) dx = \\ = (n-1)\int_0^{2\pi} P_\Lambda\left(u_\Lambda^2\right) P_\Lambda\left(u_\Lambda^{n-2} \frac{\partial u_\Lambda}{\partial x}\right) dx. \end{aligned} \tag{2.21}$$

We can see that, in general, equations (2.20) and (2.21) cannot be satisfied simultaneously unless $n = 1$, 2 or 3.

Before concluding this section, we observe that Galilean invariance leads to a useful symmetry of the truncated Burgers-Hopf equations (2.14) (which obviously holds for the original Burgers-Hopf equations (2.1)). In particular, let $\hat{u}_0$ denote the average of the

given solution function $u_\Lambda(x,t)$ in the interval $0 < x < 2\pi$, that is,

$$\hat{u}_0 = \frac{1}{2\pi}\int_0^{2\pi} u_\Lambda(x,t)\,dx.$$

In other words, $\hat{u}_0$ equals the zeroth Fourier coefficient of $u_\Lambda(x,t)$ and also equals the momentum Casimir invariant $C[u_\Lambda]$ in (2.18). Therefore, it is independent of the time t. Clearly, since $u_\Lambda(x,t)$ is real, then so is $\hat{u}_0$. Let

$$v_\Lambda(x,t) = u_\Lambda(x,t) - \hat{u}_0.$$

Then

$$C\left[v_\Lambda\right] = 0,$$

$$E\left[v_\Lambda\right] = E\left[u_\Lambda\right] - \frac{1}{2}\left|\hat{u}_0\right|^2,$$

$$H\left[v_\Lambda\right] = H\left[u_\Lambda\right] - \hat{u}_0 E\left[u_\Lambda\right] + \frac{1}{3}\hat{u}_0^3,$$

and equations (2.14) become

$$\left(v_\Lambda\right)_t + \hat{u}_0\left(v_\Lambda\right)_x + \frac{1}{2}\frac{\partial}{\partial x}P_\Lambda\left(v_\Lambda^2\right) = 0.$$

The shift of the time variable $t \to t - \hat{u}_0 x$ transforms this equation back into

$$\left(v_\Lambda\right)_t + \frac{1}{2}\frac{\partial}{\partial x}P_\Lambda\left(v_\Lambda^2\right) = 0,$$

that is, equation (2.14). This argument shows that with no loss of generality we can consider solutions $u_\Lambda(x,t)$ with zero mean.

We remark here that the construction given above establishes that the truncated Burgers-Hopf equation in (2.14) is a Hamiltonian system with (2.13) replaced by any arbitrary finite dimensional projection P. However, here we always use P_Λ in (2.13).

2.1.3 Hamiltonian representation of the truncated Burgers-Hopf equation in spectral space

In the spectral space of Fourier coefficients, the Hamiltonian equation (2.4) assumes the form

$$\frac{\partial \hat{u}_k}{\partial t} = \sum_{k'=-\infty}^{\infty} \hat{J}_{kk'} \frac{\partial \mathcal{H}}{\partial \hat{u}^*_{k'}}. \tag{2.22}$$

Here, $\hat{u}_k$ is the k-th Fourier coefficient, which we recall satisfies the reality condition

$$\hat{u}_k = \hat{u}^*_{-k}, \tag{2.23}$$

$\mathcal{H}$ is the Hamiltonian written in spectral space, and $\hat{J}$ is the infinite symplectic matrix

$$\hat{J}_{kk'} = \left(\frac{\delta \hat{u}_k}{\delta u}\right) J \left(\frac{\delta \hat{u}_{k'}}{\delta u}\right)^{\dagger},$$

with † denoting the Hermitean-conjugate operator. The operator J is the original symplectic operator in physical space.

Transforming the Hamiltonian representation (2.8) and (2.10) for the Burgers-Hopf equation (2.1) into the above-described spectral form, we find

$$\begin{aligned} \hat{J}_{kk'} = \left(\frac{\delta \hat{u}_k}{\delta u}\right) J \left(\frac{\delta \hat{u}_{k'}}{\delta u}\right)^{\dagger} = \\ = -\int_0^{2\pi} \frac{1}{2\pi} e^{-ikx} 2\pi \frac{\partial}{\partial x} \frac{1}{2\pi} e^{ik'x}\, dx = -ik'\delta^k_{k'}, \end{aligned} \tag{2.24a}$$

$$\begin{aligned} \mathcal{H} = \frac{1}{12\pi}\int_0^{2\pi} u^3 dx = \frac{1}{12\pi} \sum_{k_1,k_2,k_3} \hat{u}_{k_1}\hat{u}_{k_2}\hat{u}_{k_3} \int_0^{2\pi} e^{i(k_1+k_2+k_3)x}\, dx \\ = \frac{1}{6} \sum_{k_1+k_2+k_3=0} \hat{u}_{k_1}\hat{u}_{k_2}\hat{u}_{k_3}. \end{aligned} \tag{2.24b}$$

Here, $\delta^k_{k'}$ denotes the Kronecker delta.

In the previous section, we have shown that the truncation (2.14) that restricts the equation (2.1) to its first $(2\Lambda + 1)$ Fourier modes is Hamiltonian with the Hamiltonian function (2.15). Projecting the above results in equations (2.24) onto the first $(2\Lambda + 1)$ Fourier modes yields the truncated symplectic matrix as

$$\hat{J}_{kk'} = -ik'\delta^k_{k'}, \quad |k|, |k'| \leq \Lambda, \tag{2.25}$$

and the spectral representation of the Hamiltonian (2.15) as

$$H = \frac{1}{6} \sum_{\substack{k_1+k_2+k_3=0, \\ |k_1|,|k_2|,|k_3| \leq \Lambda}} \hat{u}_{k_1} \hat{u}_{k_2} \hat{u}_{k_3}. \tag{2.26}$$

Equation (2.14) thus becomes

$$\frac{\partial \hat{u}_k}{\partial t} = -\frac{ik}{2} \sum_{\substack{|k|,|k'| \leq \Lambda \\ |k-k'| \leq \Lambda}} \hat{u}_{k-k'} \hat{u}_{k'} = -ik \frac{\partial H}{\partial \hat{u}_k^*}. \tag{2.27}$$

The projected momentum Casimir invariant (2.18) in the spectral representation assumes the particularly simple form

$$C = \hat{u}_0, \tag{2.28}$$

and the conserved energy (2.19) is transformed into

$$E = \frac{1}{2} \sum_{|k| \leq \Lambda} \hat{u}_k \hat{u}_{-k} = \frac{1}{2} \sum_{|k| \leq \Lambda} |\hat{u}_k|^2 = \frac{|\hat{u}_0|^2}{2} + \sum_{k=1}^{\Lambda} |\hat{u}_k|^2 . \tag{2.29}$$

The last two equalities in this formula are true because of the reality condition (2.23).

2.2 Equilibrium statistical mechanics for the truncated Burgers-Hopf Equation

2.2.1 Gibbs ensemble for the energy

In order to set up an equilibrium statistical mechanics theory of the truncated Burgers-Hopf equations (2.27), we first need to establish that they satisfy the Liouville property. For a system of real ordinary differential equations

$$\dot{\vec{w}} = \vec{F}(\vec{w}), \tag{2.30}$$

with $\vec{w} = (w_1, \ldots, w_N)$ and $\vec{F}(\vec{w}) = (F_1(\vec{w}), \ldots, F_N(\vec{w}))$, the Liouville property is the requirement that the divergence of the vector field $\vec{F}(\vec{w})$ vanish, that is,

$$\nabla \cdot \vec{F}(\vec{w}) = \sum_{k=1}^{N} \frac{\partial F_k(\vec{w})}{\partial w_k} = 0. \tag{2.31}$$

For equations (2.27), we establish the Liouville property as follows: We assume with no loss of generality as at the end of Section 2.1.2 that $\hat{u}_0 = 0$. We let $N = 2\Lambda$, and use the

vector notation

$$\vec{w} = (w_1, \ldots, w_{2\Lambda}), \quad \hat{u}_k = w_{2k-1} + iw_{2k}, \quad k = 1, \ldots, \Lambda, \tag{2.32}$$

to rewrite equations (2.27) in their real form as

$$\dot{w}_{2k-1} = A_k(\vec{w}), \qquad \dot{w}_{2k} = B_k(\vec{w}).$$

Then, by using (2.27), we find

$$\frac{\partial A_k}{\partial w_{2k-1}} + \frac{\partial B_k}{\partial w_{2k}} = -ik\frac{\partial^2 H}{\partial \hat{u}_k \partial \hat{u}_k^*} + ik\frac{\partial^2 H}{\partial \hat{u}_k^* \partial \hat{u}_k} = 0.$$

After summing on k, the Liouville property (2.31),

$$\sum_{k=1}^{\Lambda} \left(\frac{\partial A_k}{\partial w_{2k-1}} + \frac{\partial B_k}{\partial w_{2k}} \right) = 0,$$

follows. (See also [18] for a direct derivation not involving the Hamiltonian structure.)

Densities on $\mathbb{R}^N$ of probability measures for statistical ensembles of solutions of the equations (2.30) satisfy the Liouville equation,

$$\frac{\partial f}{\partial t} + \nabla \cdot \left[f\, \vec{F}(\vec{w}) \right] = 0, \qquad f|_{t=0} = f_0, \tag{2.33}$$

where f_0 is the density of the initial probability measure, and thus satisfies the conditions

$$f_0 \geq 0 \quad \text{and} \quad \int_{\mathbb{R}^N} f_0(\vec{w})\, d\vec{w} = 1.$$

Because of the Liouville property (2.31), any function $G(K)$ of any conserved quantity K of the equations (2.30) must necessarily be a stationary solution of the Liouville equation (2.33).

For the truncated Burgers-Hopf equation (2.27), the discussion of the previous paragraph implies that any function of the momentum C in (2.28), the energy E in (2.29), and the Hamiltonian H in (2.26) is the density of a stationary probability measure for statistical ensembles of its solutions, provided that it is normalizable. In particular, this is true for the densities G_β of the energy-based Gibbs measures,

$$G_\beta = C_\beta e^{-\beta E} = C_\beta e^{-\beta|\vec{w}|^2} = \tag{2.34}$$
$$= C_\beta \exp\left(-\beta \sum_{k=1}^{\Lambda} |\hat{u}_k|^2\right), \qquad \beta > 0,$$

where β is the "inverse temperature," $\vec{w}$ is the vector introduced in (2.32), and

$$|\vec{w}| = \left(\sum_{j=1}^{2\Lambda} w_j^2\right)^{\frac{1}{2}} \tag{2.35}$$

is the length of the vector $\vec{w}$. It is known [11] that the measures in (2.34) are the unique densities that maximize over all the probability densities the information theoretic entropy,

$$S(p) = -\int_{\mathbb{R}^N} p(\vec{w}) \ln p(\vec{w})\, d\vec{w}, \qquad p > 0, \qquad \int_{\mathbb{R}^N} p(\vec{w})\, d\vec{w} = 1,$$

subject to the constraint

$$\bar{E} = \int_{\mathbb{R}^N} E(\vec{w}) p(\vec{w})\, d\vec{w}.$$

Here, $\bar{E}$ is a positive constant representing the mean value of the energy E over the distribution $p(\vec{w})$, and the inverse temperature β is the Lagrange multiplier associated with the maximization problem. The energy-based Gibbs measure (2.34) predicts that the energy should be equipartitioned among all the Fourier modes, and that the mean energy per mode should be

$$\bar{E}_{p/m}(\Lambda) = \frac{\bar{E}}{2\Lambda} = \frac{1}{2\beta}. \tag{2.36}$$

In direct numerical simulations, the stationary probability measure is sampled by following long-time trajectories. If the system is ergodic, then given an initial time T_0 and a function $g\left(\hat{u}_{k_1}, \ldots, \hat{u}_{k_j}\right)$, its expected value with respect to the measure that is being sampled equals its time average,

$$\langle g \rangle = \int_{\mathbb{R}^N} g(\vec{w}) p(\vec{w})\, d\vec{w} = \frac{1}{T} \int_{T_0}^{T+T_0} g\left(\hat{u}_{k_1}(t), \ldots, \hat{u}_{k_j}(t)\right)\, dt \tag{2.37}$$

in the limit $T \to \infty$, where T is the length of the averaging window. In numerical simulations, the times T and T_0 are fixed at a sufficiently large value so that the numbers on the right-hand side of (2.37) exhibit numerical convergence for the desired functionals

g. In particular, the mean energy of the k-th mode $\hat{u}_k$ is computed as

$$\frac{1}{2}\left\langle |\hat{u}_k|^2 \right\rangle = \frac{1}{2T}\int_{T_0}^{T+T_0} |\hat{u}_k(t)|^2 \, dt, \tag{2.38}$$

and the temporal correlation function $c_k(\tau)$ of the k-th mode as

$$c_k(\tau) = \frac{1}{T\left\langle |\hat{u}_k|^2 \right\rangle}\int_{T_0}^{T+T_0} \Big(\hat{u}_k(t) - \langle \hat{u}_k \rangle\Big)\Big(\hat{u}_k(t+\tau) - \langle \hat{u}_k \rangle\Big)^* \, dt. \tag{2.39}$$

By using (2.39), we also define the correlation time T_k for the k-th Fourier mode as

$$T_k = \int_0^{\infty} |c_k(\tau)| \, d\tau. \tag{2.40}$$

In [18, 19], for the truncated Burgers-Hopf equations (2.27), the energy equipartition prediction (2.36) that follows from the energy-based Gibbs measure (2.34) was verified with remarkable accuracy when compared with the computed mean energy per mode in (2.38) for a wide variety of deterministic and random initial data. This was a severe test, since only the microcanonical statistics for an individual trajectory of the equations (2.27) were sampled rather than a Monte-Carlo average over a large number of random initial data as given by the energy-based Gibbs ensemble. In addition, a remarkable correlation scaling theory was developed in [18, 19], which states that the correlation time T_k in (2.40) is proportional to the eddy turnover time,

$$T_k = C_0 \frac{\sqrt{\beta}}{|k|}, \qquad 1 \le |k| \le \Lambda, \tag{2.41}$$

with a universal proportionality constant C_0. The results of [18, 19] also show excellent agreement between the correlation times computed numerically by using formula (2.40) and those predicted analytically from formula (2.41) with the constant C_0 chosen to exactly match the correlation time for the mode with $k = 1$.

In most large Hamiltonian systems, the energy and the Hamiltonian are one and the same, and the energy-based Gibbs measure (2.34) is the canonical Gibbs measure of the system. In the truncated Burgers-Hopf equation (2.27), however, this is not the case. The energy E is not the Hamiltonian of the system. Instead, the Hamiltonian is the cubic function H in (2.26). A question thus arises as to the role of this Hamiltonian in the invariant measure for the statistical mechanics of the equation (2.27), in the shape of the

correlation functions (2.39), and the correlation scaling law prediction (2.41). We begin addressing this question in the next section, and address it again in Sections 2.3 and 2.4.

2.2.2 Mixed microcanonical energy and canonical Hamiltonian ensembles

The truncated Burgers-Hopf equations (2.14), or equivalently (2.27), possess three conserved quantities, the momentum Casimir C in (2.28), the energy E in (2.29), and the Hamiltonian H in (2.26). In this section, we address the relevance of these quantities for the equilibrium statistical mechanics of the equations (2.14). By the argument made at the end of Section 2.1.2, it is clear that the Casimir C can be ignored completely, because, by a simple coordinate change, any solution of equations (2.14) can be mapped into a solution of the same set of equations (2.14) for which $C = 0$. Thus, from now on, we will always assume that every solution $u_\Lambda(x,t)$ of the truncated Burgers-Hopf equations (2.14) that we will investigate has zero mean, that is, its zeroth Fourier coefficient $\hat{u}_0$ vanishes. We therefore turn our attention to the relevance of the Hamiltonian H in (2.26).

In this section, we present a number of numerical and analytical arguments that classify the values of the Hamiltonian H in (2.26) as "typical" and "atypical." While the precise definition is given below, at the very end of this section, roughly speaking, typical values of the Hamiltonian are those that are the most likely to be attained along randomly chosen trajectories. The computational results described in Section 2.3 put forth strong numerical evidence that the typical values of the Hamiltonian H are irrelevant for the statistical mechanics associated with the corresponding solutions of the truncated Burgers-Hopf equation (2.27) in the sense that these solutions exhibit the equipartition energy spectrum in (2.38) and an essentially universal correlation structure by obeying the scaling law (2.41) and exhibiting the same structure for the correlation functions (2.39). On the other hand, our numerical results show that the trajectories of (2.27) with atypical values of the Hamiltonian H exhibit a considerable tilt of the energy spectrum, as well as significant oscillations of the correlation functions (2.39) while retaining the overall correlation scaling law in (2.41). An explanation and quantitative prediction through equilibrium statistical mechanics of the tilt in this spectrum for atypical values is developed in Section 2.4 below.

In order to set up an equilibrium statistical mechanics theory for the truncated Burgers-Hopf equations (2.27), we first need to choose an appropriate stationary probability measure for statistical ensembles of solutions. In particular, we need to take into

account the fact that equations (2.27) possess two conserved quantities, the energy E in (2.29) and the Hamiltonian H in (2.26), so that the motion of trajectories is confined to the joint isosurfaces of these two conserved quantities. If the Hamiltonian H in (2.26) were a convex function of its arguments, the natural guess for this stationary probability measure would be the canonical distribution in both the energy and the Hamiltonian with the density

$$G_{\beta,\theta} = C_{\beta,\theta}\, e^{-\beta E - \theta H} = \tag{2.42}$$
$$= C_{\beta,\theta}\, \exp\left(-\beta \sum_{k=1}^{\Lambda} |\hat{u}_k|^2 - \frac{\theta}{6} \sum_{k_1+k_2+k_3=0} \hat{u}_{k_1} \hat{u}_{k_2} \hat{u}_{k_3} \right).$$

Here, $\beta > 0$ and $\theta > 0$ are two constants, an "inverse temperature" and a "chemical potential." However, formula (2.42) cannot possibly represent a probability density, since its integral over the phase space diverges due to the sign-indefiniteness of the Hamiltonian H.

Instead, the correct route is suggested by the fact that all the simulations are performed microcanonically by following long-time trajectories. In particular, the energy E is kept constant during each simulation. Therefore, in order to study which values of the Hamiltonian H are relevant for the statistical mechanics, we may restrict our attention to fixed energy isosurfaces. Since equation (2.29) shows that these are spheres, they are compact, and therefore we can use the canonical distribution of the Hamiltonian confined to one of these spheres without fear that the integral of its density will diverge. The statistical mechanical ensemble that we thus obtain is the mixed microcanonical energy and canonical Hamiltonian ensemble. Next, we will describe it in detail as well as justify its use more precisely.

2.2.2.1 Microcanonical energy ensemble

We begin by recalling the microcanonical energy distribution, given by the uniform measure $d\nu_{\bar{E},\Lambda}$ on the $(2\Lambda - 1)$-dimensional sphere $S_{\bar{E},\Lambda}$ of fixed energy in the 2Λ-dimensional real space with coordinates $\vec{w} = (w_1, \ldots, w_{2\Lambda})$ as in (2.32),

$$S_{\bar{E},\Lambda} = \left\{ \vec{w} \;\middle|\; |\vec{w}|^2 = E(\vec{w}) = \sum_{k=1}^{\Lambda} |\hat{u}_k|^2 = \bar{E} \right\}. \tag{2.43}$$

Here $|\vec{w}|$ is the Euclidean length of the vector $\vec{w}$ given in formula (2.35), the radius of this sphere $S_{\bar{E},\Lambda}$ is $R = |\vec{w}| = \sqrt{\bar{E}}$, and the energy $E(\vec{w}) = |\vec{w}|^2 = \sum_{k=1}^{\Lambda} |\hat{u}_k|^2$ is given by (2.29) with $\hat{u}_0 = 0$. The microcanonical energy distribution is given by the formula

$$d\nu_{\bar{E},\Lambda} = \left[\mathcal{A}\left(S_{\bar{E},\Lambda}\right)\right]^{-1} \delta\left(E(\vec{w}) - \bar{E}\right)\, dw_1 \ldots dw_{2\Lambda}, \tag{2.44}$$

where $\mathcal{A}\left(S_{\bar{E},\Lambda}\right)$ is the area of the $(2\Lambda - 1)$-dimensional sphere $S_{\bar{E},\Lambda}$.

2.2.2.2 Mixed microcanonical energy and canonical Hamiltonian ensembles

In order to find the distribution of the cubic Hamiltonian H (2.26) on the sphere $S_{\bar{E},\Lambda}$ of fixed energy in (2.43) and subsequently classify the typical and atypical values of H, we first ask what is the least biased probability measure on $S_{\bar{E},\Lambda}$ which gives the effect of the Hamiltonian (2.26) given its mean value $\bar{H}$. A standard argument [11, 17] yields the above-mentioned mixed canonical-micro-canonical measure

$$G_{\bar{E},\Lambda,\theta} = \frac{e^{-\theta H(\vec{w})} d\nu_{\bar{E},\Lambda}}{\displaystyle\int_{S_{\bar{E},\Lambda}} e^{-\theta H(\vec{w})} d\nu_{\bar{E},\Lambda}}, \qquad \theta > 0 \tag{2.45}$$

where θ is again an "inverse temperature."

2.2.2.3 Probability distribution of the Hamiltonian on the microcanonical energy surface

To classify the values of the Hamiltonian H on the energy surface $S_{\bar{E},\Lambda}$ as typical or atypical, we need to compute and study the probability measure

$$\mathrm{Prob}_{\bar{E},\Lambda}\left\{\alpha < H(\vec{w}) < \beta\right\} = \int_{\alpha}^{\beta} p_{\bar{E},\Lambda}(\lambda)\, d\lambda \tag{2.46}$$

that describes the distribution of the values of the Hamiltonian H on the sphere of constant energy, $S_{\bar{E},\Lambda}$.

Monte-Carlo algorithm for generating a uniformly distributed sequence of points on the energy sphere. Now we describe a Monte-Carlo algorithm for generating a set of points uniformly distributed on the constant-energy sphere $S_{\bar{E},\Lambda}$ in (2.43) for numerical quadrature of integrals on $S_{\bar{E},\Lambda}$ for large values of Λ between 10 and 100. Here we use this algorithm to compute the Hamiltonian probability distribution function

$p_{\bar{E},\Lambda}(\lambda)$ in (2.46) to give us a natural rough classification of values of the Hamiltonian into typical and atypical ones. We also use this procedure extensively in Section 2.4 below. Since a detailed reference does not seem to be available in the literature we describe this algorithm in some detail below.

We begin by describing a number of geometric properties of the uniform measure (2.44) on the fixed energy sphere $S_{\bar{E},\Lambda}$ that enable us to construct the desired Monte-Carlo algorithm. First, we recall that the uniform measure $\nu_{\bar{E},\Lambda}$ in formula (2.44) on the sphere $S_{\bar{E},\Lambda}$ is characterized by the property that

$$\begin{aligned} \int_{S_{\bar{E},\Lambda}} \varphi\left(\sqrt{\bar{E}}\frac{\vec{w}}{|\vec{w}|}\right)\, d\nu_{\bar{E},\Lambda} = \\ = \left[\mathcal{A}\left(S_{\bar{E},\Lambda}\right)\right]^{-1} \int_{\mathbb{R}^{2\Lambda}} \varphi(\vec{w})\, \delta\left(E(\vec{w}) - \bar{E}\right)\, dw_1 \dots dw_{2\Lambda} \end{aligned} \tag{2.47}$$

for any function φ continuous on the sphere $S_{\bar{E},\Lambda}$. Here, $\mathcal{A}\left(S_{\bar{E},\Lambda}\right)$ is the area of the $(2\Lambda-1)$-dimensional sphere $S_{\bar{E},\Lambda}$.

Next, we recall that the normalized surface measure (2.44) is the unique probability measure on the energy sphere $S_{\bar{E},\Lambda}$ that is invariant under all rotations, that is,

$$\int_{S_{\bar{E},\Lambda}} \varphi\left(\mathcal{O}\vec{w}\right)\, d\nu_{\bar{E},\Lambda} = \int_{S_{\bar{E},\Lambda}} \varphi\left(\vec{w}\right)\, d\nu_{\bar{E},\Lambda} \tag{2.48}$$

for any rotation matrix $\mathcal{O}$. (Recall that a rotation matrix is any orthogonal transformation $\mathcal{O}$ with determinant 1, that is, $\mathcal{O}\vec{w}\cdot\mathcal{O}\vec{v} = \vec{w}\cdot\vec{v}$ and $\det \mathcal{O} = 1$.)

Thus, we have

Claim 1 *If a sequence of measures converges to a measure ν with the property that*

- *ν is supported on the energy sphere $S_{\bar{E},\Lambda}$ in (2.43),*
- *$\int_{S_{\bar{E},\Lambda}} \varphi\left(\mathcal{O}\vec{w}\right)\, d\nu = \int_{S_{\bar{E},\Lambda}} \varphi\left(\vec{w}\right)\, d\nu$ for any rotation matrix $\mathcal{O}$ and any continuous function φ on the sphere $S_{\bar{E},\Lambda}$,*

then $\nu = \nu_{\bar{E},\Lambda}$, the normalized uniform measure on the sphere.

We proceed to show how the the uniform measure $\nu_{\bar{E},\Lambda}$ on the constant energy sphere $S_{\bar{E},\Lambda}$ can be realized as a mapping of a radial Gaussian measure on $\mathbb{R}^{2\Lambda}$. To this end, let

$$G_\sigma(w) = \frac{1}{\sqrt{2\pi}\sigma} e^{-\frac{w^2}{2\sigma^2}} \tag{2.49}$$

denote a Gaussian random variable with zero mean and variance σ, and let

$$G_\sigma(\vec{w}) = \prod_{j=1}^{2\Lambda} G_\sigma(w_i) \tag{2.50}$$

be the 2Λ-dimensional Gaussian distribution with the same variance. Consider the mapping $P:\ \mathbb{R}^{2\Lambda} \to S_{\bar{E},\Lambda}$ given by

$$\vec{w} \to \vec{y} = \sqrt{\bar{E}}\frac{\vec{w}}{|\vec{w}|}, \tag{2.51}$$

with $\vec{w} \in \mathbb{R}^{2\Lambda}$, $\vec{w} \neq 0$, $P\vec{w} = \vec{y}$, and $|\vec{y}| = |P\vec{w}| = \sqrt{\bar{E}}$. Here, as in (2.35), $|\vec{w}|$ is the length of the vector $\vec{w}$. This mapping induces a probability measure ν^* on the energy sphere $S_{\bar{E},\Lambda}$ via the formula [10]

$$\int_{S_{\bar{E},\Lambda}} \varphi(\vec{y})\ d\nu^*(\vec{y}) = \int_{\mathbb{R}^{2\Lambda}} G_\sigma(\vec{w})\, \varphi(P(\vec{w}))\ dw_1 \ldots dw_{2\Lambda}, \tag{2.52}$$

that holds for any function φ, continuous on the energy sphere $S_{\bar{E},\Lambda}$.

Claim 2 *The measure ν^* in (2.52) is precisely $\nu_{\bar{E},\Lambda}$, the normalized uniform measure on the sphere $S_{\bar{E},\Lambda}$.*

To prove this claim, we must show that the measure ν^* is invariant under rotations, that is, that it satisfies a condition analogous to (2.48). We first notice that $\mathcal{O}P\vec{w} = P\mathcal{O}\vec{w}$ for any rotation matrix $\mathcal{O}$. After the coordinate change $\vec{w} \to \mathcal{O}^{-1}\vec{w}$, we find

$$\int_{S_{\bar{E},\Lambda}} \varphi(\mathcal{O}\vec{y})\ d\nu^*(\vec{y}) = \int_{\mathbb{R}^{2\Lambda}} G_\sigma\left(\mathcal{O}^{-1}\vec{w}\right) \varphi(P(\vec{w}))\ \ dw_1 \ldots dw_{2\Lambda}.$$

Since the Gaussian distribution $G_\sigma(\vec{w})$ in (2.50) is radial, $G_\sigma\left(\mathcal{O}^{-1}\vec{w}\right) = G_\sigma(\vec{w})$, which, together with Claim 2 concludes the proof.

By using the mapping in (2.52) and Claim 2, we can construct the following convergent Monte-Carlo algorithm:

- Let $\left\{G_{\sigma,i}(\lambda)\ \middle|\ i = 1, \ldots, 2\Lambda\right\}$ be independent, identically distributed Gaussian random variables with mean zero and variance σ.
- Choose each $w_i^{(j)}$ from the distribution $G_{\sigma,i}$ at random and independently of all other

$w_k^{(j)}$. Form the vector $\vec{w}^{(j)} = \left(w_1^{(j)}, \ldots, w_{2\Lambda}^{(j)}\right)$, and let

$$\vec{y}^{(j)} = \sqrt{\bar{E}} \frac{\vec{w}^{(j)}}{\left|\vec{w}^{(j)}\right|},$$

where $\left|\vec{w}^{(j)}\right|$ is the length of the vector $\vec{w}^{(j)}$ defined as in (2.35).

Clearly, each $\vec{y}^{(j)}$ belongs to the fixed-energy sphere $S_{\bar{E},\Lambda}$.

Claim 1, Claim 2 and the law of large numbers [10] let us conclude

Claim 3 *For any function φ, continuous on the fixed energy sphere $S_{\bar{E},\Lambda}$, and almost every sequence $\left\{\vec{y}^{(j)} \mid j = 1, 2, \ldots\right\}$, we have*

$$\lim_{M\to\infty} \frac{\sum_{j=1}^{M} \varphi\left(\vec{y}^{(j)}\right)}{M} = \int_{S_{\bar{E},\Lambda}} \varphi \, d\nu_{\bar{E},\Lambda}. \tag{2.53}$$

In other words, almost every sequence $\left\{\vec{y}^{(j)} \mid j = 1, 2, \ldots\right\}$ generated by the above Monte-Carlo algorithm is distributed uniformly over the sphere $S_{\bar{E},\Lambda}$ and can be used as a convergent quadrature procedure for calculating the integral in (2.53).

Computation of the Hamiltonian probability distribution by the Monte-Carlo algorithm. Now we can use the Monte-Carlo algorithm listed above Claim 3 to compute the probability density distribution $p_{\bar{E},\Lambda}(\lambda)$ of the Hamiltonian H in (2.26) on the sphere $S_{\bar{E},\Lambda}$ of constant energy $\bar{E}$. Here again, $\vec{w}$ is defined as in (2.32),

$$\vec{w} = (w_1, \ldots, w_{2\Lambda}), \qquad \hat{u}_k = w_{2k-1} + i w_{2k}, \qquad k = 1, \ldots, \Lambda,$$

and $H(\vec{w})$ is computed as in (2.26),

$$H(\vec{w}) = \frac{1}{6} \sum_{\substack{k_1+k_2+k_3=0, \\ |k_1|,|k_2|,|k_3|\le\Lambda}} \hat{u}_{k_1} \hat{u}_{k_2} \hat{u}_{k_3}.$$

We compute the probability density $p_{\bar{E},\Lambda}(\lambda)$ via the formula

$$\int_{\alpha}^{\beta} p_{\bar{E},\Lambda}(\lambda)\, d\lambda = \mathrm{Prob}_{\bar{E},\Lambda}\{\alpha < H(\vec{w}) < \beta\} = \int_{S_{\bar{E},\Lambda}} \varphi \, d\nu_{\bar{E},\Lambda}, \tag{2.54}$$

where we choose the function φ to be

$$\varphi\left(\vec{w}\right) = \chi_{\{\vec{w}|\alpha<H(\vec{w})<\beta\}}\left(\vec{w}\right), \tag{2.55}$$

and

$$\chi_S(x) = \begin{cases} 1, & x \in S, \\ 0, & \text{otherwise}, \end{cases} \tag{2.56}$$

is the characteristic function of the set S. Equations (2.54) and (2.55), together with Claim 3, now provide the following convergent algorithm:

Claim 4 *From almost every sequence of vectors,* $\left\{\vec{y}^{(j)} \mid j = 1, 2, \ldots\right\}$, *generated by the Monte-Carlo algorithm described above Claim 3, the probability*

$$\text{Prob}_{\bar{E},\Lambda}\left\{\alpha < H\left(\vec{w}\right) < \beta\right\}$$

can be computed as

$$\text{Prob}_{\bar{E},\Lambda}\left\{\alpha < H\left(\vec{w}\right) < \beta\right\} = \lim_{M\to\infty} \frac{N_{(\alpha,\beta)}}{M}, \tag{2.57}$$

where $N_{(\alpha,\beta)}$ *is the number of the vectors* $\vec{y}^{(j)}$, *with* $j = 1, \ldots, M$, *for which the corresponding values of the Hamiltonian* H *satisfy the inequality* $\alpha < H\left(\vec{y}^{(j)}\right) < \beta$.

The Monte-Carlo algorithm described above Claim 4 can be used to compute the probability density $p_{\bar{E},\Lambda}(\lambda)$ in (2.46) of the values of the Hamiltonian H in (2.26) on the sphere $S_{\bar{E},\Lambda}$ by "bin-counting." In particular, we choose a large interval, say $[-h, h]$, within which we expect the values of the Hamiltonian H to lie. We partition it into N equal sub-intervals, each so small that the value of $p_{\bar{E},\Lambda}(\lambda)$ in it can be taken as approximately constant, and form an array of counters. At each computational step, we choose a point on the sphere $S_{\bar{E},\Lambda}$ by the Monte-Carlo algorithm of Claim 3, and evaluate the Hamiltonian function (2.26) at that point. Depending on which sub-interval the computed value of the Hamiltonian H is contained in, the value of the corresponding counter increases by one. Each counter is then divided by the total number of the computed points and the bin size to find the approximate value of $p_{\bar{E},\Lambda}(\lambda)$ in the corresponding bin. In our computations, for each density $p_{\bar{E},\Lambda}(\lambda)$, one million, i.e. 10^6 values of the Hamiltonian H were generated via the Monte-Carlo algorithm of Claim 3. The standard deviation σ of the Gaussian

Λ	Bin size
10	$3.5 \cdot 10^{-4}$
20	$3 \cdot 10^{-4}$
50	$2 \cdot 10^{-4}$
100	$1.5 \cdot 10^{-4}$
200	10^{-4}

Table 2.1: The bin sizes in the bin-counting computation of the Hamiltonian probability distribution $p_{\bar{E},\Lambda}(\lambda)$ for fixed energy $E = 0.1$

$E = 0.1$, flatness		$E = 0.1$, dependence $\sigma_H(\Lambda)$	
Λ	M_4/M_2^2	Λ	$\sigma_H(\Lambda)$
10	3.5130	10	$6.2 \cdot 10^{-3}$
20	3.4518	20	$4.7 \cdot 10^{-3}$
50	3.2646	50	$3.2 \cdot 10^{-3}$
100	3.1466	100	$2.4 \cdot 10^{-3}$
200	3.0732	200	$1.8 \cdot 10^{-3}$

Table 2.2: On the left, the flatness (ratio between the fourth moment and squared second moment) of PDF's, $p_{\bar{E},\Lambda}(\lambda)$, of the Hamiltonian for fixed energy $E = 0.1$ and different values of Λ. On the right, the dependence of $\sigma_H(\Lambda)$ on Λ for fixed energy, $E = 0.1$

distribution (2.50) used in the Monte-Carlo algorithm was $\sigma = 1$. The number of bins in each case was 200. The sizes of the bins are presented in Table 2.1.

Probability density of the Hamiltonian. There are two natural limits to discuss as the number of degrees of freedom increases: the first one is very natural for an analogue model for geophysical applications and involves increasing Λ for fixed mean energy. This is also the natural numerical analysis limit that arises from increasing the number of Fourier modes for fixed initial data. By analogy with the ordinary extensive thermodynamic limit, the behavior as Λ increases while the energy per mode is held constant is also interesting. Here we report the results for both situations.

Self-Similar scaling at fixed total energy. For the case of fixed energy, $E = \bar{E} = 0.1$, we display the computed probability densities $p_{\bar{E},\Lambda}(\lambda)$ in Figures 2.1 and 2.2. We observe that these probability measures are Gaussian-like, and while they are not Gaussian, they have an approximately self-similar form, that is,

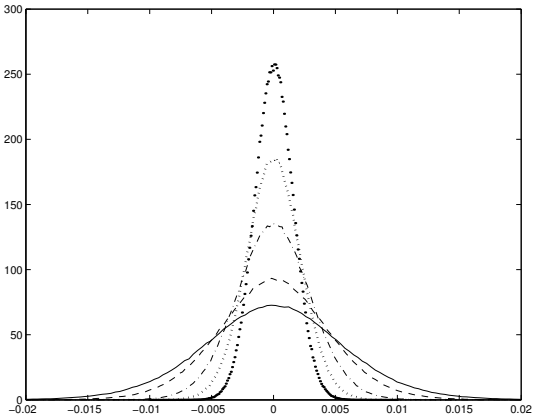

The PDF's of Hamiltonian, fixed energy $E = 0.1$, solid line – $\Lambda = 10$, dashed line – $\Lambda = 20$, dash-dotted line – $\Lambda = 50$, dotted line – $\Lambda = 100$, dots – $\Lambda = 200$

Figure 2.1: The PDF's $p_{\bar{E},\Lambda}(\lambda)$ of the Hamiltonian at fixed energy $E = 0.1$

$$p_{\bar{E},\Lambda}(\lambda) = \sigma_H(\Lambda)\, p_{\bar{E}}\left(\frac{\lambda}{\sigma_H(\Lambda)}\right). \tag{2.58}$$

Here,

$$\sigma_H(\Lambda) = \sqrt{\int_{-\infty}^{\infty} \lambda^2 p_{\bar{E},\Lambda}(\lambda)\, d\lambda} \tag{2.59}$$

is the width of the distribution $p_{\bar{E},\Lambda}(\lambda)$, and $p_{\bar{E}}(\lambda)$ is a symmetric probability distribution which is slightly super-Gaussian, that is, it has flatness

$$\frac{M_4}{M_2^2} = \frac{\displaystyle\int_{-\infty}^{\infty} \lambda^4 p_{\bar{E},\Lambda}(\lambda)\, d\lambda}{\left(\displaystyle\int_{-\infty}^{\infty} \lambda^2 p_{\bar{E},\Lambda}(\lambda)\, d\lambda\right)^2} > 3.$$

In particular, the flatness of $p_{\bar{E}}(\lambda)$ is represented in Table 2.2. The values of the width $\sigma_H(\Lambda)$ as a function of the truncation size Λ are also presented in Table 2.2. Data from Table 2.2 are used to rescale the distributions $p_{\bar{E},\Lambda}(\lambda)$ and confirm the self-similar scaling form (2.58). The results are shown in Figure 2.2.

After plotting $\sigma_H(\Lambda)$ versus Λ and $\log(\sigma_H(\Lambda))$ versus $\log(\Lambda)$ with a remarkable straight line fit in Figure 2.3, we see that the results presented in Table 2.2 furnish powerful numerical evidence that the width $\sigma_H(\Lambda)$ scales with the truncation size Λ according to

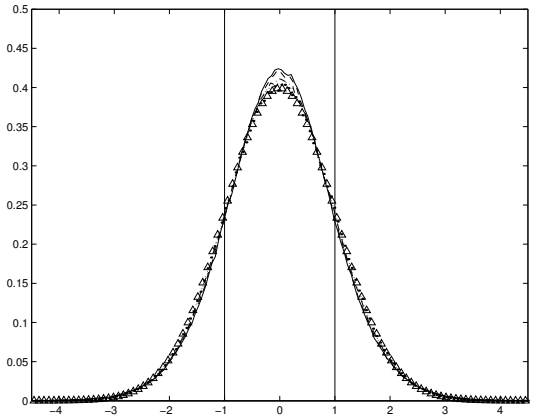

The rescaled PDF's of Hamiltonian, fixed energy $E = 0.1$, solid line – $\Lambda = 10$, dashed line – $\Lambda = 20$, dash-dotted line – $\Lambda = 50$, dotted line – $\Lambda = 100$, dots – $\Lambda = 200$, triangles – Gaussian fit $\sigma = 1$, vertical lines denote standard deviation

Figure 2.2: The rescaled PDF's $p_{\bar{E}}(\Lambda)$ of the Hamiltonian: the self-similarity

$E/2\Lambda = 0.005$, flatness		$E/2\Lambda = 0.005$, dependence $\sigma_H(\Lambda)$	
Λ	M_4/M_2^2	Λ	$\sigma_H(\Lambda)$
10	3.5130	10	$6.2 \cdot 10^{-3}$
20	3.4425	20	$1.26 \cdot 10^{-2}$
50	3.2639	50	$3.35 \cdot 10^{-2}$
100	3.1501	100	$6.83 \cdot 10^{-2}$

Table 2.3: On the left, the flatness (ratio between the fourth moment and squared second moment) of PDF's, $p_{\bar{E},\Lambda}(\lambda)$, of the Hamiltonian for fixed energy per mode $E/2\Lambda = 0.005$ and different values of Λ. On the right, the dependence $\sigma_H(\Lambda)$ on Λ for fixed energy per mode $E/2\Lambda = 0.005$

the formula

$$\sigma_H(\Lambda) = A_0 \Lambda^{\alpha}, \qquad \alpha = -0.413899 \pm 8.98 \cdot 10^{-4}, \tag{2.60}$$

where A_0 was determined to be $A_0 = 1.615 \cdot 10^{-2}$. The systematic decrease of the flatness in Table 2.2 to the Gaussian value 3 as Λ increases as well as the essentially Gaussian rescaled PDF's in Figure 2.2 clearly suggest that the Hamiltonian obeys a central limit theorem.

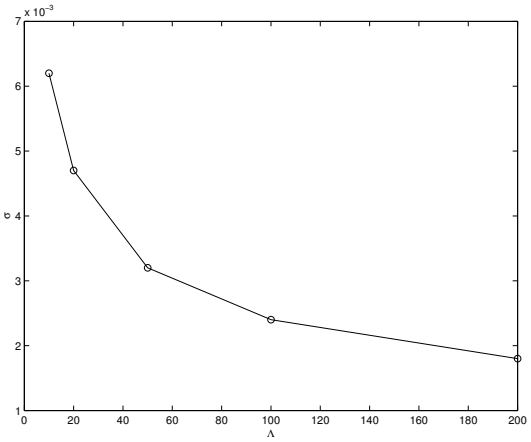

The plot σ_H vs Λ, $E = 0.1$

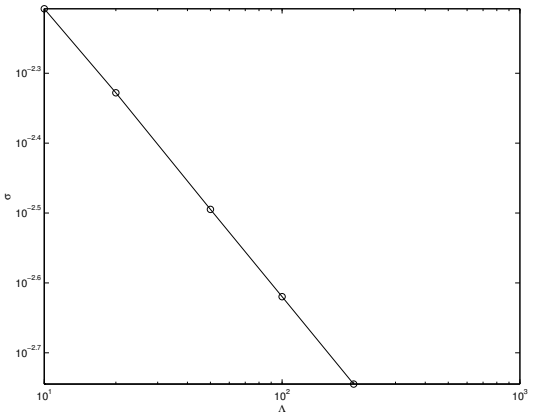

The plot $\log(\sigma_H)$ vs $\log(\Lambda)$, $E = 0.1$

Figure 2.3: $\sigma_H(\Lambda)$ **versus** Λ **and** $\log(\sigma_H)$ **versus** $\log(\Lambda)$. **On the second plot we see the power law** $\sigma_H(\Lambda) = A_0\Lambda^\alpha$.

Self-similar scaling at fixed energy per mode. For the case of fixed energy per mode, $E/2\Lambda = \bar{E}/2\Lambda = 0.005$, we display the computed probability densities $p_{\bar{E},\Lambda}(\lambda)$ in Figure 2.4. These densities are again super-Gaussian with flatness > 3, as shown in Table 2.3. Densities $p_{\bar{E},\Lambda}(\lambda)$, rescaled by using (2.58) and the values of $\sigma_H(\Lambda)$ from Table 2.3 are displayed in Figure 2.5 to numerically confirm the validity of the self-similarity form in (2.58). After plotting $\sigma_H(\Lambda)$ versus Λ in Figure 2.6, we observe that $\sigma_H(\Lambda)$ scales linearly with Λ, and compute by least squares that

$$\sigma_H(\Lambda) = \alpha\Lambda, \qquad \alpha = 6.92255 \cdot 10^{-4} \pm 8.406 \cdot 10^{-6}.$$

Here, $\sigma_H(\Lambda)$ scales linearly with Λ which is indicative of a more straightforward central limit theorem behavior in the thermodynamic limit.

Mixed canonical micro-canonical distribution in the large Λ limit at fixed energy. In order to understand why the Hamiltonian is largely a statistically irrelevant conserved quantity in the large Λ limit at fixed energy E, here we consider statistical ensembles of solutions of the truncated Burgers-Hopf equation (2.27), distributed according to the mixed micro-canonical-canonical distribution (2.45), and show that the values of the Hamiltonian H are expected to be very close to zero in this limit.

We exploit the empirical self-similar scaling law verified in the last section and a

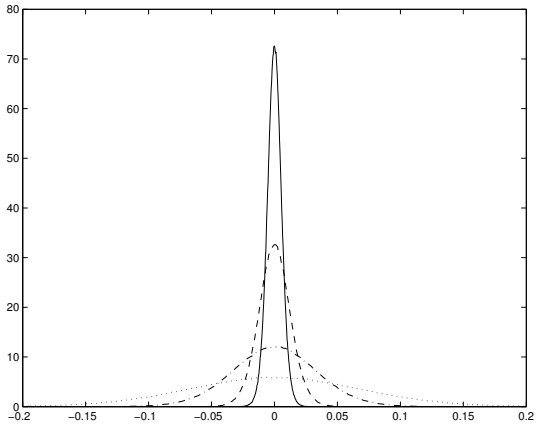

The PDF's of Hamiltonian, fixed energy per mode $E/2\Lambda = 0.005$, solid line – $\Lambda = 10$, dashed line – $\Lambda = 20$, dash-dotted line – $\Lambda = 50$, dotted line – $\Lambda = 100$

Figure 2.4: The PDF's, $p_{\bar{E},\Lambda}(\lambda)$, for the Hamiltonian at fixed energy per mode $E/2\Lambda = 0.005$.

simple small deviation argument to establish this below. Our numerical results of direct simulation, presented in Section 2.3, show that, in the near-zero regime, the Hamiltonian is indeed irrelevant.

The key feature that we need to understand is how the Hamiltonian scales on average in the limit as the truncation size Λ increases, $\Lambda \to \infty$, with the energy $\bar{E}$ fixed. We begin by computing the average value of the Hamiltonian from (2.45) with respect to such a measure as

$$\bar{H} = \frac{\displaystyle\int_{S_{\bar{E},\Lambda}} H(u) e^{-\theta H(u)} d\nu_{\bar{E},\Lambda}}{\displaystyle\int_{S_{\bar{E},\Lambda}} e^{-\theta H(u)} d\nu_{\bar{E},\Lambda}}. \tag{2.61}$$

With the probability density, $p_{\bar{E},\Lambda}(\lambda)$, we have

$$\bar{H} = \frac{\displaystyle\int_{-\infty}^{\infty} \lambda e^{-\theta\lambda} p_{\bar{E},\Lambda}(\lambda)\, d\lambda}{\displaystyle\int_{-\infty}^{\infty} e^{-\theta\lambda} p_{\bar{E},\Lambda}(\lambda)\, d\lambda}, \tag{2.62}$$

and by combining the empirical equation in (2.58) with (2.62) and rescaling $\lambda \to \sigma_H(\Lambda)\,\lambda$,

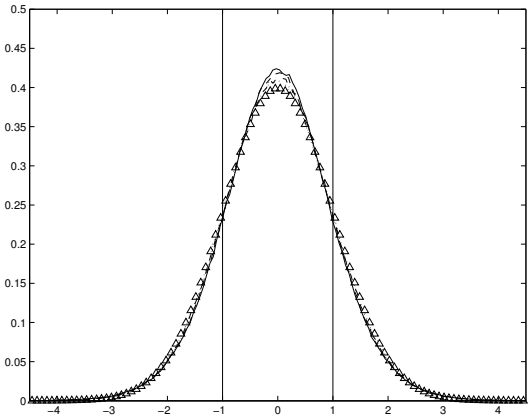

The rescaled PDF's of Hamiltonian, $E/2\Lambda = 0.005$, solid line – $\Lambda = 10$, dashed line – $\Lambda = 20$, dash-dotted line – $\Lambda = 50$, dotted line – $\Lambda = 100$, circles – Gaussian fit $\sigma = 1$, vertical lines denote standard deviation

Figure 2.5: The rescaled PDF's $p_{\bar{E}}(\Lambda)$ of the Hamiltonian: self-similarity

we conclude

$$\bar{H}(\theta) = \frac{\sigma_H(\Lambda) \int_{-\infty}^{\infty} \lambda e^{-\sigma_H(\Lambda)\theta\lambda} p_{\bar{E}}(\lambda)\, d\lambda}{\int_{-\infty}^{\infty} e^{-\sigma_H(\Lambda)\theta\lambda} p_{\bar{E}}(\lambda)\, d\lambda}. \tag{2.63}$$

Thus, for any fixed θ, due to (2.60), Taylor expanding (2.63) yields

$$\lim_{\Lambda\to\infty} \frac{\bar{H}(\theta)}{\sigma_H(\Lambda)} = -\int_{-\infty}^{\infty} \lambda^2 p_{\bar{E}}(\lambda)\, d\lambda, \tag{2.64}$$

that is,

$$\bar{H}(\theta) = -\sigma_H(\Lambda)^2 \theta \bar{\sigma}^2 + o\left(\sigma_H(\Lambda)\right)^2, \tag{2.65}$$

where

$$\bar{\sigma}^2 = \int_{-\infty}^{\infty} \lambda^2 p_{\bar{E}}(\lambda)\, d\lambda.$$

In particular, statistical values of the Hamiltonian H indeed concentrate very sharply near zero for a fixed inverse temperature θ, that is,

$$\left|\bar{H}(\theta)\right| = O\left(\sigma_H(\Lambda)^2 \bar{\sigma}^2\right) \ll 1. \tag{2.66}$$

In other words, for a fixed inverse temperature θ and energy $\bar{E}$ and in the limit as $\Lambda \to \infty$,

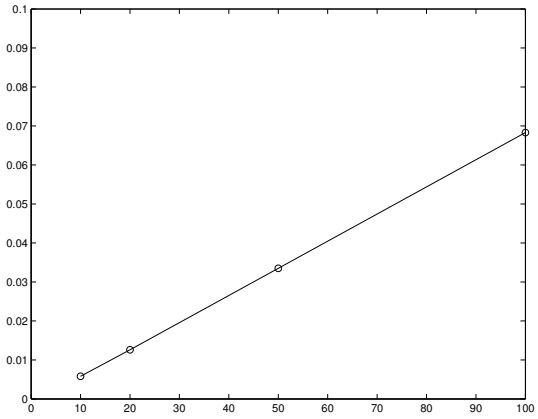

Figure 2.6: $\sigma_H(\Lambda)$ **versus** Λ **for** $E/2\Lambda = 0.005$**. We see the linear law** $\sigma_H(\Lambda) = \alpha\Lambda$**.**

the expected values of the Hamiltonian H in a mixed micro-canonical energy and canonical Hamiltonian ensemble are typical values of the distribution (2.45), and thus, according to our computational results presented below in Section 2.3, irrelevant for the statistical mechanics of the Burgers-Hopf equations (2.27).

Statistically relevant and irrelevant values of the Hamiltonian We now give precise definitions of the terms relevant and irrelevant values of the Hamiltonian H in (2.26) for the statistical mechanics of the truncated Burgers-Hopf equations (2.27). In particular,

- An irrelevant value of the Hamiltonian H means
  - Equipartition spectrum (2.38).
  - Essentially universal correlation structure.
- A relevant value of the Hamiltonian H means
  - A significant tilt to the spectrum
  - Longer tails of the correlation functions on large-scale modes.

Our computations, described in the forthcoming sections, show that relevant and irrelevant values of the Hamiltonian can be identified in terms of its probability distribution function $p_{\bar{E},\Lambda}(\lambda)$. We have seen in the previous sections that the probability distribution function $p_{\bar{E},\Lambda}(\lambda)$ of the Hamiltonian H in (2.26), generated by the above-described Monte-Carlo simulation, possesses two key properties:

1. $p_{\bar{E},\Lambda}(\lambda)$ is a symmetric probability distribution about zero, and, for fixed energy $\bar{E}$, $p_{\bar{E},\Lambda}(\lambda)$ has an increasingly small variance as $\Lambda \to \infty$.

2. $p_{\bar{E},\Lambda}(\lambda)$ is approximately self-similar according to the formula (2.58),

$$p_{\bar{E},\Lambda}(\lambda) = \sigma_H(\Lambda)\, p_{\bar{E}}\left(\frac{\lambda}{\sigma_H(\Lambda)}\right),$$

   with $\sigma_H(\Lambda) \to 0$ as $\Lambda \to \infty$.

Property 1 yields, for fixed $\bar{E}$ and $\Lambda \to \infty$, the concentration of the probability density $p_{\bar{E},\Lambda}(\lambda)$ of the Hamiltonian H near the hypersurface $H(u) = 0$. Property 2 allows us to access the rare events of the distribution.

The Monte-Carlo generated equilibrium probability distribution $p_{\bar{E},\Lambda}(\lambda)$ leads to the classification

- Typical values of the Hamiltonian H are the ones within the standard deviation $\sigma_H(\Lambda)$.

- Atypical values of the Hamiltonian H are, in absolute value, larger than $\sigma_H(\Lambda)$, and occupy a set of vanishingly small measure as Λ increases for any fixed mixed canonical-microcanonical Gibbs measure according to (2.66). Recall from (2.66) that the mean value of H scales like σ_H^2.

In the rest of this chapter we present strong numerical evidence that the typical values of the Hamiltonian are statistically irrelevant in the sense described above.

2.2.3 The Numerical Algorithm and a Basic Simulation

All the numerical data presented in this chapter were obtained by utilizing a standard numerical method to compute the solutions of the truncated Burgers-Hopf equation (2.14). The method solves the truncated Burgers-Hopf equation (2.14) pseudo-spectrally in de-aliased form. In particular, the fast Fourier transform procedure, $\mathrm{FFT}\left\{\left[\mathrm{FFT}^{-1}(u_\Lambda)\right]^2\right\}$, is used to compute the nonlinear term. For this algorithm we use an expanded array of $2(2\Lambda+1)+1$ Fourier terms, setting all but the ones with indices $|k| \le \Lambda$ equal to zero in order to avoid aliasing. This method calls for only $\mathcal{O}(\Lambda \log(\Lambda))$ floating point operations. We use the 6th-order Adams-Bashforth linear multistep method [4] for integration in time. With the time step 0.001, this algorithm conserves the energy (2.29) within 10^{-8} % and the Hamiltonian (2.26) within 10^{-9} % for all simulations presented in this chapter.

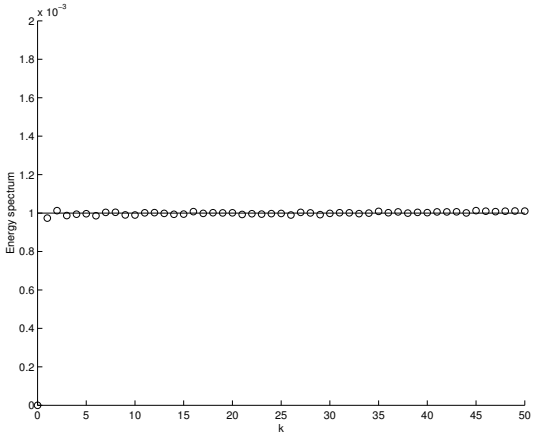

The energy spectrum for $\sin(x) + 0.5\cos(4x)$ initial data, $\Lambda = 50$, $E = 0.1$, circles – numerical simulation with $H = 0$, horizontal line implies equipartitioned spectrum

Figure 2.7: The energy spectrum for the case with $H = 0$ and $\Lambda = 50$.

Besides the mean energy per mode in (2.38), the correlation functions (2.39), and the correlation times (2.40), in this chapter, we also employ as diagnostic tools the probability distribution functions of each mode (PDF's), given by the formulas

$$\begin{aligned} \text{Prob}\,\{\alpha < \text{Re}(\hat{u}_k) < \beta\} &= \int_\alpha^\beta \rho_{\text{Re}(\hat{u}_k)}(\lambda)\, d\lambda, \\ \text{Prob}\,\{\alpha < \text{Im}(\hat{u}_k) < \beta\} &= \int_\alpha^\beta \rho_{\text{Im}(\hat{u}_k)}(\lambda)\, d\lambda. \end{aligned} \tag{2.67}$$

In order to compute the PDF's, we again use "bin-counting." In particular, in our computations, we follow the modes $\hat{u}_k(t)$, $k = 1, \ldots, \Lambda$, for $T_0 < t < T_0 + T$, where T_0 is the initial time and T is the length of the averaging window. (In most of the computations, $T_0 = 1000$ and $T = 20000$.) We choose an interval, say $[-L, L]$, in which we expect the random values of $\text{Re}(\hat{u}_k(t))$ and $\text{Im}(\hat{u}_k(t))$ to be distributed, and partition it into N equal sub-intervals. For each $\text{Re}(\hat{u}_k(t))$ or $\text{Im}(\hat{u}_k(t))$, we then form an array of N counters, each of whose values increases by one at the n-th time step (of size Δt) if the value of the current random variable $\text{Re}(\hat{u}_k(T_0 + n\Delta t))$ or $\text{Im}(\hat{u}_k(T_0 + n\Delta t))$ is contained in the corresponding sub-interval. Finally, we divide each element of the array of counters by the total number of time steps and multiply it by $N/2L$, so that the distribution is normalized on the interval $[-L, L]$. For all the computational results in this chapter, we have always

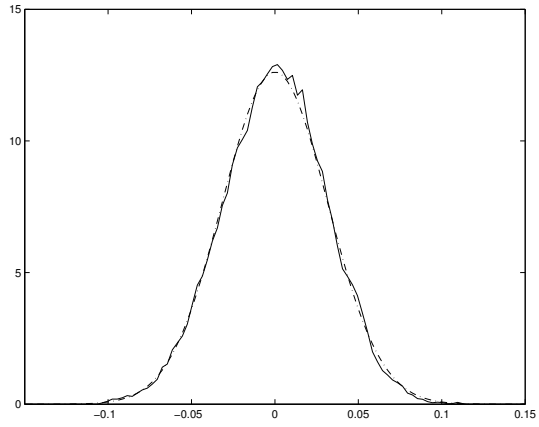

The PDF for $\sin(x) + 0.5\cos(4x)$ initial data, $\Lambda = 50$, $E = 0.1$, mode $k = 1$, solid line – numerical result, dashed line – Gaussian with the same variance

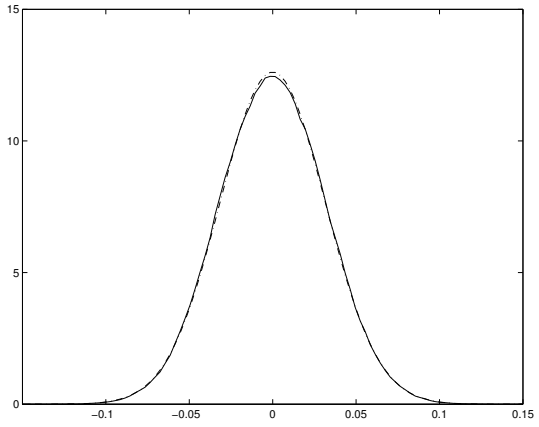

The PDF for $\sin(x) + 0.5\cos(4x)$ initial data, $\Lambda = 50$, $E = 0.1$, mode $k = 20$, solid line – numerical result, dashed line – Gaussian with the same variance

Figure 2.8: The PDF's for the case with $H = 0$ and $\Lambda = 50$.

chosen to display the PDF's of the imaginary parts of the modes, $\mathrm{Im}(\hat{u}_k(T_0 + n\Delta t))$. The sizes and numbers of bins are shown with the results of each computation.

Here, we present a prototypical simulation where $H = 0$, which is clearly the most irrelevant value of the Hamiltonian for the equilibrium statistical mechanics of the truncated Burgers-Hopf equations (2.27). For this simulation, the truncation size is $\Lambda = 50$, and the initial condition is $u_\Lambda(x, 0) = \sin x + 0.5\cos 4x$. This initial condition indeed satisfies the equation $H = 0$. It also has no special symmetry, that is, it is neither an odd or an even function nor a spatial shift of one. We use the pseudo-spectral method to compute the corresponding solution. The time step is $\Delta t = 10^{-3}$, the initial averaging time is $T_0 = 1000$, and the averaging window $T = 20000$. The energy in (2.29) and the Hamiltonian in (2.26) are conserved within 10^{-8} % and 10^{-9} %, respectively. The number of bins in the bin-counting procedure was 200, and the size of each bin was $1.5 \cdot 10^{-2}$. As expected, the energy spectrum in Figure 2.7 is completely flat, and in excellent agreement with the analytical prediction (2.38). The PDF's for representative modes $k = 1$, $k = 20$ in Figure 2.8 are indistinguishable from the Gaussians predicted from the analytical energy-based Gibbs formula (2.34). The computed correlation functions for modes $k > 1$ exhibit almost no oscillations, and the corresponding correlation times agree almost perfectly with the analytical scaling prediction (2.41). In order to condense the number of figures in this chapter, we refer the reader to the corresponding figures in [18] since our results are identical to the ones presented there. However, the PDF results in Figure 2.8

are new.

The original work of [18, 19] on the truncated Burgers-Hopf equation (2.27) employed the pseudo-spectral method together with a host of initial conditions to study statistical properties of this equation. The deterministic initial conditions were either small perturbations of initial data generating exact solutions with subharmonic instability [19] or the classical data $2\sin(x)$ [18]. The Hamiltonian vanishes identically for these deterministic initial data. In the cases with random initial data [19], the procedure utilized to select the initial data automatically guarantees statistically irrelevant values for the Hamiltonian in the precise sense in the previous section. All types of initial conditions led to the robust statistical behavior also observed in our simulation described in the previous paragraph, namely, energy equipartition (2.36) and correlation time scaling proportional to the eddy turnover time (2.41).

Paradoxically, our simulations using the direct summation method and the initial condition $2\sin x$ do not always lead to robust statistical behavior. In particular, as we show in Section 2.2.4.3, our computations indicate that odd initial data often lie on a large homoclinic manifold that can be tracked by the direct summation method for far longer times than by the pseudo-spectral method due to different round-off errors incurred by each method. When the pseudo-spectral method is used, round-off error pushes the solution off of this homoclinic manifold within a moderate amount of time, thus recovering the statistically robust regime.

2.2.4 Dynamics on the subspace of odd functions

In this section we present numerical evidence for a variety of dynamics in the subspace of odd functions and their translates for the truncated Burgers-Hopf equation (2.14), including non-robust dynamics of homoclinic-type. Since the subspace of odd functions and their translates is contained in the level set $H = 0$ of the Hamiltonian (2.15), it has measure zero in the phase space of the full truncated Burgers-Hopf equation (2.14). Thus, this subspace does not contribute to the robust statistical features of the Burgers-Hopf dynamics. In what is to follow, it is sufficient to consider the subspace of odd functions, since all its translates are treated in the same fashion.

2.2.4.1 Burgers-Hopf equation on the subspace of odd functions

The subspace of odd functions is invariant under the dynamics of the truncated Burgers-Hopf equation (2.14) since odd initial data lead to odd solutions of the equation

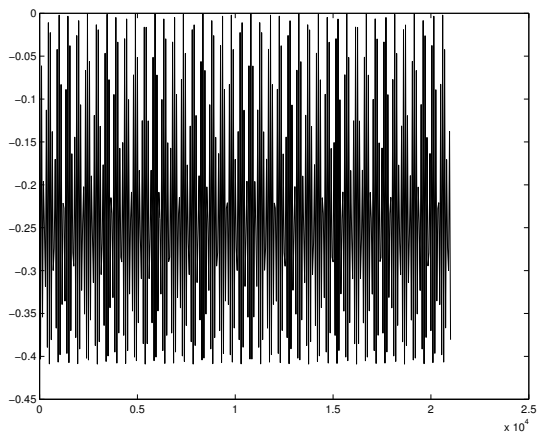

The time evolution for q_3, $\Lambda = 3$, $\sin(x)$ initial data

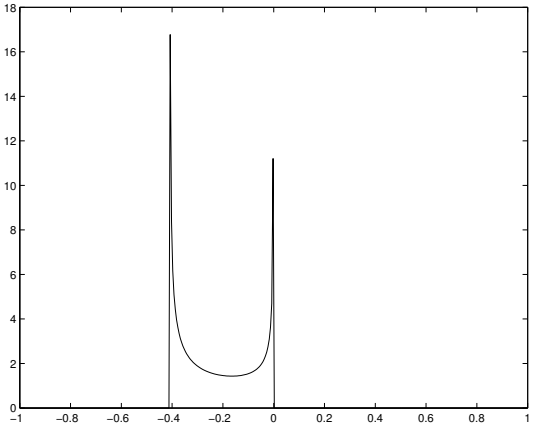

The probability density function for q_3, $\Lambda = 3$, $\sin(x)$ initial data

Figure 2.9: The time evolution and the PDF for the case with $\Lambda = 3$, $\sin(x)$ initial data.

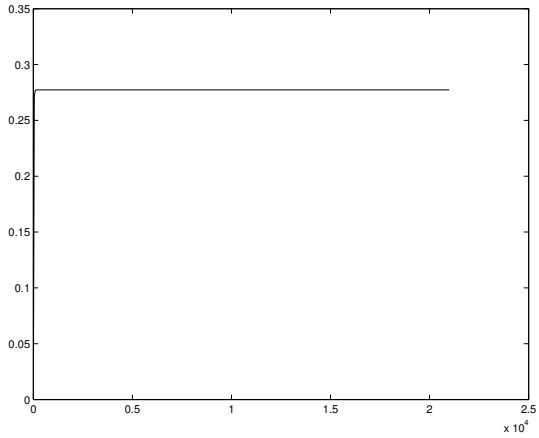

The time evolution for q_4, $\Lambda = 4$, $\sin(x)$ initial data

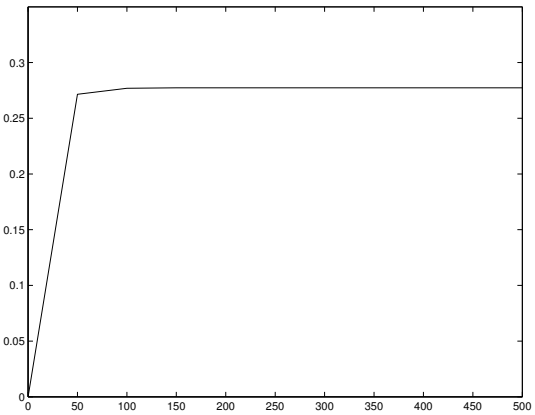

The time evolution (magnified) for q_4, $\Lambda = 4$, $\sin(x)$ initial data

Figure 2.10: The time evolution for the case with $\Lambda = 4$, $\sin(x)$ initial data. Right plot shows magnified left portion of the left plot

(2.14). Odd real functions in the physical space have pure imaginary Fourier coefficients

$$\tilde{u}_k = iq_k, \qquad q_k \text{ real}, \quad q_k = -q_{-k}, \tag{2.68}$$

where the last equation is implied by the reality condition (2.23). This argument allows us to rewrite the Fourier representation of the truncated Burgers-Hopf equation, given by

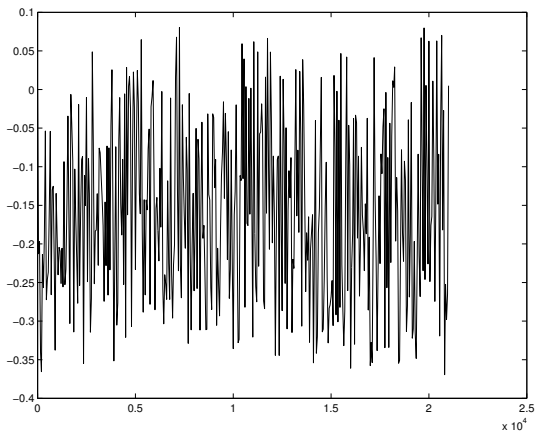

The time evolution for q_5, $\Lambda = 5$, $\sin(x)$ initial data

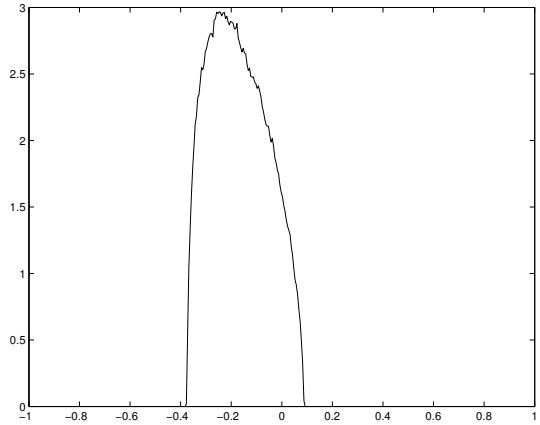

The probability density function for q_5, $\Lambda = 5$, $\sin(x)$ initial data

Figure 2.11: The time evolution and the PDF for the case with $\Lambda = 5$, $\sin(x)$ initial data.

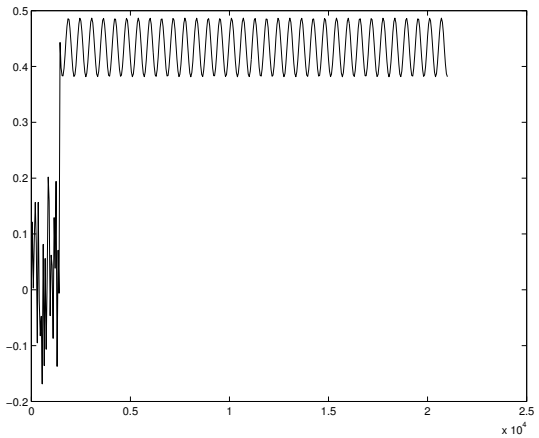

The time evolution for q_2, $\Lambda = 7$, $\sin(x)$ initial data

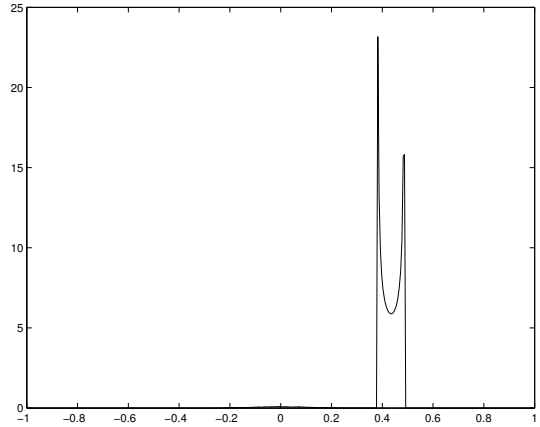

The probability density function for q_2, $\Lambda = 7$, $\sin(x)$ initial data

Figure 2.12: The time evolution and the PDF for the case with $\Lambda = 7$, $\sin(x)$ initial data.

(2.27), as

$$\dot{q}_k = \frac{k}{2} \sum_{\substack{|k'| \leq \Lambda \\ |k-k'| \leq \Lambda}} q_{k-k'} q_{k'}. \tag{2.69}$$

For odd initial data (and their spatial translates), the Hamiltonian H in (2.26) vanishes identically, $H \equiv 0$, and thus does not represent a conserved quantity for equa-

tions (2.69). However, the energy E in (2.29),

$$E = \sum_{k=1}^{\Lambda} q_k^2,$$

is still a conserved quantity of (2.69).

2.2.4.2 Numerical experiments on the subspace of odd initial data

We consider truncations of sizes $\Lambda = 3$, 4, 5, 6, and 7. Equations (2.69) were solved by the direct summation method. In all the computations, the time step was $\Delta t = 5 \cdot 10^{-3}$, the initial averaging time was $T_0 = 1000$, and the averaging window $T = 20000$. The energy was always conserved within 10^{-8} %. The number of bins in the procedure for calculating the PDF's was 200, and the size of each bin was 10^{-2}.

We first describe the results of the simulations with the initial condition $\sin(x)$. For $\Lambda = 3$, the trajectory appears quasiperiodic. Figure 2.9 shows the time evolution of the third mode, as well as the PDF of this mode. For $\Lambda = 4$, the trajectory asymptotes for large times towards an equilibrium point, as does the trajectory for $\Lambda = 6$, as seen in Figure 2.10. For $\Lambda = 5$, the trajectory appears chaotic. Its time evolution and PDF are shown in Figure 2.11. Finally, for $\Lambda = 7$, the trajectory asymptotes towards a periodic solution. Odd modes all vanish along this solution; all three even modes are excited. The time evolution and PDF for mode q_2 are shown in Figure 2.12.

We have performed additional numerical experiments with random odd initial data. These data are generated as follows: the complex Fourier coefficients $\tilde{u}_k$ with $k > 0$ are picked from a uniform distribution of the modulus (between 0 and 1) and a uniform distribution of the phase (between 0 to 2π). The variables q_k are obtained as $q_k = \mathrm{Im}(\tilde{u}_k)$ for $k > 0$ and as $q_k = -\mathrm{Im}(\tilde{u}_{-k})$ for $k < 0$. In these experiments, $\Lambda = 10$ and $\Lambda = 15$ are chosen. For each value of Λ, the outcomes of sixteen experiments are presented in the following table:

dynamics	$\Lambda = 10$	$\Lambda = 15$
asymptotic to (quasi-)periodic	4 out of 16	3 out of 16
asymptotic to equilibrium	11 out of 16	13 out of 16
chaotic	1 out of 16	0 out of 16

The results of this section furnish convincing numerical evidence that a considerable subset of odd initial data lies exactly on stable manifolds of low-dimensional objects such

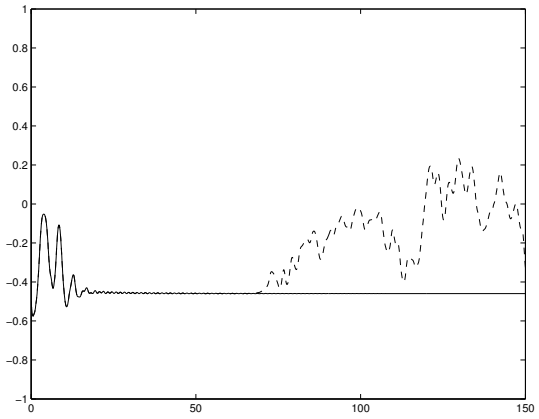

Figure 2.13: The discrepancy between the solutions obtained by the direct-summation and pseudo-spectral methods.

as equilibria and periodic solutions, and thus the corresponding trajectories do not exhibit robust statistical behavior. Nevertheless, as we show in the next section, the necessary instability [3] of these objects combined with the round-off error is likely to eventually push the numerically computed trajectories back into the statistically relevant regime.

2.2.4.3 Effects of round-off error

In this section, we show how the two numerical methods, direct summation and pseudo-spectral, differ when used for computing solutions of the truncated Burgers-Hopf equation (2.14), or its spectral equivalent (2.27), with odd initial data. For the case illustrating the difference between the two methods, shown in Figure 2.13, the initial data $\sin x + \sin 2x$ and $\Lambda = 7$ were taken. The time step was $\Delta t = 5 \cdot 10^{-3}$. One can observe that both solutions virtually coincide in their approach to an equilibrium point until the time $t \approx 65$, when the solution computed by the pseudo-spectral method flies away along an unstable direction. Despite this instability, in both computations the energy in (2.29) and the Hamiltonian in (2.26) were conserved within 10^{-8} % and 10^{-9} %, respectively.

The discussion contained in the previous paragraph explains the apparent paradox, mentioned in Section 2.2.3, that the pseudo-spectral computations of [18, 19] display robust statistical behavior despite the oddness of their initial condition $2 \sin x$. In particular, in those computations, round-off error pushes the computed solutions off of the odd subspace

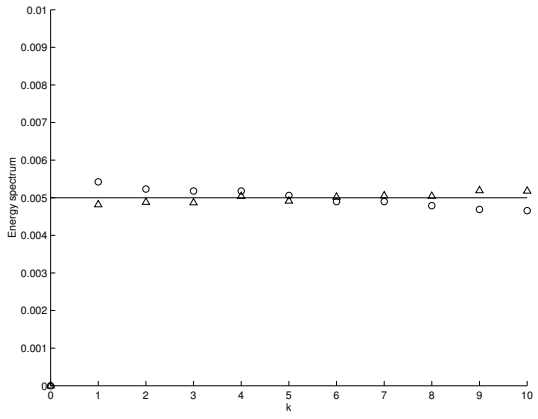

The energy spectrum for random initial data, $\Lambda = 10$, $E = 0.1$, circles – $H = 10^{-2}$, triangles – $H = -1.9 \cdot 10^{-3}$, horizontal line implies equipartitioned spectrum

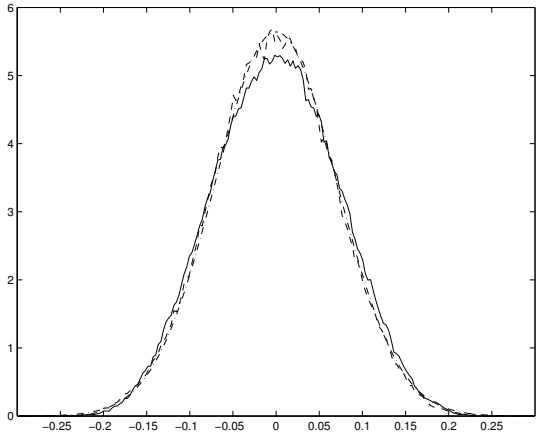

The PDF for random initial data, $\Lambda = 10$, $E = 0.1$, mode $k = 1$, solid line – $H = 10^{-2}$, dashed line – $H = -1.9 \cdot 10^{-3}$, dash-dotted line – Gaussian fit with the same variance centered at zero

Figure 2.14: The energy spectrum and PDF for $\Lambda = 10$.

into the surrounding statistically robust part of the phase space.

2.3 When is the Hamiltonian a statistically irrelevant conserved quantity?: a numerical study

In this section, we present powerful numerical evidence utilizing the numerical procedure in Section 2.2.3 of the role of the Hamiltonian H in (2.26) for the equilibrium statistical mechanics of the truncated Burgers-Hopf equations as described in Sections 2.2.1 and 2.2.2. The experiments confirm the precise quantitative guidelines for statistically relevant and irrelevant values of the Hamiltonian developed at the end of Section 2.2.2 In particular, our simulations furnish powerful numerical evidence that typical values of the Hamiltonian are irrelevant in the sense that they do not significantly affect the energy equipartition in (2.38) and that the corresponding correlation functions exhibit little oscillation, while atypical values of the Hamiltonian are relevant in the sense that they produce a significant spectral tilt, and slower decay with large oscillations in the correlation functions.

In the results reported below we have used both the deterministic initial condition

$$u_\Lambda(x, 0) = \sqrt{2E}\,(\sin x + \cos 2x)\,, \tag{2.70}$$

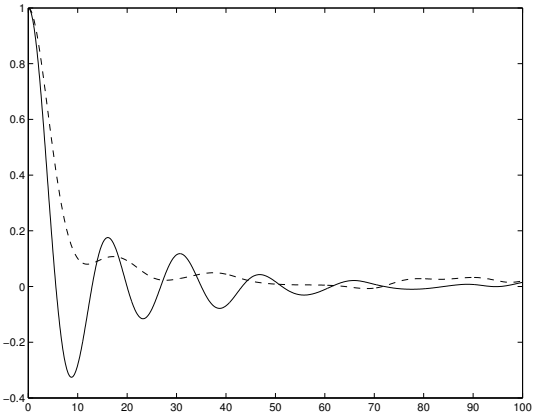

The time correlations for random initial data, $\Lambda = 10$, $E = 0.1$, mode $k = 1$, solid line – $H = 10^{-2}$, dashed line – $H = -1.9 \cdot 10^{-3}$

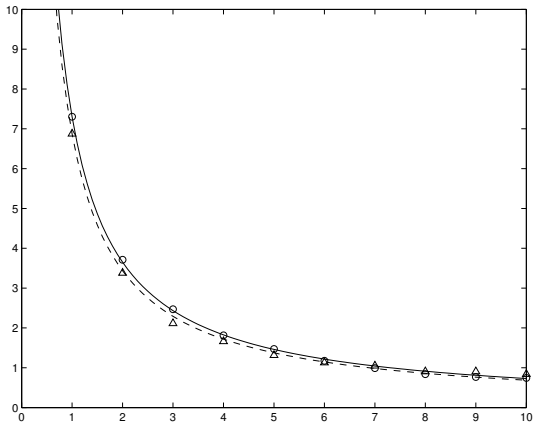

The correlation times for $\Lambda = 10$, $E = 0.1$, circles – $H = 10^{-2}$, triangles – $H = -1.9 \cdot 10^{-3}$, solid line – fit $C\sqrt{\beta}/k$ for circles, $C = 0.7303$, dashed line – fit $C\sqrt{\beta}/k$ for triangles, $C = 0.6875$

Figure 2.15: The correlation function and the correlation time scaling for $\Lambda = 10$

which is not a shift of an odd function, as well as random initial conditions generated by one step of the Monte-Carlo procedure above Claim 3 in Section 2.2.2.3. In the initial conditions (2.70), the multiplicative constant is chosen so that the initial condition and the subsequent solution satisfy the predetermined value of the energy E in (2.29).

As in [18, 19], in all our calculations with the deterministic initial data (2.70), we observe that the solution passes through three stages of randomization. The first stage is the deterministic stage before shocks develop in the corresponding untruncated Burgers-Hopf solution, the second the stage shortly after the breaking time when ripples appear on top of the still-deterministic solution, and the third the completely randomized stage. These stages are shown in Figure 1 of [18] and are not repeated here.

2.3.1 Computations with fixed energy (geophysical limit)

We present the case with the energy fixed at $E = 0.1$ and increasing truncation sizes $\Lambda = 10$, 20, 50, 100, and 200. The pseudo-spectral method was used in the computations, the time step was $\Delta t = 10^{-3}$, the initial averaging time was $T_0 = 1000$, and the averaging window $T = 20000$. Two sets of simulations with random initial conditions are presented. One set of deterministic initial conditions (2.70) is also presented for $\Lambda = 20$ and 50. Table 2.2 shows the widths $\sigma_H(\Lambda)$ of the Hamiltonian probability distribution functions $p_{\bar{E},\Lambda}(\lambda)$ for these values of Λ. For the deterministic initial data (2.70), the value of the

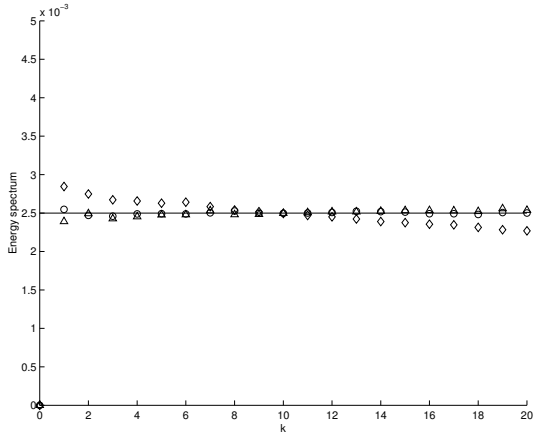

The energy spectrum for random and deterministic initial data, $\Lambda = 20$, $E = 0.1$, circles – $H = -4.7 \cdot 10^{-3}$, triangles – $H = -2.2 \cdot 10^{-3}$, diamonds – $H = -1.1 \cdot 10^{-2}$, horizontal line implies equipartitioned spectrum

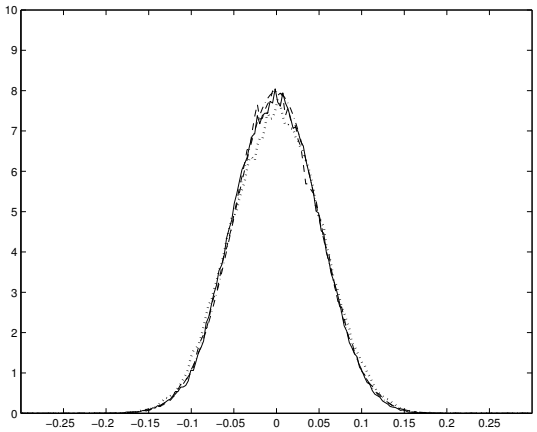

The PDF for random and deterministic initial data, $\Lambda = 20$, $E = 0.1$, mode $k = 1$, solid line – $H = -4.7 \cdot 10^{-3}$, dashed line – $H = -2.2 \cdot 10^{-3}$, dotted line – $H = -1.1 \cdot 10^{-2}$, dash-dotted line – Gaussian fit with the same variance centered at zero

Figure 2.16: The energy spectrum and the PDF for $\Lambda = 20$

Hamiltonian function is $H = -1.1 \cdot 10^{-2}$, which is never a typical value, since Table 2.2 shows shows that its magnitude always exceeds the standard deviation $\sigma_H(\Lambda)$. In all the computations, the energy in (2.29) and the Hamiltonian in (2.26) were conserved within 10^{-8} % and 10^{-9} %, respectively. The number of bins in the bin-counting procedure for constructing the PDF's of the modes is 200 in all the cases. The sizes of the bins are shown in Table 2.4.

The numerical results presented below give clear evidence that for atypical values of the Hamiltonian, the energy spectra are tilted compared to the equipartition prediction (2.38). We display the sizes of the tilts in Table 2.5, for which we assume the linear fit $E_k = a_0 + a_1 k$, and record the values of the coefficient a_1. Moreover, in Table 2.6, we provide the L_2 errors between the numerically computed PDF's and the predicted analytical Gaussian from the energy-based Gibbs distribution (2.34).

For $\Lambda = 10$ and random initial data, the values of the Hamiltonian H are $H = 10^{-2}$ and $H = -1.9 \cdot 10^{-3}$, respectively. The former is highly atypical, and the latter is typical. This is confirmed by the energy spectra in Figure 2.14 and the recorded tilts in Table 2.5, where the spectrum corresponding to $H = 10^{-2}$ is considerably more tilted. The average PDF over all modes is also less Gaussian in the atypical case according to Table 2.6. The correlation function for the $H = 10^{-2}$ case also exhibits considerably larger oscillations

Λ	Bin size
10	$3 \cdot 10^{-3}$
20	$3 \cdot 10^{-3}$
50	$1.5 \cdot 10^{-3}$
100	$1.5 \cdot 10^{-3}$
200	10^{-3}

Table 2.4: The bin sizes in the bin-counting computation of the PDF's of the modes for fixed energy $E = 0.1$

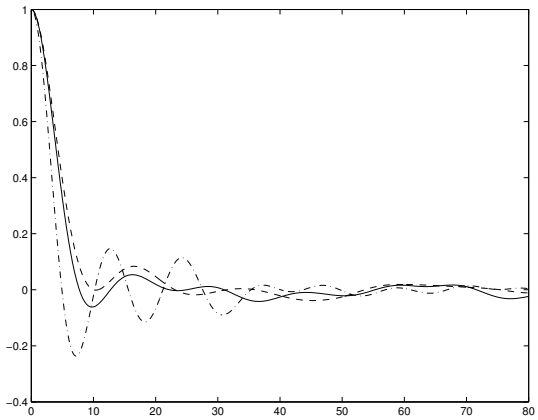

The time correlations for random and deterministic initial data, $\Lambda = 20$, $E = 0.1$, mode $k = 1$, solid line – $H = -4.7 \cdot 10^{-3}$, dashed line – $H = -2.2 \cdot 10^{-3}$, dash-dotted line – $H = -1.1 \cdot 10^{-2}$

Figure 2.17: The time correlations for $\Lambda = 20$

than the correlation function for the $H = -1.9 \cdot 10^{-3}$ case. The correlation functions for the $k = 1$ mode are shown in Figure 2.15. For both cases the correlation times obey formula for the scaling law in (2.41) quite accurately, as is also shown in Figure 2.15.

For $\Lambda = 20$, both values of the Hamiltonian H for random initial data, $H = -4.7 \cdot 10^{-3}$ and $H = -2.2 \cdot 10^{-3}$, are typical. As shown in Figure 2.16 and Tables 2.5 and 2.6, their energy spectra and PDF's agree very well with the theoretical predictions (2.38) and the Gaussian form implied by (2.34), respectively. The energy spectrum of the solution with the deterministic initial data (2.70) is considerably more tilted, and the PDF is farther away from the Gaussian; see Tables 2.5 and 2.6. While the correlation functions for the solutions corresponding to the two sets of random initial data are close to one another and exhibit only small oscillations, the correlation function for the solutions corresponding to

$\Lambda = 10,\ H = 10^{-2}$	$a_1 = -8.279 \cdot 10^{-5}$
$\Lambda = 10,\ H = -1.9 \cdot 10^{-3}$	$a_1 = 3.895 \cdot 10^{-5}$
$\Lambda = 20,\ H = -4.7 \cdot 10^{-3}$	$a_1 = 5.797 \cdot 10^{-7}$
$\Lambda = 20,\ H = -1.9 \cdot 10^{-3}$	$a_1 = 3.266 \cdot 10^{-6}$
$\Lambda = 20,\ H = -1.1 \cdot 10^{-2}$	$a_1 = -2.693 \cdot 10^{-5}$
$\Lambda = 50,\ H = 8 \cdot 10^{-3}$	$a_1 = -1.982 \cdot 10^{-6}$
$\Lambda = 50,\ H = 2 \cdot 10^{-3}$	$a_1 = 1.543 \cdot 10^{-7}$
$\Lambda = 50,\ H = -1.1 \cdot 10^{-2}$	$a_1 = -3.603 \cdot 10^{-6}$
$\Lambda = 100,\ H = -1.1 \cdot 10^{-3}$	$a_1 = 2.843 \cdot 10^{-8}$
$\Lambda = 100,\ H = -2.2 \cdot 10^{-3}$	$a_1 = 1.018 \cdot 10^{-8}$
$\Lambda = 200,\ H = -6.3 \cdot 10^{-4}$	$a_1 = 2.843 \cdot 10^{-8}$
$\Lambda = 200,\ H = 3.8 \cdot 10^{-5}$	$a_1 = 1.018 \cdot 10^{-8}$

Table 2.5: The tilt in the energy spectra. The results are fitted with $E_k = a_0 + a_1 k$ at fixed energy $E = 0.1$

$\Lambda = 10,\ H = 10^{-2}$	$L_{err} = 1.59 \cdot 10^{-1}$
$\Lambda = 10,\ H = -1.9 \cdot 10^{-3}$	$L_{err} = 9.29 \cdot 10^{-2}$
$\Lambda = 20,\ H = -4.7 \cdot 10^{-3}$	$L_{err} = 1.01 \cdot 10^{-1}$
$\Lambda = 20,\ H = -1.9 \cdot 10^{-3}$	$L_{err} = 1.54 \cdot 10^{-1}$
$\Lambda = 20,\ H = -1.1 \cdot 10^{-2}$	$L_{err} = 2.18 \cdot 10^{-1}$
$\Lambda = 50,\ H = 8 \cdot 10^{-3}$	$L_{err} = 1.12 \cdot 10^{-1}$
$\Lambda = 50,\ H = 2 \cdot 10^{-3}$	$L_{err} = 1.11 \cdot 10^{-1}$
$\Lambda = 50,\ H = -1.1 \cdot 10^{-2}$	$L_{err} = 3.26 \cdot 10^{-1}$
$\Lambda = 100,\ H = -1.1 \cdot 10^{-3}$	$L_{err} = 1.29 \cdot 10^{-1}$
$\Lambda = 100,\ H = -2.2 \cdot 10^{-3}$	$L_{err} = 1.11 \cdot 10^{-1}$
$\Lambda = 200,\ H = -6.3 \cdot 10^{-4}$	$L_{err} = 1.70 \cdot 10^{-1}$
$\Lambda = 200,\ H = 3.8 \cdot 10^{-5}$	$L_{err} = 1.48 \cdot 10^{-1}$

Table 2.6: The L_2 error between the numerically obtained PDF's and their Gaussian analytical fits at fixed energy $E = 0.1$

the deterministic initial data oscillates more strongly, as shown in Figure 2.17. Both sets of data produce a reasonably good fit with the correlation scaling law (2.41), as shown in Figure 2.18.

For $\Lambda = 50$, random initial data yield the values of the Hamiltonian $H = 8 \cdot 10^{-3}$ and $H = 2 \cdot 10^{-3}$, respectively. The former is atypical, and the latter is typical. This is reflected in the tilts of the energy spectra in Figure 2.19 and Table 2.5, and, to a lesser extent, the oscillations of the correlation functions. The PDF's are close to Gaussian; see Table 2.6. The tilt for the deterministic initial data is considerably larger, since the corresponding value of the Hamiltonian, $H = -1.1 \cdot 10^{-2}$, is highly atypical, and the PDF

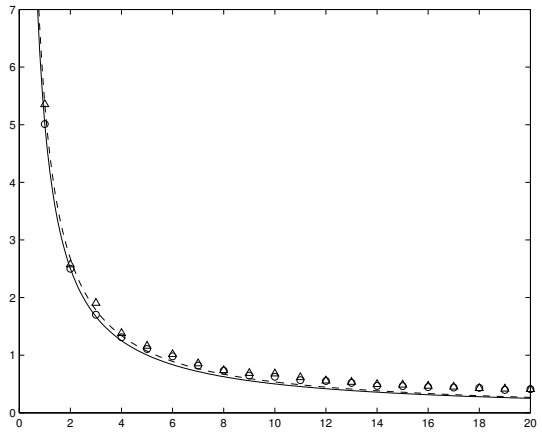

The correlation times for $\Lambda = 20$, $E = 0.1$, random initial data, circles – $H = -4.7 \cdot 10^{-3}$, triangles – $H = -2.2 \cdot 10^{-3}$, solid line – fit $C\sqrt{\beta}/k$ for circles, $C = 0.3544$, dashed line – fit $C\sqrt{\beta}/k$ for triangles, $C = 0.3786$

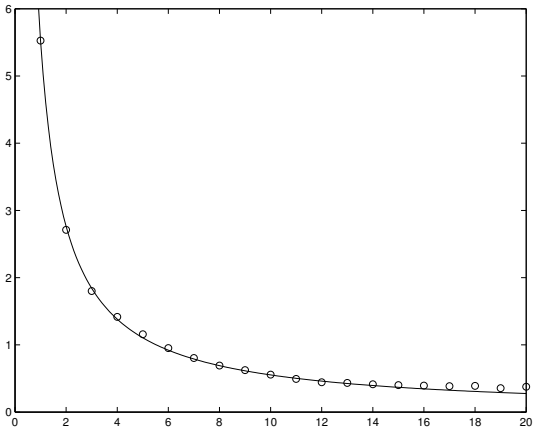

The correlation times for $\Lambda = 20$, $E = 0.1$, $\sin(x) + \cos(2x)$ initial data, circles – $H = 1.1 \cdot 10^{-2}$, solid line – fit $C\sqrt{\beta}/k$, $C = 0.3908$

Figure 2.18: The correlation time scaling for random and deterministic initial data with $\Lambda = 20$.

is much farther away from the Gaussian than the PDF for random initial data, as shown in Figure 2.19 and Tables 2.5 and 2.6. Correlation scaling formula (2.41) is a good fit in all three cases, as seen in Figure 2.20.

For $\Lambda = 100$, the values of the Hamiltonian along the solutions generated by the random initial data are $H = -1.1 \cdot 10^{-3}$ and $H = -2.2 \cdot 10^{-3}$, respectively. Both of these values are typical. The energy spectra and the PDF's are almost indistinguishable from their theoretically predicted counterparts, as shown in Figure 2.21 and Tables 2.5 and 2.6. Except for $k = 1$, the correlation functions are also indistinguishable. The fit of the correlation times with the scaling formula (2.41) is excellent, as shown in Figure 2.23.

For $\Lambda = 200$, the values of the Hamiltonian corresponding to the two randomly-generated sets of initial data are $H = -6.3 \cdot 10^{-4}$ and $H = 3.8 \cdot 10^{-5}$, respectively, which are both typical. They give excellent agreement with the theoretical predictions, as shown in Figures 2.22, 2.23 and Tables 2.5, 2.6. These last two cases confirm the robustness of the predictions of the statistical theory based solely on the Gibbs measure for energy [18, 19].

The results of this section thus furnish strong numerical evidence in support of the prediction of Section 2.2.2 that typical values of the Hamiltonian H in (2.26) are irrelevant for the statistical mechanics of the Burgers-Hopf equations in (2.27). This is reflected in the fact that the corresponding solutions exhibit negligible spectral tilts, essentially

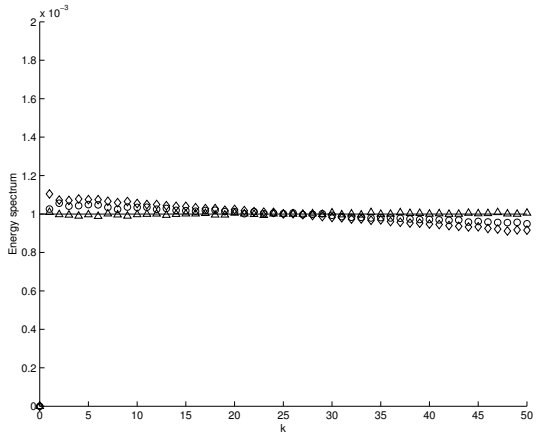

The energy spectrum for random initial data, $\Lambda = 50$, $E = 0.1$, circles – $H = 8 \cdot 10^{-3}$, triangles – $H = 2 \cdot 10^{-3}$, diamonds – $H = -1.1 \cdot 10^{-2}$, horizontal line implies equipartitioned spectrum

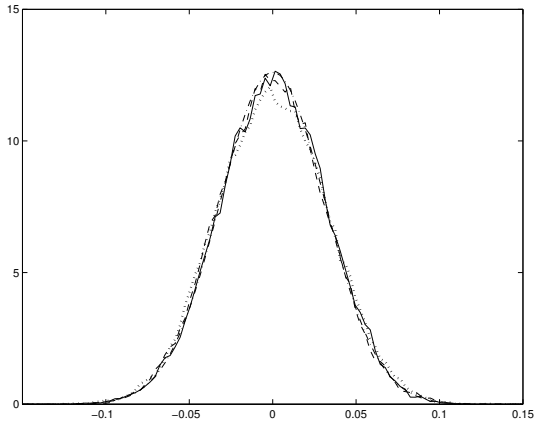

The PDF for random initial data, $\Lambda = 50$, $E = 0.1$, mode $k = 1$, solid line – $H = 8 \cdot 10^{-3}$, dashed line – $H = 2 \cdot 10^{-3}$, dotted line – $H = -1.1 \cdot 10^{-2}$, dash-dotted line – Gaussian fit with the same variance centered at zero

Figure 2.19: The energy spectrum and PDF for $\Lambda = 50$.

universal structure of the correlation functions with very small oscillations, and PDF's close to Gaussian. On the other hand, we have also provided strong numerical evidence that atypical values of the Hamiltonian are relevant in the sense that the the corresponding solutions exhibit considerable spectral tilts, strong oscillations of the correlation functions, and PDF's farther away from Gaussian. However, the correlation scaling law is also valid for the atypical cases.

2.3.2 Computations with fixed energy per mode (thermodynamical limit)

The second case we present is a set of numerical experiments with random initial data for which the energy per mode is fixed at

$$\frac{E}{2\Lambda} = 0.005.$$

The chosen range of Λ is $\Lambda = 10$, 20, 50, and 100. The pseudo-spectral method was used in the computation, the time step was $\Delta t = 10^{-3}$, the initial averaging time was $T_0 = 1000$, and the averaging window $T = 20000$. The standard deviations $\sigma_H(\Lambda)$ of the Hamiltonian probability distribution functions $p_{\bar{E},\Lambda}(\lambda)$ for these values of Λ are presented in the Table 2.3. The energy in (2.29) and the Hamiltonian in (2.26) were conserved within 10^{-8} % and 10^{-9} %, respectively, in all the computations. The number of bins in the bin-

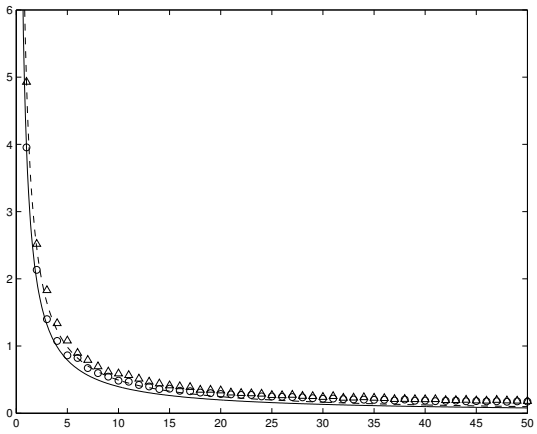

The correlation times for $\Lambda = 50$, $E = 0.1$, random initial data, circles – $H = 8 \cdot 10^{-3}$, triangles – $H = 2 \cdot 10^{-3}$, solid line – fit $C\sqrt{\beta}/k$ for circles, $C = 0.1769$ dashed line – fit $C\sqrt{\beta}/k$ for triangles, $C = 0.2204$

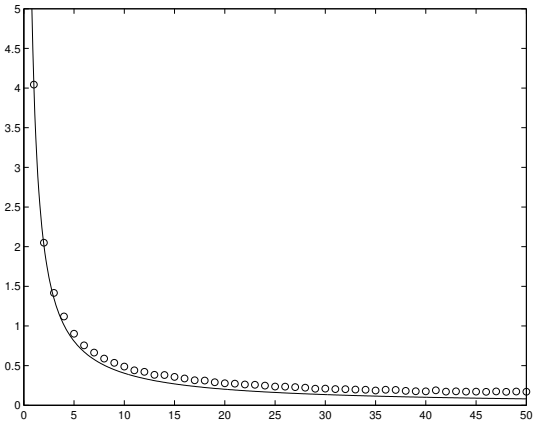

The correlation times for $\Lambda = 50$, $E = 0.1$, $\sin(x) + \cos(2x)$ initial data, circles – $H = 1.1 \cdot 10^{-2}$, solid line – fit $C\sqrt{\beta}/k$, $C = 0.1808$

Figure 2.20: The correlation time scaling for random and deterministic initial data with $\Lambda = 50$

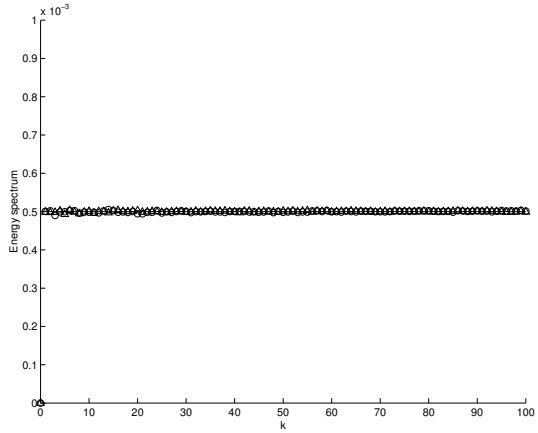

The energy spectrum for random initial data, $\Lambda = 100$, $E = 0.1$, circles – $H = -1.1 \cdot 10^{-3}$, triangles – $H = -2.2 \cdot 10^{-3}$, horizontal line implies equipartitioned spectrum

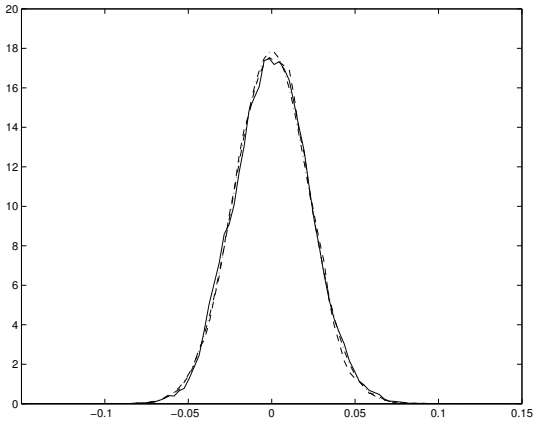

The PDF for random initial data, $\Lambda = 100$, $E = 0.1$, mode $k = 1$, solid line – $H = -1.1 \cdot 10^{-3}$, dashed line – $H = -2.2 \cdot 10^{-3}$, dash-dotted line – Gaussian fit with the same variance centered at zero

Figure 2.21: The energy spectrum and PDF for $\Lambda = 100$.

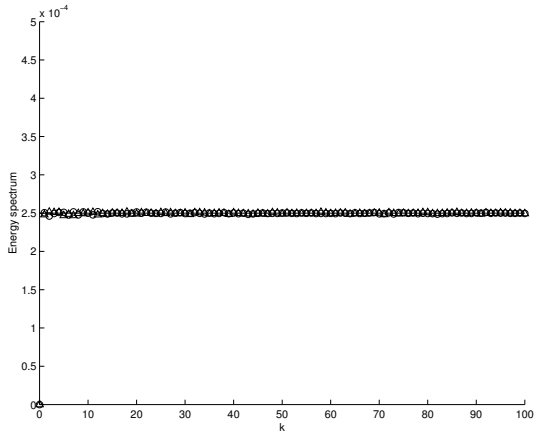

The energy spectrum for random initial data, $\Lambda = 200$, $E = 0.1$, circles – $H = -6.3 \cdot 10^{-4}$, triangles – $H = 3.8 \cdot 10^{-5}$, horizontal line implies equipartitioned spectrum

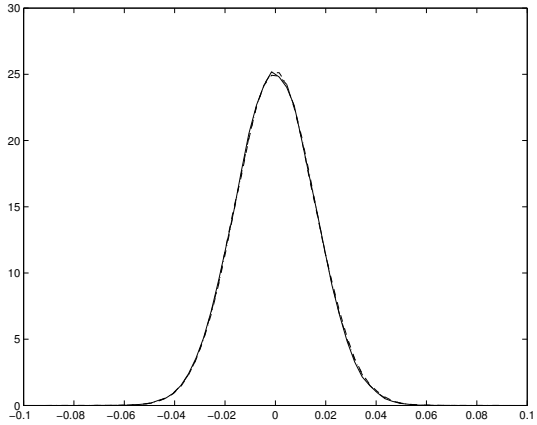

The PDF for random initial data, $\Lambda = 200$, $E = 0.1$, mode $k = 1$, solid line – $H = -6.3 \cdot 10^{-4}$, dashed line – $H = 3.8 \cdot 10^{-5}$, dash-dotted line – Gaussian fit with the same variance centered at zero

Figure 2.22: The energy spectrum and PDF for $\Lambda = 200$.

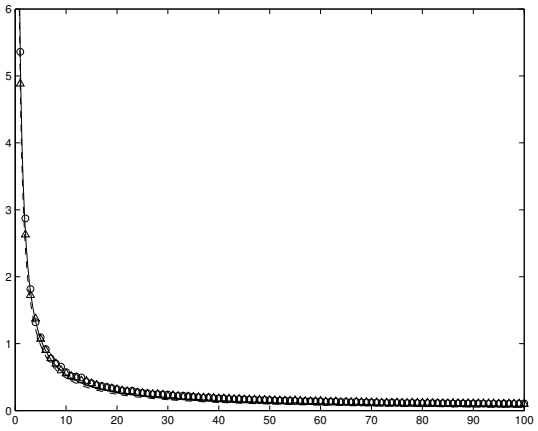

The correlation times for $\Lambda = 100$, $E = 0.1$, random initial data, circles – $H = -1.1 \cdot 10^{-3}$, triangles – $H = -2.2 \cdot 10^{-3}$, solid line – fit $C\sqrt{\beta}/k$ for circles, $C = 0.1695$, dashed line – fit $C\sqrt{\beta}/k$ for triangles, $C = 0.1544$

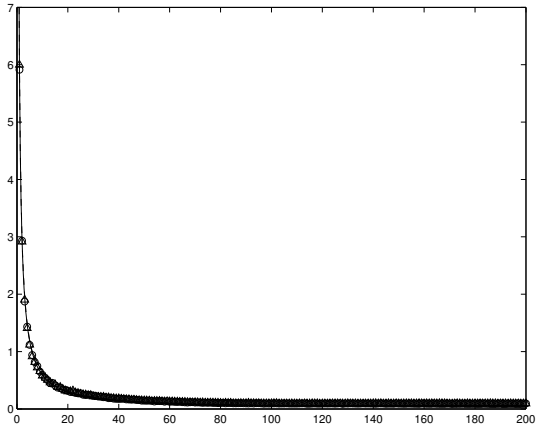

The correlation times for $\Lambda = 200$, $E = 0.1$, circles – $H = -6.3 \cdot 10^{-4}$, triangles – $H = 3.8 \cdot 10^{-5}$, solid line – fit $C\sqrt{\beta}/k$ for circles, $C = 0.1322$, dashed line – fit $C\sqrt{\beta}/k$ for triangles, $C = 0.1341$

Figure 2.23: The energy spectrum, PDF, and correlation time scaling for $\Lambda = 100$ and $\Lambda = 200$.

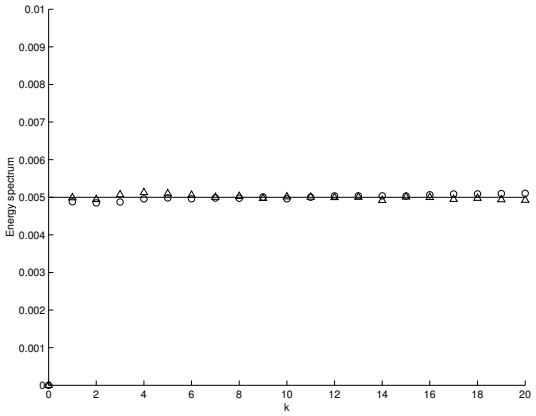

The energy spectrum for random initial data, $\Lambda = 20$, $E = 0.2$, circles – $H = 7.3 \cdot 10^{-5}$, triangles – $H = -1.6 \cdot 10^{-2}$, horizontal line implies equipartitioned spectrum

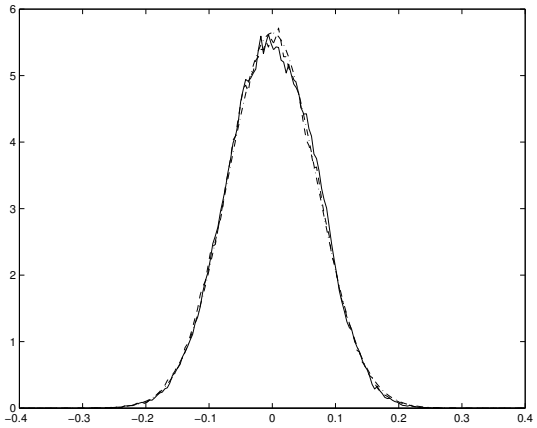

The PDF for random initial data, $\Lambda = 20$, $E = 0.2$, mode $k = 1$, solid line – $H = 7.3 \cdot 10^{-5}$, dashed line – $H = -1.6 \cdot 10^{-2}$, dash-dotted line – Gaussian fit with the same variance centered at zero

Figure 2.24: The energy spectrum and PDF for $\Lambda = 20$ at fixed energy per mode.

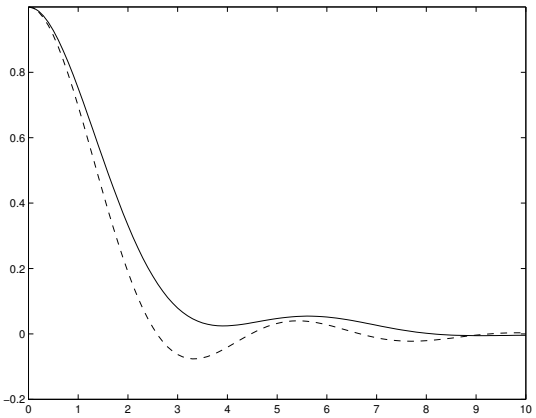

The time correlations for random initial data, $\Lambda = 20$, $E = 0.2$, mode $k = 1$, solid line – $H = 7.3 \cdot 10^{-5}$, dashed line – $H = -1.6 \cdot 10^{-2}$

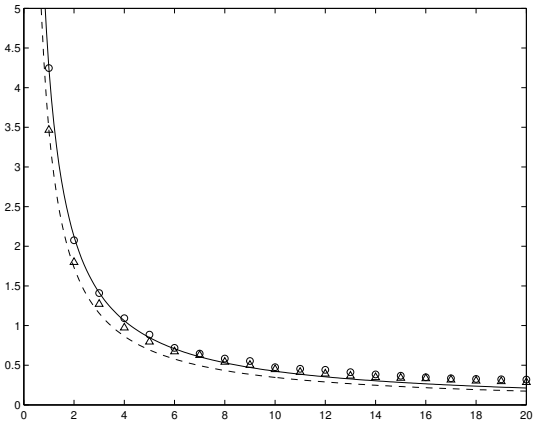

The correlation times for $\Lambda = 20$, $E = 0.2$, circles – $H = 7.3 \cdot 10^{-5}$, triangles – $H = -1.6 \cdot 10^{-2}$, solid line – fit $C\sqrt{\beta}/k$ for circles, $C = 0.4247$, dashed line – fit $C\sqrt{\beta}/k$ for triangles, $C = 0.3466$

Figure 2.25: The correlation function and the correlation time scaling for $\Lambda = 20$ at fixed energy per mode.

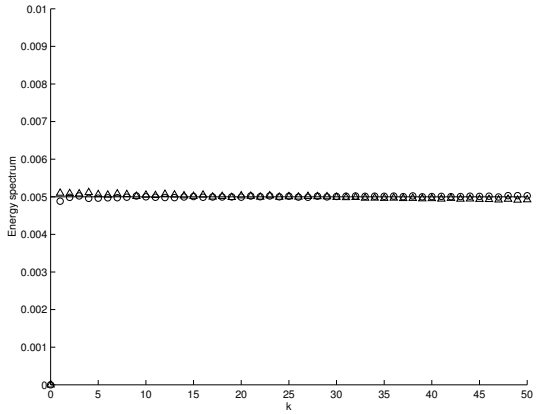

The energy spectrum for random initial data, $\Lambda = 50$, $E = 0.5$, circles – $H = 2.6 \cdot 10^{-2}$, triangles – $H = -5.7 \cdot 10^{-2}$, horizontal line implies equipartitioned spectrum

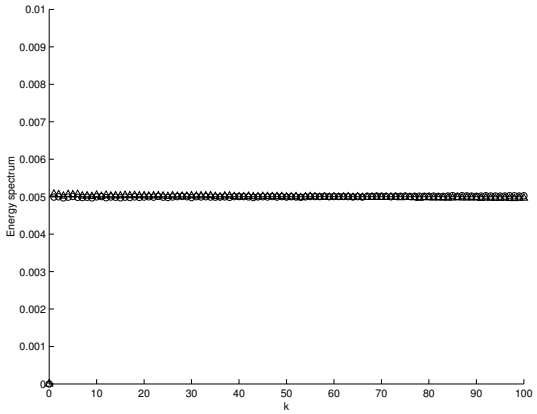

The energy spectrum for random initial data, $\Lambda = 100$, $E = 1.0$, circles – $H = -6.9 \cdot 10^{-3}$, triangles – $H = 1.2 \cdot 10^{-1}$, horizontal line implies equipartitioned spectrum

Figure 2.26: The energy spectrum for $\Lambda = 50$ and $\Lambda = 100$ at fixed energy per mode.

$\Lambda = 10,\ H = 10^{-2}$	$a_1 = -8.279 \cdot 10^{-5}$
$\Lambda = 10,\ H = -1.9 \cdot 10^{-3}$	$a_1 = 3.895 \cdot 10^{-5}$
$\Lambda = 20,\ H = 7.3 \cdot 10^{-5}$	$a_1 = 5.464 \cdot 10^{-6}$
$\Lambda = 20,\ H = -1.6 \cdot 10^{-2}$	$a_1 = -1.191 \cdot 10^{-5}$
$\Lambda = 50,\ H = 2.6 \cdot 10^{-2}$	$a_1 = 1.001 \cdot 10^{-6}$
$\Lambda = 50,\ H = -5.7 \cdot 10^{-2}$	$a_1 = -3.354 \cdot 10^{-6}$
$\Lambda = 100,\ H = -6.9 \cdot 10^{-3}$	$a_1 = 3.908 \cdot 10^{-7}$
$\Lambda = 100,\ H = 1.2 \cdot 10^{-1}$	$a_1 = -8.695 \cdot 10^{-7}$

Table 2.7: The tilt in energy spectra: the results are fitted with $E_k = a_0 + a_1 k$ at fixed energy per mode $E/2\Lambda = 0.005$

counting procedure for constructing the PDF's of the modes is 200, and the size of each bin is $4 \cdot 10^{-3}$ in all the computed cases. The sizes of the tilts are displayed in Table 2.7, for which we again assume the linear fit $E_k = a_0 + a_1 k$, and record the values of the coefficient a_1. Table 2.8, provides the L_2 errors between the numerically computed PDF's and Gaussians predicted analytical from the energy-based Gibbs distribution (2.34).

For $\Lambda = 10$, we consider the same random initial condition as in the previous section. The results are shown in Figures 2.14 and 2.15, and Tables 2.7 and 2.8.

For $\Lambda = 20$, the values of the Hamiltonian on the two solutions generated by the random initial data are $H = 7.3 \cdot 10^{-5}$ and $H = -1.6 \cdot 10^{-2}$, respectively, the first being typical and the second atypical. The energy spectrum for the atypical value of the

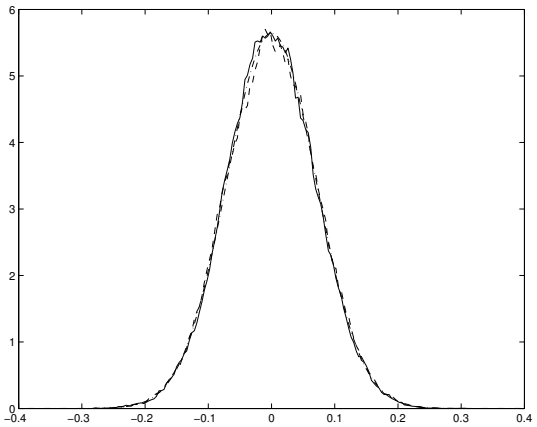

The PDF for random initial data, $\Lambda = 50$, $E = 0.5$, mode $k = 1$, solid line – $H = 2.6 \cdot 10^{-2}$, dashed line – $H = -5.7 \cdot 10^{-2}$, dash-dotted line – Gaussian fit with the same variance centered at zero

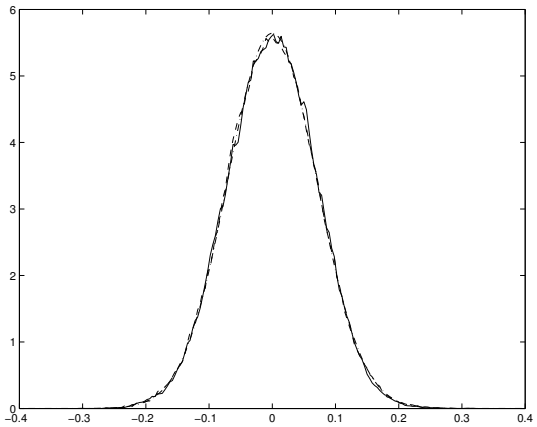

The PDF for random initial data, $\Lambda = 100$, $E = 1.0$, mode $k = 1$, solid line – $H = -6.9 \cdot 10^{-3}$, dashed line – $H = 1.2 \cdot 10^{-1}$, dash-dotted line – Gaussian fit with the same variance centered at zero

Figure 2.27: The PDF's for $\Lambda = 50$ and $\Lambda = 100$ at fixed energy per mode.

$\Lambda = 10$, $H = 10^{-2}$	$L_{err} = 1.59 \cdot 10^{-1}$
$\Lambda = 10$, $H = -1.9 \cdot 10^{-3}$	$L_{err} = 9.29 \cdot 10^{-2}$
$\Lambda = 20$, $H = 7.3 \cdot 10^{-5}$	$L_{err} = 7.95 \cdot 10^{-2}$
$\Lambda = 20$, $H = -1.6 \cdot 10^{-2}$	$L_{err} = 5.51 \cdot 10^{-2}$
$\Lambda = 50$, $H = 2.6 \cdot 10^{-2}$	$L_{err} = 5.19 \cdot 10^{-2}$
$\Lambda = 50$, $H = -5.7 \cdot 10^{-2}$	$L_{err} = 6.17 \cdot 10^{-2}$
$\Lambda = 100$, $H = -6.9 \cdot 10^{-3}$	$L_{err} = 4.89 \cdot 10^{-2}$
$\Lambda = 100$, $H = 1.2 \cdot 10^{-1}$	$L_{err} = 4.07 \cdot 10^{-2}$

Table 2.8: The L_2 error between the numerically obtained PDF's and their analytical Gaussian fits at fixed energy per mode $E/2\Lambda = 0.005$

Hamiltonian is slightly more tilted than that for the typical value, as shown in Figure 2.24 and Table 2.7. The PDF's, as also shown in Figure 2.24, are in good agreement with analytical prediction; see Table 2.8. The atypical value of the Hamiltonian produces somewhat larger oscillations of the correlation functions. Both solutions produce good agreement with the correlation time scaling formula (2.41), as shown in Figure 2.25.

For $\Lambda = 50$, the values of the Hamiltonian for the two tracked solutions are $H = 2.6 \cdot 10^{-2}$ and $H = -5.7 \cdot 10^{-2}$, and for $\Lambda = 100$, they are $H = -6.9 \cdot 10^{-3}$ and $H = 1.2 \cdot 10^{-1}$, respectively. In both cases, the first value is typical and the second atypical. The energy spectra corresponding to the the atypical Hamiltonian values exhibit barely noticeable tilts, as seen in Figure 2.26 and Table 2.7. The PDF's in Figure 2.27 in any of these

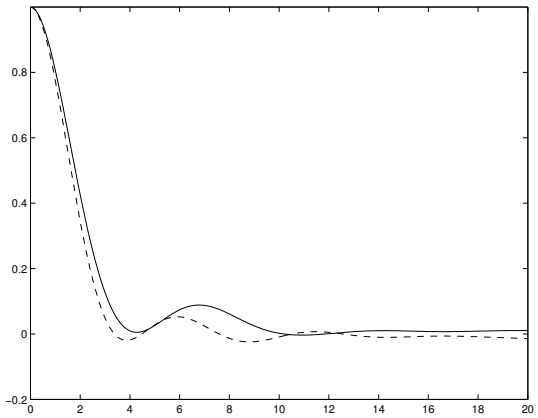

The time correlations for random initial data, $\Lambda = 50$, $E = 0.5$, mode $k = 1$, solid line – $H = 2.6 \cdot 10^{-2}$, dashed line – $H = -5.7 \cdot 10^{-2}$

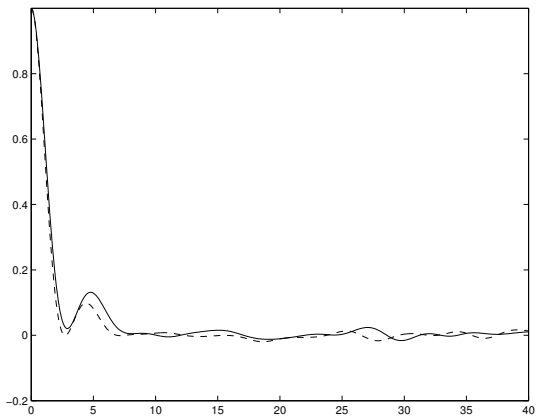

The time correlations for random initial data, $\Lambda = 100$, $E = 1.0$, mode $k = 1$, solid line – $H = -6.9 \cdot 10^{-3}$, dashed line – $H = 1.2 \cdot 10^{-1}$

Figure 2.28: The correlation functions for $\Lambda = 50$ and $\Lambda = 100$ at fixed energy per mode.

cases do not significantly differ from the Gaussian analytic prediction that follows from (2.34), which can also be seen from Table 2.8. For both $\Lambda = 50$ and $\Lambda = 100$, the correlation functions for the two solutions exhibit comparable oscillations; see Figure 2.28. For $\Lambda = 50$, the agreement between the theoretically predicted correlation times (2.41) and their computed counterparts is very good, and for $\Lambda = 100$, this agreement is good for mode numbers $k \leq 20$; see Figure 2.29.

For the high modes in the $\Lambda = 100$ case, the computed correlation times T_k do not decay to zero. This is an artifact of the numerical integration, explained as follows: All the correlation functions $c_k(\tau)$ in (2.39) satisfy $c_k(0) = 1$, which is also the maximum possible value of the integrand in the formula (2.40) for the correlation time T_k. Due to the discretization, there is a minimal possible value of the numerically computed integral in (2.40), which is $I_{min} = \frac{\Delta\tau}{n}$, where $\Delta\tau$ is the discretization interval, and n depends on the order of the numerical integration method. For the trapezoidal rule, which we use for the integration, $n = 2$.

The overall evidence furnished by the numerical results in this section is again that typical values of the Hamiltonian H are irrelevant, and atypical are relevant in the sense described at the end of the previous section and also at the end of Section 2.2.2.

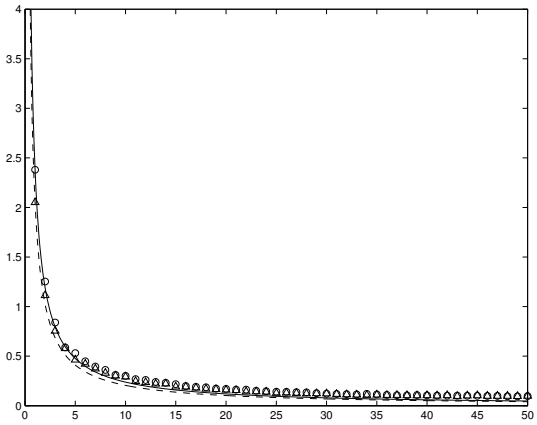

The correlation times for $\Lambda = 50$, $E = 0.5$, circles – $H = 2.6 \cdot 10^{-2}$, triangles – $H = -5.7 \cdot 10^{-2}$, solid line – fit $C\sqrt{\beta}/k$ for circles, $C = 0.2380$, dashed line – fit $C\sqrt{\beta}/k$ for triangles, $C = 0.2051$

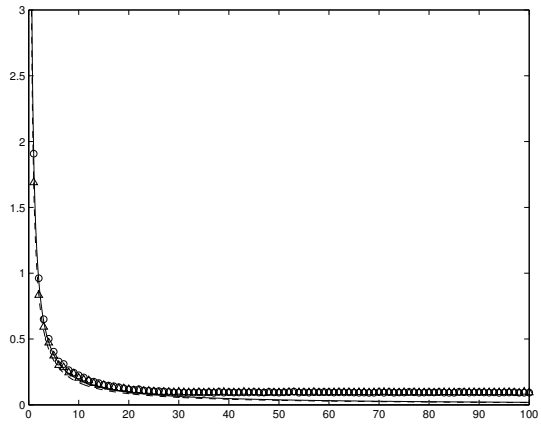

The correlation times for $\Lambda = 100$, $E = 1.0$, circles – $H = -6.9 \cdot 10^{-3}$, triangles – $H = 1.2 \cdot 10^{-1}$, solid line – fit $C\sqrt{\beta}/k$ for circles, $C = 0.1908$, dashed line – fit $C\sqrt{\beta}/k$ for triangles, $C = 0.1689$

Figure 2.29: The correlation time scaling for $\Lambda = 50$ and $\Lambda = 100$ at fixed energy per mode.

2.4 Equilibrium statistical predictions for the spectral tilt for statistically relevant values of the Hamiltonian.

Since the spectral tilts observed in Section 2.3 correspond to more energy at large scales and less energy at small scales, as in a spectrum for the Burgers equation associated with shock formation and nonlinear energy transfer, the skeptical reader might attribute this behavior to numerical artifacts. Here we show that such concerns are unwarranted. In this section, we present a purely equilibrium statistical-mechanical Monte-Carlo computation that predicts the spectral tilt seen in the numerical solutions of the truncated Burgers-Hopf equations (2.27) with statistically relevant initial data. Since all the statistics presented in the previous section were gathered micro-canonically by following long-time trajectories, here we also compute the energy spectra by using the micro-canonical distribution in both the energy (2.29) and the Hamiltonian (2.26) in conjunction with a modification of the basic Monte-Carlo algorithm discussed above Claim 3. It is clear that this purely equilibrium statistical computation can only be successful if the computed trajectories are ergodic on the joint isosurfaces of the energy E and the Hamiltonian H, and, in fact, the remarkable agreement between the spectra computed from equilibrium statistical mechanics by the Monte-Carlo method and those computed by direct numerical simulations provides additional strong numerical evidence that this ergodicity truly takes

place.

We first compute the restriction of the measure (2.44) to the joint isosurface of the energy E in (2.29) and the Hamiltonian H in (2.26), $E = \bar{E}$ and $H = \bar{H}$, which is given by the formula

$$d\mu_{\bar{H},\bar{E},\Lambda} = \Gamma\delta\left(H(u_\Lambda) - \bar{H}\right) d\nu_{\bar{E},\Lambda}, \tag{2.71}$$

where Γ is a normalizing factor. The energy spectrum restricted to this isosurface is computed from the formula

$$\frac{1}{2}\langle|\hat{u}_k|^2\rangle = \frac{1}{2}\int_{S_{\bar{E},\Lambda}} |\hat{u}_k|^2 \, d\mu_{\bar{H},\bar{E},\Lambda}. \tag{2.72}$$

The Monte-Carlo algorithm of Section 2.2.2 for generating an approximately uniform distribution of points on the constant energy sphere $S_{\bar{E},\Lambda}$ provides a good numerical approximation of the measure (2.44). Our task remains to include the numerical version of the term $\delta\left(H(u_\Lambda) - \bar{H}\right)$ in (2.71).

To this end, we regularize the delta-function $\delta(\lambda)$ by the expression

$$F_\varepsilon(\lambda) = \varepsilon^{-1}\chi_{A_\varepsilon}(\lambda), \tag{2.73}$$

where

$$A_\varepsilon = \left\{\lambda : |\lambda| \leq \frac{\varepsilon}{2}\right\},$$

and $\chi_S(x)$ is the characteristic function of the set S, as defined in formula (2.56). Since $F_\varepsilon(\lambda) \to \delta(\lambda)$ as $\varepsilon \to 0$, we can write an approximation for (2.72) as

$$\langle|\hat{u}_k|^2\rangle_\varepsilon = \frac{\displaystyle\int_{S_{\bar{E},\Lambda}} |\hat{u}_k|^2 \, F_\varepsilon\left[H(u_\Lambda) - \bar{H}\right] d\nu_{\bar{E},\Lambda}}{\displaystyle\int_{S_{\bar{E},\Lambda}} F_\varepsilon\left[H(u_\Lambda) - \bar{H}\right] d\nu_{\bar{E},\Lambda}}. \tag{2.74}$$

In practice, our Monte-Carlo computation proceeds as follows: We first choose the truncation size Λ, the energy value $\bar{E}$, the value of the Hamiltonian $\bar{H}$, and a small ε. We then generate a sequence of vectors $(\hat{u}_1^{(i)}, \ldots, \hat{u}_\Lambda^{(i)})$, $i = 1, 2, \ldots$ by using the Monte-Carlo algorithm described above Claim 3 with $\bar{E}$ as the energy value. If $\left|H(u_\Lambda^{(i)}) - \bar{H}\right| \leq \varepsilon/2$, the vector $(\hat{u}_1^{(i)}, \ldots, \hat{u}_\Lambda^{(i)})$ is recorded. The recorded vectors are re-numbered as $(\hat{u}_1^{(j)}, \ldots, \hat{u}_\Lambda^{(j)})$,

$j = 1, \ldots, M$. The energy spectrum is then computed from the formula

$$\frac{1}{2}\langle |\hat{u}_k|^2 \rangle = \frac{1}{2M} \sum_{j=1}^{M} |\hat{u}_k^{(j)}|^2, \qquad k = 1, \ldots, \Lambda. \tag{2.75}$$

The convergence of this algorithm for fixed E in the limit as $M \to \infty$ to the true expected values (2.72) of the spectral coefficients on the slightly regularized joint isosurfaces of the energy and the Hamiltonian is guaranteed via the law of large numbers.

2.4.1 Comparison of Equilibrium Statistical Predictions and Direct Numerical Simulation for the Spectrum

In Figures 2.30 and 2.31, we present several examples of energy spectra of the truncated Burgers-Hopf equation (2.27) computed from (2.75) via the Monte-Carlo algorithm described above Claim 3 and compared with the direct simulation. We have chosen the values of the energy $E = 0.1$ and the Hamiltonian $H = 1.1 \cdot 10^{-2}$. We compare the results of these Monte-Carlo-based spectral computations to direct simulations of the truncated Burgers-Hopf equations (2.27) with the initial condition $\sqrt{2E}(\sin x + \cos 2x)$. For this initial condition, the value of the energy is $E = 0.1$, and the value of the Hamiltonian is atypical, $H = 1.1 \cdot 10^{-2}$. For the Monte-Carlo computations, we have chosen $\varepsilon = 10^{-4}$. The chosen truncation sizes are $\Lambda = 10$, $\Lambda = 20$ and $\Lambda = 50$. In all the direct simulations, the time step is $\Delta t = 10^{-3}$, the initial averaging time is $T_0 = 1000$, the averaging window $T = 20000$, the energy (2.29) is conserved within 10^{-8} % and the Hamiltonian (2.26) within 10^{-9} %.

As we can see from Figures 2.30 and 2.31, the results of the equilibrium Monte-Carlo computations and the direct truncated Burgers-Hopf simulations both yield spectral tilts which are in excellent agreement. In particular, their maximal mutual relative error is 3.23 %. This agreement provides a clear numerical confirmation of the accuracy of our equilibrium Monte-Carlo predictions in the micro-canonical setting, as well a clear validation of the assumption that the trajectories of the truncated Burgers-Hopf equations (2.27) are ergodic on the joint isosurfaces of the energy and the Hamiltonian.

The computed energy spectra for the atypical values of the Hamiltonian H shown in Section 2.3 and the preceding paragraph, and the values of the spectral tilt displayed in Tables 2.5, furnish strong numerical evidence for the following characteristics of the tilt:

- The tilt is a linear function of the mode number k, and the spectral values are

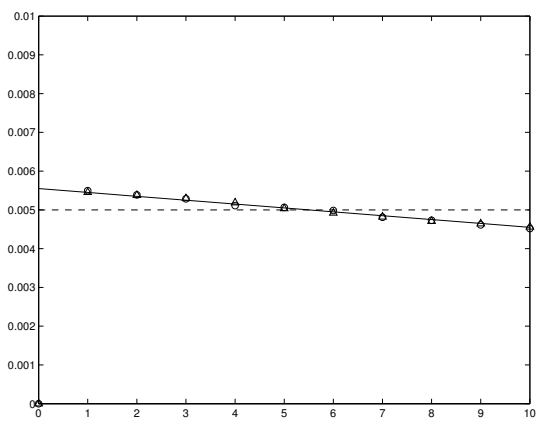

The energy spectrum for $\Lambda = 10$, $E = 0.1$, $H = 1.1 \cdot 10^{-2}$, circles – Burgers-Hopf, triangles – Monte-Carlo, solid line shows the analytical fit, dashed horizontal line implies equipartitioned spectrum

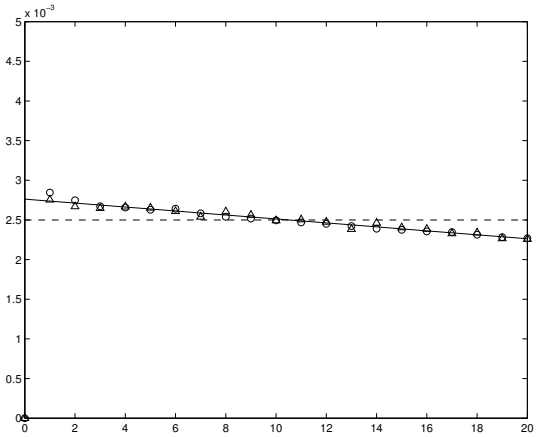

The energy spectrum for $\Lambda = 20$, $E = 0.1$, $H = 1.1 \cdot 10^{-2}$, circles – Burgers-Hopf, triangles – Monte-Carlo, solid line shows the analytical fit, dashed horizontal line implies equipartitioned spectrum

Figure 2.30: The energy spectra computed from the solution of the Burgers-Hopf truncation with deterministic initial data $\sqrt{2E}(\sin(x) + \cos(2x))$ and from the Monte-Carlo simulation for $\Lambda = 10$ and $\Lambda = 20$.

decreasing with increasing k.

- The spectrum is tilted about the point $(\Lambda + 1)/2$, where it crosses the horizontal line at $E_{p/m}(\Lambda) = E/2\Lambda$, which is the mean energy per mode predicted by the equipartition formula (2.36).

2.4.2 A Heuristic Universal Formula for the Spectral Tilt

By using these two observations, here we propose a heuristic formula for quantifying the tilt in the energy spectrum

$$\frac{1}{2}\langle|\hat{u}_k|^2\rangle = E_{p/m}(\Lambda)\left(1 + \alpha(E,H)\frac{(\Lambda+1)/2 - k}{\Lambda}\right), \tag{2.76}$$

where $\alpha(E,H)$ is a function that we now determine. Note that, since

$$\sum_{k=1}^{\Lambda}[(\Lambda+1)/2 - k] = 0$$

for all truncation sizes Λ, the terms multiplied by $\alpha(E,H)$ do not affect the total energy.

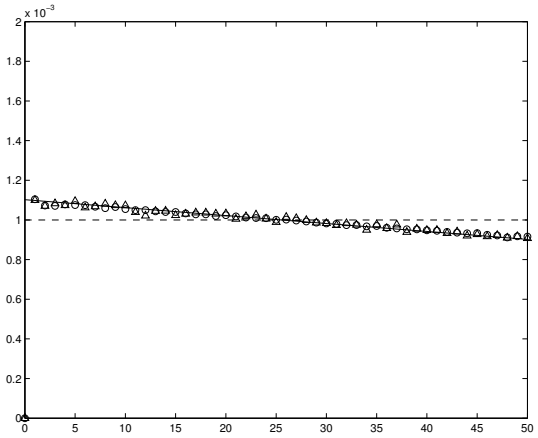

The energy spectrum for $\Lambda = 50$, $E = 0.1$, $H = 1.1 \cdot 10^{-2}$, circles – Burgers-Hopf, triangles – Monte-Carlo, solid line shows the analytical fit, dashed horizontal line implies equipartitioned spectrum

Figure 2.31: The energy spectra computed from the solution of the Burgers-Hopf truncation with deterministic initial data $\sqrt{2E}(\sin(x) + \cos(2x))$ and from the Monte-Carlo simulation for $\Lambda = 50$.

In all three cases presented in the paragraphs above, we find the parameter $\alpha(E, H)$ to be

$$\alpha(E, H) = 0.2.$$

We thus conclude that $\alpha(E, H)$ is independent of the truncation size Λ.

Since $H = 0$ is an irrelevant value and no tilt occurs for it, $\alpha(E, H)$ must satisfy

$$\alpha(E, 0) = 0,$$

and since $\alpha(E, H)$ is non-dimensional, we must have

$$\alpha(E, H) = \alpha(H^2/E^3)$$

for some nonlinear function α. For $(H^2/E^3) \ll 1$, which is true in all our computations, we can Taylor expand $\alpha(H^2/E^3)$ and only keep the first term,

$$\alpha(E, H) = \mu \frac{H^2}{E^3}. \tag{2.77}$$

Thus, the expression (2.76) finally becomes

$$\frac{1}{2}\langle|\hat{u}_k|^2\rangle = E_{p/m}(\Lambda)\left(1+\mu\frac{H^2}{E^3}\,\frac{(\Lambda+1)/2-k}{\Lambda}\right). \tag{2.78}$$

Assuming the form (2.77) of $\alpha(E,H)$ we have revisited the numerical experiments of Section 2.3, in which the energy is fixed at $E=0.1$, whereas the values of the Hamiltonian H vary from $3\cdot 10^{-3}$ to $1.1\cdot 10^{-2}$, and the values of Λ vary from 10 to 200. From these experiments we determine that μ is also constant within about 5%, i.e.

$$\mu = 1.60438 \pm 8.031\cdot 10^{-2}.$$

Thus, the heuristic formula in (2.78) provides an excellent fit for all of the spectral tilts which have been observed in numerical simulations with Burgers-Hopf truncation for $E=0.1$. Also this formula is completely self-consistent with the fact that no spectral tilt occurs for statistically irrelevant values of the Hamiltonian.

2.5 Concluding discussion

At the end of the chapter we would like to briefly summarize the results. We considered the two natural limits as number of degrees of freedom becomes infinitely large: geophysical and thermodynamical. The relevance of the Hamiltonian in each situation was established as the quantitative and heuristic connection between a probabilistic weight of Hamiltonian and its influence. The results in this chapter were established through a combination of numerical simulations of the truncated Burgers-Hopf equation, Monte-Carlo simulations for equilibrium ensembles, and simple mathematical arguments suggest several new problems in equilibrium statistical mechanics which merit further study through completely rigorous mathematical analysis. The first of these is a central limit theorem for the probability density of the Hamiltonian on a microcanonical energy surface for both of the limits for either fixed mean energy or fixed mean energy per mode as $\Lambda\to\infty$. The second main problem involves a suitable large deviation principle for the statistically relevant values of H which confirms the spectral tilt seen in both the simulations and confirmed by the equilibrium statistical Monte-Carlo simulations in Section 2.4. A rigorous proof of the heuristic formula for this spectral tilt for Section 2.4 for finite Λ or a suitable generalization also would be very interesting.

CHAPTER 3
EQUATIONS FOR BAROTROPIC FLOW AND EQUILIBRIUM STATISTICAL THEORIES

The two-dimensional equations for barotropic flow with topography can be considered as a good simple model for the inviscid flow which includes the influence of the landscape shape below. The important pieces of this model are, first, the non-linear advection term, which is a key feature in any of the real weather models, and, second, the presence of the special topographic function, which represents the changes in the potential energy of the flow depending on the spatial location. Needless to say, this model is significantly more advanced in the sense of complexity of the statistical behavior, than the truncated Burgers-Hopf equation. First, the presence of the topographic function creates a non-trivial mean flow, the feature which has not been either predicted or observed in the truncated Burgers-Hopf equation. Second, the equilibrium statistical theory for the equations for barotropic flow involves more than one conserved quantity and therefore is much more complex than that for the truncated Burgers-Hopf equation. Third, the transition from 1D to 2D by itself adds complexity, if not analytically, than at least in the numerical sense.

In this chapter we consider the equations for barotropic flow with topography on a periodic domain. One may argue that the periodic domain would be too idealized representation of the real world conditions, however it gives us certain advantages. First, the equations for barotropic flow on a periodic domain possess the non-canonical Hamiltonian structure with the vast number of the Casimir invariants, which are to be considered as the additional conserved quantities in the system. Second, periodicity allows the use of the Fourier representation of the equations for barotropic flow, and, from the practical point of view, helps to truncate the equations for barotropic flow such that the numerical experiments can be done with the truncated equations. As well as the equations for barotropic flow themselves, in this chapter we also present the empirical statistical theory for the equations for barotropic flow, and the complete statistical theory for the truncated equations. Here, however, we will limit ourselves to the description of statistical predictions which we are later going to check numerically. For more extensive coverage on the statistical theories for the equations for barotropic flow, see Majda and Wang [17], and references therein.

3.1 Equations for barotropic flow with topography

In this section we introduce the equations for barotropic flow with topography. For various purposes which later will become clear, we assume that the domain is periodic.

The equations for barotropic flow are

$$\frac{\partial q}{\partial t} + \nabla^{\perp}\psi \cdot \nabla q = 0, \tag{3.1a}$$

$$q = \Delta\psi + h, \tag{3.1b}$$

where

$$\nabla^{\perp}\psi = \begin{pmatrix} -\psi_y \\ \psi_x \end{pmatrix} = \mathbf{v}$$

is the velocity of the flow at given position and time. $q = q(x, y, t)$ is a *potential vorticity*, $\psi = \psi(x, y, t)$ is a *stream function*, and $h = h(x, y)$ is a *topography*. In the above context we assume that q, ψ and h are 2π-periodic.

The equations (3.1) describe the flow on a surface with a topographic effect. The equations are obtained as an approximation to the inviscid Navier-Stokes equations under the assumption of strongly stratified (i.e. horizontally layered) flow with no interaction between different layers.

The equations (3.1) have many conserved quantities. The most fundamental property is the conservation of the potential vorticity

$$M = \frac{1}{4\pi^2}\int q \,\mathrm{d}x\,\mathrm{d}y, \tag{3.2a}$$

$$\frac{\mathrm{d}M}{\mathrm{d}t} = 0, \tag{3.2b}$$

which is equivalent to the conservation of mass. Another very important property is the conservation of kinetic energy

$$E = \frac{1}{8\pi^2}\int \mathbf{v}^2 \,\mathrm{d}x\,\mathrm{d}y = \frac{1}{8\pi^2}\int (\nabla\psi)^2 \,\mathrm{d}x\,\mathrm{d}y. \tag{3.3a}$$

$$\frac{\mathrm{d}E}{\mathrm{d}t} = 0. \tag{3.3b}$$

The proof of conservation for these fundamental quantities, as well as for other important ones, will be given in the next section.

3.1.1 Equations for barotropic flow as a Hamiltonian system

The equation (3.1) can be written in the form

$$\frac{\partial q}{\partial t} = \mathcal{J}\frac{\delta H}{\delta q}, \tag{3.4}$$

where

$$\mathcal{J} = 4\pi^2(\nabla q \cdot \nabla^\perp) \quad \text{is the symplectic operator,} \tag{3.5a}$$

$$H = E = \frac{1}{8\pi^2}\int (\nabla\psi)^2 \,\mathrm{d}x\,\mathrm{d}y \quad \text{is the Hamiltonian.} \tag{3.5b}$$

The Poisson bracket for the operator $\mathcal{J}$ is skew-symmetric:

$$\int f\mathcal{J}g \,\mathrm{d}x\,\mathrm{d}y = \int f(-q_x g_y + q_y g_x)\,\mathrm{d}x\,\mathrm{d}y =$$
$$= \int g(q_x f_y - q_y f_x)\,\mathrm{d}x\,\mathrm{d}y = -\int g\mathcal{J}f \,\mathrm{d}x\,\mathrm{d}y,$$

which ensures the conservation of energy. We do not prove the Jacobi identity for $\mathcal{J}$, because the canonical representation of (3.1) is not needed.

The fact that E is the Hamiltonian for (3.1) follows from

$$\frac{\delta E}{\delta q} = \frac{\delta}{\delta q}\frac{1}{8\pi^2}\int (\nabla\psi)^2 \,\mathrm{d}x\,\mathrm{d}y = -\frac{\delta}{\delta q}\frac{1}{8\pi^2}\int \psi(q-h)\,\mathrm{d}x\,\mathrm{d}y = -\frac{1}{4\pi^2}\psi,$$

and therefore

$$\mathcal{J}\frac{\delta E}{\delta q} = -\nabla^\perp\psi \cdot \nabla q.$$

Let us now talk about Casimir invariants of the system. With help of the identity

$$\nabla^\perp q \cdot \nabla q \equiv 0$$

we find that any quantity of the form

$$C[q] = \frac{1}{4\pi^2}\int f(q)\,\mathrm{d}x\,\mathrm{d}y \tag{3.6}$$

is a Casimir invariant for (3.4). This proves the conservation of potential vorticity and also

gives access to the large family of additional conserved quantities. The second moment of the potential vorticity

$$\mathcal{E} = \frac{1}{8\pi^2} \int q^2 \, \mathrm{d}x \, \mathrm{d}y \tag{3.7}$$

is a very important quantity, which we will call *enstrophy*. Later in this chapter we will introduce an equilibrium statistical theory for the most probable statistical macrostate which takes into account energy and enstrophy only. However, the higher moments of potential vorticity

$$C_n = \frac{1}{4\pi^2} \int q^n \, \mathrm{d}x \, \mathrm{d}y, \quad n \geq 3 \tag{3.8}$$

are left unaccounted.

The family of additional conserved quantities (3.8) is of great interest to us in a statistical-mechanical sense. So far the influence of (3.8) on the system has not been quantified. We find that the role these additional conserved quantities play is much more interesting and complicated than that in the truncated Burgers-Hopf case. The theory and numerical techniques applied to our study are presented in the subsequent chapters.

3.1.2 Equations for barotropic flow in the Fourier space

The two-dimensional vorticity equation on a double-periodic plane transformed with the two-dimensional Fourier transform takes the form of a system of ODE's:

$$\frac{\mathrm{d}\hat{q}_k}{\mathrm{d}t} = \sum_{k_1', k_2' = -\infty}^{\infty} \frac{\mathbf{k} \times \mathbf{k}'}{|\mathbf{k}'|^2} \hat{q}_{\mathbf{k}+\mathbf{k}'} (\hat{q}_{-\mathbf{k}'} - \hat{h}_{-\mathbf{k}'}), \tag{3.9}$$

The dimension of (3.9) is infinite. $\hat{q}_{\mathbf{k}}$ denotes the spectral coefficient associated with the two-dimensional wave vector $\mathbf{k}$, whose components are integers. The skew-symmetric scalar product $\mathbf{k} \times \mathbf{k}'$ is $k_1 k_2' - k_2 k_1'$, and the norm $|\mathbf{k}|$ is $\sqrt{k_1^2 + k_2^2}$. Since q is real, then $\hat{q}_{\mathbf{k}}^* = \hat{q}_{-\mathbf{k}}$. In order to derive (3.9), first we look at the second equation in (3.1) and conclude that in the Fourier space it becomes

$$\hat{q}_{\mathbf{k}} = -|\mathbf{k}|^2 \hat{\psi}_{\mathbf{k}} + \hat{h}_{\mathbf{k}}, \tag{3.10}$$

such that

$$\hat{\psi}_{\mathbf{k}} = -\frac{1}{|\mathbf{k}|^2}(\hat{q}_{\mathbf{k}} - \hat{h}_{\mathbf{k}}). \tag{3.11}$$

Now, let us write ψ_x, ψ_y, q_x, q_y in terms of Fourier coefficients:

$$\begin{aligned}
\psi_x &= \sum_{\mathbf{k}} (ik_1)\hat{\psi}_{\mathbf{k}} e^{i(k_1 x + k_2 y)}, \\
\psi_y &= \sum_{\mathbf{k}} (ik_2)\hat{\psi}_{\mathbf{k}} e^{i(k_1 x + k_2 y)}, \\
q_x &= \sum_{\mathbf{k}} (ik_1)\hat{q}_{\mathbf{k}} e^{i(k_1 x + k_2 y)}, \\
q_y &= \sum_{\mathbf{k}} (ik_2)\hat{q}_{\mathbf{k}} e^{i(k_1 x + k_2 y)}.
\end{aligned}$$

Then we write (3.1) in terms of Fourier coefficients:

$$\frac{\mathrm{d}}{\mathrm{d}t}\sum_{\mathbf{k}} \hat{q}_{\mathbf{k}} e^{i\mathbf{k}\mathbf{x}} = \sum_{\mathbf{k}'}\sum_{\mathbf{k}''} (k_1' k_2'' - k_2' k_1'')\hat{\psi}_{\mathbf{k}'}\hat{q}_{\mathbf{k}''} e^{i(\mathbf{k}'+\mathbf{k}'')\mathbf{x}}.$$

Now we substitute $\mathbf{k} = \mathbf{k}' + \mathbf{k}''$ and collect terms with equal exponents:

$$\frac{\mathrm{d}}{\mathrm{d}t}\hat{q}_{\mathbf{k}} = -\sum_{\mathbf{k}'} (k_2' k_1 - k_1' k_2)\hat{\psi}_{\mathbf{k}'}\hat{q}_{\mathbf{k}-\mathbf{k}'}.$$

Changing $\mathbf{k}' \to -\mathbf{k}'$ yields

$$\frac{\mathrm{d}}{\mathrm{d}t}\hat{q}_{\mathbf{k}} = -\sum_{\mathbf{k}'} (\mathbf{k} \times \mathbf{k}')\hat{q}_{\mathbf{k}+\mathbf{k}'}\hat{\psi}_{-\mathbf{k}'},$$

and, substituting the expression (3.11) for $\hat{\psi}_{\mathbf{k}}$, we obtain (3.9).

The infinite-dimensional equation (3.9) has the Hamiltonian structure

$$\frac{\mathrm{d}}{\mathrm{d}t}\hat{q}_{\mathbf{k}} = \mathbf{J}_{\mathbf{k}\mathbf{k}'}\frac{\partial H}{\partial \hat{q}_{\mathbf{k}}} \tag{3.12}$$

with

$$\mathbf{J}_{\mathbf{k}\mathbf{k}'} = -(\mathbf{k} \times \mathbf{k}')\hat{q}_{\mathbf{k}+\mathbf{k}'} \tag{3.13}$$

and

$$H = E = \frac{1}{2}\sum_{\mathbf{k}} |\mathbf{k}|^2 |\hat{\psi}_{\mathbf{k}}|^2 = \frac{1}{2}\sum_{\mathbf{k}} \frac{|\hat{q}_{\mathbf{k}} - \hat{h}_{\mathbf{k}}|^2}{|\mathbf{k}|^2}, \tag{3.14a}$$

$$\frac{\partial H}{\partial \hat{q}_{\mathbf{k}}} = \frac{1}{|\mathbf{k}|^2}(\hat{q}_{-\mathbf{k}} - \hat{h}_{-\mathbf{k}}), \tag{3.14b}$$

so that again energy plays the role of Hamiltonian. The fact that $\mathbf{J_{kk'}}$ is skew-symmetric follows from $\mathbf{J_{kk'}} = -\mathbf{J_{k'k}}$. The proof of Jacobi identity follows directly from (1.2):

$$\begin{aligned}
&\sum_{\mathbf{l}} (\mathbf{J_{il}}\partial_{\mathbf{l}}\mathbf{J_{jk}} + \mathbf{J_{kl}}\partial_{\mathbf{l}}\mathbf{J_{ij}} + \mathbf{J_{jl}}\partial_{\mathbf{l}}\mathbf{J_{ki}}) = \\
&\qquad = \sum_{\mathbf{l}=\mathbf{j}+\mathbf{k}} (\mathbf{i}\times\mathbf{l})(\mathbf{j}\times\mathbf{k})\hat{q}_{\mathbf{i}+\mathbf{j}+\mathbf{k}} + \\
&\qquad + \sum_{\mathbf{l}=\mathbf{i}+\mathbf{j}} (\mathbf{k}\times\mathbf{l})(\mathbf{i}\times\mathbf{j})\hat{q}_{\mathbf{i}+\mathbf{j}+\mathbf{k}} + \\
&\qquad + \sum_{\mathbf{l}=\mathbf{k}+\mathbf{i}} (\mathbf{j}\times\mathbf{l})(\mathbf{k}\times\mathbf{i})\hat{q}_{\mathbf{i}+\mathbf{j}+\mathbf{k}} = \\
&= \sum_{\mathbf{l}=\mathbf{j}+\mathbf{k}} (\mathbf{i}\times(\mathbf{j}+\mathbf{k}))(\mathbf{j}\times\mathbf{k})\hat{q}_{\mathbf{i}+\mathbf{j}+\mathbf{k}} + \\
&\quad + \sum_{\mathbf{l}=\mathbf{i}+\mathbf{j}} (\mathbf{k}\times(\mathbf{i}+\mathbf{j}))(\mathbf{i}\times\mathbf{j})\hat{q}_{\mathbf{i}+\mathbf{j}+\mathbf{k}} + \\
&\quad + \sum_{\mathbf{l}=\mathbf{k}+\mathbf{i}} (\mathbf{j}\times(\mathbf{k}+\mathbf{i}))(\mathbf{k}\times\mathbf{i})\hat{q}_{\mathbf{i}+\mathbf{j}+\mathbf{k}} = \\
&= \sum_{\mathbf{l}=\mathbf{j}+\mathbf{k}} (\mathbf{i}\times\mathbf{j})(\mathbf{j}\times\mathbf{k}) - (\mathbf{k}\times\mathbf{i})(\mathbf{j}\times\mathbf{k})\hat{q}_{\mathbf{i}+\mathbf{j}+\mathbf{k}} + \\
&\quad + \sum_{\mathbf{l}=\mathbf{i}+\mathbf{j}} (\mathbf{k}\times\mathbf{i})(\mathbf{i}\times\mathbf{j}) - (\mathbf{j}\times\mathbf{k})(\mathbf{i}\times\mathbf{j})\hat{q}_{\mathbf{i}+\mathbf{j}+\mathbf{k}} + \\
&+ \sum_{\mathbf{l}=\mathbf{k}+\mathbf{i}} (\mathbf{j}\times\mathbf{k})(\mathbf{k}\times\mathbf{i}) - (\mathbf{i}\times\mathbf{j})(\mathbf{k}\times\mathbf{i})\hat{q}_{\mathbf{i}+\mathbf{j}+\mathbf{k}} = 0.
\end{aligned} \tag{3.15}$$

The system (3.9) also has Casimir invariants of the form

$$\hat{C}_N = \sum_{\sum_{j=1}^{N} \mathbf{k}_j = 0} \left(\prod_{j=1}^{N} \hat{q}_{\mathbf{k}_j} \right), \tag{3.16}$$

which are the Fourier space analogues of (3.8). The proof of conservation is direct:

$$\sum_{\mathbf{j}} \mathbf{J}_{\mathbf{jk}} \frac{\partial C_N}{\partial \hat{q}_{\mathbf{j}}} = \sum_{\mathbf{j}} \mathbf{J}_{\mathbf{jk}} \left(N \sum_{\sum_l^{N-1} \mathbf{m}_l = -\mathbf{j}} \prod_l^{N-1} \hat{q}_{\mathbf{m}_l} \right) =$$

$$= N \sum_{\mathbf{j}} \sum_{\sum_l^{N-1} \mathbf{m}_l = -\mathbf{j}} (\mathbf{j} \times \mathbf{k}) \hat{q}_{\mathbf{j}+\mathbf{k}} \prod_l^{N-1} \hat{q}_{\mathbf{m}_l} =$$

$$= N \sum_{\mathbf{j}} \sum_{\sum_l^{N-1} \mathbf{m}_l = -\mathbf{j}} ((\mathbf{j} + \mathbf{k}) \times \mathbf{k}) \hat{q}_{\mathbf{j}+\mathbf{k}} \prod_l^{N-1} \hat{q}_{\mathbf{m}_l} =$$

$$= N \sum_{\mathbf{i}} \sum_{\sum_l^{N-1} \mathbf{m}_l = \mathbf{k}-\mathbf{i}} (\mathbf{i} \times \mathbf{k}) \hat{q}_{\mathbf{i}} \prod_l^{N-1} \hat{q}_{\mathbf{m}_l} =$$

$$= N! \sum_{\sum_l^{N} \mathbf{m}_l = \mathbf{0}} (\mathbf{k} \times \mathbf{k}) \prod_l^{N} \hat{q}_{\mathbf{m}_l} = \mathbf{0}$$

since $\mathbf{k} \times \mathbf{k} \equiv 0$. The conservation of potential vorticity (which is the first Casimir invariant) now becomes trivial since

$$\frac{\mathrm{d}}{\mathrm{d}t} \frac{1}{4\pi^2} \int q \, \mathrm{d}x \, \mathrm{d}y = \frac{\mathrm{d}}{\mathrm{d}t} \hat{q}_{0,0} = 0.$$

The enstrophy is essentially the second Casimir invariant:

$$\mathcal{E} = \frac{1}{2} \sum_{\mathbf{k}} |\hat{q}_{\mathbf{k}}|^2.$$

However, we can not solve (3.9) numerically as long as it stays infinite. There exist different methods to truncate (3.9), and the most straightforward one is to sum on the finite set of Fourier coefficients. This type of truncation, which we call *traditional*, is introduced in the next section.

3.1.3 Traditional spectral truncation of the equations for barotropic flow

The traditional truncation of the infinite-dimensional equation (3.9) is

$$\frac{\mathrm{d}\hat{q}_k}{\mathrm{d}t} = \sum_{k_1', k_2' = -M}^{M} \frac{\mathbf{k} \times \mathbf{k}'}{|\mathbf{k}'|^2} \hat{q}_{\mathbf{k}+\mathbf{k}'} (\hat{q}_{-\mathbf{k}'} - \hat{h}_{-\mathbf{k}'}), \tag{3.17}$$

so that the summation occurs on the $(2M+1)\times(2M+1)$ domain of Fourier coefficients. This truncation is aliased, i.e. the periodicity of Fourier coefficients is assumed in the sense that whenever $\mathbf{k}+\mathbf{k}'$ is out of bounds, the corresponding $\hat{q}_{\mathbf{k}+\mathbf{k}'}$ is aliased from the opposite side of the domain. The traditional truncation (3.17) does not retain the Hamiltonian structure.

The dynamics of the system changes significantly. Only three conserved quantities survive the truncation. The first quantity is the spatial integral of the potential vorticity (the truncation does not affect the conservation of zero Fourier coefficient). The second conserved quantity is the energy:

$$E = \frac{1}{2}\sum_{\mathbf{k}} |\mathbf{k}|^2 |\hat{\psi}_{\mathbf{k}}|^2 = \frac{1}{2}\sum_{\mathbf{k}} \frac{|\hat{q}_{\mathbf{k}} - \hat{h}_{\mathbf{k}}|^2}{|\mathbf{k}|^2}. \tag{3.18}$$

The third conserved quantity is the enstrophy

$$\mathcal{E} = \frac{1}{2}\sum_{\mathbf{k}} |\hat{q}_{\mathbf{k}}|^2. \tag{3.19}$$

The energy and enstrophy conservation can be proven directly:

- Energy

$$\begin{aligned}\frac{\mathrm{d}E}{\mathrm{d}t} = \sum_{\mathbf{m}} \frac{\partial E}{\partial \tilde{q}_{\mathbf{m}}}\frac{\mathrm{d}\tilde{q}_{\mathbf{m}}}{\mathrm{d}t} = \sum_{\mathbf{m}}\sum_{\mathbf{n}} (\tilde{q}_{-\mathbf{m}} - \tilde{h}_{-\mathbf{m}})(\tilde{q}_{-\mathbf{n}} - \tilde{h}_{-\mathbf{n}})\tilde{q}_{\mathbf{m}+\mathbf{n}}\frac{\mathbf{m}\times\mathbf{n}}{|\mathbf{m}|^2|\mathbf{n}|^2} = \\ = \frac{1}{2}\sum_{\mathbf{m}}\sum_{\mathbf{n}} (\tilde{q}_{-\mathbf{m}} - \tilde{h}_{-\mathbf{m}})(\tilde{q}_{-\mathbf{n}} - \tilde{h}_{-\mathbf{n}})\tilde{q}_{\mathbf{m}+\mathbf{n}}\frac{\mathbf{m}\times\mathbf{n}}{|\mathbf{m}|^2|\mathbf{n}|^2} + \\ + \frac{1}{2}\sum_{\mathbf{m}}\sum_{\mathbf{n}} (\tilde{q}_{-\mathbf{m}} - \tilde{h}_{-\mathbf{m}})(\tilde{q}_{-\mathbf{n}} - \tilde{h}_{-\mathbf{n}})\tilde{q}_{\mathbf{m}+\mathbf{n}}\frac{\mathbf{n}\times\mathbf{m}}{|\mathbf{m}|^2|\mathbf{n}|^2} = 0.\end{aligned}$$

  Here we split the sum into two identical parts and swap $\mathbf{m}$ and $\mathbf{n}$ in the second part.

- Enstrophy

$$\begin{aligned}\frac{\mathrm{d}\mathcal{E}}{\mathrm{d}t} = \sum_{\mathbf{m}} \frac{\partial \mathcal{E}}{\partial \tilde{q}_{\mathbf{m}}}\frac{\mathrm{d}\tilde{q}_{\mathbf{m}}}{\mathrm{d}t} = 2\sum_{\mathbf{m}}\sum_{\mathbf{n}} \tilde{q}_{-\mathbf{m}}(\tilde{q}_{-\mathbf{n}} - \tilde{h}_{-\mathbf{n}})\tilde{q}_{\mathbf{m}+\mathbf{n}}\frac{\mathbf{m}\times\mathbf{n}}{|\mathbf{n}|^2} = \\ = 2\sum_{\mathbf{m}}\sum_{\mathbf{n}} \tilde{q}_{-\mathbf{m}}\tilde{q}_{-\mathbf{n}}\tilde{q}_{\mathbf{m}+\mathbf{n}}\frac{\mathbf{m}\times\mathbf{n}}{|\mathbf{n}|^2} - 2\sum_{\mathbf{m}}\sum_{\mathbf{n}} \tilde{q}_{-\mathbf{m}}\tilde{h}_{-\mathbf{n}}\tilde{q}_{\mathbf{m}+\mathbf{n}}\frac{\mathbf{m}\times\mathbf{n}}{|\mathbf{n}|^2} = \\ = \sum_{\mathbf{m}}\sum_{\mathbf{s}} \tilde{q}_{-\mathbf{m}}\tilde{q}_{\mathbf{m}+\mathbf{s}}\tilde{q}_{-\mathbf{s}}\frac{\mathbf{s}\times\mathbf{m}}{|\mathbf{m}+\mathbf{s}|^2} + \sum_{\mathbf{m}}\sum_{\mathbf{s}} \tilde{q}_{-\mathbf{m}}\tilde{q}_{\mathbf{m}+\mathbf{s}}\tilde{q}_{-\mathbf{s}}\frac{\mathbf{m}\times\mathbf{s}}{|\mathbf{m}+\mathbf{s}|^2} + \\ + \sum_{\mathbf{m}}\sum_{\mathbf{s}} \tilde{q}_{-\mathbf{m}}\tilde{h}_{\mathbf{m}+\mathbf{s}}\tilde{q}_{-\mathbf{s}}\frac{\mathbf{m}\times\mathbf{s}}{|\mathbf{m}+\mathbf{s}|^2} + \sum_{\mathbf{m}}\sum_{\mathbf{s}} \tilde{q}_{-\mathbf{m}}\tilde{h}_{\mathbf{m}+\mathbf{s}}\tilde{q}_{-\mathbf{s}}\frac{\mathbf{s}\times\mathbf{m}}{|\mathbf{m}+\mathbf{s}|^2} = 0.\end{aligned}$$

Here we use the same trick as for the energy, and also denote $\mathbf{s} = -\mathbf{m} - \mathbf{n}$.

The above conserved quantities restrain the motion of the system to the manifold of constant energy and constant enstrophy, which allows simple statistical description of the system similar to the truncated Burgers-Hopf case. In the next few sections we will give the coverage on different statistical theories which describe the dynamics of the equations for barotropic flow and the traditional truncation.

3.2 Equilibrium statistical theories

In this section we present the basic principles of the statistical theories which will be used to describe the system of barotropic flow equations in terms of equilibrium statistical mechanics. The contents of this section are based upon Prof. Majda's lecture notes.

The objective of the theories we introduce here is to predict the most probable statistical state of the system. In other words, we assume that the system is located in a statistical equilibrium (meaning that the probability measure does not change in time), and try to determine the most probable statistical macrostate among all possible equilibrium states. The main tool we use is the empirical *maximum entropy principle*, which will be presented later.

We begin with defining the probability density ρ for the potential vorticity q:

Definition 2 *A probability density $\rho(\vec{x}, \lambda)$ for the potential vorticity q is a function defined on $\Omega \times \mathbb{R}^1 \times \mathbb{R}^1$ which satisfies the following properties:*

- *ρ is non-negative with unit mass, i.e. $\rho \geq 0$, $\frac{1}{\Omega} \int_\Omega \mathrm{d}\vec{x} \int_{-\infty}^{\infty} \rho(\vec{x}, \lambda)\, \mathrm{d}\lambda = 1$.*
- *For almost all $\vec{x} \in \Omega$ $\rho(\vec{x}, \lambda)$ yields a probability measure in $\mathbb{R}^1$,*

$$\int \rho(\vec{x}, \lambda)\, \mathrm{d}\lambda = 1.$$

- *For almost all $\vec{x} \in \Omega$ $\rho(\vec{x}, \lambda)$ is the probability density for the potential vorticity q at the point $\vec{x}$:*

$$\int_a^b \rho(\vec{x}, \lambda)\, \mathrm{d}\lambda = Prob\{a \leq q(\vec{x}) \leq b\}.$$

Thus, given any quantity $F(q)$, its expected value at almost any point $\vec{x}$ can be computed by

$$\bar{F} = \int F(q)\rho(\vec{x}, \lambda)\, \mathrm{d}\lambda. \tag{3.20}$$

3.2.1 Maximum entropy principle

The maximum entropy principle presented here utilizes ideas from the information theory developed by Shannon [24] and Jaynes [8] in late forties – mid fifties of the last century. This alternative approach to the statistical description of the system provides very efficient tool of determining the large-scale behavior of the system. Unlike conventional techniques, this method allows us to predict the most probable probability measure taking into account the prior information about the system. In order to employ this method, first we define the *entropy* as a functional on the space of probability densities:

Definition 3 *Given the probability density $\rho(\vec{x}, \lambda)$, which is defined by Definition 2, the Shannon entropy of ρ is defined by*

$$\mathcal{S}[\rho] = -\int \rho \ln(\rho)\, \mathrm{d}\lambda. \tag{3.21}$$

The entropy (3.21) is a universal quantity which measures the amount of uncertainty in a probability distribution. The idea is that, knowing various constraints and the prior information on the system, we can maximize the entropy under given constraints, thus allowing the largest amount of uncertainty in the probability density under given constraints and prior information. Suppose that we aware about N conserved quantities in the system with their mean values $\bar{E}_1 \dots \bar{E}_N$. Then we define the maximum entropy principle as

Definition 4 *The most probable probability density ρ^* corresponding to the flow satisfying the constraints $\bar{E}_1 \dots \bar{E}_N$ is the one which maximizes the Shannon entropy given by Definition 3 subject to the constraints $\bar{E}_1 \dots \bar{E}_N$, and is a solution for the equation*

$$\left.\frac{\delta \mathcal{S}}{\delta \rho}\right|_{\rho=\rho^*} = \sum_i^N \theta_i \left.\frac{\delta \bar{E}_i}{\delta \rho}\right|_{\rho=\rho^*}, \tag{3.22}$$

where θ_i are corresponding Lagrange multipliers.

From the above equation we can determine the most probable probability density ρ^*. In the later chapters we will widely use this technique to predict the most probable statistical states of the barotropic flow. We will see that the above method predicts the most probable statistical state for the truncation of the equations for barotropic flow with astonishing accuracy if we know enough information about the system.

3.2.1.1 Maximum entropy principle with prior distribution

However, apart from the constraints provided by conserved quantities, we may know some other information about the system. Let us assume that we performed direct numerical simulation with the system and measured the probability distribution "as is", by some numerical means. The distribution we measured may, of course, contain errors, since direct numerical simulations approximate an original system in some way. Still, we now know some other prior information about the system apart from the conserved quantities. The following definition allows us to incorporate this prior knowledge into the statistical predictions:

Definition 5 *Given the probability density $\rho(\vec{x}, \lambda)$, which is defined by Definition 2, the Shannon entropy of ρ, relative to the known prior distribution ρ_0, is defined by*

$$\mathcal{S}[\rho] = -\int \rho \ln\left(\frac{\rho}{\rho_0}\right) \mathrm{d}\lambda. \tag{3.23}$$

Now, with help of the above definition, we can take into account the prior distribution, if it is known to us. The maximum entropy principle is the same as in (3.22). In the later chapters we will consider the case where we have to use the numerically obtained prior distribution in order to predict the most probable mean state for the special truncation of barotropic flow equations.

3.2.2 Empirical statistical theory for barotropic flow equations

In this section we apply the maximum entropy principle to the predictions of the most probable statistical state for barotropic flow equations. The statistical theory we introduce here is empirical because only two conserved quantities, energy and enstrophy, are taken into account, whereas, as we already know, the Poisson bracket for the equations possesses large family of Casimir invariants. However, as we will later see, for the vast amount of natural initial conditions the high order Casimir invariants are irrelevant to the dynamics of barotropic flow.

First we write the equation (3.22) for the two constraints:

$$\left.\frac{\delta \mathcal{S}}{\delta \rho}\right|_{\rho=\rho^*} = \theta \left.\frac{\delta \bar{E}}{\delta \rho}\right|_{\rho=\rho^*} + \alpha \left.\frac{\delta \bar{\mathcal{E}}}{\delta \rho}\right|_{\rho=\rho^*},$$

where θ and α are the Lagrange multipliers for energy and enstrophy, respectively. Now, with help of the formula (3.20), we write down the variational derivatives for the energy,

enstrophy, and Shannon entropy:

$$\frac{\delta \bar{E}}{\delta \rho} = -\frac{1}{4\pi^2}\psi\lambda, \tag{3.24a}$$

$$\frac{\delta \bar{\mathcal{E}}}{\delta \rho} = \frac{1}{8\pi^2}\lambda^2, \tag{3.24b}$$

$$\frac{\delta \mathcal{S}}{\delta \rho} = -\ln(\rho) - 1, \tag{3.24c}$$

and for the most probable probability density obtain

$$\ln(\rho^*) = -\frac{1}{8\pi^2}\alpha\left(\lambda - \frac{\theta}{\alpha}\bar{\psi}^*\right)^2 + \frac{1}{8\pi^2}\frac{\theta^2(\bar{\psi}^*)^2}{\alpha} - 1, \tag{3.25}$$

where ψ^* is the mean stream function associated to the most probable statistical state. To simplify the matter, we did not formally include the additional constraint, namely the restriction for the ρ^* to have unit mass, so we include it in the last step and also hide there all terms which do not contain λ:

$$\rho^*(\vec{x}, \lambda) = \Gamma(\vec{x}) \exp\left(-\frac{\alpha}{8\pi^2}[\lambda - \mu\bar{\psi}^*(\vec{x})]^2\right). \tag{3.26}$$

In the above equation we also denote $\mu = \theta/\alpha$.

We have obtained the probability density for the most probable statistical state for the equations for barotropic flow. Looking at (3.26), we make several important conclusions about one-point statistics of the system:

- **Normalizing factor does not depend on location.** Indeed, in order to normalize ρ^* at any point $\vec{x}$ it is sufficient to have

$$\Gamma = \sqrt{\frac{\alpha}{8\pi^3}}. \tag{3.27}$$

- **Relation between mean potential vorticity and stream function.** The density (3.26) is Gaussian centered at $\mu\psi^*$, so we conclude that the mean field equation for $\bar{q}^*$ and $\bar{\psi}^*$ is

$$\bar{q}^* = \mu\bar{\psi}^*, \tag{3.28}$$

  i.e. the relation between $\bar{q}^*$ and $\bar{\psi}^*$ is linear.

- **Mean state equation.** Taking into account the second equation in (3.1) we find

that

$$\mu\bar{\psi}^* = \Delta\bar{\psi}^* + h, \tag{3.29}$$

i.e. the mean state depends exclusively on μ and topography. This is a very important observation, which tells us that topography creates a non-trivial mean flow in different geophysical applications.

- **Perturbations around mean state.** All high order moments around mean state do not depend on $\vec{x}$. In particular, the variance of q around the mean state $\bar{q}^*$ is

$$\mathrm{Var}(q) = \int (\lambda - \bar{q}^*)\rho^* \,\mathrm{d}\lambda = 4\pi^2\alpha^{-1}, \tag{3.30}$$

the skewness (normalized third order moment) is zero, and the flatness (normalized fourth order moment) is 3.

The above observations are, nonetheless, based on the empirical statistical theory which does not take into account additional conserved quantities. Nor it is possible to confirm this theory numerically since the truncation of the equations is a completely different dynamical system. However, for the truncation itself the complete statistical theory can be developed since we are aware of all conserved quantities in the system. We present the complete statistical theory for the truncation of barotropic flow in the next section.

3.2.3 Complete statistical theory for the truncated equations

In this section we present the complete equilibrium statistical theory for the truncated equation (3.17). We know that it possesses two conserved quantities – energy and enstrophy (the zero Fourier coefficient does not play any role in the dynamics as a conserved quantity and we discard it). Therefore, we can take into account all conserved quantities and predict the most probable probability density knowing the complete information about the constraints. The maximum entropy principle essentially tells us that the most probable probability density is the uniform one on the manifold in the phase space where the motion occurs. However, it is not clear whether that measure would be invariant, unless we check the Liouville property.

3.2.3.1 Liouville property

Let us first write the equation (3.17) in the form

$$\frac{\mathrm{d}}{\mathrm{d}t}\hat{\mathbf{q}} = \vec{F}(\hat{\mathbf{q}}). \tag{3.31}$$

The corresponding Liouville equation for the evolution of the probability density associated with $\hat{\mathbf{q}}$ along its phase space trajectory is

$$\frac{\partial}{\partial t}\rho(\hat{\mathbf{q}},t) + \mathrm{div}\left[\rho(\hat{\mathbf{q}},t)\vec{F}(\hat{\mathbf{q}})\right] = 0, \tag{3.32}$$

where $\vec{F}$ is the right-hand side from (3.17). We are looking for the steady solution of the Liouville equation (invariant measure). Now, let us assume that we have a uniform probability density on the manifold of motion at the initial time. What would be the constraint on $\vec{F}$, such that the uniform measure on the manifold would be an invariant? The answer is obvious:

$$\mathrm{div}\vec{F} = 0. \tag{3.33}$$

The condition (3.33) is called *the Liouville property*. It assures that on almost any manifold of motion (surface of constant energy and enstrophy, for example) the uniform measure is an invariant. Our system (3.17) satisfies the Liouville property:

$$\begin{aligned}\mathrm{div}\vec{F} &= \sum_{\mathbf{k}}\left(\frac{\partial \mathrm{Re}(F_{\mathbf{k}})}{\partial \mathrm{Re}(\hat{q}_{\mathbf{k}})} + \frac{\partial \mathrm{Im}(F_{\mathbf{k}})}{\partial \mathrm{Im}(\hat{q}_{\mathbf{k}})}\right) = \\ &= \sum_{\mathbf{k}}\sum_{\mathbf{k}'}\frac{\mathbf{k}\times\mathbf{k}'}{|\mathbf{k}'|^2}\mathrm{Re}(\hat{q}_{\mathbf{k}+\mathbf{k}'}) - \sum_{\mathbf{k}}\sum_{\mathbf{k}'}\frac{\mathbf{k}\times\mathbf{k}'}{|\mathbf{k}'|^2}\mathrm{Re}(\hat{q}_{\mathbf{k}+\mathbf{k}'}) = 0,\end{aligned}$$

therefore the uniform measure on the surface of constant energy and enstrophy is an invariant probability measure.

3.2.3.2 Most probable probability density and associated one-point statistics

In order to employ the maximum entropy principle (3.22) for the truncated equations, first we should write the variational derivatives of the constraints. Again, for the mean energy and the mean enstrophy we use the formula (3.20):

$$\frac{\delta\bar{E}}{\delta\rho} = \frac{1}{2}\sum_{\mathbf{k}}|\mathbf{k}|^2|\hat{\psi}_{\mathbf{k}}|^2, \tag{3.34a}$$

$$\frac{\delta \bar{\mathcal{E}}}{\delta \rho} = \frac{1}{2} \sum_{\mathbf{k}} |\hat{q}_{\mathbf{k}}|^2, \tag{3.34b}$$

$$\frac{\delta \mathcal{S}}{\delta \rho} = -\ln \rho - 1. \tag{3.34c}$$

At risk of confusing the reader, in the above equation $\hat{\psi}_{\mathbf{k}}$ and $\hat{q}_{\mathbf{k}}$ play the role of λ in (3.25). Now we substitute the above formulas into the maximum entropy principle (3.22) and obtain

$$-\ln \rho^* - 1 = \frac{\theta}{2} \sum_{\mathbf{k}} |\mathbf{k}|^2 |\hat{\psi}_{\mathbf{k}}|^2 + \frac{\alpha}{2} \sum_{\mathbf{k}} |\hat{q}_{\mathbf{k}}|^2, \tag{3.35}$$

where θ and α are the Lagrange multipliers for energy and enstrophy, respectively. Similar to what we did to the continuous case, we denote $\mu = \theta/\alpha$, express $\hat{q}_{\mathbf{k}}$ in terms of $\hat{\psi}_{\mathbf{k}}$ via (3.10) and dump everything which does not contain $\hat{\psi}_{\mathbf{k}}$ into normalizing factor:

$$\rho^*(\hat{\psi}) = \Gamma_{\hat{\psi}} \exp\left(-\frac{\alpha}{2} \sum_{\mathbf{k}} (\mu + |\mathbf{k}|^2) |\mathbf{k}|^2 \left| \hat{\psi}_{\mathbf{k}} - \frac{\hat{h}_{\mathbf{k}}}{\mu + |\mathbf{k}|^2} \right|^2 \right). \tag{3.36}$$

Note that this most probable measure is associated with the spectral coefficients of the stream function. The most probable probability density for the spectral coefficients of the potential vorticity is derived in a similar way and equals

$$\rho^*(\hat{q}) = \Gamma_{\hat{q}} \exp\left(-\frac{\alpha}{2} \sum_{\mathbf{k}} (\mu + |\mathbf{k}|^2) |\mathbf{k}|^{-2} \left| \hat{q}_{\mathbf{k}} - \frac{\mu \hat{h}_{\mathbf{k}}}{\mu + |\mathbf{k}|^2} \right|^2 \right). \tag{3.37}$$

Both probability densities are Gaussian, and we can make several important conclusions about one-point statistics:

- **Normalizing factors.** Direct calculation yields

$$\Gamma_{\hat{\psi}} = \left(\frac{\alpha}{2\pi} \right)^N \prod_{\mathbf{k}} (\mu + |\mathbf{k}|^2)^{-1/2} |\mathbf{k}|^{-1}, \tag{3.38}$$

$$\Gamma_{\hat{q}} = \left(\frac{\alpha}{2\pi} \right)^N \prod_{\mathbf{k}} (\mu + |\mathbf{k}|^2)^{-1/2} |\mathbf{k}|. \tag{3.39}$$

  where N is the total number of spectral coefficients in the truncation.

- **Mean state relation** The mean state satisfies the relation

$$\bar{\hat{q}}_{\mathbf{k}} = \mu \bar{\hat{\psi}}_{\mathbf{k}}, \tag{3.40}$$

  which is consistent with (3.28).

- **Mean field equations.** The mean field $\bar{\hat{\psi}}_{\mathbf{k}}$ and $\bar{\hat{q}}_{\mathbf{k}}$ satisfy the relations

$$\bar{\hat{\psi}}_{\mathbf{k}} = \frac{\hat{h}_{\mathbf{k}}}{\mu + |\mathbf{k}|^2}, \tag{3.41}$$

$$\bar{\hat{q}}_{\mathbf{k}} = \frac{\mu \hat{h}_{\mathbf{k}}}{\mu + |\mathbf{k}|^2}, \tag{3.42}$$

  which is consistent with (3.40) and (3.29).

- **Perturbations around mean state.** For the variances of $\hat{\psi}_{\mathbf{k}}$ and $\hat{q}_{\mathbf{k}}$ we find that

$$\mathrm{Var}(\hat{\psi}_{\mathbf{k}}) = \frac{1}{\alpha(\mu + |\mathbf{k}|^2)|\mathbf{k}|^2}, \tag{3.43}$$

$$\mathrm{Var}(\hat{q}_{\mathbf{k}}) = \frac{|\mathbf{k}|^2}{\alpha(\mu + |\mathbf{k}|^2)}. \tag{3.44}$$

  We can see that the variance for $\hat{\psi}_{\mathbf{k}}$ vanish as $\mathbf{k}$ increases, and therefore the energy (which is a function of $\hat{\psi}_{\mathbf{k}}$) concentrates on the large scales, and no equipartition of energy takes place. However the variance for $\hat{q}_{\mathbf{k}}$ converges to α^{-1} as $\mathbf{k}$ increases and does not vanish. This means that the enstrophy is important on the small scales. Since the density is Gaussian for both $\hat{\psi}_{\mathbf{k}}$ and $\hat{q}_{\mathbf{k}}$, the high moments obey the standard relations (skewness is zero, and flatness is 3).

- **Energy and enstrophy.** If we compute the means of energy and enstrophy (which are, of course, equal energy and enstrophy themselves), then we will see that each of them naturally separates into two parts:

$$E = \bar{E} + E', \quad \mathcal{E} = \bar{\mathcal{E}} + \mathcal{E}', \tag{3.45}$$

where $\bar{E}$ and $\bar{\mathcal{E}}$ are the energy and enstrophy of the mean flow, respectively, and E' and $\mathcal{E}'$ are the parts which correspond to perturbations. Their values are:

$$\bar{E} = \frac{1}{2}\sum_{\mathbf{k}} \frac{|\mathbf{k}|^2 \hat{h}_{\mathbf{k}}}{(\mu + |\mathbf{k}|^2)^2}, \tag{3.46a}$$

$$\bar{\mathcal{E}} = \frac{1}{2}\sum_{\mathbf{k}} \frac{\mu^2 \hat{h}_{\mathbf{k}}}{(\mu + |\mathbf{k}|^2)^2}, \tag{3.46b}$$

$$E' = \frac{1}{2\alpha}\sum_{\mathbf{k}} \frac{1}{\mu + |\mathbf{k}|^2}, \tag{3.46c}$$

$$\mathcal{E}' = \frac{1}{2\alpha}\sum_{\mathbf{k}} \frac{|\mathbf{k}|^2}{\mu + |\mathbf{k}|^2}. \tag{3.46d}$$

As we could expect, the mean parts depend on topography and vanish if there is no topography present. However, the parts which correspond to perturbations do not depend on topography, so the topography contributes to mean flow only and not to perturbations.

- **Pseudo-energy.** Since both energy and enstrophy are conserved, their linear combination will be conserved as well. The following linear combination of energy and enstrophy

$$\begin{aligned} pE = \mathcal{E} + \mu E - \frac{1}{2}\sum_{\mathbf{k}} \frac{\mu |\hat{h}_{\mathbf{k}}|^2}{\mu + |\mathbf{k}|^2} = \\ = \frac{1}{2}\sum_{\mathbf{k}} (\mu + |\mathbf{k}|^2)|\mathbf{k}|^2 |\hat{\psi}_{\mathbf{k}} - \bar{\hat{\psi}}_{\mathbf{k}}|^2 \end{aligned} \tag{3.47}$$

is called *pseudo-energy*, or energy of perturbations. As we can see, it depends on perturbations around the mean state only. The natural variables for the pseudo-energy are

$$p_{\mathbf{k}} = \sqrt{\mu + |\mathbf{k}|^2}|\mathbf{k}|\hat{\psi}_{\mathbf{k}} - \frac{|\mathbf{k}|\hat{h}_{\mathbf{k}}}{\sqrt{\mu + |\mathbf{k}|^2}}, \tag{3.48}$$

such that the pseudo-energy in the pseudo-energy variables is

$$pE = \frac{1}{2}\sum_{\mathbf{k}} |p_{\mathbf{k}}|^2. \tag{3.49}$$

The pseudo-energy variables are very useful when used for the probability. The most probable probability density written in terms of these variables becomes

$$\rho^*(pE) = \left(\frac{\alpha}{2\pi}\right)^N \exp\left(-\frac{\alpha}{2}\sum_{\mathbf{k}} |p_{\mathbf{k}}|^2\right) = \left(\frac{\alpha}{2\pi}\right)^N \exp\left(-\alpha\, pE\right), \tag{3.50}$$

which means that the pseudo-energy written in terms of pseudo-energy variables is equipartitioned with variance α^{-1}.

The one-point statistics described above is a very important indicator for the numerical confirmation of the statistical theory. This type of statistical calculations can be easily encoded into the numerical checks of the theory, and it is a very good indicator of either validity or inconsistency of the theoretical predictions. In the later chapters we will gather the information about mean flow, pseudo-energy partition and other important one-point statistics of the generic truncation for the barotropic equations (3.17). We will see that for this type of truncation the above statistical theory is valid. However, there exist a special finite-dimensional truncation of the equations for barotropic flow, which possesses a Hamiltonian structure with vast amount of Casimir invariants as well as energy and enstrophy. The purpose of our work in the later chapters will be to determine the relevance of the additional Casimir invariants to the dynamics predicted by the theory. The special truncation with many conserved quantities is described in the next chapter.

CHAPTER 4
TRUNCATION WITH MANY CONSERVED QUANTITIES AND CORRESPONDING NUMERICAL METHODS

In this chapter we introduce the special spectral truncation of the equations for barotropic flow with topography, which possesses the Hamiltonian structure and many additional conserved quantities. The Poisson bracket of this truncation, however, is of the form different than in the spectral representation of the equations for barotropic flow (3.9). The new scheme, which is called the *sine-bracket truncation* possesses the vast number of the Casimir invariants similar to those in (3.16), and is considered as an alternative to (3.17). The dynamics of the new system is restricted on the surface of constant energy, enstrophy and additional Casimir invariants and may differ significantly from that in (3.17). The new truncation was independently proposed by Zeitlin in [25], and by Miller, Weichman, and Cross in [21].

In addition to the new sine-bracket truncation, in this chapter we also present the numerical methods used with this truncation. In the Section 4.2 we present the special symplectic numerical time integrator which allows to preserve the Casimir invariants of the sine-bracket truncation with the machine precision. We show explicitly, that the standard numerical integration schemes like Runge-Kutta fail to preserve the enstrophy and higher order Casimir invariants. Also in the Section 4.3 we introduce the iterative optimization procedure, which allows to generate initial conditions for the sine-bracket truncation with pre-defined conserved quantities, which later proves to be very useful in the numerical experiments.

4.1 Hamiltonian structure and Casimir invariants of the truncation with many conserved quantities

The new type of truncation is

$$\frac{\mathrm{d}}{\mathrm{d}t}\hat{q}_{\mathbf{k}} = \sum_{k_1',k_2'=-M}^{M} \frac{1}{\varepsilon}\frac{\sin(\varepsilon \mathbf{k}\times\mathbf{k}')}{|\mathbf{k}'|^2}\hat{q}_{\mathbf{k}+\mathbf{k}'}(\hat{q}_{-\mathbf{k}'} - \hat{h}_{-\mathbf{k}'}), \quad \varepsilon = \frac{2\pi}{2M+1}, \tag{4.1}$$

so that the summation occurs on the $(2M+1)\times(2M+1)$ domain of the Fourier coefficients. This truncation will further be referenced to as *the sine-bracket truncation*. The name of the truncation follows, first, from the presence of a sine function, and, second, due to

the fact that the truncation can be written in its "bracket" form as a commutator defined on the group of unitary $(2M+1)\times(2M+1)$ matrices, which we will show later. The convergence of the sine-bracket truncation to the infinite-dimensional equations (3.9) can be proven using the methods described in Chapter 10 of [12]. The truncation possesses the Hamiltonian structure with the symplectic operator

$$\mathbf{J_{kk'}} = -\frac{1}{\varepsilon}\sin(\varepsilon\mathbf{k}\times\mathbf{k'})\hat{q}_{\mathbf{k}+\mathbf{k'}} \tag{4.2}$$

and Hamiltonian

$$H = E = \frac{1}{2}\sum_{\mathbf{k}}|\mathbf{k}|^2|\hat{\psi}_{\mathbf{k}}|^2 = \frac{1}{2}\sum_{\mathbf{k}}\frac{|\hat{q}_{\mathbf{k}}-\hat{h}_{\mathbf{k}}|^2}{|\mathbf{k}|^2}, \tag{4.3a}$$

$$\frac{\partial H}{\partial\hat{q}_{\mathbf{k}}} = \frac{1}{|\mathbf{k}|^2}(\hat{q}_{-\mathbf{k}}-\hat{h}_{-\mathbf{k}}). \tag{4.3b}$$

There is no need in demonstrating the direct proof of the energy conservation in the sine-bracket truncation (4.1) like we did for the traditional truncation (3.17) in Section 3.1.3, since the energy *is* the Hamiltonian for (4.1), and the conservation of the Hamiltonian is the general property of a Hamiltonian system, which is shown in (1.6).

Due to the sine function the symplectic matrix is skew-symmetric and the Jacobi identity also holds: $\forall\,\mathbf{i},\mathbf{j},\mathbf{k}$ we have

$$\begin{aligned}
&\sum(\mathbf{J_{il}}\partial_{\mathbf{l}}\mathbf{J_{jk}}+\mathbf{J_{kl}}\partial_{\mathbf{l}}\mathbf{J_{ij}}+\mathbf{J_{jl}}\partial_{\mathbf{l}}\mathbf{J_{ki}}) = \\
&=\sum[\sin(\varepsilon\mathbf{i}\times(\mathbf{j}+\mathbf{k}))\sin(\varepsilon\mathbf{j}\times\mathbf{k})+\sin(\varepsilon\mathbf{k}\times(\mathbf{i}+\mathbf{j}))\sin(\varepsilon\mathbf{i}\times\mathbf{j})+ \\
&+\sin(\varepsilon\mathbf{j}\times(\mathbf{k}+\mathbf{i}))\sin(\varepsilon\mathbf{k}\times\mathbf{i})]\hat{q}_{\mathbf{i}+\mathbf{j}+\mathbf{k}} = [\sin(\varepsilon\mathbf{i}\times\mathbf{j})\cos(\varepsilon\mathbf{i}\times\mathbf{k})\sin(\varepsilon\mathbf{j}\times\mathbf{k})- \\
&-\cos(\varepsilon\mathbf{i}\times\mathbf{j})\sin(\varepsilon\mathbf{k}\times\mathbf{i})\sin(\varepsilon\mathbf{j}\times\mathbf{k})+\sin(\varepsilon\mathbf{k}\times\mathbf{i})\cos(\varepsilon\mathbf{k}\times\mathbf{j})\sin(\varepsilon\mathbf{i}\times\mathbf{j})- \\
&-\cos(\varepsilon\mathbf{k}\times\mathbf{i})\sin(\varepsilon\mathbf{j}\times\mathbf{k})\sin(\varepsilon\mathbf{i}\times\mathbf{j})+\sin(\varepsilon\mathbf{j}\times\mathbf{k})\cos(\varepsilon\mathbf{j}\times\mathbf{i})\sin(\varepsilon\mathbf{k}\times\mathbf{i})- \\
&-\cos(\varepsilon\mathbf{j}\times\mathbf{k})\sin(\varepsilon\mathbf{i}\times\mathbf{j})\sin(\varepsilon\mathbf{k}\times\mathbf{i})]\hat{q}_{\mathbf{i}+\mathbf{j}+\mathbf{k}} = 0.
\end{aligned}$$

The sine-bracket truncation (4.1) conserves $2M$ independent Casimir invariants of the form

$$C_N = \sum_{Z^N} \hat{q}_{\mathbf{i}_1} \dots \hat{q}_{\mathbf{i}_N} \cos[\varepsilon A(\mathbf{i}_1, \dots, \mathbf{i}_N)],$$
$$Z^N = \{(\mathbf{i}_1, \dots, \mathbf{i}_N), \sum_{j=1}^{N} \mathbf{i}_j = \mathbf{0}\}, \tag{4.4}$$

where

$$A(\mathbf{i}_1, \dots, \mathbf{i}_N) = \mathbf{i}_2 \times \mathbf{i}_1 + \mathbf{i}_3 \times (\mathbf{i}_1 + \mathbf{i}_2) + \dots + \mathbf{i}_N \times (\mathbf{i}_1 + \dots + \mathbf{i}_{N-1}).$$

The Casimir invariants (4.4) differ from their counterparts (3.16) of the infinite-dimensional equation (3.9). However, the enstrophy (3.19) remains intact due to $A(\mathbf{i}, -\mathbf{i}) = 0$.

In order to prove the existence of the Casimir invariants (4.4), let us consider the family of $(2M+1) \times (2M+1)$ matrices $\mathbf{D_n}$ which have the form

$$\mathbf{D_n} = \sigma^{n_1 n_2/2} g^{n_1} h^{n_2},$$

where the unitary $(2M+1) \times (2M+1)$ matrices h and g satisfy

$$hg = \sigma gh \quad \text{and} \quad g^{2M+1} = h^{2M+1} = I. \tag{4.5}$$

We choose $(2M+1)$ to be prime and

$$\sigma = \exp\left(\frac{4\pi i}{2M+1}\right).$$

For our choice of σ the matrices g and h are

$$g = \begin{pmatrix} 1 & 0 & 0 & \cdots & 0 \\ 0 & \sigma & 0 & \cdots & 0 \\ 0 & 0 & \sigma^2 & \cdots & 0 \\ \vdots & \vdots & \vdots & \ddots & \vdots \\ 0 & 0 & 0 & \cdots & \sigma^{2M} \end{pmatrix}, \quad h = \begin{pmatrix} 0 & 1 & 0 & \cdots & 0 \\ 0 & 0 & 1 & \cdots & 0 \\ \vdots & \vdots & \vdots & \ddots & \vdots \\ 0 & 0 & 0 & \cdots & 1 \\ 1 & 0 & 0 & \cdots & 0 \end{pmatrix}.$$

We can see that if h is applied to the given matrix from the left, it shifts the given matrix upwards, and if it is applied from the right, it shifts the given matrix to the right. Taking

this into account, (4.5) can be easily proven. First, $g^{2M+1} = I$ is obvious for our choice of σ. Second, $h^{2M+1} = I$ because h shifts itself $2M$ times into the identity position. Then,

$$hg = \begin{pmatrix} 0 & \sigma & 0 & \cdots & 0 \\ 0 & 0 & \sigma^2 & \cdots & 0 \\ \vdots & \vdots & \vdots & \ddots & \vdots \\ 0 & 0 & 0 & \cdots & \sigma^{2M} \\ 1 & 0 & 0 & \cdots & 0 \end{pmatrix} \quad \text{and} \quad \sigma gh = \begin{pmatrix} 0 & \sigma & 0 & \cdots & 0 \\ 0 & 0 & \sigma^2 & \cdots & 0 \\ \vdots & \vdots & \vdots & \ddots & \vdots \\ 0 & 0 & 0 & \cdots & \sigma^{2M} \\ \sigma^{2M+1} & 0 & 0 & \cdots & 0 \end{pmatrix}$$

and since $\sigma^{2M+1} = 1$ we obtain $hg = \sigma gh$.

The set of $\mathbf{D_n}$'s is the group of unitary matrices which satisfy the following relations:

$$\begin{aligned} \mathbf{D}_\mathbf{n}^\dagger &= \mathbf{D}_{-\mathbf{n}} = (\mathbf{D}_\mathbf{n})^{-1}, \\ \mathbf{D}_\mathbf{n}\mathbf{D}_\mathbf{m} &= \exp(i\varepsilon(\mathbf{m} \times \mathbf{n}))\mathbf{D}_{\mathbf{n}+\mathbf{m}}, \\ \frac{1}{2M+1}\mathrm{Tr}(\mathbf{D}_\mathbf{m}) &= \delta^\mathbf{0}_\mathbf{m}, \end{aligned} \tag{4.6}$$

where $\varepsilon = 2\pi/(2M+1)$. We present the proof for the three statements in (4.6) below.

- First statement in (4.6):

$$\begin{aligned} \mathbf{D}_\mathbf{n}^{-1} = \exp\left(-\frac{2\pi i n_1 n_2}{2M+1}\right)(g^{n_1}h^{n_2})^{-1} &= \exp\left(-\frac{2\pi i n_1 n_2}{2M+1}\right)(h^{n_2})^{-1}(g^{n_1})^{-1} = \\ = \exp\left(-\frac{2\pi i n_1 n_2}{2M+1}\right)(h^{n_2})^\dagger(g^{n_1})^\dagger &= \exp\left(-\frac{2\pi i n_1 n_2}{2M+1}\right)(g^{n_1}h^{n_2})^\dagger = \mathbf{D}_\mathbf{n}^\dagger. \\ \mathbf{D}_\mathbf{n}^{-1} = \exp\left(-\frac{2\pi i n_1 n_2}{2M+1}\right)(g^{n_1}h^{n_2})^{-1} &= \exp\left(\frac{2\pi i n_1 n_2}{2M+1}\right)\sigma^{-n_1 n_2}h^{-n_2}g^{-n_1} = \\ &= \exp\left(\frac{2\pi i n_1 n_2}{2M+1}\right)g^{-n_1}h^{-n_2} = \mathbf{D}_{-\mathbf{n}}. \end{aligned}$$

- Second statement in (4.6):

$$\begin{aligned}\mathbf{D_n D_m} = \exp\left(\frac{2\pi i(n_1 n_2 + m_1 m_2)}{2M+1}\right) g^{n_1} h^{n_2} g^{m_1} h^{m_2} = \\ \exp\left(\frac{2\pi i(n_1 n_2 + m_1 m_2)}{2M+1}\right) \sigma^{m_1 k} g^{n_1} h^{n_2-k} g^{m_1} h^{m_2+k} = \\ \exp\left(\frac{2\pi i(n_1 n_2 + m_1 m_2 + 2m_1 n_2)}{2M+1}\right) g^{m_1+n_1} h^{m_2+n_2} = \\ \exp\left(\frac{2\pi i[(m_1+m_2)(n_1+n_2) + (m_1 n_2 - m_2 n_1)]}{2M+1}\right) g^{m_1+n_1} h^{m_2+n_2} = \\ = \exp(i\varepsilon(\mathbf{m}\times\mathbf{n}))\mathbf{D_{n+m}}.\end{aligned}$$

- Third statement in (4.6): first note that

$$\mathrm{Tr}(\mathbf{D_k}) = \sigma^{k_1 k_2/2}\mathrm{Tr}(g^{k_1} h^{k_2}).$$

Then, $\mathrm{Tr}(g^j) = 0$ for $j \neq (2M+1)s_1$, $s_1 \in \mathcal{Z}$, because

$$\sum_{p=0}^{2M} \exp\left(\frac{4\pi i j p}{2M+1}\right) = 0, \quad j \neq (2M+1)s_1.$$

Now we can see that $\mathrm{Tr}(g^j h^k) = 0$ for $k \neq (2M+1)s_2$, $s_2 \in \mathcal{Z}$, because h^k shifts non-zero entries of g^j off the diagonal position. Otherwise, we obtain $\mathrm{Tr}(g^j h^k) = \mathrm{Tr}(I) = 2M+1$ for $j = (2M+1)s_1$ and $k = (2M+1)s_2$. Taking into account that our indices are between $-M$ and M we have

$$\mathrm{Tr}(\mathbf{D_k}) = \begin{cases} 2M+1, & \mathbf{k} = \mathbf{0}, \\ 0, & \mathbf{k} \neq \mathbf{0}, \end{cases}$$

which gives the third statement of (4.6).

From (4.6) immediately follows

$$\begin{aligned}[\mathbf{D_n}, \mathbf{D_m}] &= 2i\sin(\varepsilon(\mathbf{m}\times\mathbf{n}))\mathbf{D_{n+m}}, \\ [\mathbf{D_n}, \mathbf{D_m}]_+ &= 2\cos(\varepsilon(\mathbf{m}\times\mathbf{n}))\mathbf{D_{n+m}},\end{aligned} \tag{4.7}$$

where $[\cdot,\cdot]$ and $[\cdot,\cdot]_+$ are the commutation and anti-commutation operators, respectively defined as follows:

$$[x,y] = xy - yx, \quad [x,y]_+ = xy + yx.$$

Now we will show how to write the sine-bracket equation in its "bracket" form via the commutation rule (4.7). We denote

$$Q = \sum_{\mathbf{n}} \hat{q}_{\mathbf{n}} \mathbf{D}_{\mathbf{n}} \quad \text{and} \quad F = \sum_{\mathbf{n}} f_{\mathbf{n}} \mathbf{D}_{\mathbf{n}},$$

where

$$f_{\mathbf{k}} = \frac{\partial H}{\partial \hat{q}_{\mathbf{k}}},$$

H is an arbitrary Hamiltonian. We write the analogue of the sine-bracket truncation (4.1) with the arbitrary Hamiltonian in the form

$$\dot{Q} = \frac{i}{2\varepsilon}[Q,F]. \tag{4.8}$$

In order to show that (4.8) is true, let us first write what the commutator $[Q,F]$ is:

$$\begin{aligned}\frac{i}{2\varepsilon}[Q,F] &= \frac{i}{2\varepsilon}\left(\sum_{\mathbf{n}} \hat{q}_{\mathbf{n}}\mathbf{D}_{\mathbf{n}}\right)\left(\sum_{\mathbf{m}} f_{\mathbf{m}}\mathbf{D}_{\mathbf{m}}\right) - \left(\sum_{\mathbf{m}} f_{\mathbf{m}}\mathbf{D}_{\mathbf{m}}\right)\left(\sum_{\mathbf{n}} \hat{q}_{\mathbf{n}}\mathbf{D}_{\mathbf{n}}\right) = \\ &= \frac{i}{2\varepsilon}\sum_{\mathbf{n},\mathbf{m}} \hat{q}_{\mathbf{n}} f_{\mathbf{m}}(\mathbf{D}_{\mathbf{n}}\mathbf{D}_{\mathbf{m}} - \mathbf{D}_{\mathbf{m}}\mathbf{D}_{\mathbf{n}}) = \frac{1}{\varepsilon}\sum_{\mathbf{n},\mathbf{m}} \sin(\varepsilon(\mathbf{m}\times\mathbf{n}))\hat{q}_{\mathbf{n}} f_{\mathbf{m}}\mathbf{D}_{\mathbf{m}+\mathbf{n}} = \\ &= -\frac{1}{\varepsilon}\sum_{\mathbf{k},\mathbf{m}} \sin(\varepsilon(\mathbf{k}\times\mathbf{m}))\hat{q}_{\mathbf{k}+\mathbf{m}} f_{-\mathbf{m}}\mathbf{D}_{\mathbf{k}}.\end{aligned}$$

Here we denote $\mathbf{k} = \mathbf{m} + \mathbf{n}$ and then change $\mathbf{m}$ to $-\mathbf{m}$. Now we write what $\dot{Q}$ is:

$$\dot{Q} = \sum_{\mathbf{k}} \dot{\hat{q}}_{\mathbf{k}} \mathbf{D}_{\mathbf{k}},$$

and (4.8) becomes

$$\sum_{\mathbf{k}} \dot{\hat{q}}_{\mathbf{k}} \mathbf{D}_{\mathbf{k}} = -\frac{1}{\varepsilon}\sum_{\mathbf{k},\mathbf{m}} \sin(\varepsilon(\mathbf{k}\times\mathbf{m}))\hat{q}_{\mathbf{k}+\mathbf{m}} f_{-\mathbf{m}}\mathbf{D}_{\mathbf{k}}. \tag{4.9}$$

The matrices $\mathbf{D}_{\mathbf{k}}$ are linearly independent, therefore the equality (4.9) must hold separately for each $\mathbf{D}_{\mathbf{k}}$, hence (4.8) is equivalent to (4.1).

We expect Casimirs to be traces of Q^k. To show this, first note that from the commutation rule, we can see that $\mathrm{Tr}[\mathbf{D_n}, \mathbf{D_m}] = 0$. From (4.6), Q^k is a linear combination of $\mathbf{D}$'s so that time-derivative of Q^k is a set of $\mathbf{D}$-commutators, therefore $\mathrm{Tr}(Q^k)$ are conserved in time with arbitrary Hamiltonian. Explicitly

$$\begin{aligned}
\frac{1}{2M+1}\mathrm{Tr}(Q^k) = \frac{1}{2M+1}\mathrm{Tr}\left(\sum_{\mathbf{i}} \hat{q}_{\mathbf{i}}\mathbf{D_i}\right)^k = \\
= \frac{1}{2M+1}\sum_{\mathbf{i}_1,\ldots,\mathbf{i}_k} \hat{q}_{\mathbf{i}_1},\ldots,\hat{q}_{\mathbf{i}_k}\mathrm{Tr}(\mathbf{D}_{\mathbf{i}_1},\ldots,\mathbf{D}_{\mathbf{i}_k}) = \\
\sum_{\sum_j^k \mathbf{i}_j=0} \hat{q}_{\mathbf{i}_1},\ldots,\hat{q}_{\mathbf{i}_k}\exp\{i\varepsilon[\mathbf{i}_2\times\mathbf{i}_1 + \mathbf{i}_3\times(\mathbf{i}_1+\mathbf{i}_2) + \\
+\ldots+\mathbf{i}_{k-1}\times(\mathbf{i}_1+\ldots+\mathbf{i}_{k-2})]\} = \\
\sum_{\sum_j^k \mathbf{i}_j=0} \hat{q}_{\mathbf{i}_1},\ldots,\hat{q}_{\mathbf{i}_k}\cos\{\varepsilon[\mathbf{i}_2\times\mathbf{i}_1 + \mathbf{i}_3\times(\mathbf{i}_1+\mathbf{i}_2) + \\
+\ldots+\mathbf{i}_{k-1}\times(\mathbf{i}_1+\ldots+\mathbf{i}_{k-2})]\},
\end{aligned} \tag{4.10}$$

i.e. (4.10) coincides with (4.4).

The fact that the sine-bracket truncation conserves the same low-order quantities as (3.17) does makes it very convenient to study the dynamics of the truncation with many conserved quantities as a comparison to the generic energy-enstrophy conserving truncation. In the later chapters we will see that the additional conserved quantities play an important role for the special sets of initial conditions.

In the current work we perform computations with up to 23×23 square array of Fourier coefficients. The truncation (4.1) of this size possesses, apart from the momentum, energy and enstrophy, 20 additional Casimir invariants. In the Section 4.4 we will show that the standard numerical time integrators preserve energy, but do not preserve enstrophy and higher order Casimir invariants. The special type of integrator which allows to preserve all Casimir invariants with machine precision is presented in the next section.

4.2 Symplectic numerical integrator for the truncation with many conserved quantities

In this section we describe the special kind of time integrator which allows us to preserve the Poisson bracket. This integrator was suggested in the paper [20] by R. I. McLachlan. If the symplectic structure is preserved explicitly, then the Casimir invariants

associated with corresponding Poisson bracket will be conserved with machine precision. The integrator we describe here uses the symplectic splitting method, the idea of which is that if the Poisson bracket is linear with respect to $\hat{q}_{\mathbf{k}}$ (also called *Lie-Poisson bracket*), then, splitting the Hamiltonian in a special way, we can make the system to be linear. Of course, splitting the Hamiltonian calls for an approximate solution, and here we describe the first-order symplectic integrator followed by the simple second-order extension. The integrator can as well be used to integrate the traditional truncation (3.17) despite the fact that it lacks the Hamiltonian structure and the family of Casimir invariants (4.4). In that case only the enstrophy should be preserved with machine precision.

Our symplectic matrix $\mathbf{J}_{\mathbf{k}\mathbf{k}'}$ is linear with respect to $\hat{q}_{\mathbf{k}}$:

$$\mathbf{J}_{\mathbf{k}\mathbf{k}'} = -\frac{1}{\varepsilon}\sin(\varepsilon\mathbf{k}\times\mathbf{k}')\hat{q}_{\mathbf{k}+\mathbf{k}'}.$$

Let us define the special subset σ of the two-dimensional space of integers such that

$$\sigma \subset \mathcal{Z}^2,\ \mathbf{J}_{\mathbf{k}\mathbf{k}'} = 0\ \ \forall \mathbf{k}, \mathbf{k}' \in \sigma.$$

If the Hamiltonian is

$$H(\hat{q}_{\mathbf{k}_1}, \ldots, \hat{q}_{\mathbf{k}_n}) = H(\sigma) \tag{4.11}$$

for some $\mathbf{k}_1, \ldots, \mathbf{k}_n \in \sigma$ then the system

$$\frac{\mathrm{d}}{\mathrm{d}t}\hat{q}_{\mathbf{k}} = \mathbf{J}_{\mathbf{k}\mathbf{k}'}\frac{\partial H}{\partial \hat{q}_{\mathbf{k}'}}$$

is linear. This happens because the variables $\hat{q}_{\mathbf{k}'}$, which belong to the Hamiltonian, are conserved in time. For the linear system we can find an analytic solution.

Our Hamiltonian (3.18) does not belong to such class. However note that the Hamiltonian is a sum of small pieces, and each piece depends on a single spectral coefficient $\hat{q}_{\mathbf{k}}$. We split the Hamiltonian into smaller pieces such that each of them separately belongs to (4.11):

$$H = \sum_j H_j(\sigma_j),\ [\sigma_j \subset \mathcal{Z}^2,\ \mathbf{J}_{\mathbf{k}\mathbf{k}'} = 0\ \ \forall \mathbf{k}, \mathbf{k}' \in \sigma_j]\ \forall j.$$

Now for a small time step we can integrate the system sequentially for all $H_j(\sigma_j)$ which will give us a first-order approximation to the exact solution. What we essentially do is

that we analytically integrate same Poisson bracket with different Hamiltonians, therefore the Casimirs (which are the property of Poisson bracket alone) are preserved with machine precision.

In our case with the sine-bracket equation for any $\mathbf{k} = (k_1, k_2)$ we denote

$$\sigma(\mathbf{k}) = \{n\mathbf{k} : -M \leq n \leq M\}.$$

To split the Hamiltonian we need the set $\mathbf{K}$ which consists of several vectors $\mathbf{k}_j$ and satisfies the following: let us denote $\sigma(\mathbf{K}) = \cup_j \sigma(\mathbf{k}_j)$, then $\sigma(\mathbf{K})$ should be such, that $\forall m_1, m_2 \in [-M, M]$ we would have $\mathbf{m} \in \sigma(\mathbf{K})$. Also $\mathbf{K}$ should satisfy $\sigma(\mathbf{k}_1) \cap \sigma(\mathbf{k}_2) = \emptyset \ \forall \mathbf{k}_1, \mathbf{k}_2 \in \mathbf{K}$. In other words, $\mathbf{K}$ should be such that $\sigma(\mathbf{K})$ would be a disjoint set which covers the whole lattice. When $(2M + 1)$ is a prime, the possible choice of $\mathbf{K}$ is

$$\mathbf{K} = \{(0, 1)\} \cup \{(1, m) : -M \leq m \leq M\}. \tag{4.12}$$

We can see that for this choice $\sigma(\mathbf{K})$ is not completely disjoint, but the point in the origin never evolves in time, so (4.12) suffices. Then for the Hamiltonian we have

$$H = \frac{1}{2} \sum_{n_1, n_2 = -N}^{N} \frac{|\hat{q}_{\mathbf{n}} - \hat{h}_{\mathbf{n}}|^2}{|\mathbf{n}|^2} = \sum_{\mathbf{k} \in \mathbf{K}} H_{\mathbf{k}}, \qquad H_{\mathbf{k}} = \frac{1}{2} \sum_{n=-N}^{N} \frac{(\hat{q}_{n\mathbf{k}} - \hat{h}_{n\mathbf{k}})(\hat{q}_{-n\mathbf{k}} - \hat{h}_{-n\mathbf{k}})}{|n\mathbf{k}|^2}. \tag{4.13}$$

In the above equation we should take into account that the expression $n\mathbf{k}$ in the denominator of $H_{\mathbf{k}}$ is aliased, i.e. whenever $n\mathbf{k}$ is out of bounds, the value is aliased from the opposite side of the domain.

Now we need to solve $\dot{\hat{\mathbf{q}}} = \mathbf{J} \nabla H_{\mathbf{k}}$ (sequentially for all $\mathbf{k} \in \mathbf{K}$, of course). For aforementioned $\mathbf{K}$ we can write (4.1) in the form

$$\dot{z}_m = \sum_{n=-M}^{M} a_n z_{m-n}, \tag{4.14}$$

where $z_m = \hat{q}_{\mathbf{j}+m\mathbf{k}}$, $\mathbf{j} = (0, j), 0 < j \leq M$ for $\mathbf{k} = (1, 0)$ and $\mathbf{j} = (j, 0), 0 < j \leq M$ for the rest of $\mathbf{k}$'s $\in \mathbf{K}$ (Here we took into account the fact that $\hat{q}_{\mathbf{m}} = \hat{q}^*_{-\mathbf{m}}$, so that we can solve only for the half of the lattice). Also

$$a_n = -\frac{\sin(\varepsilon n \mathbf{j} \times \mathbf{k})}{\varepsilon |n\mathbf{k}|^2} (\hat{q}_{n\mathbf{k}} - \hat{h}_{n\mathbf{k}}).$$

The system (4.14) is linear and therefore can be solved analytically. The following trick helps us to diagonalize the system. Note that (4.14) is essentially the discretized convolution, hence using the discrete Fourier transform yields the disjoint set of equations:

$$\dot{\hat{z}}_p = \sum_{m=0}^{2M+1} z_m e^{-2\pi i p m/(2M+1)} = \sum_{m=0}^{2M+1} \sum_{n=-M}^{M} a_n z_{m-n} e^{-2\pi i p m/(2M+1)} =$$
$$= \sum_{n=-M}^{M} \sum_{s=-n}^{2M+1-n} a_n z_s e^{-2\pi i p (n+s)/(2M+1)} =$$
$$= \sum_{n=-M}^{M} a_n e^{-2\pi i p n/(2M+1)} \sum_{s=-n}^{2M+1-n} z_s e^{-2\pi i p s/(2M+1)} = \hat{a}_p \hat{z}_p.$$

Thus (4.14) in Fourier space has the form

$$\dot{\hat{z}}_i = \Lambda_{ij} \hat{z}_j, \quad \Lambda_{ij} = \begin{cases} \hat{a}_i: & i = j \\ 0: & i \neq j \end{cases}, \text{ where } \hat{\mathbf{a}} = FFT(\mathbf{a})$$

which is explicitly integrable:

$$\hat{z}_p(t + \Delta t) = e^{\Delta t \Lambda_{pp}} \hat{z}_p(t),$$

and (4.14) can be written in the explicit form

$$\mathbf{z}(t + \Delta t) = FFT^{-1} e^{\Delta t \Lambda} FFT \mathbf{z}(t).$$

Thus, each equation $\dot{\mathbf{q}} = \mathbf{J} \nabla H_{\mathbf{k}}$ can be solved *exactly* using fast Fourier transform $3M$ times (forward, backward and for a_n). This means that the conservation of symplectic matrix properties (such as Casimirs) should happen close to round-off error. Taking into account that we have $2(M+1)$ $\mathbf{k}$'s $\in \mathbf{K}$, the whole amount of FFT's is $6M(M+1)$ for each step of integration.

4.2.1 Second order symplectic integrator

The Casimir invariants (4.4), including enstrophy, should be conserved with machine precision with the above method of symplectic integration. However, the energy (3.18) is not a Casimir invariant, and therefore the extent to which the energy is conserved is determined by an order of approximation provided by the integrator. So far we described

the symplectic integrator of the first order, which ability to conserve energy is rather mediocre. A simple extension of the first order symplectic integrator to the second order approximation can be obtained at almost complete absence of additional complexity, which allows for more precise conservation of the energy.

When we sequentially integrate the system for the Hamiltonians $H_j(\sigma_j)$ we use the fact that

$$e^{\Delta t(A+B)} = e^{\Delta tA}e^{\Delta tB} + \mathcal{O}(\Delta t^2),$$

where A, B are matrices, that is why we have the first order integrator. Using the fact that

$$e^{\Delta t(A+B)} = e^{\Delta tA/2}e^{\Delta tB}e^{\Delta tA/2} + \mathcal{O}(\Delta t^3),$$

or, for many matrices,

$$e^{\Delta t(A_1+\ldots+A_n)} = e^{\Delta tA_1/2}\ldots e^{\Delta tA_{n-1}/2}e^{\Delta tA_n}e^{\Delta tA_{n-1}/2}\ldots e^{\Delta tA_1/2} + \mathcal{O}(\Delta t^3),$$

we construct the second order symplectic integrator. The second order symplectic integrator is twice as slow as the first order symplectic integrator, but it decreases the error's order of magnitude twice in comparison with the first order integrator.

4.3 Initial conditions with predefined conserved quantities

Our purpose is to study the statistical influence of the conserved quantities on the system, so it is highly desirable to generate initial conditions with predefined conserved quantities for the sine-bracket truncation. The method of generating initial conditions we present here, allows us to fetch energy, enstrophy, and an arbitrary number of Casimir invariants prior to solving the system.

4.3.1 Gradient descent

The constraint for the initial conditions is

$$\mathbf{f}(\mathbf{q}) = \mathbf{0}, \tag{4.15}$$

where

$$f_1(\mathbf{q}) = E(\mathbf{q}) - E_0,$$
$$f_2(\mathbf{q}) = \mathcal{E}(\mathbf{q}) - \mathcal{E}_0,$$
$$f_n(\mathbf{q}) = C_n(\mathbf{q}) - C_{n0}, \quad n > 2,$$

where $E_0, \mathcal{E}_0, C_{n0}$ are the predefined conserved quantities. As we can see, the dimension of $\mathbf{q}$ exceeds the dimension of $\mathbf{f}$, so that the solution, if exists, is not necessarily unique. However, we do not need to find all possible solutions of (4.15), we just need to pick only one point out of the subspace of solutions. In order do that, we transform the problem from the original form to the more suitable form for our purpose. Instead of directly solve (4.15) we will be solving the problem

$$\mathbf{q} = \arg\left(\min(\mathbf{f}^2)\right), \tag{4.16}$$

which is equivalent to (4.15). Rewriting the above argument in more general form, we obtain

$$\mathbf{x} = \arg\left[\min(F(\mathbf{x}))\right], \tag{4.17}$$

where F is at least differentiable. We note that ∇F always points to the direction (in $\mathbf{x}$-space) along which F increases most rapidly. Consequently, $-\nabla F$ points to the direction along which F *decreases* most rapidly. Thus if we take a small enough step in that direction, the F calculated in new point will be smaller than that in the previous point. So, if we set up iterations of the form

$$\mathbf{x}_{n+1} = \mathbf{x}_n - \alpha \nabla F(\mathbf{x}_n), \quad \alpha > 0, \tag{4.18}$$

then, for small enough α, we expect $\{\mathbf{x}_n\}$ to converge to a local minimum for F. If F is a convex functional, then it has the unique minimum and $\{\mathbf{x}_n\}$ converges to a minimum for any starting vector $\mathbf{x}_0$. However if F is not convex, it may (not necessarily, though) have some local minima, where $\{\mathbf{x}_n\}$ may accidentally converge. In this case we should either pick another starting vector or go uphill until we leave the "zone of influence" of that local minimum.

4.3.2 Steepest descent

Note that in the previous section we wrote "for small enough α". So there is the question: how small? And is it necessary for α to be a constant for all steps of iteration?

Indeed, we can choose α for each iteration step. For this purpose we write (4.18) as

$$\mathbf{x}_{n+1} = \mathbf{x}_n - \alpha_n \nabla F(\mathbf{x}_n), \quad \alpha_n > 0. \tag{4.19}$$

Now, what would be the criterion for α_n at each step? The reasonable argument is that α should be such that we go in the direction pointed out by $-\nabla F$ until F starts increasing (note that it always decreases in the beginning). In other words, we must find (possibly smallest) α such that

$$\left.\frac{\partial F}{\partial \alpha}\right|_{\mathbf{x}_n} = 0. \tag{4.20}$$

One way to do it is using the so called *bisection algorithm*. The way this algorithm works is the following:

- Note that
$$\left.\frac{\partial F}{\partial \alpha}\right|_{\mathbf{x}_n, \alpha=0} \leq 0.$$
- Find α in the direction given by $-\nabla F$ for which
$$\left.\frac{\partial F}{\partial \alpha}\right|_{\mathbf{x}_n} > 0.$$
- Find the sign of the derivative in the middle point, and depending on the sign, decide which interval will be next for bisection.
- Do it until the derivative is close enough to zero (choose tolerance).

The gradient descent with the above criterion for α is called *steepest descent*.

Note that (4.20) is equivalent to

$$\nabla F(\mathbf{x}_n) \cdot \nabla F(\mathbf{x}_{n+1}) = 0, \tag{4.21}$$

i.e. the next direction of descent is always perpendicular to the previous one. In the current work we use the steepest descent method to pin-point initial energy, enstrophy,

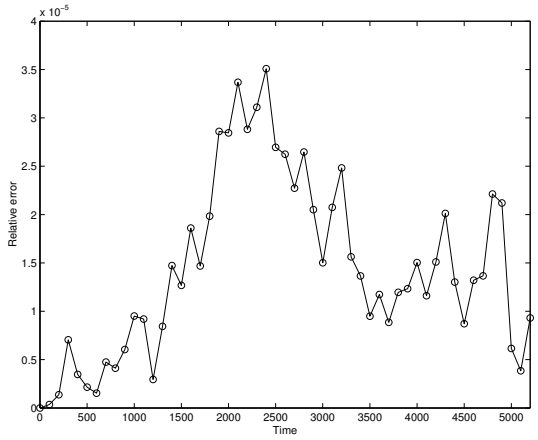

The relative error of energy for the traditional truncation. Number of modes 11×11, integration time $T = 5200$, time step $\Delta t = 0.01$, scale 10^{-5}.

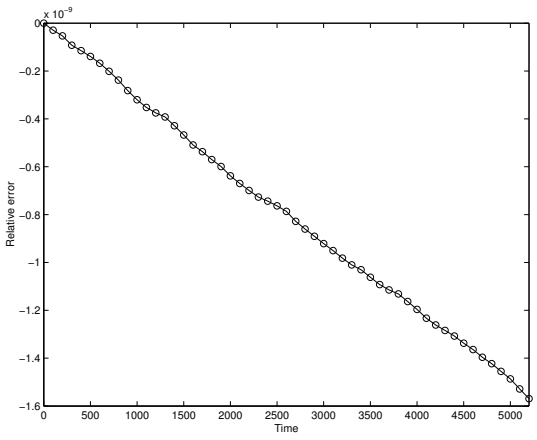

The relative error of enstrophy for the traditional truncation. Number of modes 11×11, integration time $T = 5200$, time step $\Delta t = 0.01$, scale 10^{-9}.

Figure 4.1: The conservation of energy and enstrophy for the traditional truncation

and the third Casimir invariant for the sine-bracket truncation, and, despite its drawbacks, this method works fine for our purposes.

4.4 Numerical validation of the second order symplectic integrator

In this section we present the results of numerical validation of the second order symplectic integrator for the two truncations. We check that the traditional truncation preserves the energy (3.18) and the enstrophy (3.19), and does not preserve any other Casimir invariants from (4.4), and that the sine-bracket truncation preserves the energy, enstrophy, and Casimir invariants. Moreover, we check that neither truncation preserves the truncated versions of infinite-dimensional Casimir invariants (3.16), which we here refer to as $\hat{C}_N$. In addition, we show that the standard numerical integrators do not preserve the enstrophy and the high order Casimir invariants.

4.4.1 Conservation of the energy and the Casimir invariants

For the all numerical experiments we choose the random initial conditions with fixed energy and enstrophy. We take 11×11 square domain of Fourier coefficients and integrate the system for the time $T = 5200$. The time step $\Delta t = 0.01$. We pick the energy to be $E = 7$, and enstrophy $\mathcal{E} = 20$.

We expect both traditional (3.17) and sine-bracket (4.1) truncations to preserve en-

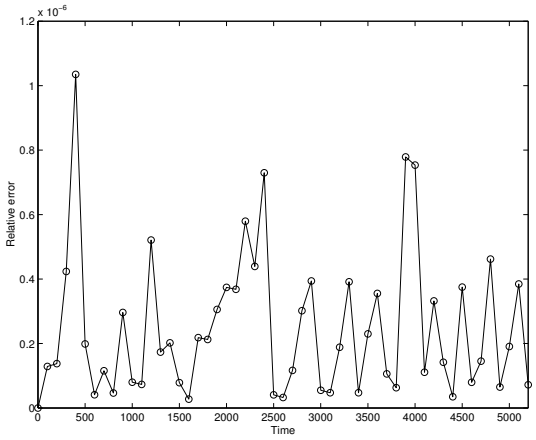

The relative error of energy for the sine-bracket truncation. Number of modes 11×11, integration time $T = 5200$, time step $\Delta t = 0.01$, scale 10^{-6}.

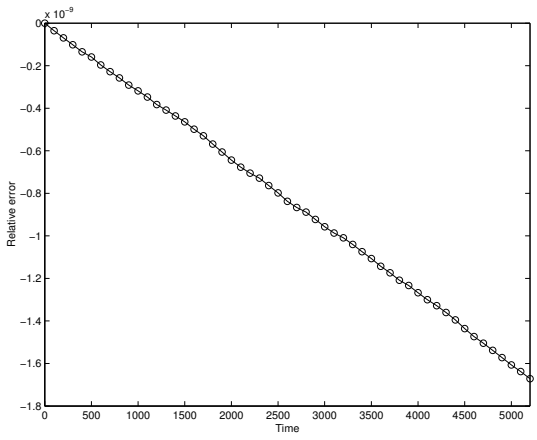

The relative error of enstrophy for the sine-bracket truncation. Number of modes 11×11, integration time $T = 5200$, time step $\Delta t = 0.01$, scale 10^{-9}.

Figure 4.2: The conservation of energy and enstrophy for the sine-bracket truncation

ergy and enstrophy when used in combination with the second order symplectic integrator. The results of numerical validations for energy and enstrophy are shown in Figure 4.1 for the traditional truncation, and Figure 4.2 for the sine-bracket truncation. As we can see, the energy is preserved within $4 \cdot 10^{-5}$ relative error for the traditional truncation, and $1.2 \cdot 10^{-6}$ for the sine-bracket truncation. The enstrophy is preserved with machine precision for both truncations.

Next, we would like to show that the sine-bracket truncation preserves the Casimir invariants (4.4), and the traditional truncation does not preserve them. In addition, we also make sure that neither truncation preserves the truncated versions of infinite-dimensional Casimir invariants (3.16). The results are shown in Figures 4.3 for the traditional truncation, and 4.4 for the sine-bracket truncation. Figure 4.3 shows the time evolution of $\hat{C}_4$ and the relative error of C_4 conservation for the traditional truncation. The $\hat{C}_4$ jumps within 800 and 1300, which means that the relative error for $\hat{C}_4$ is about 50%. The relative error for C_4 for the traditional truncation is 30%, thus neither C_4 or $\hat{C}_4$ is conserved for the traditional truncation. Figure 4.4 shows the time evolution of $\hat{C}_4$ and the relative error of C_4 conservation for the sine-bracket truncation. The $\hat{C}_4$, again, jumps within 800 and 1300, which means that the relative error for $\hat{C}_4$ is about 50%, and the sine-bracket truncation does not conserve $\hat{C}_4$. However, the relative error for C_4 is within $3.5 \cdot 10^{-9}$ for the sine-bracket truncation, which means that C_4 is conserved within the machine

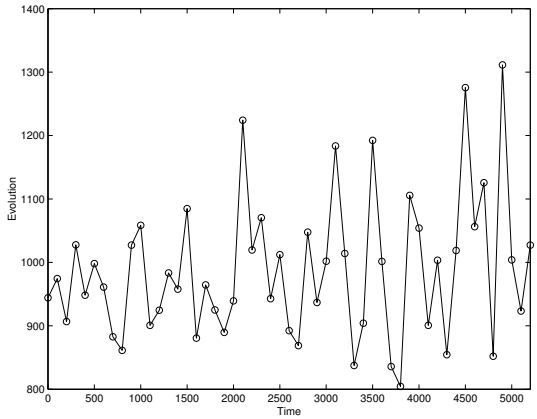

The evolution of $\hat{C}_4$ for the traditional truncation. Number of modes 11×11, integration time $T = 5200$, time step $\Delta t = 0.01$.

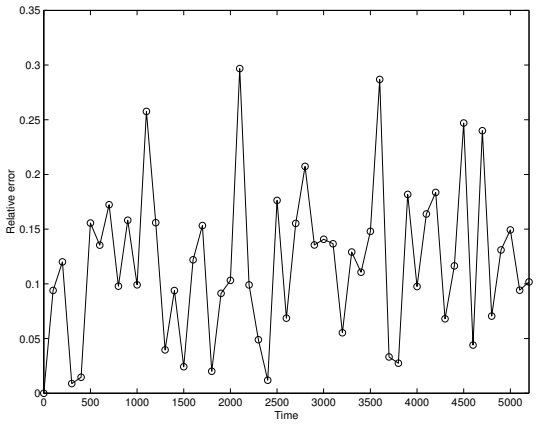

The absolute value of relative error of C_4 for the traditional truncation. Number of modes 11×11, integration time $T = 5200$, time step $\Delta t = 0.01$.

Figure 4.3: The time evolution of $\hat{C}_4$ and C_4 for the traditional truncation

precision by the sine-bracket truncation.

4.4.2 Unstable behavior of standard numerical schemes

One can ask the following question: is there any real need to use the complicated symplectic integrator while there is plenty of standard high-order methods of integration like Runge-Kutta or Adams-Bashforth family? In this section we check whether the two standard methods of integration can be used to solve at least the traditional truncation with two conserved quantities. It happens so that while both methods preserve the energy quite well, the enstrophy is not conserved by both methods.

We perform the computations with the traditional truncation (3.17) using standard methods of integration. We calculate the sum in the right-hand side of (3.17) using the Fast Fourier Transform, which yields $\sim N^2 \log(N)$ floating point operations per time step. To exclude the modes which exceed the range of the lattice we use the twice-extended in both directions array for the Fast Fourier Transform. For the integration in time we use two methods:

- the standard Runge-Kutta method of 4th order
- the Adams-Bashforth-Moulton predictor-corrector method of 4th order

We compute the traditional truncation (3.17) for the 11×11 size of truncation for the time $T = 5200$ and the time step $\Delta t = 0.001$. The same values of energy and

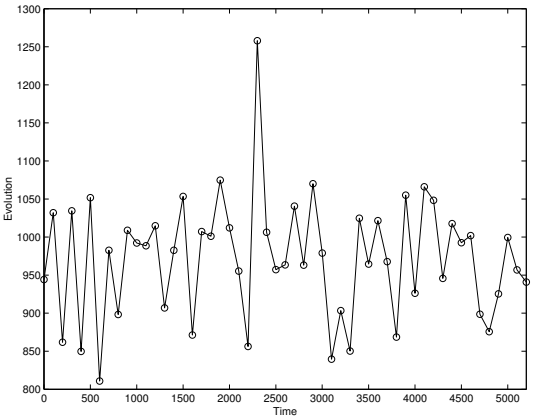

The evolution of $\hat{C}_4$ for the sine-bracket truncation. Number of modes 11×11, integration time $T = 5200$, time step $\Delta t = 0.01$.

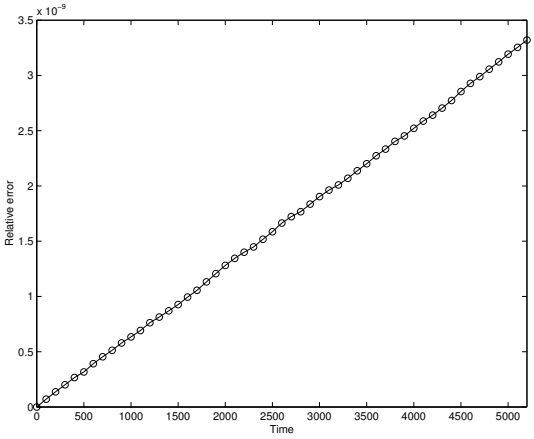

The absolute value of relative error of C_4 for the sine-bracket truncation. Number of modes 11×11, integration time $T = 5200$, time step $\Delta t = 0.01$. The vertical scale is 10^{-9}.

Figure 4.4: The time evolution of $\hat{C}_4$ and the conservation of C_4 for the sine-bracket truncation

enstrophy ($E = 7$, $\mathcal{E} = 20$) were used for this numerical experiment. As we can see, the conservation of energy is satisfactory for this integration time, as shown in Figure 4.5. However, the enstrophy is conserved only up to the time $T \approx 400$, and then its relative error goes sky-high for both Runge-Kutta and Adams-Bashforth-Moulton methods, as shown in Figure 4.6.

As a test, we also calculate (3.17) using Runge-Kutta 4th order method for the smaller lattice of 5×5 Fourier coefficients. The reason for that is to see how the truncation size can affect the stability of the solution. We can see that the enstrophy is not conserved either, but the blow-up time for the enstrophy conservation is larger, $T \approx 1000$, which is shown in Figure 4.7.

In the current work we do not study the possible reasons of this unstable behavior for the standard time-integration schemes. Instead, for the direct numerical simulations with both traditional and sine-bracket truncations we will use the second order symplectic integrator with its guaranteed stability and conservation of the Casimir invariants.

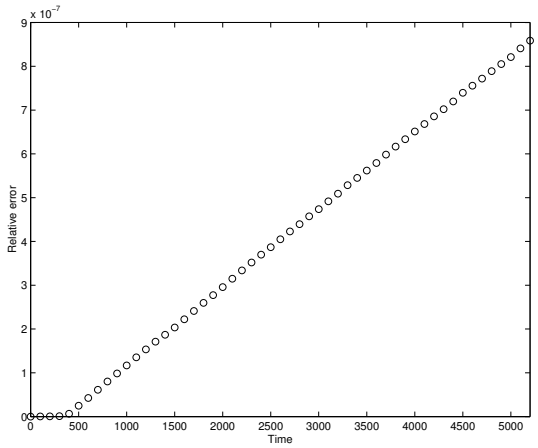

The relative error of energy for the Runge-Kutta 4th order method, $\mathcal{E} = 20$, scale 10^{-7}.

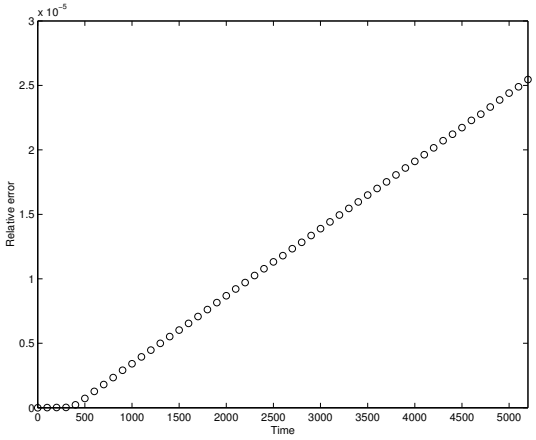

The relative error of energy for the Adams-Bashforth-Moulton 4th order predictor-corrector method, $\mathcal{E} = 20$, scale 10^{-5}.

Figure 4.5: The conservation of energy for the two standard time integrators, 11×11 truncation size

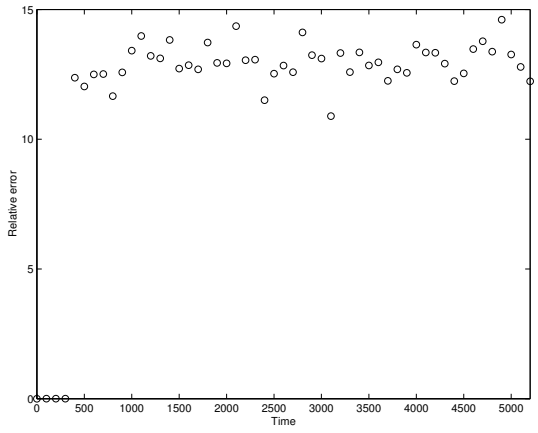

The relative error of enstrophy for the Runge-Kutta 4th order method.

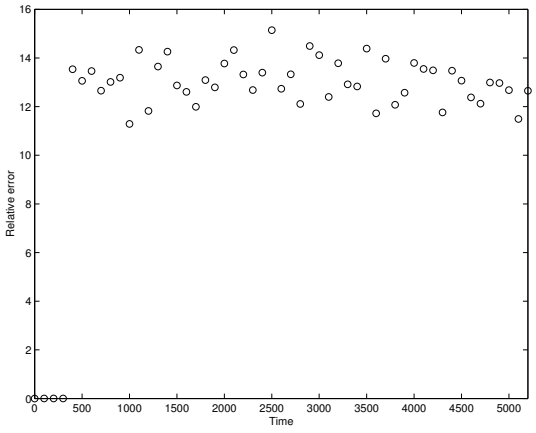

The relative error of enstrophy for the Adams-Bashforth-Moulton 4th order predictor-corrector method, $\mathcal{E} = 20$.

Figure 4.6: The conservation of enstrophy for the two standard time integrators, 11×11 truncation size

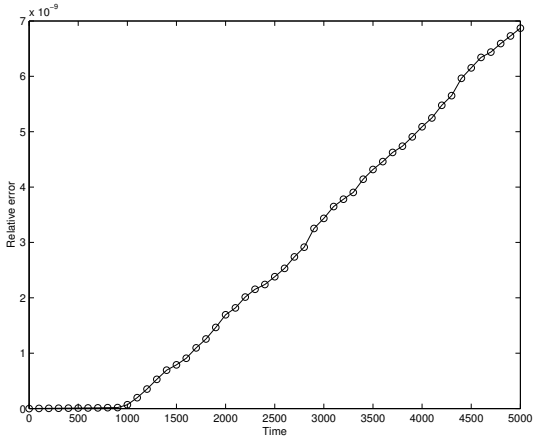

The relative error of energy, 5×5 Fourier coefficients, Runge-Kutta 4th order method, $\mathcal{E} = 20$.

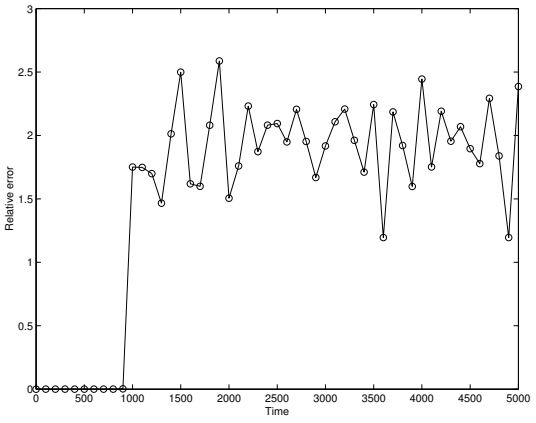

The relative error of enstrophy, 5×5 Fourier coefficients, Runge-Kutta 4th order method, $\mathcal{E} = 20$.

Figure 4.7: The conservation of enstrophy for the two standard time integrators, 5×5 truncation size

CHAPTER 5
BASIC NUMERICAL SIMULATIONS FOR STATISTICAL PREDICTIONS WITH THREE PROTOTYPE GEOPHYSICAL SITUATIONS, TRADITIONAL TRUNCATION

In this chapter we introduce the direct numerical simulations with the traditional truncation (3.17), which preserves energy (3.18) and enstrophy (3.19) only. As shown in Chapter 3, the standard equilibrium statistical theory exists for this truncation, and therefore first we would like to check some of the statistical predictions with direct numerical simulations.

For the completeness of the research, we choose three types of topographies to perform the simulations with, to represent different geophysical situations. The types of topographies we employ are:

- No topography.
- Random topography shown in Figure 5.1. Note that this topography has no Fourier components in the large scale modes with $|\mathbf{k}|^2 = 1$.
- Layered topography

$$h = 0.2\cos(x) + 0.4\cos(2x). \tag{5.1}$$

This topography is layered in y-direction, while being varied in x-direction.

Random topography. The random topography is generated in the Fourier space by the following algorithm: for all $\mathbf{k}$ such that $|\mathbf{k}|^2 = 2$ and $|\mathbf{k}|^2 = 4$ we pick the fixed amplitude 0.5, and generate the phase using uniform distribution from 0 to 2π. We also keep the reality condition $\tilde{h}_{\mathbf{k}} = \tilde{h}^*_{-\mathbf{k}}$. After the topography is generated, it is normalized in such a way, that the relative height between the highest and the lowest points of the topography would be the predefined number. In our calculations we choose the the relative height between the highest and the lowest points of the topography to be 1, i.e.

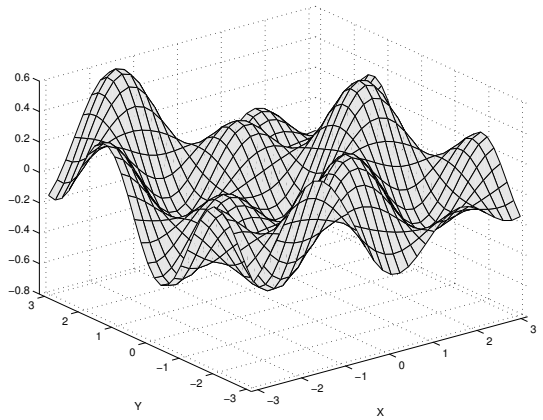

Figure 5.1: The random topography with free largest scale mode

$$\max[h] - \min[h] = H,$$
$$\text{we choose } H = 1.$$

The random topography is shown in Figure 5.1. The purpose of our numerical experiments here is to obtain the statistical results for the truncation with two conserved quantities, which will be compared later to the equilibrium statistical predictions of the theory and the results obtained by means of the sine-bracket truncation. Also in this chapter we present the full description of means by which the statistical results were obtained. Later on we will employ the same statistical numerical procedures with the sine-bracket truncation. The statistical quantities we obtain and present here are:

- The mean flows and their moments;
- The energy of the mean state and the pseudo-energy;
- The "Corr" functions introduced by Majda and Holen in [13] and the scatterplots of $\bar{q}$ vs $\bar{\psi}$;
- The time correlation functions;
- The probability density functions.

5.0.3 Numerical definitions for the statistical quantities

Here we represent the definitions and numerical algorithms which are used to compute the aforementioned statistical values.

The mean stream function and its moments. By "mean value" of a quantity we assume its time average. Thus, we compute the mean stream function via the formula

$$\bar{\psi}(x,y) = \frac{1}{T}\int_{T_0}^{T_0+T} \psi(x,y,t)dt. \tag{5.2}$$

Here T_0 is the time we skip before proceeding with statistical calculations, T is the averaging window. As well as the stream function itself, we also compute the various moments of the mean stream function which are defined by the formula

$$M_N = \langle(\psi - \langle\psi\rangle)^N\rangle, \tag{5.3}$$

where $\langle\cdot\rangle$ means time-averaging in the sense given in (5.2). Here we compute the lower moments of the stream function M_2, $M_3/M_2^{3/2}$, and M_4/M_2^2, which are the variance, skewness, and flatness, respectively.

Energy of the mean and the pseudo-energy. Along with the mean stream functions and their moments we also calculate spectrum of energy of the mean state and the spectrum of the pseudo-energy, whereas the pseudo-energy is given by (3.47). We calculate the energy of the mean state by, first, calculating the mean stream function using (5.2), and then calculating the the energy spectrum (energy per Fourier mode) of the Fourier transform of the result:

$$\bar{E}_{\mathbf{k}} = \frac{1}{2}|\mathbf{k}|^2|\bar{\hat{\psi}}_{\mathbf{k}}|^2. \tag{5.4}$$

The pseudo-energy spectrum is obtained by the time averaging of squared absolute value of the individual pseudo-energy variables given in (3.47):

$$p\bar{E}_{\mathbf{k}} = \frac{1}{T}\int_{T_0}^{T_0+T} |p_{\mathbf{k}}|^2 \,\mathrm{d}t. \tag{5.5}$$

The Corr functions and the scatterplots. Statistical theory predicts the linear relation (3.28) between the mean stream function and the mean potential vorticity. In order

to check that relation, we employ so-called "Corr" functions, which were suggested by Majda and Holen in [13]. The function $\mathrm{Corr}[\psi, q]$ is defined as

$$\mathrm{Corr}[\psi, q] = \frac{(\psi, q)}{\|\psi\| \cdot \|q\|}, \tag{5.6}$$

where

$$(\psi, q) = \int_S \psi q \, \mathrm{d}x \, \mathrm{d}y, \qquad \|\psi\| = \sqrt{(\psi, \psi)}.$$

As can see, the Corr function shows the extent to which ψ and q are collinear. $\mathrm{Corr}[\psi, q] = 1, -1$ if $\psi = \mathrm{const} \cdot q$.

However, we are not looking at $\mathrm{Corr}[\psi, q]$ at a given time. Instead, the arguments of the Corr function in our case are the running time averages of the stream function and potential vorticity

$$\langle \psi \rangle_\tau = \frac{1}{\tau} \int_{T_0}^{T_0+\tau} \psi \, \mathrm{d}t,$$

$$\langle q \rangle_\tau = \frac{1}{\tau} \int_{T_0}^{T_0+\tau} q \, \mathrm{d}t,$$

such that in our context

$$\mathrm{Corr}[\psi, q] = \mathrm{Corr}[\langle \psi \rangle_\tau, \langle q \rangle_\tau](\tau). \tag{5.7}$$

Thus defined Corr functions show the amount of collinearity between $\langle \psi \rangle_\tau$ and $\langle q \rangle_\tau$ as they approach the mean states $\bar{\psi}$ and $\bar{q}$.

As well as the Corr functions, we will plot the scatterplots $\bar{q}$ vs $\bar{\psi}$ which are determined by the procedure in (5.2). The scatterplots will show whether the mean state is collinear, or if not, then what it looks like.

Time correlation functions. We define the time correlation functions of the Fourier coefficients of the potential vorticity as

$$r(\mathbf{k}, \tau) = \frac{Re \int_{T_0}^{T_0+T} (\hat{q}_\mathbf{k}(t) \hat{q}^*_\mathbf{k}(t+\tau) - |\bar{\hat{q}}_\mathbf{k}|^2) dt}{\int_{T_0}^{T_0+T} (|\hat{q}_\mathbf{k}(t)|^2 - |\bar{\hat{q}}_\mathbf{k}|^2) dt}, \tag{5.8}$$

where the mean value $\bar{\hat{q}}_\mathbf{k}$ is calculated by the time averaging procedure defined in (5.2). As in (5.2), T_0 is the time we skip before proceeding with statistical calculations, T is

the averaging window. Obviously, $r(\mathbf{k}, 0) = 1$, so all correlation functions begin with 1. The rate of decay to zero shows the amount of mixing in the system, and is the numerical evidence of the ergodicity. While performing the statistical calculations, we must look at the decay of time correlation functions to see whether the time averaging window was long enough to ensure the validity of the statistical results.

Probability density functions. In order to compare the predicted mean state with the numerical result, it is useful to look at the numerically obtained probability density functions (PDF). To calculate PDF's we use the "bin-counting" which is thoroughly described in Chapter 2, Section 2.2.2.3. Here we present the probability density functions for the real parts of the Fourier components of the potential vorticity (where we use bin-counting directly), and also the spatially averaged probability density functions for q with removed mean. As we know from the Chapter 3, only the mean of q depends on the spatial coordinates, but not the higher moments, therefore the PDF's of q taken in different physical space points must have the same shape but different means. The algorithm used to obtain the PDF's is the following:

- At a given moment of time we calculate physical space potential vorticity via the Fast Fourier Transform;
- We compute the PDF of the potential vorticity at each physical space point via bin-counting;
- In the end of calculation, we remove the mean from each PDF and then average PDF's over physical space points.

Coarse-graining. The process of coarse-graining provides us with the powerful tool of distinguishing the scales on which a statistical phenomenon occurs. We recall that the spatial scaling is represented in the Fourier space by the wavenumber of the Fourier mode: the smaller is the wavenumber, the larger the spatial scale represented by this mode. Thus, in order to establish the distinction between different scales, for some of the statistical quantities we make the calculations on the two lattices of Fourier modes: the total lattice, which is of the size of the truncation, and the coarse-grained lattice, which is also centered at the origin but of smaller size. Thus we can determine the scales on which a phenomenon occurs by comparing the results obtained on total and coarse-grained lattices.

Now let us show the calculations and statistical results obtained using the traditional truncation. First we represent the basic computational parameters for our direct simulations:

- Truncation size: 11×11 and 23×23 Fourier modes (121 and 529 Fourier modes altogether, respectively);
- Coarse-grained lattice: 5×5 Fourier modes;
- Averaging window: $T = 10000$;
- Time skipped before gathering statistics: $T_0 = 1000$ for 11×11 and $T_0 = 12000$ for 23×23;
- Overall time: $T_0 + T = 11000$ for 11×11 and $T_0 + T = 22000$ for 23×23;
- Time step $\Delta t = 0.01$;
- Initial energy $E = 7$;
- Initial enstrophy $\mathcal{E} = 20$.

Next three sections show the results obtained with three different geophysical situations for the traditional truncation.

5.1 Simulations with no topography

In this section we represent the results obtained for the most simple geophysical case without topography. We perform the simulations with two different sizes of truncations. For the 11×11 size of truncation we represent the pseudo-energy spectra, "Corr" functions, correlation functions and PDF's for the potential vorticity. For the 23×23 truncation size, in addition to the above, we present the mean stream functions, their variances, skewnesses and flatnesses.

5.1.1 Mean stream functions and their moments

The equilibrium statistical theory and the maximum entropy principle establish the most probable mean state for the dynamics of the traditional truncation (3.17). Here we obtain the mean state stream functions which will later be used as a testbed for the simulation with the sine-bracket truncation. We use the equations (5.2) and (5.3) described

Total grid	
skewness	flatness
$1.936 \cdot 10^{-2}$	2.032
Coarse-grained grid	
skewness	flatness
$1.935 \cdot 10^{-2}$	2.030

Table 5.1: The spatially averaged skewness and flatness of the mean stream functions for the 23×23 traditional truncation, no topography

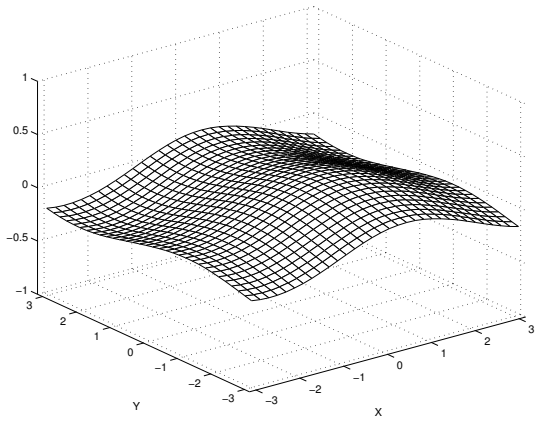

The total mean stream function for the traditional truncation, 23×23 truncation size, no topography

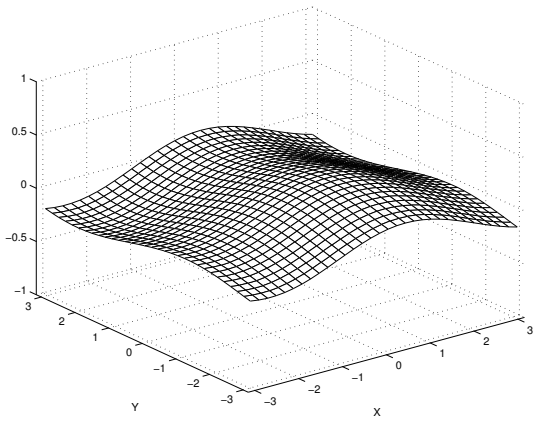

The coarse-grained mean stream function for the traditional truncation, 23×23 truncation size, no topography

Figure 5.2: The total and coarse-grained mean stream functions, 23×23 traditional truncation, no topography

in Section 5.0.3 to compute the mean stream functions and corresponding higher moments. The total and coarse-grained mean stream functions for the 23×23 size of traditional truncation (3.17) are presented in Figure 5.2. The most probable mean state is given by the statistical theory in (3.29), and is equal to zero in the absence of topography. Here we can see that the calculated mean state diverges from zero by at most ± 0.25 for both total and coarse-grained results, and thus the mean state which is predicted by the theory is confirmed well by the direct numerical simulations. The spatially averaged skewness and flatness are shown in Table 5.1. The variances for the mean stream functions are expected to be flat (do not depend on physical space coordinates), according to (3.30), and the direct numerical simulations confirm this fact within 10-15% relative error (see Figure 5.3). The skewness of the mean stream function is predicted to be zero according to the Gaussian distribution (3.26), and, as shown in Figure 5.4 and Table 5.1, it is indeed

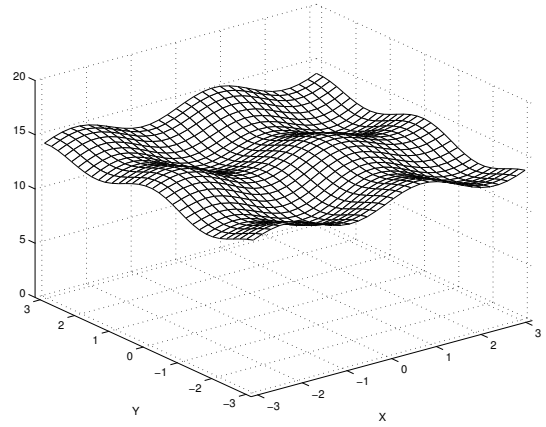

The variance of total mean stream function for the traditional truncation, 23×23 truncation size, no topography

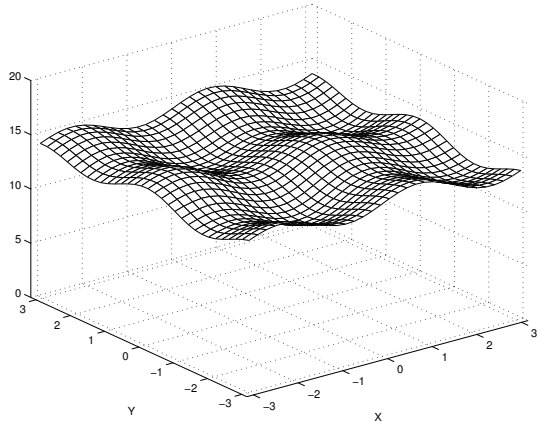

The variance of the coarse-grained mean stream function for the traditional truncation, 23×23 truncation size, no topography

Figure 5.3: The variances of the total and coarse-grained mean stream functions, 23×23 traditional truncation, no topography

very small (the averaged skewness is about 0.02). As for the flatness of the mean stream function, it should be 3 in case with the Gaussian distribution (3.26), however here it is centered at 2, as can be seen in Figure 5.5 and Table 5.1. Nonetheless, the predicted flatness does not depend on spatial coordinates, and it is confirmed by the Figure 5.5 within about 10% relative error.

Let us pay attention to the following fact: the first Fourier mode clearly dominates in the mean stream function (see Figure 5.2), whereas it should be zero as predicted. However, the explanation for this fact is the following: first, note that μ is close to -1 (Table 5.2), which is the first eigenvalue of the Laplace operator. Then, we can write the equation for the mean as

$$-(\Delta - \mu)\bar{\psi} = h. \tag{5.9}$$

Now we recall that the topography is zero on the first eigenvalue of the Laplace operator, and by the Fredholm alternative we obtain that (5.9) has a non-unique solution for the first Fourier mode. That explains the behavior of the mean stream function on the first mode.

5.1.2 The mean energy and pseudo-energy spectra

The pseudo-energy spectrum and energy of the mean spectrum calculated by the traditional truncation (3.17) are presented in Figures 5.6 and 5.7. We use the equa-

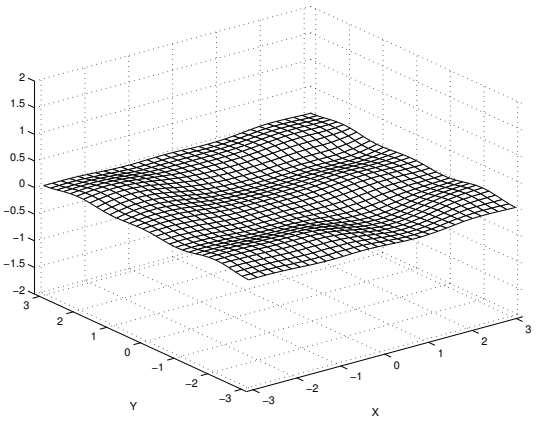

The skewness of total mean stream function for the traditional truncation, 23×23 truncation size, no topography

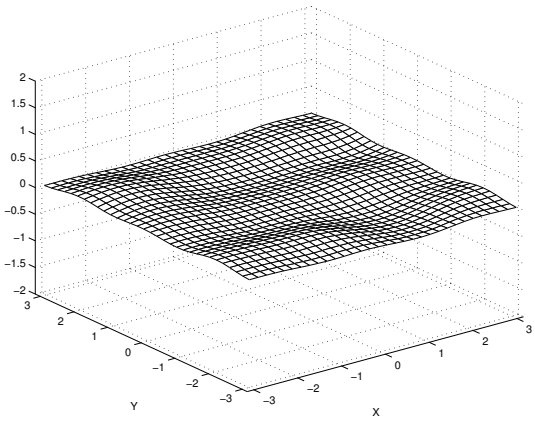

The skewness of the coarse-grained mean stream function for the traditional truncation, 23×23 truncation size, no topography

Figure 5.4: The skewness of the total and coarse-grained mean stream functions, 23×23 traditional truncation, no topography

11×11		23×23	
μ	α	μ	α
-1.065	4.984	-1.005	20.55

Table 5.2: The numerically determined parameters μ and α for the traditional truncation, no topography

tions (5.4) and (5.5) described in Section 5.0.3 to compute the mean energy and pseudo-energy spectra. In order to represent the result for the pseudo-energy in the pseudo-energy variables (3.48), we used the numerically calculated parameters μ and α which are shown in Table 5.2. According to the theoretical prediction in (3.50), the pseudo-energy should be equipartitioned in spectral space. As we can see in Figures 5.6 and 5.7, the equipartition holds very well for the pseudo-energy except for the first Fourier mode for both sizes of truncations. The discrepancy in the first Fourier mode occurs due to the fact that the numerically determined μ-parameter in (3.40) is close to -1, and therefore the factor $(\mu + |\mathbf{k}|^2)$ in the term with $|\mathbf{k}|^2 = 1$ of (3.47) is very sensitive to the numerical errors in μ. Thus, the pseudo-energy in the first Fourier mode may have significant errors. As for the rest of the pseudo-energy spectrum, the equipartition holds within 3-5% relative error, which is a very good confirmation of the statistical theory. As for the energy of the mean state, the statistical theory in (3.46a) states that in the absence of the topography it should be zero. As shown in Figures 5.6 and 5.7, the amount of energy in a single Fourier

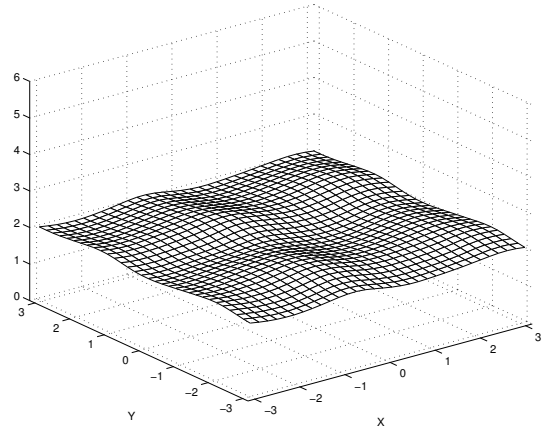

The flatness of total mean stream function for the traditional truncation, 23×23 truncation size, no topography

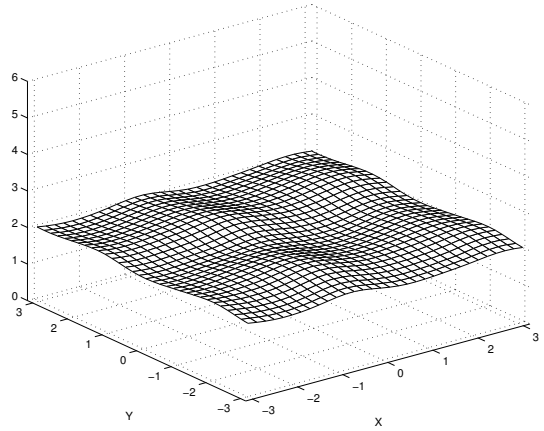

The flatness of the coarse-grained mean stream function for the traditional truncation, 23×23 truncation size, no topography

Figure 5.5: The flatness of the total and coarse-grained mean stream functions, 23×23 traditional truncation, no topography

mode does not exceed $1.2 \cdot 10^{-3}$ for the 11×11 traditional truncation, and $2.5 \cdot 10^{-3}$ for the 23×23 traditional truncation. Again, note that the error in the mean energy occurs in the first Fourier mode. If we look at the equation (3.46a), we can see that the error happens for the same reason it happens for the pseudo-energy in the first Fourier mode in case with μ close to -1. The mean energy is vanishingly small for the rest of the Fourier modes, which is very good confirmation of the statistical theory.

5.1.3 "Corr" functions and scatterplots

The total and coarse-grained Corr functions for the numerical simulations with the 11×11 and 23×23 traditional truncations (3.17) are shown in Figures 5.8 and 5.9. We use the equation (5.7) described in Section 5.0.3 to compute the Corr functions and associated scatterplots. The theoretical relation (3.28) predicts that the Corr functions must eventually converge to -1. Figures 5.8 and 5.9 show that the Corr functions are indeed very close to -1 (about -0.95 for 11×11 traditional truncation, and -0.99 for 23×23 traditional truncation), which means that the numerical mean state is very collinear. Also we can see, the Corr functions for the 23×23 traditional truncation (Figure 5.9) show more collinearity than those for 11×11 traditional truncation (Figure 5.8). This happens because the 23×23 truncation is the better approximation to the actual dynamics due to its higher resolution. Also for each truncation size the coarse-grained Corr function shows

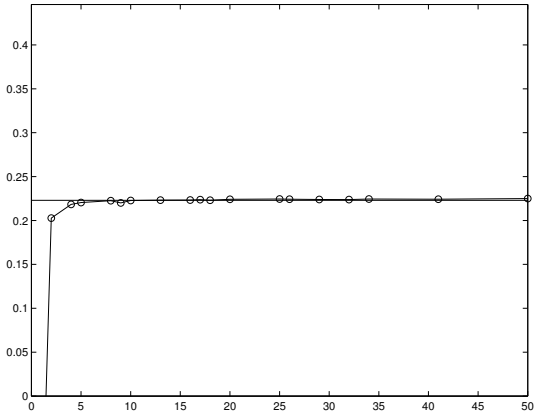

The pseudo-energy spectrum for the traditional truncation, 11×11 truncation size, no topography, horizontal line represents theoretical prediction

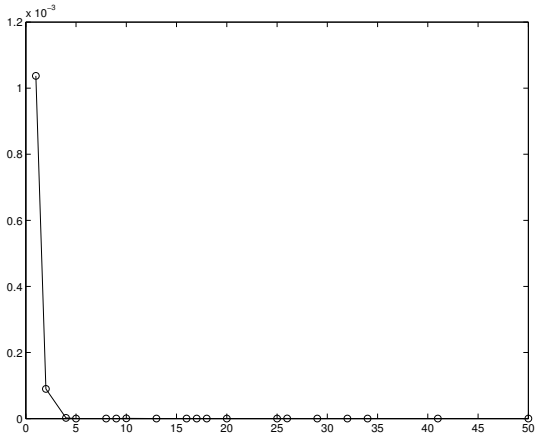

The spectrum of energy of the mean for the traditional truncation, 11×11 truncation size, no topography

Figure 5.6: The pseudo-energy spectrum and the spectrum of energy of the mean, 11×11 traditional truncation, no topography

more collinearity than the total one which means that the theory works better on large scales.

As well as Corr function, we present the scatterplots $\bar{q}$ vs $\bar{\psi}$ for all points in the physical space grid. The scatterplots are shown in Figures 5.10 and 5.11. As we can see, the scatterplots for 11×11 traditional truncation, shown in Figure 5.10, do not exhibit much of collinearity between $\bar{\psi}$ and $\bar{q}$. However, the scatterplots for 23×23 traditional truncation (Figure 5.11) indeed look collinear. The μ-parameter determined by least squares procedure is $\mu = -1.065$ for 11×11 traditional truncation and $\mu = -1.005$ for 23×23 truncation.

5.1.4 Time correlation functions

The time correlation functions (5.8) for different Fourier modes for the two truncation sizes are shown in Figures 5.12 and 5.13. We use the equation (5.8) described in Section 5.0.3 to compute the time correlation functions. As we can see, the large scales (small wavenumbers) exhibit slower rate of decay, which is typical for actual weather systems, because global climate changes take much more time than local weather fluctuations. Also we note that the rate of decay for the largest scale depends on the truncation size, unlike the rest of the wavenumbers we present. The rate of decay for the largest scale mode $|\mathbf{k}|^2 = 1$ for the 23×23 truncation (Figure 5.12) is less than that for the 11×11

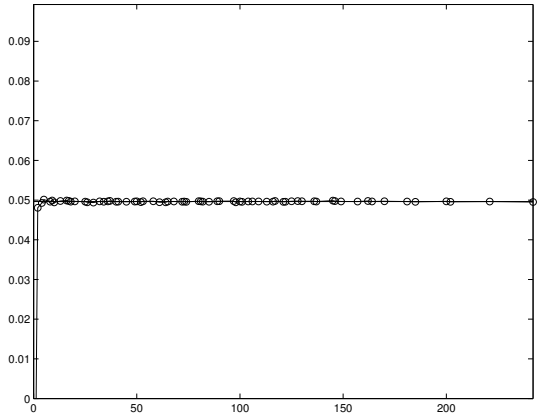

The pseudo-energy spectrum for the traditional truncation, 23×23 truncation size, no topography, horizontal line represents theoretical prediction

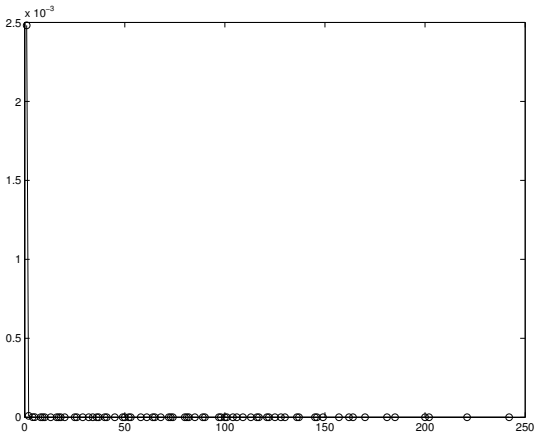

The spectrum of energy of the mean for the traditional truncation, 23×23 truncation size, no topography

Figure 5.7: The pseudo-energy spectrum and the spectrum of energy of the mean, 23×23 traditional truncation, no topography

Size	Variance	Skewness
11×11	40.02	$-5.603 \cdot 10^{-4}$
23×23	40.04	$1.142 \cdot 10^{-2}$

Table 5.3: The variance and skewness of spatially averaged probability density functions for the potential vorticity, traditional truncation with no topography

truncation (Figure 5.13). This means that the small scale resolution affects the statistical long time behavior on the large scales.

5.1.5 Probability density functions

In this section we represent the numerically computed probability density functions of the two kinds: the PDF's for the real parts of the Fourier modes of the potential vorticity, and the spatially averaged probability density functions for the potential vorticity with removed mean.

5.1.5.1 Probability density functions for the potential vorticity

We present the spatially averaged PDF with removed mean for the potential vorticity in physical space, computed with 11×11 and 23×23 traditional truncation (3.17). The numerical algorithm which was used in obtaining the PDF's in described in the Sec-

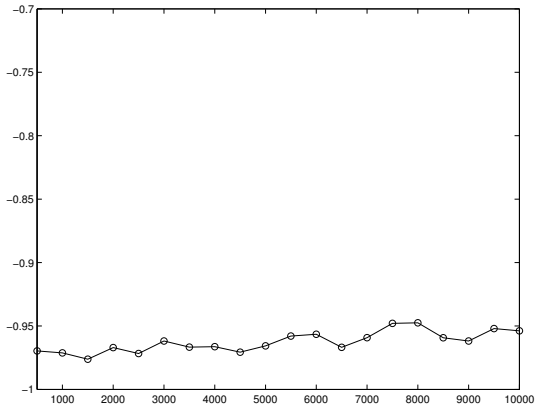

The total Corr function for the traditional truncation, 11×11 truncation size, no topography

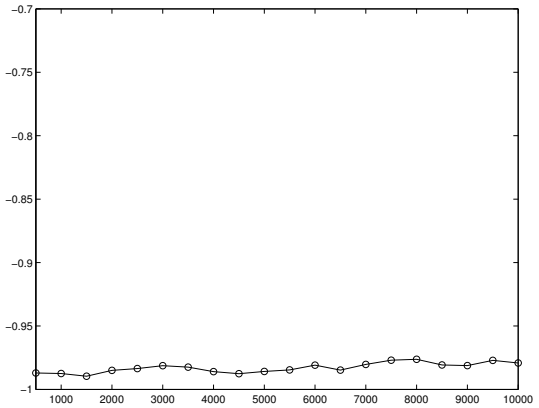

The coarse-grained Corr function for the traditional truncation, 11×11 truncation size, no topography

Figure 5.8: The total and coarse-grained Corr functions Corr$[\langle\psi\rangle_\tau, \langle q\rangle_\tau](\tau)$ for the 11×11 size traditional truncation, no topography

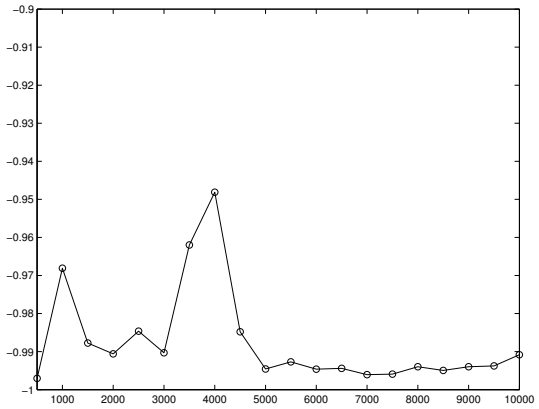

The total Corr function for the traditional truncation, 23×23 truncation size, no topography

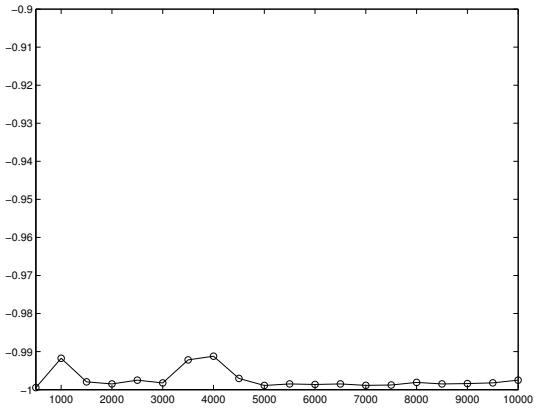

The coarse-grained Corr function for the traditional truncation, 23×23 truncation size, no topography

Figure 5.9: The total and coarse-grained Corr functions Corr$[\langle\psi\rangle_\tau, \langle q\rangle_\tau](\tau)$ for the 23×23 size traditional truncation, no topography

tion 5.0.3. Thus obtained probability density functions for the potential vorticity are represented in Figure 5.14, and their variances and skewnesses are provided in Table 5.3. As we can see, for both 11×11 and 23×23 sizes of truncations the probability density functions have a Gaussian shape, as predicted by the statistical theory in (3.26). The variances for both results are nearly equal as shown in Table 5.3, and the skewness in both cases is very close to zero. Later we will compare this result to the results obtained for the sine-bracket truncation with additional conserved quantities.

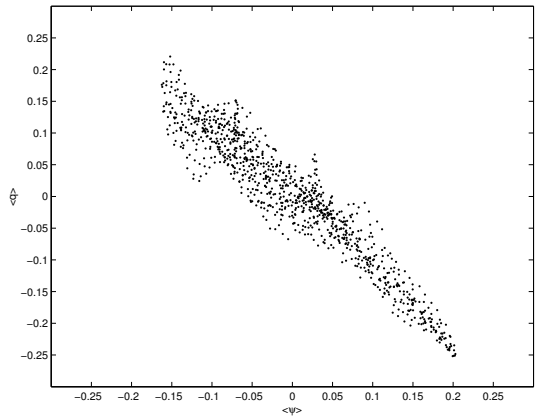

The total scatterplot $\bar{q}$ vs $\bar{\psi}$ for the traditional truncation, 11×11 truncation size, no topography

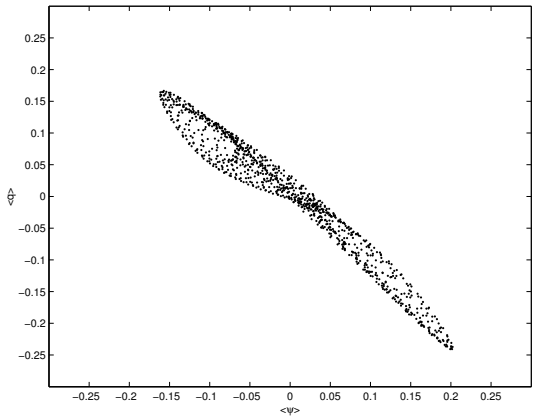

The coarse-grained scatterplot $\bar{q}$ vs $\bar{\psi}$ for the traditional truncation, 11×11 truncation size, no topography

Figure 5.10: The total and coarse-grained scatterplots $\bar{q}$ vs $\bar{\psi}$ for the 11×11 size traditional truncation, no topography

5.1.5.2 PDF's for the Fourier modes of the potential vorticity

The probability density functions for the real parts of the Fourier modes of the potential vorticity obtained with the 23×23 traditional truncation (3.17) are shown in Figures 5.15, 5.16, and 5.17. The numerical algorithm which was used in obtaining the PDF's is described in the Section 5.0.3. According to the statistical predictions (3.37), the shape of the PDF's should be Gaussian. Figure 5.15 shows that the probability density function for the large scale modes $\mathbf{k} = (0, 1)$ and $\mathbf{k} = (1, 0)$ do not have Gaussian shape, which happens due to slowly decaying correlation functions associated with these wavenumbers (see Figure 5.13). However, the rest of the Fourier modes have clearly Gaussian shape in accordance with the statistical predictions (3.37). The means and variances for PDF's of the Fourier modes for the potential vorticity are shown in Table 5.4. According to (3.42), the means for PDF's should be zero in the absence of topography, and indeed, the numerical results show the means of PDF's diverge from zero within 0.1 by their absolute value.

5.2 Simulations with random topography

In this section we represent the results obtained for the geophysical case with no largest scale topography mode (see Figure 5.1). We perform the simulations with two different sizes of truncations. For the 11×11 size of truncation we represent the pseudo-energy spectra, "Corr" functions, correlation functions and PDF's for q. For the 23×23

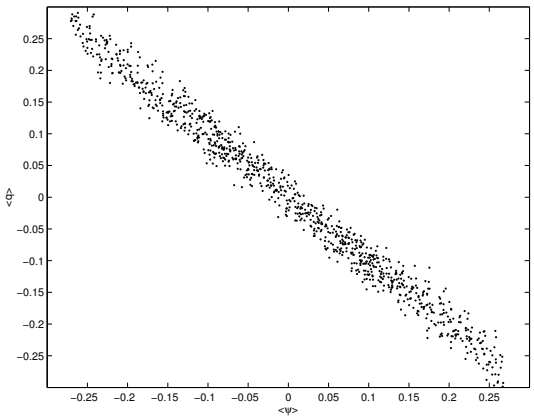

The total scatterplot $\bar{q}$ vs $\bar{\psi}$ for the traditional truncation, 23×23 truncation size, no topography

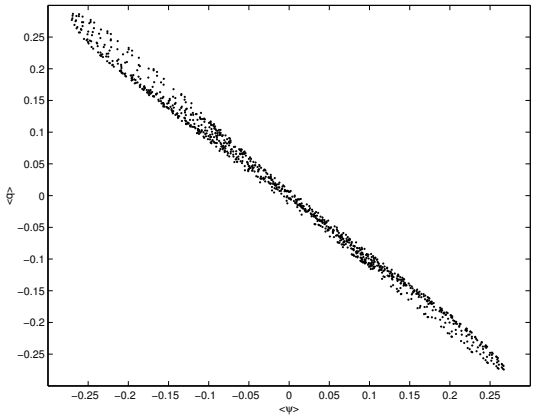

The coarse-grained scatterplot $\bar{q}$ vs $\bar{\psi}$ for the traditional truncation, 23×23 truncation size, no topography

Figure 5.11: The total and coarse-grained scatterplots $\bar{q}$ vs $\bar{\psi}$ for the 23×23 size traditional truncation, no topography

Fourier space PDF's		
Mode	Mean	Variance
$\mathbf{k} = (0, 1)$	$-1.796 \cdot 10^{-2}$	1.851
$\mathbf{k} = (1, 0)$	$-8.303 \cdot 10^{-2}$	1.823
$\mathbf{k} = (1, -1)$	$-5.221 \cdot 10^{-3}$	$4.757 \cdot 10^{-2}$
$\mathbf{k} = (1, 1)$	$2.053 \cdot 10^{-3}$	$4.900 \cdot 10^{-2}$
$\mathbf{k} = (0, 2)$	$5.642 \cdot 10^{-4}$	$3.311 \cdot 10^{-2}$
$\mathbf{k} = (2, 0)$	$-2.733 \cdot 10^{-3}$	$3.282 \cdot 10^{-2}$
$\mathbf{k} = (1, -2)$	$1.875 \cdot 10^{-3}$	$3.126 \cdot 10^{-2}$
$\mathbf{k} = (1, 2)$	$-1.304 \cdot 10^{-3}$	$3.103 \cdot 10^{-2}$
$\mathbf{k} = (2, -1)$	$6.463 \cdot 10^{-4}$	$3.123 \cdot 10^{-2}$
$\mathbf{k} = (2, 1)$	$1.870 \cdot 10^{-3}$	$3.097 \cdot 10^{-2}$
$\mathbf{k} = (2, -2)$	$-1.087 \cdot 10^{-4}$	$2.832 \cdot 10^{-2}$
$\mathbf{k} = (2, 2)$	$2.232 \cdot 10^{-3}$	$2.849 \cdot 10^{-2}$

Table 5.4: The means and variances of the PDF's of the Fourier modes for the potential vorticity, 23×23 traditional truncation, no topography

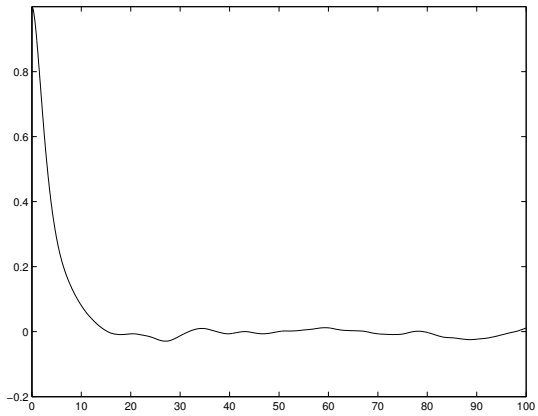

The time correlation function for the traditional truncation, $|\mathbf{k}|^2 = 1$, 11×11 truncation size, no topography

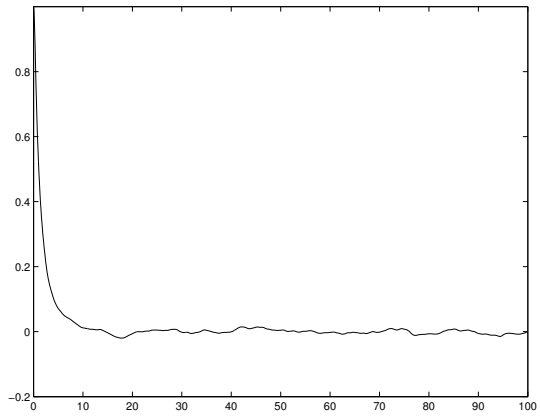

The time correlation function for the traditional truncation, $|\mathbf{k}|^2 = 2$, 11×11 truncation size, no topography

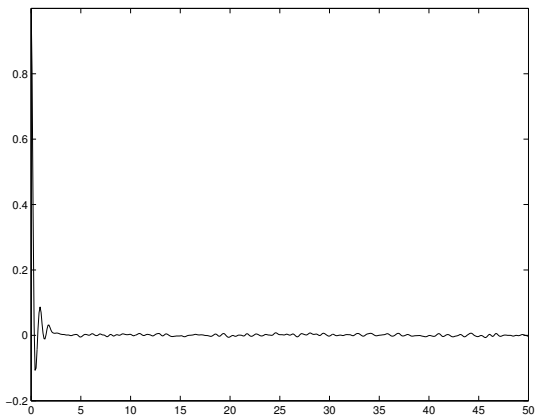

The time correlation function for the traditional truncation, $|\mathbf{k}|^2 = 8$, 11×11 truncation size, no topography

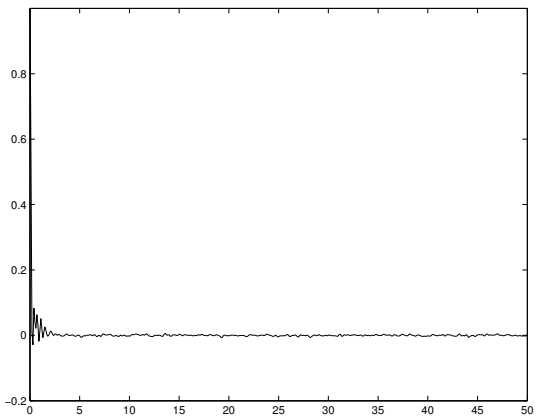

The time correlation function for the traditional truncation, $|\mathbf{k}|^2 = 16$, 11×11 truncation size, no topography

Figure 5.12: The time correlation functions for different Fourier modes for the 11×11 size traditional truncation, no topography

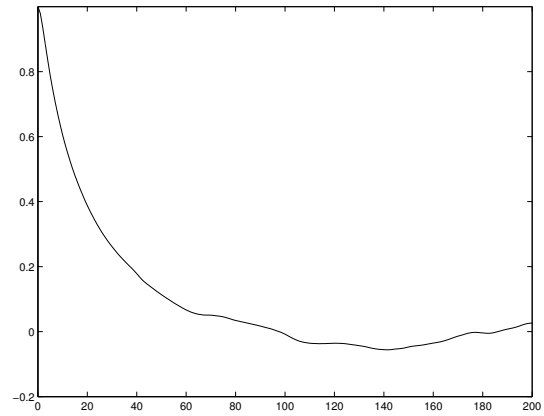

The time correlation function for the traditional truncation, $|\mathbf{k}|^2 = 1$, 23×23 truncation size, no topography

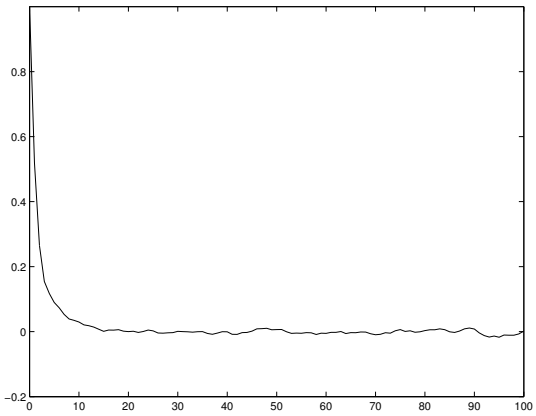

The time correlation function for the traditional truncation, $|\mathbf{k}|^2 = 2$, 23×23 truncation size, no topography

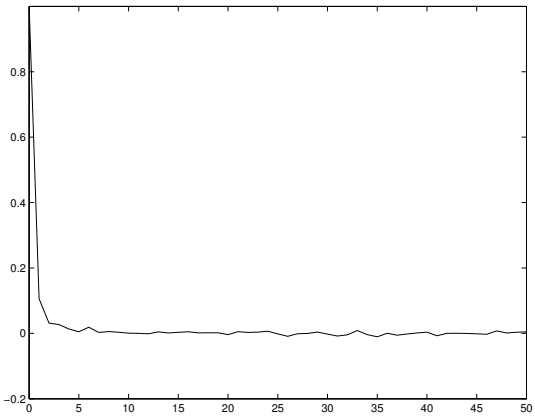

The time correlation function for the traditional truncation, $|\mathbf{k}|^2 = 8$, 23×23 truncation size, no topography

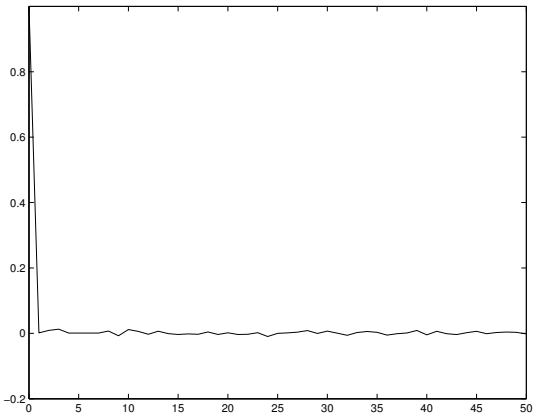

The time correlation function for the traditional truncation, $|\mathbf{k}|^2 = 16$, 23×23 truncation size, no topography

Figure 5.13: The time correlation functions for different Fourier modes for the 23×23 size traditional truncation, no topography

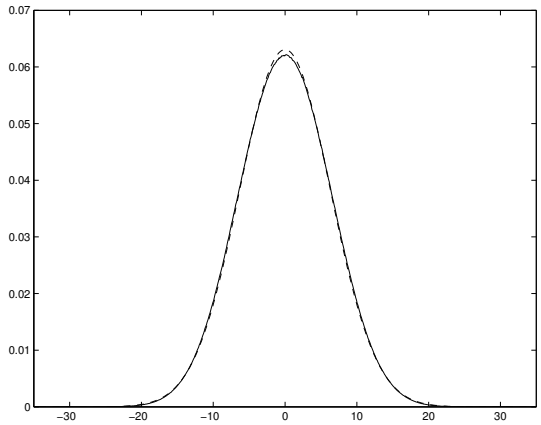

The PDF for the potential vorticity, 11×11 traditional truncation, no topography, solid line - direct numerical simulation, dashed line - analytical Gaussian with the same variance

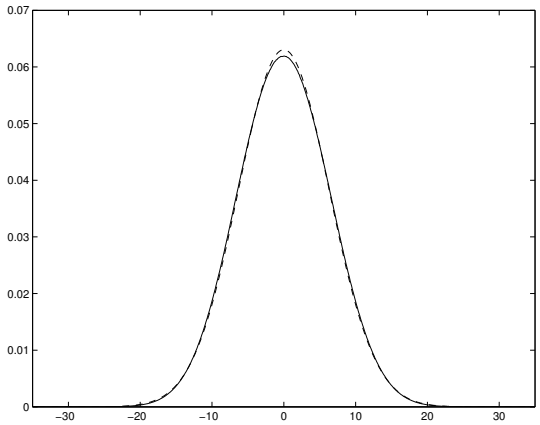

The PDF for the potential vorticity, 23×23 traditional truncation, no topography, solid line - direct numerical simulation, dashed line - analytical Gaussian with the same variance

Figure 5.14: The spatially averaged probability density functions for the potential vorticity with removed mean, no topography

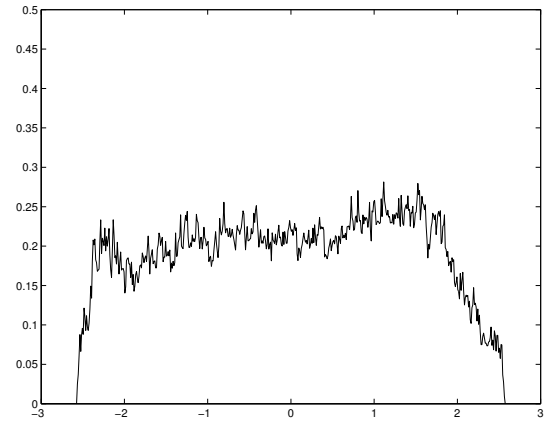

The PDF's for $\mathbf{k} = (0, 1)$, traditional truncation,
23×23 total grid, $E = 7$, $\mathcal{E} = 20$, no topography

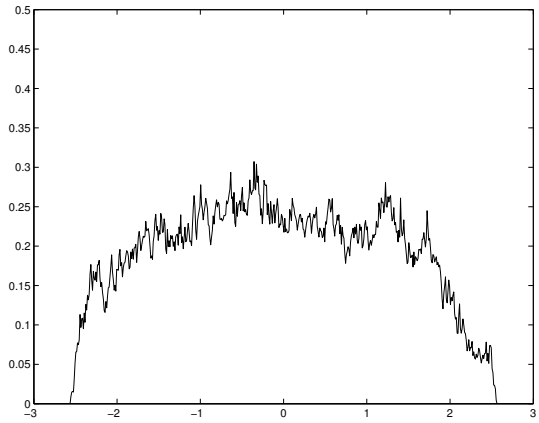

The PDF's for $\mathbf{k} = (1, 0)$, traditional truncation,
23×23 total grid, $E = 7$, $\mathcal{E} = 20$, no topography

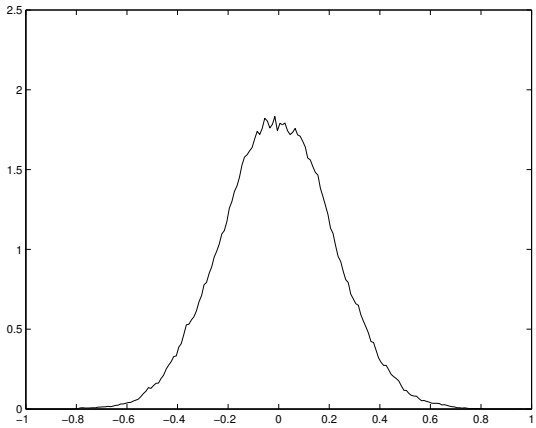

The PDF's for $\mathbf{k} = (1, -1)$, traditional truncation,
23×23 total grid, $E = 7$, $\mathcal{E} = 20$, no topography

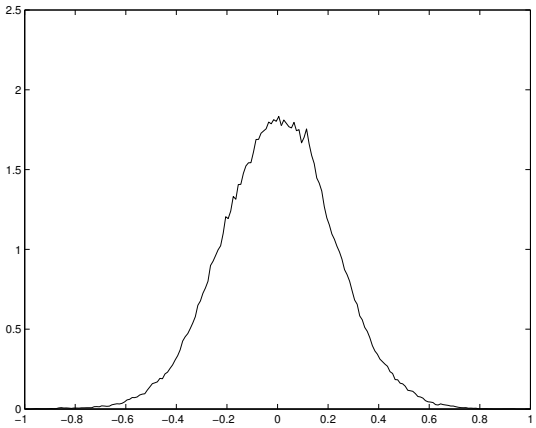

The PDF's for $\mathbf{k} = (1, 1)$, traditional truncation,
23×23 total grid, $E = 7$, $\mathcal{E} = 20$, no topography

Figure 5.15: The probability density functions for the Fourier modes of the potential vorticity, wavenumbers $(0, 1), (1, 0), (1, -1), (1, 1)$, 23×23 traditional truncation, no topography

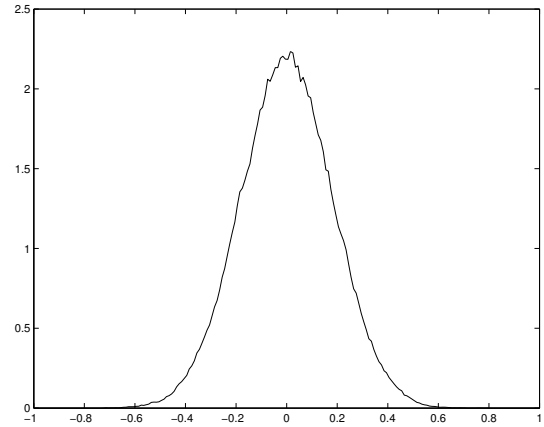

The PDF's for $\mathbf{k} = (0, 2)$, traditional truncation,
23×23 total grid, $E = 7$, $\mathcal{E} = 20$, no topography

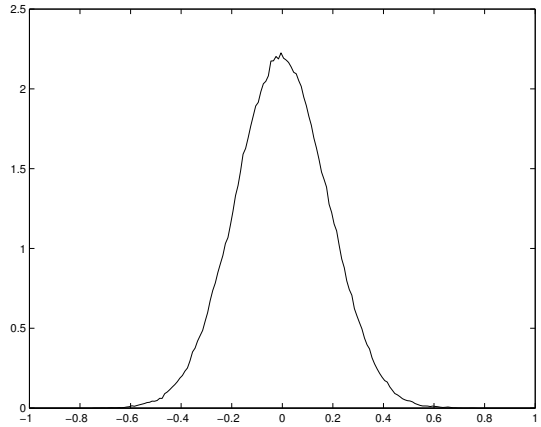

The PDF's for $\mathbf{k} = (2, 0)$, traditional truncation,
23×23 total grid, $E = 7$, $\mathcal{E} = 20$, no topography

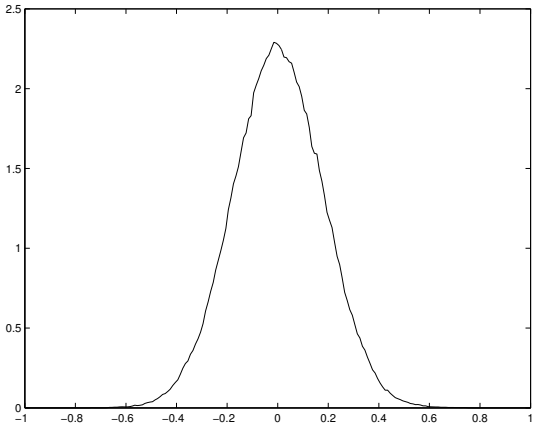

The PDF's for $\mathbf{k} = (1, -2)$, traditional truncation,
23×23 total grid, $E = 7$, $\mathcal{E} = 20$, no topography

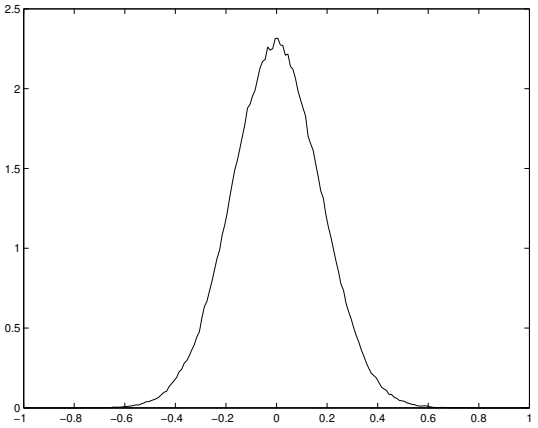

The PDF's for $\mathbf{k} = (1, 2)$, traditional truncation,
23×23 total grid, $E = 7$, $\mathcal{E} = 20$, no topography

Figure 5.16: The probability density functions for the Fourier modes of the potential vorticity, wavenumbers $(0, 2), (2.0), (1, -2), (1, 2)$, 23×23 traditional truncation, no topography

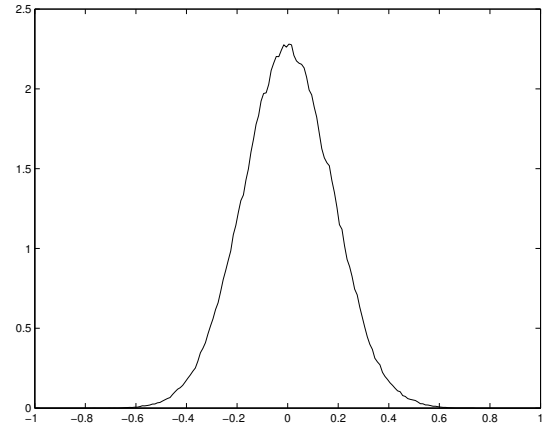

The PDF's for $\mathbf{k} = (2, -1)$, traditional truncation,
23×23 total grid, $E = 7$, $\mathcal{E} = 20$, no topography

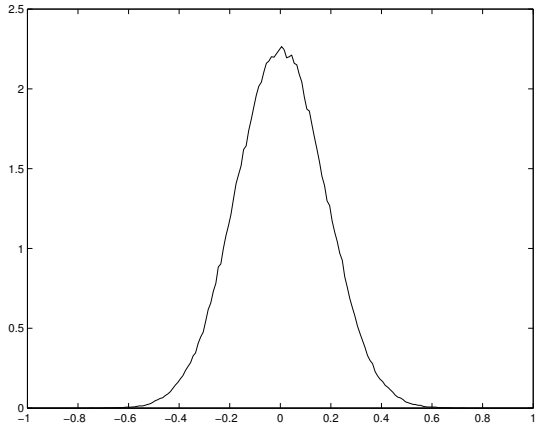

The PDF's for $\mathbf{k} = (2, 1)$, traditional truncation,
23×23 total grid, $E = 7$, $\mathcal{E} = 20$, no topography

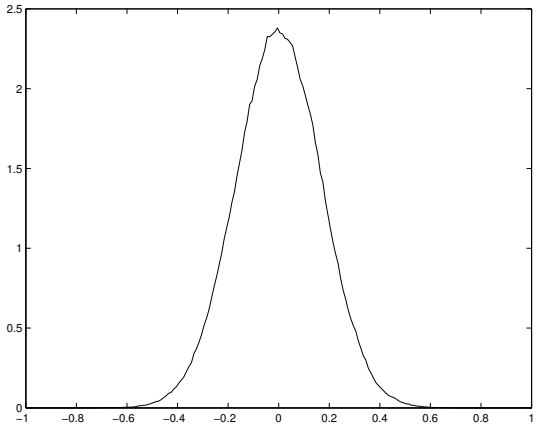

The PDF's for $\mathbf{k} = (2, -2)$, traditional truncation,
23×23 total grid, $E = 7$, $\mathcal{E} = 20$, no topography

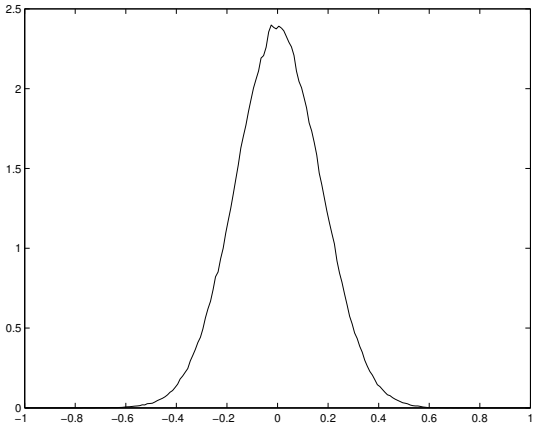

The PDF's for $\mathbf{k} = (2, 2)$, traditional truncation,
23×23 total grid, $E = 7$, $\mathcal{E} = 20$, no topography

Figure 5.17: The probability density functions for the Fourier modes of the potential vorticity, wavenumbers $(2, -1), (2.1), (2, -2), (2, 2)$, 23×23 traditional truncation, no topography

Total grid	
skewness	flatness
$6.61 \cdot 10^{-3}$	2.007
Coarse-grained grid	
skewness	flatness
$6.616 \cdot 10^{-3}$	2.004

Table 5.5: The spatially averaged skewness and flatness of the mean stream functions for the 23×23 traditional truncation, random topography

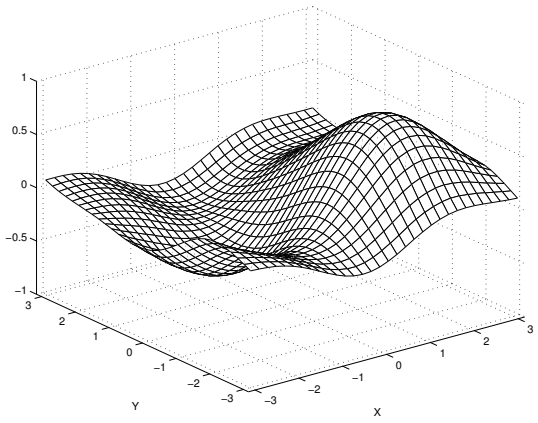

The total mean stream function for the traditional truncation, 23×23 truncation size, random topography

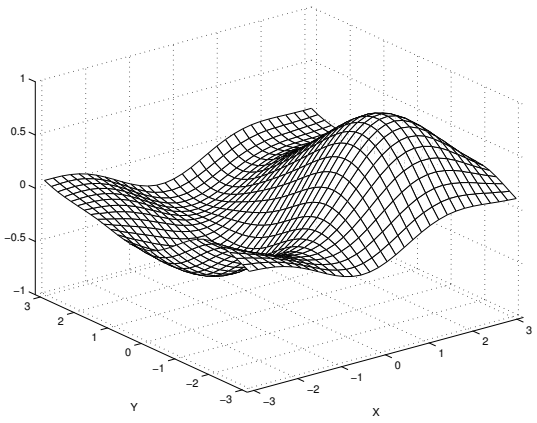

The coarse-grained mean stream function for the traditional truncation, 23×23 truncation size, random topography

Figure 5.18: The total and coarse-grained mean stream functions, 23×23 traditional truncation, random topography

truncation size, in addition to the above, we present the mean stream functions, their variances, skewnesses and flatnesses.

5.2.1 Mean stream functions and their moments

The equilibrium statistical theory and the maximum entropy principle establish the most probable mean state for the dynamics of the traditional truncation. Here we obtain the mean state stream functions which will later be used as a testbed for the simulation with the sine-bracket truncation. The total and coarse-grained mean stream functions for the 23×23 size of traditional truncation (3.17) are presented in Figure 5.18. We use the equations (5.2) and (5.3) described in Section 5.0.3 to compute the mean stream function and its moments. The most probable mean state is given by the statistical theory in (3.29). Here however, the topography is random, and all we know about it is that it

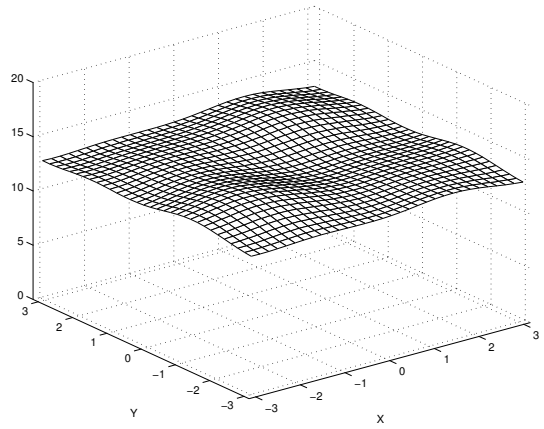

The variance of total mean stream function for the traditional truncation, 23×23 truncation size, random topography

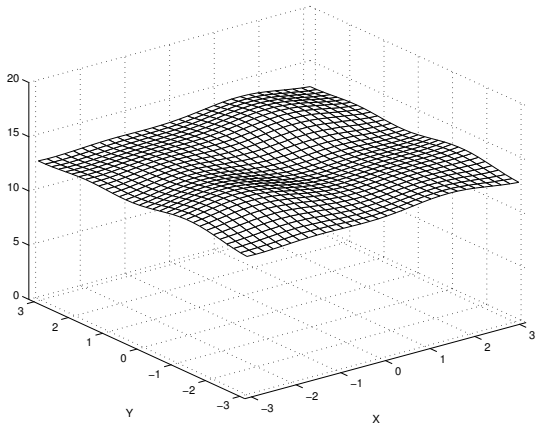

The variance of the coarse-grained mean stream function for the traditional truncation, 23×23 truncation size, random topography

Figure 5.19: The variances of the total and coarse-grained mean stream functions, 23×23 traditional truncation, random topography

has no Fourier component in the large scale mode $|\mathbf{k}|^2 = 1$. Here, however, we can see that the large scale mode $|\mathbf{k}|^2 = 1$ is the prevailing mode in the mean stream function, which occurs due to the reasons described in the Section 5.1.1 (when μ is close to -1). The spatially averaged skewness and flatness are shown in Table 5.5. The variances for the mean stream functions are expected to be flat according to (3.30), and the direct numerical simulations confirm this fact within 5-8% relative error (see Figure 5.19). The skewness of the mean stream function is predicted to be zero according to the Gaussian distribution (3.26), and, as shown in Figure 5.20 and Table 5.5, it is indeed very small (the averaged skewness is about 0.007). As for the flatness of the mean stream function, it should be 3 in case with the Gaussian distribution (3.26), however here it is centered at 2, as can be seen in Figure 5.21 and Table 5.5. Nonetheless, the predicted flatness does not depend on spatial coordinates, and it is confirmed by the Figure 5.21 within about 5% relative error.

5.2.2 The mean energy and pseudo-energy spectra

The pseudo-energy spectrum and energy of the mean spectrum calculated by the traditional truncation (3.17) are presented in Figures 5.22 and 5.23. We use the equations (5.4) and (5.5) described in Section 5.0.3 to compute the mean energy and pseudo-energy spectra. In order to represent the result for the pseudo-energy in the pseudo-energy

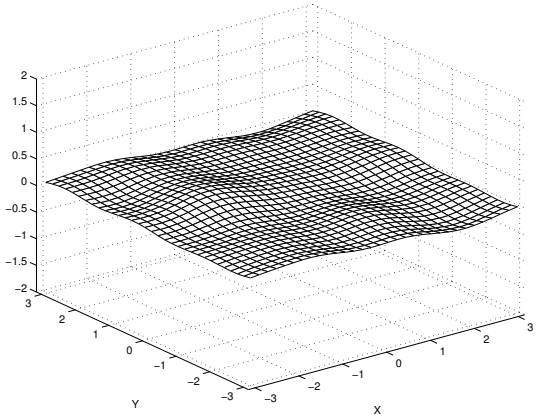

The skewness of total mean stream function for the traditional truncation, 23×23 truncation size, random topography

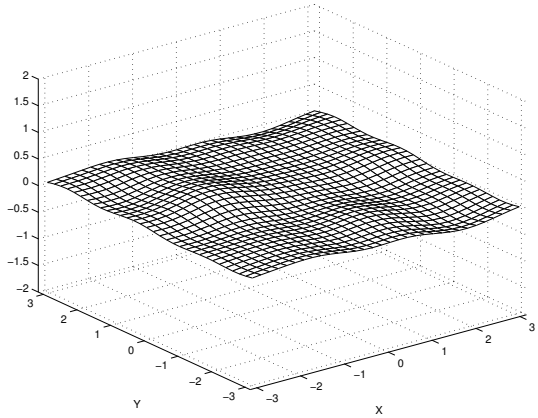

The skewness of the coarse-grained mean stream function for the traditional truncation, 23×23 truncation size, random topography

Figure 5.20: The skewness of the total and coarse-grained mean stream functions, 23×23 traditional truncation, random topography

11×11		23×23	
μ	α	μ	α
-0.9898	4.665	-0.9918	20.26

Table 5.6: The numerically determined parameters μ and α for the traditional truncation, random topography

variables (3.48), we used the numerically calculated parameters μ and α which are shown in Table 5.6. According to the theoretical prediction in (3.50), the pseudo-energy should be equipartitioned in spectral space. As we can see in Figures 5.22 and 5.23, the equipartition holds very well for the pseudo-energy except for the first Fourier mode for both sizes of truncations. The reasons for such behavior of the pseudo-energy is explained in the Section 5.1.2. As for the rest of the pseudo-energy spectrum, the equipartition holds within 3-5% relative error, which is a very good confirmation of the statistical theory. As for the energy of the mean state, the statistical theory in (3.46a) states that it should be zero in the modes with no topography. As shown in Figures 5.22 and 5.23, there is a considerable amount of energy in the Fourier modes $|\mathbf{k}|^2 = 2$ and $|\mathbf{k}|^2 = 4$, precisely where topography is, and this is confirmed by the statistical theory in (3.46a). However, we can see a lot of energy in the 23×23 traditional truncation simulation in the first Fourier mode (Figure 5.23). Again, note that the error in the mean energy occurs in the first Fourier mode. The reasons for such behavior are given in the Section 5.1.2. The mean energy is

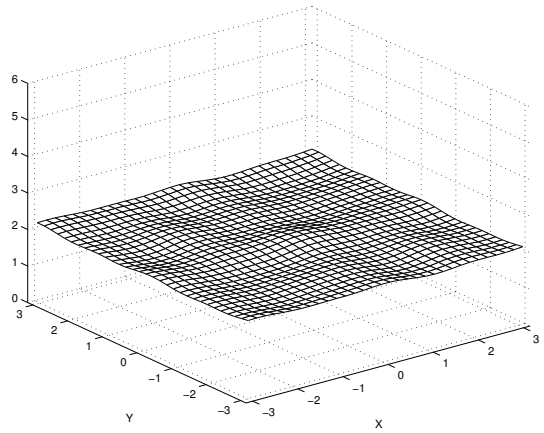

The flatness of total mean stream function for the traditional truncation, 23×23 truncation size, random topography

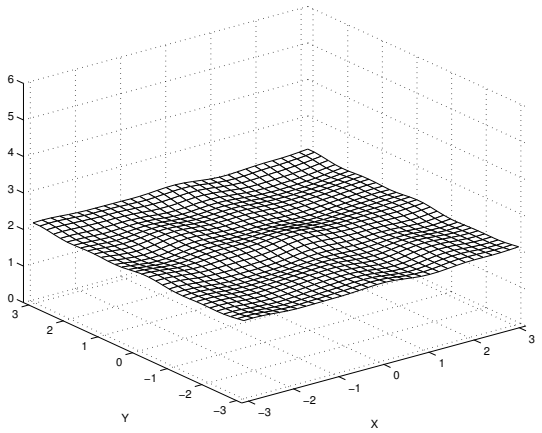

The flatness of the coarse-grained mean stream function for the traditional truncation, 23×23 truncation size, random topography

Figure 5.21: The flatness of the total and coarse-grained mean stream functions, 23×23 traditional truncation, random topography

vanishingly small for the rest of the Fourier modes, which is very good confirmation of the statistical theory.

5.2.3 "Corr" functions and scatterplots

The total and coarse-grained Corr functions for the numerical simulations with the 11×11 and 23×23 traditional truncations (3.17) are shown in Figures 5.24 and 5.25. We use the equation (5.7) described in Section 5.0.3 to compute the Corr functions and associated scatterplots. The theoretical relation (3.28) predicts that the Corr functions must eventually converge to -1. Figures 5.24 and 5.25 show that the Corr functions are indeed very close to -1, which means that the numerical mean state is very collinear. Also we can see, the Corr functions for the 23×23 traditional truncation (Figure 5.25) show more collinearity than those for 11×11 traditional truncation (Figure 5.25). This happens because the 23×23 truncation is the better approximation to the actual dynamics due to its higher resolution. Also for each truncation size the coarse-grained Corr function shows more collinearity than the total one which means that the theory works better on large scales. As well as Corr function, we present the scatterplots $\bar{q}$ vs $\bar{\psi}$ for all points in the physical space grid. The scatterplots are shown in Figures 5.26 and 5.27. As we can see, the scatterplots for 11×11 traditional truncation, shown in Figure 5.26, exhibit more collinearity between $\bar{\psi}$ and $\bar{q}$ in comparison with the results for the 11×11

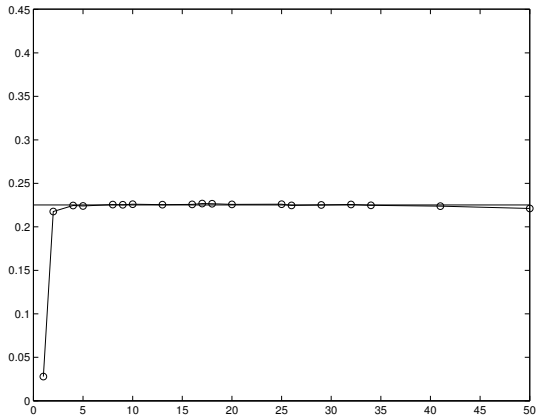

The pseudo-energy spectrum for the traditional truncation, 11×11 truncation size, random topography, horizontal line represents theoretical prediction

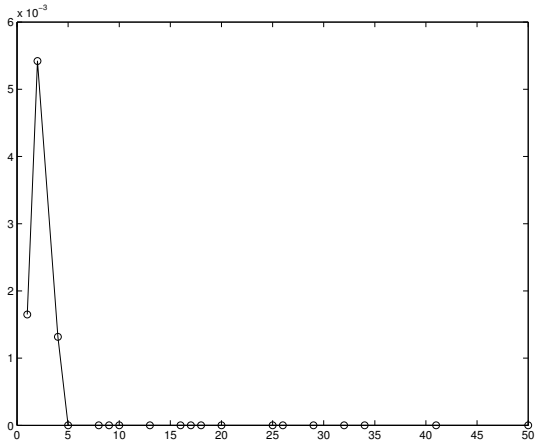

The spectrum of energy of the mean for the traditional truncation, 11×11 truncation size, random topography

Figure 5.22: The pseudo-energy spectrum and the spectrum of energy of the mean, 11×11 traditional truncation, random topography

traditional truncation with no topography (Figure 5.10). The scatterplots for 23×23 traditional truncation (Figure 5.27) look very collinear, and exhibit more collinearity than the corresponding scatterplots for the 23×23 traditional truncation with no topography (Figure 5.11). The μ-parameter determined by least squares procedure is $\mu = -0.9898$ for 11×11 traditional truncation and $\mu = -0.9918$ for 23×23 truncation.

5.2.4 Time correlation functions

The time correlation functions (5.8) for different Fourier modes for the two truncation sizes is shown in Figures 5.28 and 5.29. We use the equation (5.8) described in Section 5.0.3 to compute the time correlation functions. As we can see, the large scales (small wavenumbers) exhibit slower rate of decay, which is typical for actual weather systems, because global climate changes take much more time than local weather fluctuations. Also we note that the rate of decay for the largest scale depends on the truncation size, unlike the rest of the wavenumbers we present. The rate of decay for the largest scale mode $|\mathbf{k}|^2 = 1$ for the 23×23 truncation (Figure 5.28) is less than that for the 11×11 truncation (Figure 5.29). This means that the small scale resolution affects the statistical long time behavior on the large scales. Overall, the behavior of the correlation functions in this case barely differs from the case with no topography (Figures 5.12 and 5.13).

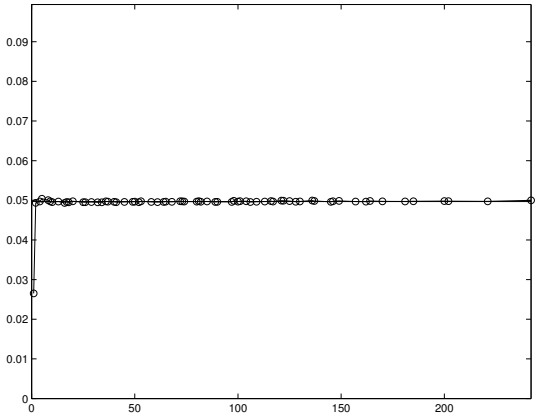

The pseudo-energy spectrum for the traditional truncation, 23×23 truncation size, random topography, horizontal line represents theoretical prediction

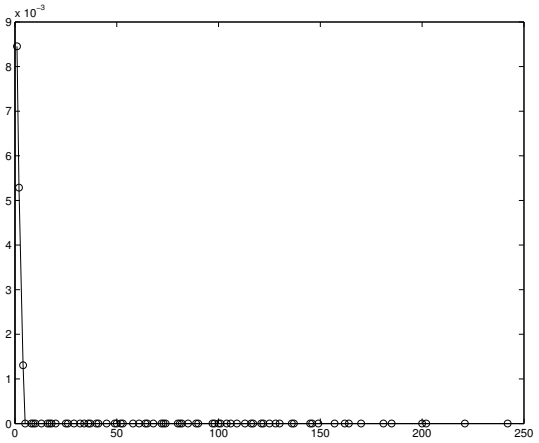

The spectrum of energy of the mean for the traditional truncation, 23×23 truncation size, random topography

Figure 5.23: The pseudo-energy spectrum and the spectrum of energy of the mean, 23×23 traditional truncation, random topography

Size	Variance	Skewness
11×11	40.09	$1.062 \cdot 10^{-3}$
23×23	40.22	$8.871 \cdot 10^{-5}$

Table 5.7: The variance and skewness of spatially averaged probability density functions for the potential vorticity, traditional truncation with random topography

5.2.5 Probability density functions

In this section we represent the numerically computed probability density functions of the two kinds: the PDF's for the real parts of the Fourier modes of the potential vorticity, and the spatially averaged probability density functions for the potential vorticity with removed mean.

5.2.5.1 Probability density functions for the potential vorticity

We present the spatially averaged PDF with removed mean for the potential vorticity in physical space, computed with 11×11 and 23×23 traditional truncation (3.17). The numerical algorithm which was used in obtaining the PDF's in described in the Section 5.0.3. Thus obtained probability density functions for the potential vorticity are represented in Figure 5.30, and their variances and skewnesses are provided in Table 5.7. As we can see, for both 11×11 and 23×23 sizes of truncations the probability density

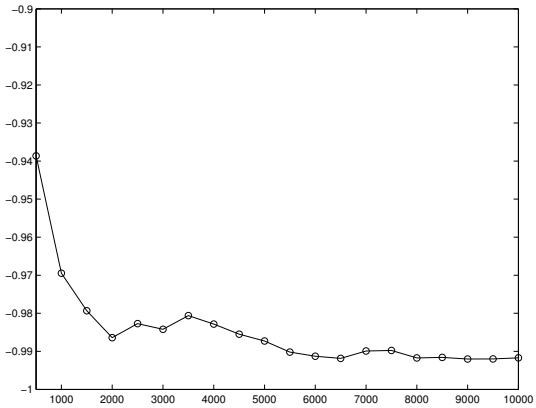

The total Corr function for the traditional truncation, 11×11 truncation size, random topography

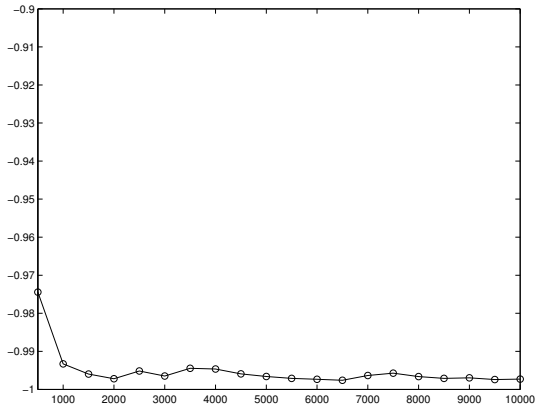

The coarse-grained Corr function for the traditional truncation, 11×11 truncation size, random topography

Figure 5.24: The total and coarse-grained Corr functions Corr$[\langle\psi\rangle_\tau, \langle q\rangle_\tau](\tau)$ for the 11×11 size traditional truncation, random topography

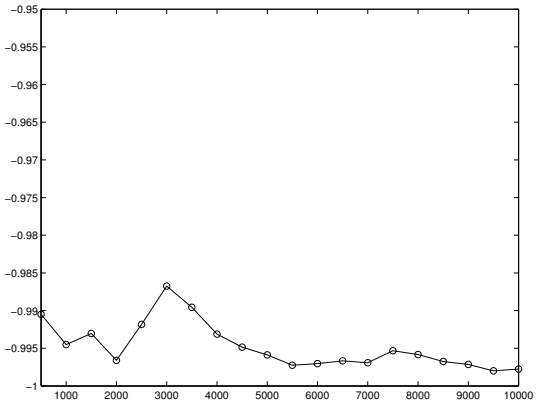

The total Corr function for the traditional truncation, 23×23 truncation size, random topography

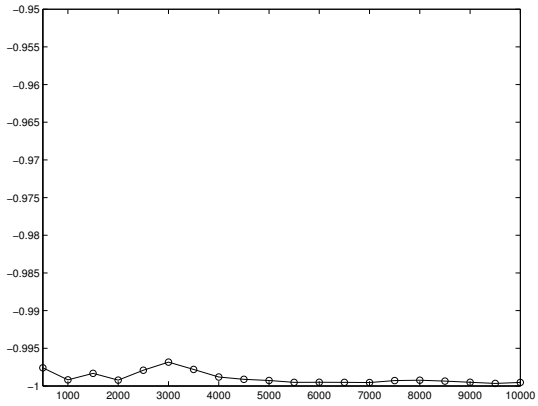

The coarse-grained Corr function for the traditional truncation, 23×23 truncation size, random topography

Figure 5.25: The total and coarse-grained Corr functions Corr$[\langle\psi\rangle_\tau, \langle q\rangle_\tau](\tau)$ for the 23×23 size traditional truncation, random topography

functions have a Gaussian shape, as predicted by the statistical theory in (3.26). The variances for both results are nearly equal as shown in Table 5.7, and the skewness in both cases is very close to zero. Later we will compare this result to the results obtained for the sine-bracket truncation with additional conserved quantities.

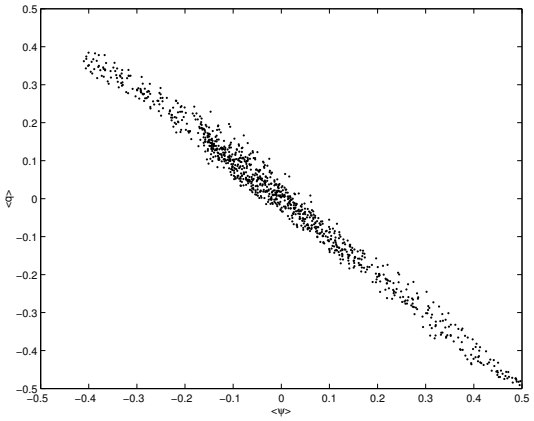

The total scatterplot $\bar{q}$ vs $\bar{\psi}$ for the traditional truncation, 11×11 truncation size, random topography

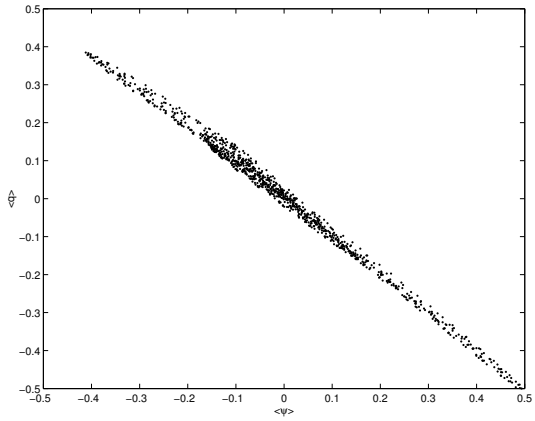

The coarse-grained scatterplot $\bar{q}$ vs $\bar{\psi}$ for the traditional truncation, 11×11 truncation size, random topography

Figure 5.26: The total and coarse-grained scatterplots $\bar{q}$ vs $\bar{\psi}$ for the 11×11 size traditional truncation, random topography

5.2.5.2 PDF's for the Fourier modes of the potential vorticity

The probability density functions for the real parts of the Fourier modes of the potential vorticity obtained with the 23×23 traditional truncation (3.17) are shown in Figures 5.31, 5.32, and 5.33. The numerical algorithm which was used in obtaining the PDF's is described in the Section 5.0.3. According to the statistical predictions (3.37), the shape of the PDF's should be Gaussian. Figure 5.31 shows that the probability density function for the large scale modes $\mathbf{k} = (0, 1)$ and $\mathbf{k} = (1, 0)$ do not have Gaussian shape, which happens due to slowly decaying correlation functions associated with these wavenumbers (see Figure 5.29). However, the rest of the Fourier modes have clearly Gaussian shape in accordance with the statistical predictions (3.37). The means and variances for PDF's of the Fourier modes for the potential vorticity are shown in Table 5.8. According to (3.42), the means for PDF's should be zero in the absence of topography, and indeed, the numerical results show the means of PDF's are very close to zero except for those associated with the modes $|\mathbf{k}| = (1, -1), (1, 1), (2, 0), (0.2)$, i.e. for $|\mathbf{k}|^2 = 2, 4$, exactly where the topography is.

5.3 Simulations with layered topography

In this section we represent the results obtained for the geophysical case with layered topography (5.1) and the traditional truncation (3.17). We perform the simulations with two different sizes of truncations. For the 11×11 size of truncation we represent the

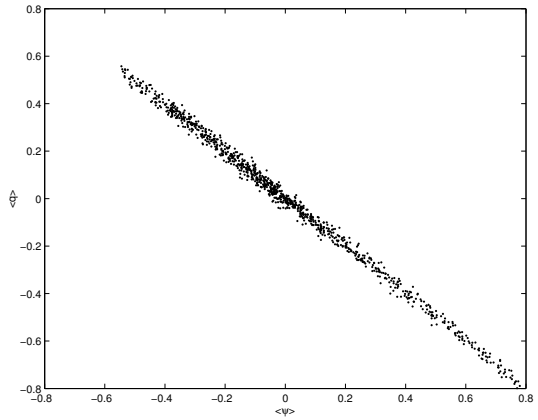

The total scatterplot $\bar{q}$ vs $\bar{\psi}$ for the traditional truncation, 23×23 truncation size, random topography

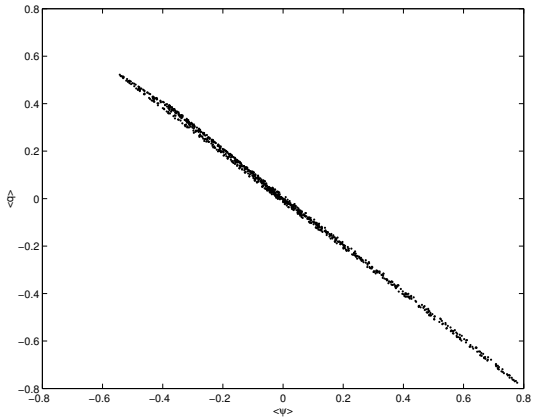

The coarse-grained scatterplot $\bar{q}$ vs $\bar{\psi}$ for the traditional truncation, 23×23 truncation size, random topography

Figure 5.27: The total and coarse-grained scatterplots $\bar{q}$ vs $\bar{\psi}$ for the 23×23 size traditional truncation, random topography

Fourier space PDF's		
Mode	Mean	Variance
$\mathbf{k} = (0, 1)$	$1.296 \cdot 10^{-2}$	1.587
$\mathbf{k} = (1, 0)$	$1.523 \cdot 10^{-2}$	1.694
$\mathbf{k} = (1, -1)$	$1.368 \cdot 10^{-2}$	$4.945 \cdot 10^{-2}$
$\mathbf{k} = (1, 1)$	$-6.528 \cdot 10^{-2}$	$4.912 \cdot 10^{-2}$
$\mathbf{k} = (0, 2)$	$2.154 \cdot 10^{-2}$	$3.256 \cdot 10^{-2}$
$\mathbf{k} = (2, 0)$	$1.706 \cdot 10^{-2}$	$3.286 \cdot 10^{-2}$
$\mathbf{k} = (1, -2)$	$-1.477 \cdot 10^{-3}$	$3.161 \cdot 10^{-2}$
$\mathbf{k} = (1, 2)$	$-1.123 \cdot 10^{-4}$	$3.171 \cdot 10^{-2}$
$\mathbf{k} = (2, -1)$	$1.132 \cdot 10^{-3}$	$3.093 \cdot 10^{-2}$
$\mathbf{k} = (2, 1)$	$-4.992 \cdot 10^{-4}$	$3.125 \cdot 10^{-2}$
$\mathbf{k} = (2, -2)$	$8.712 \cdot 10^{-4}$	$2.866 \cdot 10^{-2}$
$\mathbf{k} = (2, 2)$	$-3.678 \cdot 10^{-4}$	$2.850 \cdot 10^{-2}$

Table 5.8: The means and variances of the PDF's of the Fourier modes for the potential vorticity, 23×23 traditional truncation, random topography

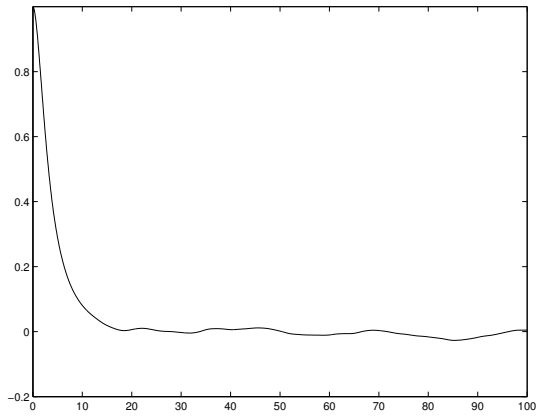

The time correlation function for the traditional truncation, $|\mathbf{k}|^2 = 1$, 11×11 truncation size, random topography

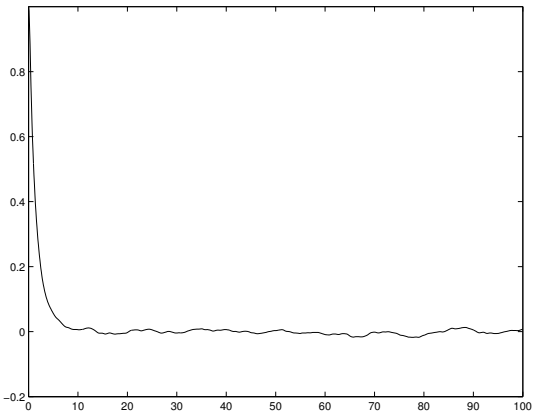

The time correlation function for the traditional truncation, $|\mathbf{k}|^2 = 2$, 11×11 truncation size, random topography

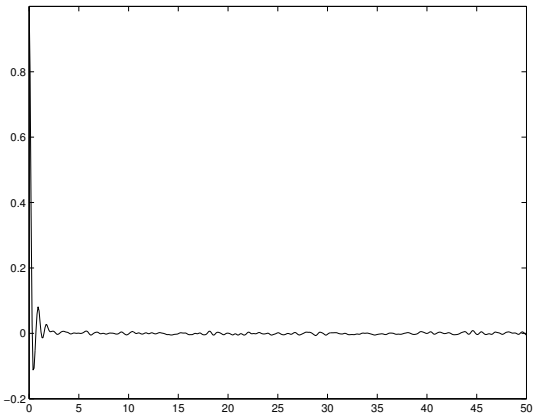

The time correlation function for the traditional truncation, $|\mathbf{k}|^2 = 8$, 11×11 truncation size, random topography

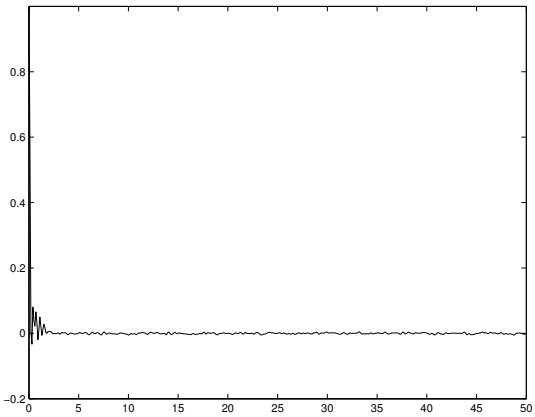

The time correlation function for the traditional truncation, $|\mathbf{k}|^2 = 16$, 11×11 truncation size, random topography

Figure 5.28: The time correlation functions for different Fourier modes for the 11×11 size traditional truncation, random topography

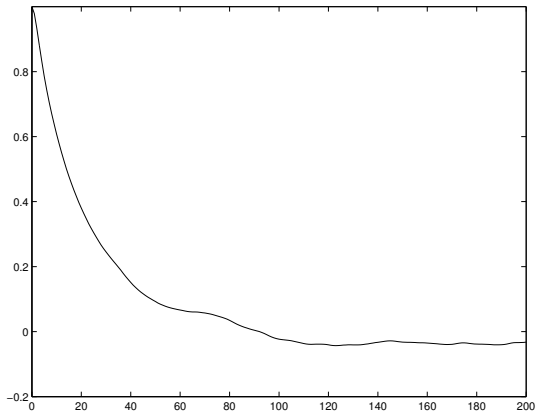

The time correlation function for the traditional truncation, $|\mathbf{k}|^2 = 1$, 23×23 truncation size, random topography

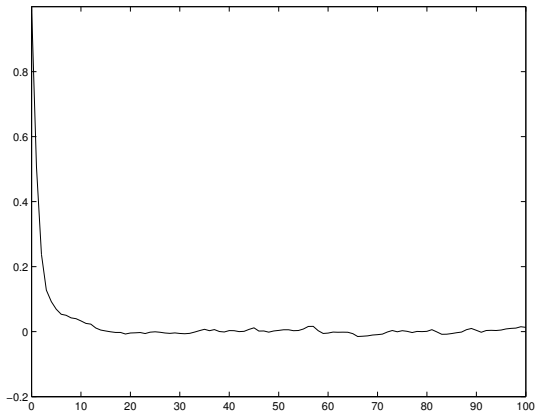

The time correlation function for the traditional truncation, $|\mathbf{k}|^2 = 2$, 23×23 truncation size, random topography

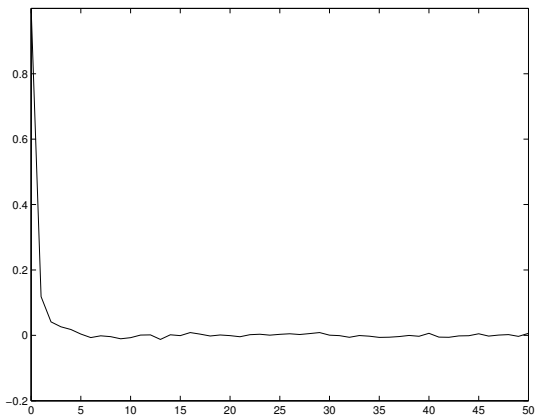

The time correlation function for the traditional truncation, $|\mathbf{k}|^2 = 8$, 23×23 truncation size, random topography

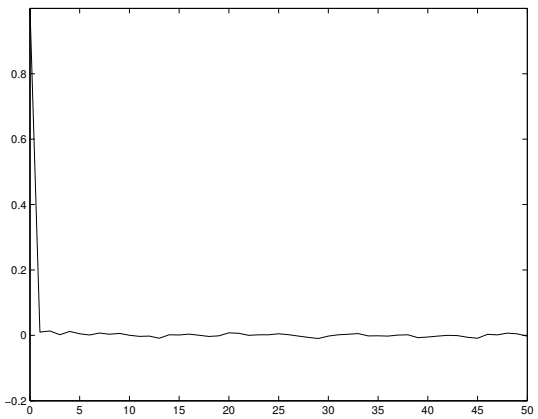

The time correlation function for the traditional truncation, $|\mathbf{k}|^2 = 16$, 23×23 truncation size, random topography

Figure 5.29: The time correlation functions for different Fourier modes for the 23×23 size traditional truncation, random topography

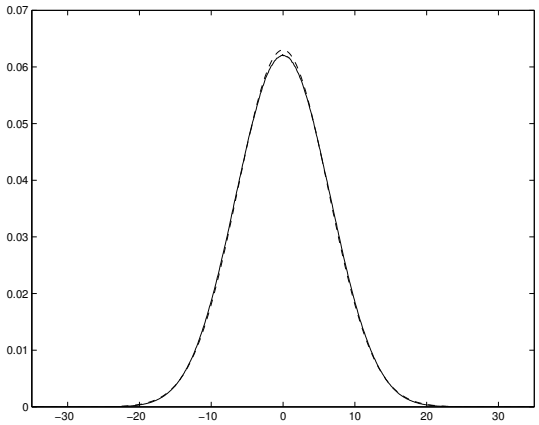

The PDF for the potential vorticity, 11×11 traditional truncation, random topography, solid line - direct numerical simulation, dashed line - analytical Gaussian with the same variance

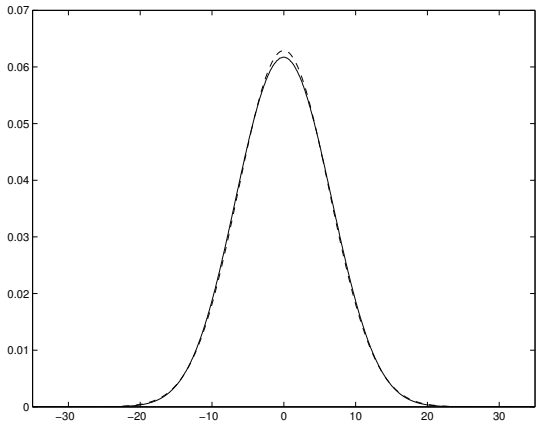

The PDF for the potential vorticity, 23×23 traditional truncation, random topography, solid line - direct numerical simulation, dashed line - analytical Gaussian with the same variance

Figure 5.30: The spatially averaged probability density functions for the potential vorticity with removed mean, random topography

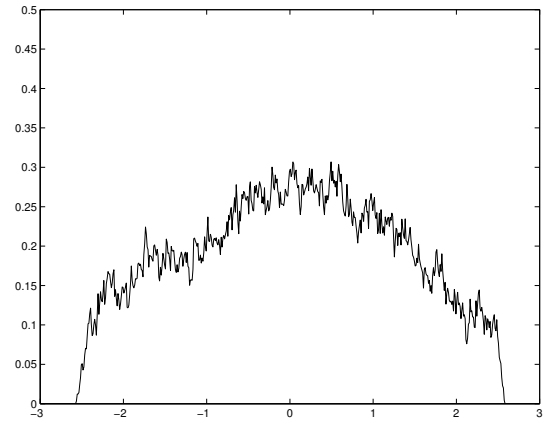

The PDF's for $\mathbf{k} = (0, 1)$, traditional truncation,
23×23 total grid, $E = 7$, $\mathcal{E} = 20$, random topography

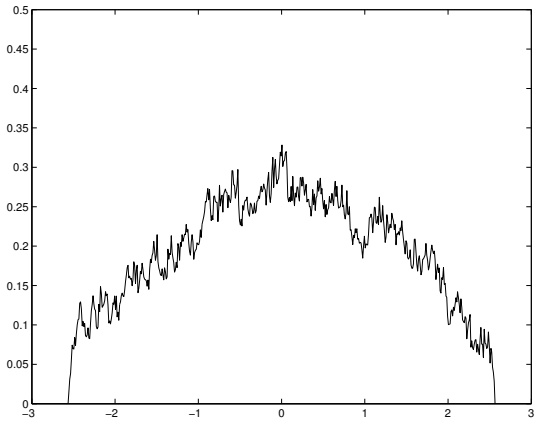

The PDF's for $\mathbf{k} = (1, 0)$, traditional truncation,
23×23 total grid, $E = 7$, $\mathcal{E} = 20$, random topography

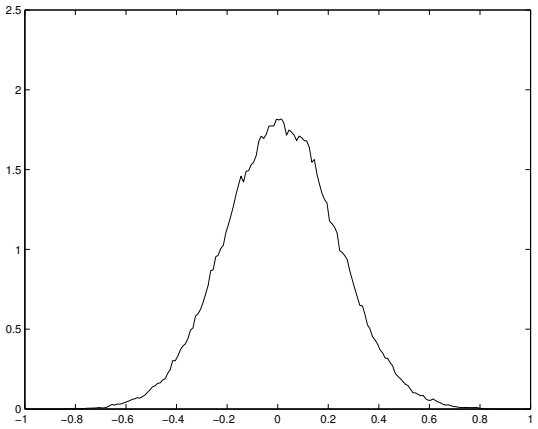

The PDF's for $\mathbf{k} = (1, -1)$, traditional truncation,
23×23 total grid, $E = 7$, $\mathcal{E} = 20$, random topography

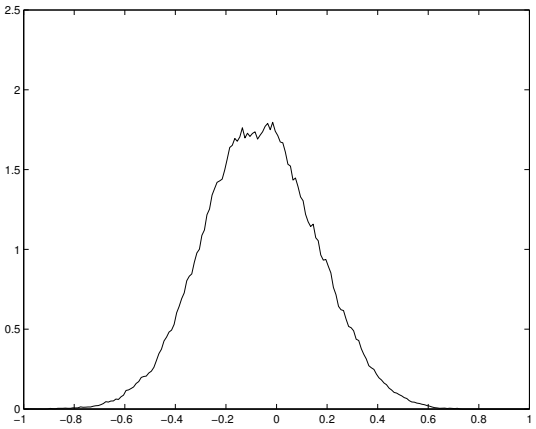

The PDF's for $\mathbf{k} = (1, 1)$, traditional truncation,
23×23 total grid, $E = 7$, $\mathcal{E} = 20$, random topography

Figure 5.31: The probability density functions for the Fourier modes of the potential vorticity, wavenumbers $(0, 1), (1, 0), (1, -1), (1, 1)$, 23×23 traditional truncation, random topography

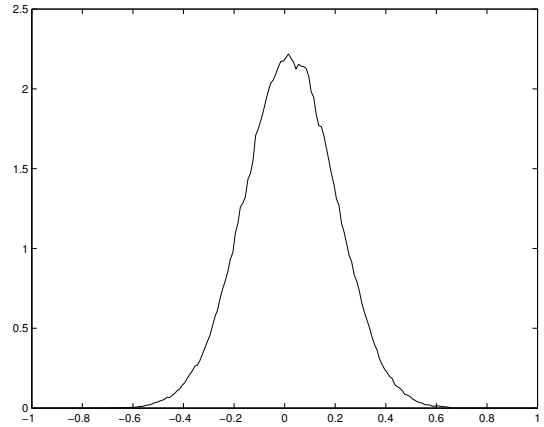

The PDF's for $\mathbf{k} = (0, 2)$, traditional truncation,
23×23 total grid, $E = 7$, $\mathcal{E} = 20$, random topography

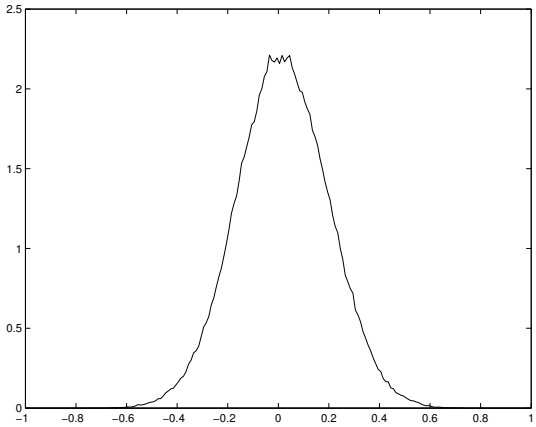

The PDF's for $\mathbf{k} = (2, 0)$, traditional truncation,
23×23 total grid, $E = 7$, $\mathcal{E} = 20$, random topography

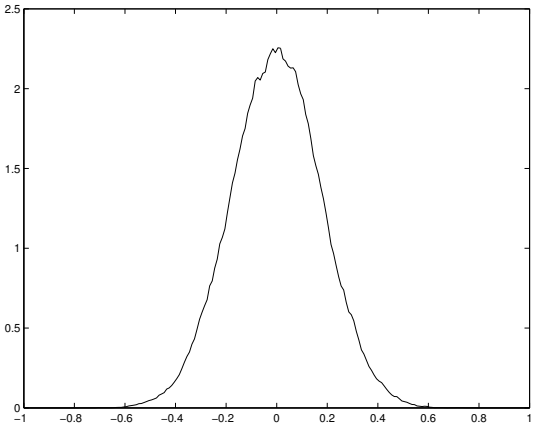

The PDF's for $\mathbf{k} = (1, -2)$, traditional truncation,
23×23 total grid, $E = 7$, $\mathcal{E} = 20$, random topography

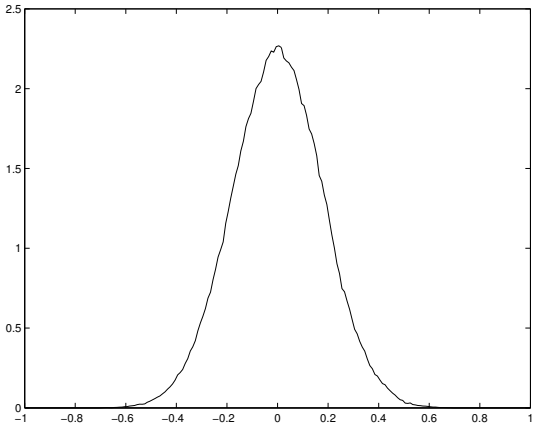

The PDF's for $\mathbf{k} = (1, 2)$, traditional truncation,
23×23 total grid, $E = 7$, $\mathcal{E} = 20$, random topography

Figure 5.32: The probability density functions for the Fourier modes of the potential vorticity, wavenumbers $(0, 2), (2.0), (1, -2), (1, 2)$, 23×23 traditional truncation, random topography

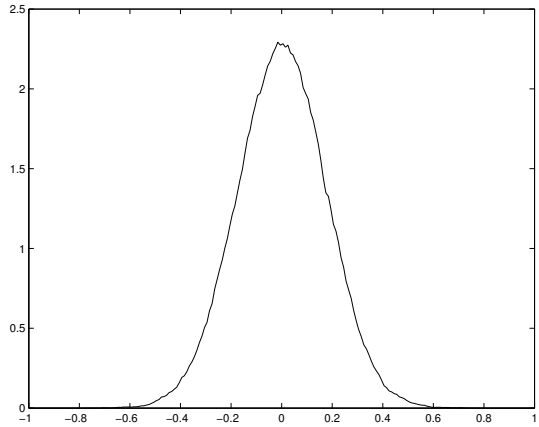

The PDF's for $\mathbf{k} = (2, -1)$, traditional truncation,
23×23 total grid, $E = 7$, $\mathcal{E} = 20$, random topography

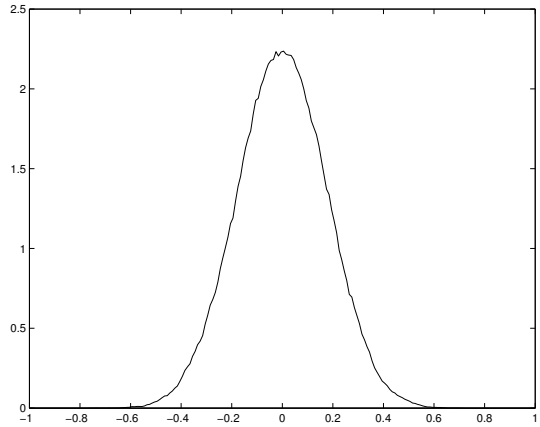

The PDF's for $\mathbf{k} = (2, 1)$, traditional truncation,
23×23 total grid, $E = 7$, $\mathcal{E} = 20$, random topography

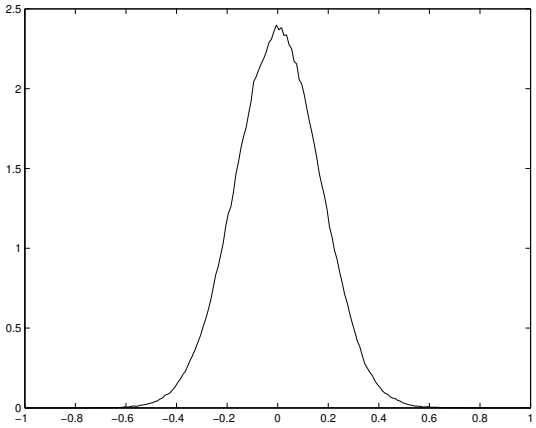

The PDF's for $\mathbf{k} = (2, -2)$, traditional truncation,
23×23 total grid, $E = 7$, $\mathcal{E} = 20$, random topography

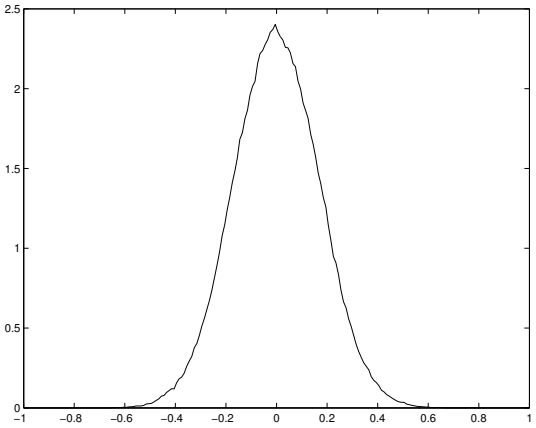

The PDF's for $\mathbf{k} = (2, 2)$, traditional truncation,
23×23 total grid, $E = 7$, $\mathcal{E} = 20$, random topography

Figure 5.33: The probability density functions for the Fourier modes of the potential vorticity, wavenumbers $(2, -1), (2.1), (2, -2), (2, 2)$, 23×23 traditional truncation, random topography

Total grid	
skewness	flatness
$9.702 \cdot 10^{-3}$	2.929
Coarse-grained grid	
skewness	flatness
$9.89 \cdot 10^{-3}$	2.928

Table 5.9: The spatially averaged skewness and flatness of the mean stream functions for the 23×23 traditional truncation, layered topography

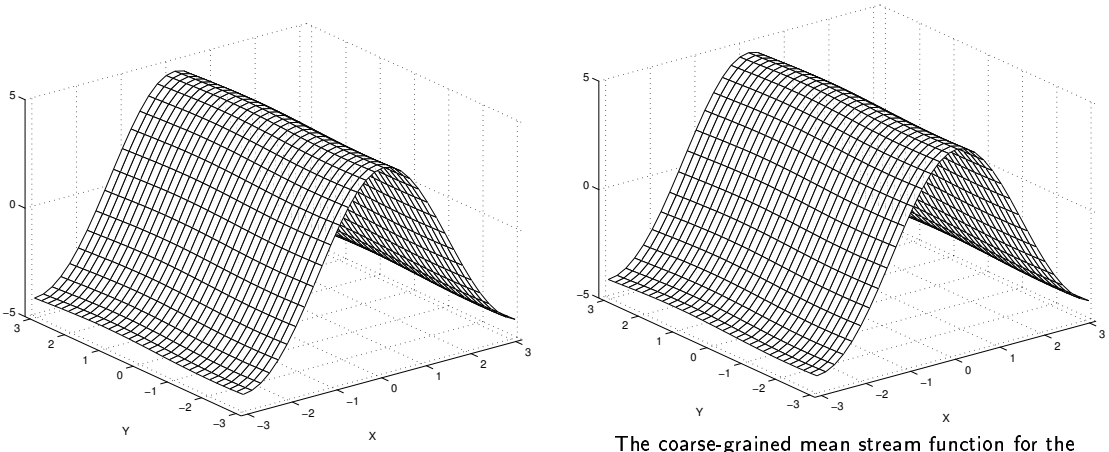

The total mean stream function for the traditional truncation, 23×23 truncation size, layered topography

The coarse-grained mean stream function for the traditional truncation, 23×23 truncation size, layered topography

Figure 5.34: The total and coarse-grained mean stream functions, 23×23 traditional truncation, layered topography

pseudo-energy spectra, "Corr" functions, correlation functions and PDF's for q. For the 23×23 truncation size, in addition to the above, we present the mean stream functions, their variances, skewnesses and flatnesses.

5.3.1 Mean stream functions and their moments

The equilibrium statistical theory and the maximum entropy principle establish the most probable mean state for the dynamics of the traditional truncation (3.17). Here we obtain the mean state stream functions which will later be used as a testbed for the simulation with the sine-bracket truncation. We use the equations (5.2) and (5.3) described in Section 5.0.3 to compute the mean stream functions and corresponding higher moments. The total and coarse-grained mean stream functions for the 23×23 size of traditional truncation (3.17) are presented in Figure 5.34. The most probable mean state is given by

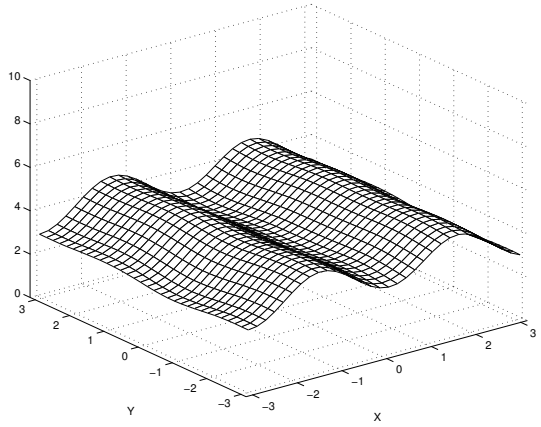

The variance of total mean stream function for the traditional truncation, 23×23 truncation size, layered topography

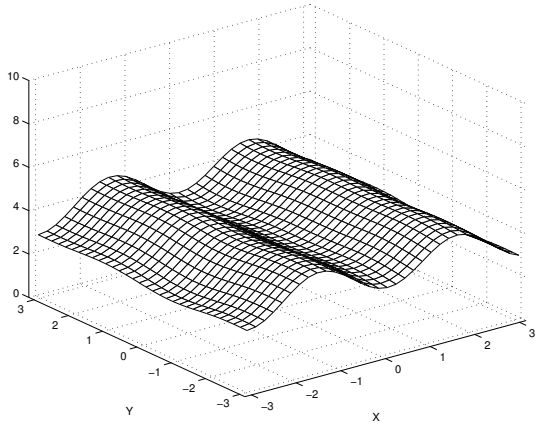

The variance of the coarse-grained mean stream function for the traditional truncation, 23×23 truncation size, layered topography

Figure 5.35: The variances of the total and coarse-grained mean stream functions, 23×23 traditional truncation, layered topography

the statistical theory in (3.29). Here we can see that the calculated mean stream function has a cosine shape in x-direction, and is layered in the y-direction for both 11×11 and 23×23 traditional truncations, as predicted by the theory in (3.29). The variances for the mean stream functions are expected to be flat according to (3.30), however numerically obtained variances fail to confirm the statistical predictions (25-30% relative error, see Figure 5.35). Note that variance depends on the spatial variables in the same manner as the layered topography does (x-direction). The spatially averaged skewness and flatness are shown in Table 5.9. The skewness of the mean stream function is predicted to be zero according to the Gaussian distribution (3.26), however, as shown in Figure 5.36, it is not flat. On the other hand, Table 5.9 shows that the averaged skewness is about 0.02). As for the flatness of the mean stream function, it should be 3 in case with the Gaussian distribution (3.26), and here it is indeed centered at 3, which can be seen in Figure 5.37 and Table 5.9. The numerically obtained flatness weakly depends on the spatial coordinates as shown in Figure 5.37 (the fluctuations are about 20% of the flatness average).

5.3.2 The mean energy and pseudo-energy spectra

The pseudo-energy spectrum and energy of the mean spectrum calculated by the traditional truncation (3.17) of 11×11 and 23×23 size are presented in Figures 5.38 and 5.39. We use the equations (5.4) and (5.5) described in Section 5.0.3 to compute

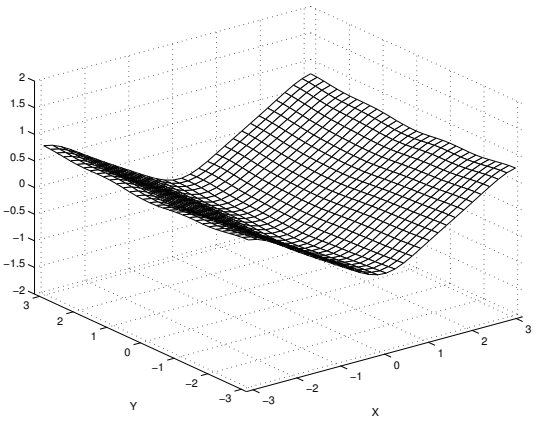

The skewness of total mean stream function for the traditional truncation, 23×23 truncation size, layered topography

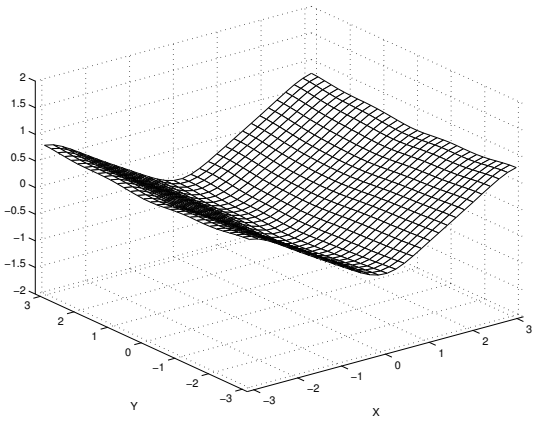

The skewness of the coarse-grained mean stream function for the traditional truncation, 23×23 truncation size, layered topography

Figure 5.36: The skewness of the total and coarse-grained mean stream functions, 23×23 traditional truncation, layered topography

11×11		23×23	
μ	α	μ	α
-0.9067	4.372	-0.9547	19.52

Table 5.10: The numerically determined parameters μ and α for the traditional truncation, layered topography

the mean energy and pseudo-energy spectra. In order to represent the result for the pseudo-energy in the pseudo-energy variables (3.48), we used the numerically calculated parameters μ and α which are shown in Table 5.10. According to the theoretical prediction in (3.50), the pseudo-energy should be equipartitioned in spectral space. As we can see in Figures 5.38 and 5.39, the equipartition holds very well for the pseudo-energy except for the first Fourier mode for both sizes of truncations. The reasons for such behavior of the pseudo-energy is explained in the Section 5.1.2, however note that here the error in the first Fourier mode is much smaller than that for the no topography and random topography cases. This occurs because in the case with layered topography the μ-parameter is farther away from -1 than in the rest of the geophysical cases (see Tables 5.2 and 5.6). As for the rest of the pseudo-energy spectrum, the equipartition holds within 3-5% relative error, which is a very good confirmation of the statistical theory. As for the energy of the mean state, the statistical theory in (3.46a) states that it should be zero in the modes with no topography. As shown in Figures 5.38 and 5.39, there is a considerable amount of

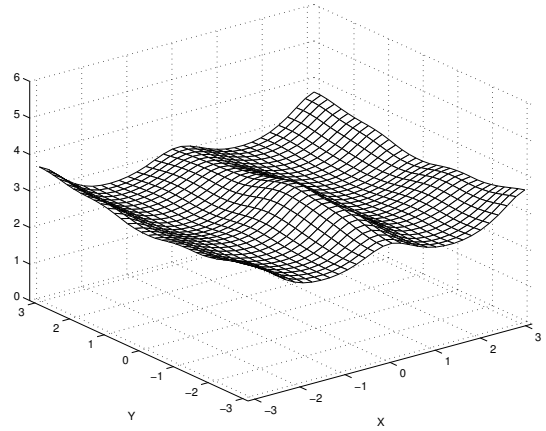

The flatness of total mean stream function for the traditional truncation, 23×23 truncation size, layered topography

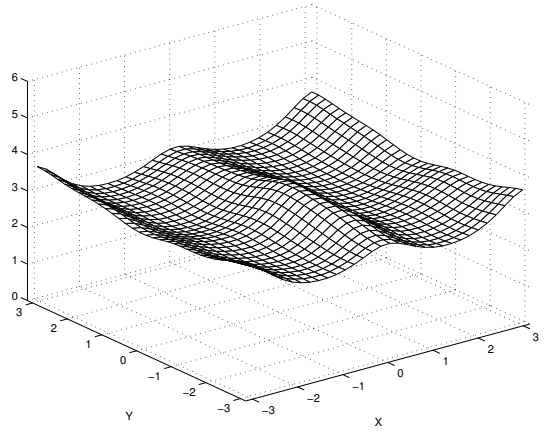

The flatness of the coarse-grained mean stream function for the traditional truncation, 23×23 truncation size, layered topography

Figure 5.37: The flatness of the total and coarse-grained mean stream functions, 23×23 traditional truncation, layered topography

energy in the Fourier mode $|\mathbf{k}|^2 = 1$ and smaller amount of energy in the mode $|\mathbf{k}|^2 = 4$ (better seen in the Figure 5.38), precisely where topography is, and this is confirmed by the statistical theory in (3.46a). The mean energy is vanishingly small for the rest of the Fourier modes, which is very good confirmation of the statistical theory.

5.3.3 "Corr" functions and scatterplots

The total and coarse-grained Corr functions for the numerical simulations with the 11×11 and 23×23 traditional truncations (3.17) are shown in Figures 5.40 and 5.41. We use the equation (5.7) described in Section 5.0.3 to compute the Corr functions and associated scatterplots. The theoretical relation (3.28) predicts that the Corr functions must eventually converge to -1. Figures 5.40 and 5.41 show that the Corr functions are almost -1, which means that the numerical mean state is almost perfectly collinear (Note the scale in the Figures 5.40 and 5.41), and the Corr functions are in fact more collinear then those for the rest of the geophysical cases (see Figures 5.8, 5.9), 5.24, and 5.25). Also we can see, the Corr functions for the 23×23 traditional truncation (Figure 5.41) show more collinearity than those for 11×11 traditional truncation (Figure 5.41). This happens because the 23×23 truncation is the better approximation to the actual dynamics due to its higher resolution. Also for each truncation size the coarse-grained Corr function shows more collinearity than the total one which means that the theory works better on

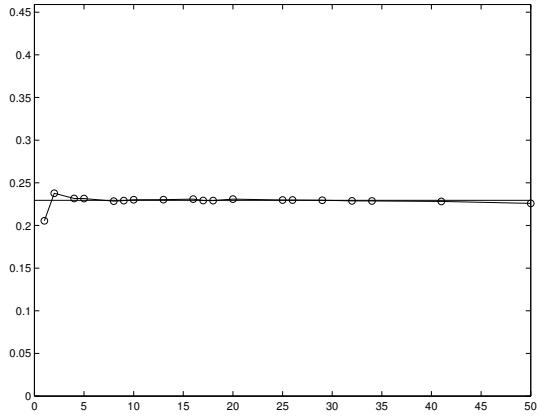

The pseudo-energy spectrum for the traditional truncation, 11×11 truncation size, layered topography, horizontal line represents theoretical prediction

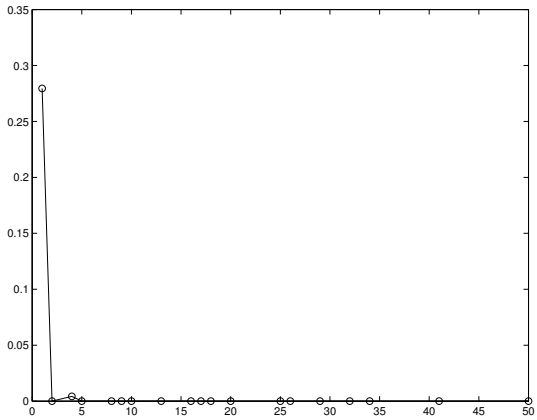

The spectrum of energy of the mean for the traditional truncation, 11×11 truncation size, layered topography

Figure 5.38: The pseudo-energy spectrum and the spectrum of energy of the mean, 11×11 traditional truncation, layered topography

large scales. As well as Corr function, we present the scatterplots $\bar{q}$ vs $\bar{\psi}$ for all points in the physical space grid. The scatterplots are shown in Figures 5.42 and 5.43. As we can see, the scatterplots for both truncation sizes are perfectly collinear. The μ-parameter determined by least squares procedure is $\mu = -0.9067$ for 11×11 traditional truncation and $\mu = -0.9547$ for 23×23 truncation.

5.3.4 Time correlation functions

The time correlation functions (5.8) for different Fourier modes for the two truncation sizes is shown in Figures 5.44 and 5.45. We use the equation (5.8) described in Section 5.0.3 to compute the time correlation functions. As we can see, the large scales (small wavenumbers) exhibit slower rate of decay, which is typical for actual weather systems, because global climate changes take much more time than local weather fluctuations. Also we note that the rate of decay for the largest scale depends on the truncation size, unlike the rest of the wavenumbers we present. The rate of decay for the largest scale mode $|\mathbf{k}|^2 = 1$ for the 23×23 truncation (Figure 5.44) is less than that for the 11×11 truncation (Figure 5.45). This means that the small scale resolution affects the statistical long time behavior on the large scales. Overall, the behavior of the correlation functions in this case barely differs from the case with no topography (Figures 5.12 and 5.13), or random topography (Figures 5.28 and 5.29).

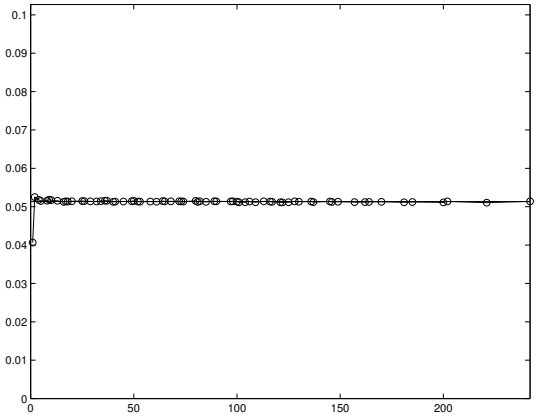

The pseudo-energy spectrum for the traditional truncation, 23×23 truncation size, layered topography, horizontal line represents theoretical prediction

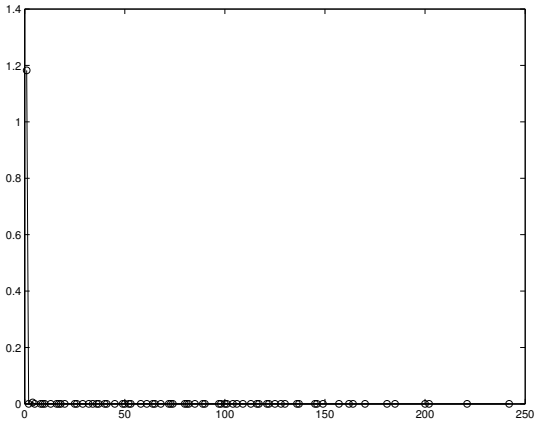

The spectrum of energy of the mean for the traditional truncation, 23×23 truncation size, layered topography

Figure 5.39: The pseudo-energy spectrum and the spectrum of energy of the mean, 23×23 traditional truncation, layered topography

Size	Variance	Skewness	Flatness
11×11	45.31	$6.654 \cdot 10^{-3}$	2.857
23×23	65.38	$4.116 \cdot 10^{-2}$	2.559

Table 5.11: The variance, skewness, and flatness of spatially averaged probability density functions for the potential vorticity, traditional truncation with layered topography

5.3.5 Probability density functions

In this section we represent the numerically computed probability density functions of the two kinds: the PDF's for the real parts of the Fourier modes of the potential vorticity, and the spatially averaged probability density functions for the potential vorticity with removed mean.

5.3.5.1 Probability density functions for the potential vorticity

We present the spatially averaged PDF with removed mean for the potential vorticity in physical space, computed with 11×11 and 23×23 traditional truncation (3.17). The numerical algorithm which was used in obtaining the PDF's in described in the Section 5.0.3. Thus obtained probability density functions for the potential vorticity are represented in Figure 5.46, and their variances and skewnesses are provided in Table 5.11. As we can see, for both 11×11 and 23×23 sizes of truncations the probability density

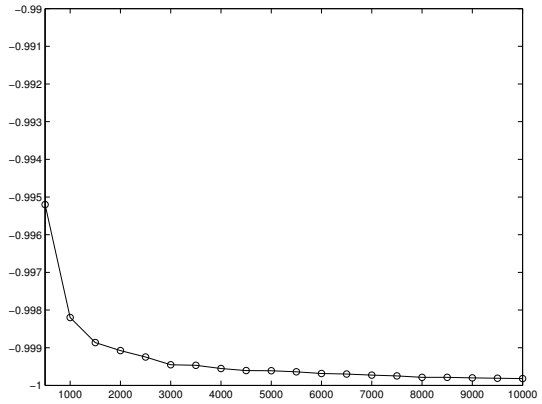

The total Corr function for the traditional truncation, 11×11 truncation size, layered topography

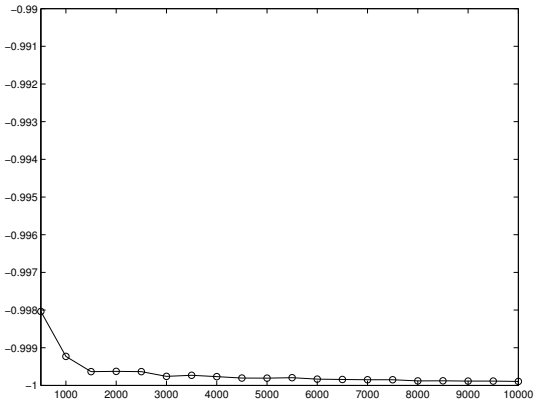

The coarse-grained Corr function for the traditional truncation, 11×11 truncation size, layered topography

Figure 5.40: The total and coarse-grained Corr functions $\mathbf{Corr}[\langle\psi\rangle_\tau, \langle q\rangle_\tau](\tau)$ for the 11×11 size traditional truncation, layered topography

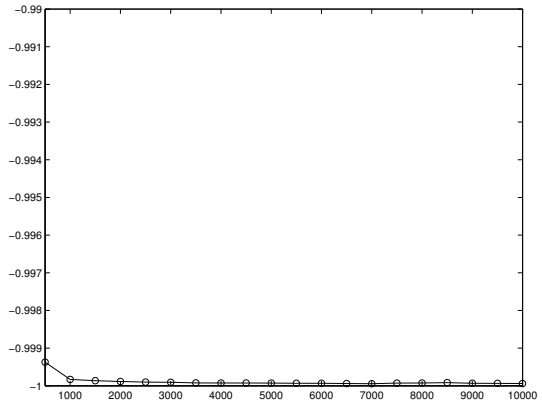

The total Corr function for the traditional truncation, 23×23 truncation size, layered topography

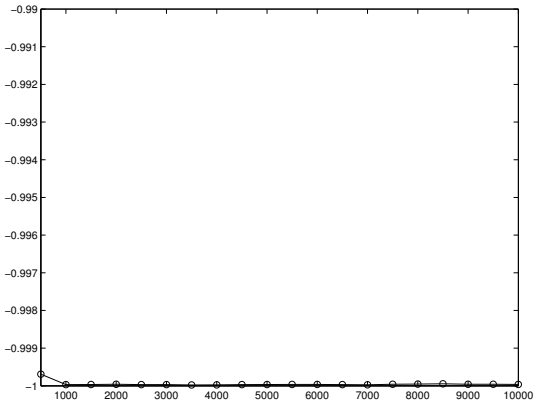

The coarse-grained Corr function for the traditional truncation, 23×23 truncation size, layered topography

Figure 5.41: The total and coarse-grained Corr functions $\mathbf{Corr}[\langle\psi\rangle_\tau, \langle q\rangle_\tau](\tau)$ for the 23×23 size traditional truncation, layered topography

functions have a Gaussian shape, as predicted by the statistical theory in (3.26), however the discrepancy in the case with 23×23 traditional truncation is larger (see Figure 5.46). The variances for both results are not equal, as shown in Table 5.11, however the skewness in both cases is very close to zero. Later we will compare this result to the results obtained for the sine-bracket truncation with additional conserved quantities.

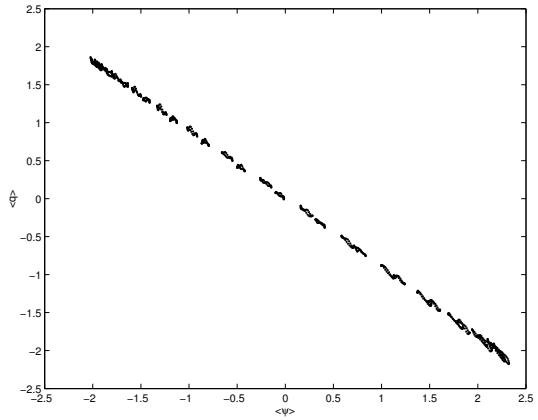

The total scatterplot $\bar{q}$ vs $\bar{\psi}$ for the traditional truncation, 11×11 truncation size, layered topography

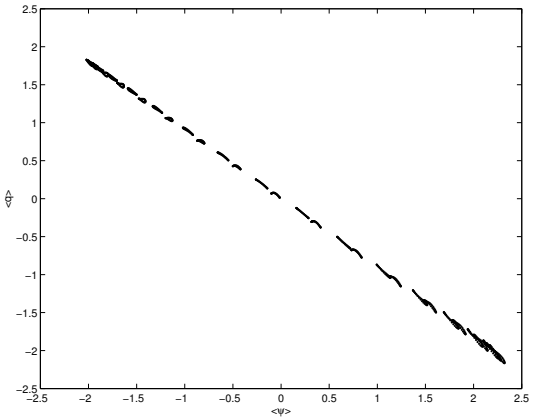

The coarse-grained scatterplot $\bar{q}$ vs $\bar{\psi}$ for the traditional truncation, 11×11 truncation size, layered topography

Figure 5.42: The total and coarse-grained scatterplots $\bar{q}$ vs $\bar{\psi}$ for the 11×11 size traditional truncation, layered topography

5.3.5.2 PDF's for the Fourier modes of the potential vorticity

The probability density functions for the real parts of the Fourier modes of the potential vorticity obtained with the 23×23 traditional truncation (3.17) are shown in Figures 5.47, 5.48, and 5.49. The numerical algorithm which was used in obtaining the PDF's is described in the Section 5.0.3. According to the statistical predictions (3.37), the shape of the PDF's should be Gaussian. Figure 5.47 shows that the probability density function for the large scale mode $\mathbf{k} = (1, 0)$ does not have Gaussian shape, non-trivial mean and is not symmetric. This happens due to the presence of the layered topography in the Fourier mode $\mathbf{k} = (1, 0)$. However, the rest of the Fourier modes have clearly Gaussian shape in accordance with the statistical predictions (3.37). The means and variances for PDF's of the Fourier modes for the potential vorticity are shown in Table 5.12, where we can see that the mode $\mathbf{k} = (1, 0)$ has a non-trivial mean -2.075 due to the topography.

5.4 Conclusions

The direct numerical simulations with the traditional truncation (3.17), presented in this chapter, confirm the predictions of the equilibrium statistical theory in Chapter 3. Three different geophysical situations were considered, and for each situation the statistical predictions were confirmed reasonably well.

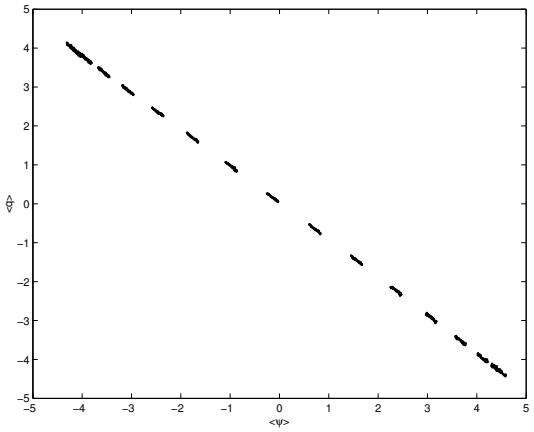

The total scatterplot $\bar{q}$ vs $\bar{\psi}$ for the traditional truncation, 23×23 truncation size, layered topography

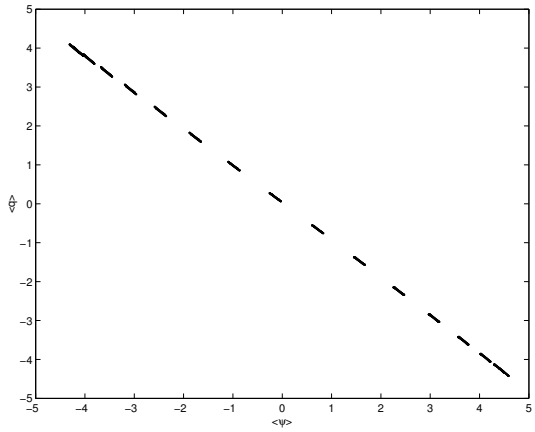

The coarse-grained scatterplot $\bar{q}$ vs $\bar{\psi}$ for the traditional truncation, 23×23 truncation size, layered topography

Figure 5.43: The total and coarse-grained scatterplots $\bar{q}$ vs $\bar{\psi}$ for the 23×23 size traditional truncation, layered topography

- **Mean stream functions and moments.** The predicted mean state (3.29) was confirmed for all geophysical cases by direct simulations with the traditional truncation (3.17) for 23×23 truncation size (Figures 5.2, 5.18, and 5.34 in Sections 5.1.1, 5.2.1, and 5.3.1). The arbitrary behavior of the first Fourier component in the mean stream function for the $\mu \approx -1$ and no topography in the mode $|\mathbf{k}|^2 = 1$ was clarified in the Section 5.1.1, equation (5.9). The major properties of the predicted moments of the stream function were also confirmed by the direct numerical simulations. The variance plots have flat shape (Figures 5.3, 5.19, and 5.35), the experimental skewness is zero (Figures 5.4 and 5.20), or at least centered at zero for the layered topography (Table 5.9). The flatness has flat shape, centered at 2 for no topography and random topography cases (Figures 5.5 and 5.21), and centered at 3 for the layered topography case (Figure 5.37).

- **Mean energy and pseudo-energy.** The partition of the mean energy spectrum was confirmed with very good precision for each geophysical case and for both 11×11 and 23×23 traditional truncation (3.17) in Figures 5.6, 5.7, 5.22, 5.23, 5.38, and 5.39, Sections 5.1.2, 5.2.2, and 5.3.2. The errors in the first Fourier mode $|\mathbf{k}|^2 = 1$ were accounted for in Section 5.1.2. The equipartition of the pseudo-energy spectrum was confirmed with very good precision for each geophysical case in Figures 5.6, 5.7, 5.22, 5.23, 5.38, and 5.39. The only source of errors was the first Fourier mode in the

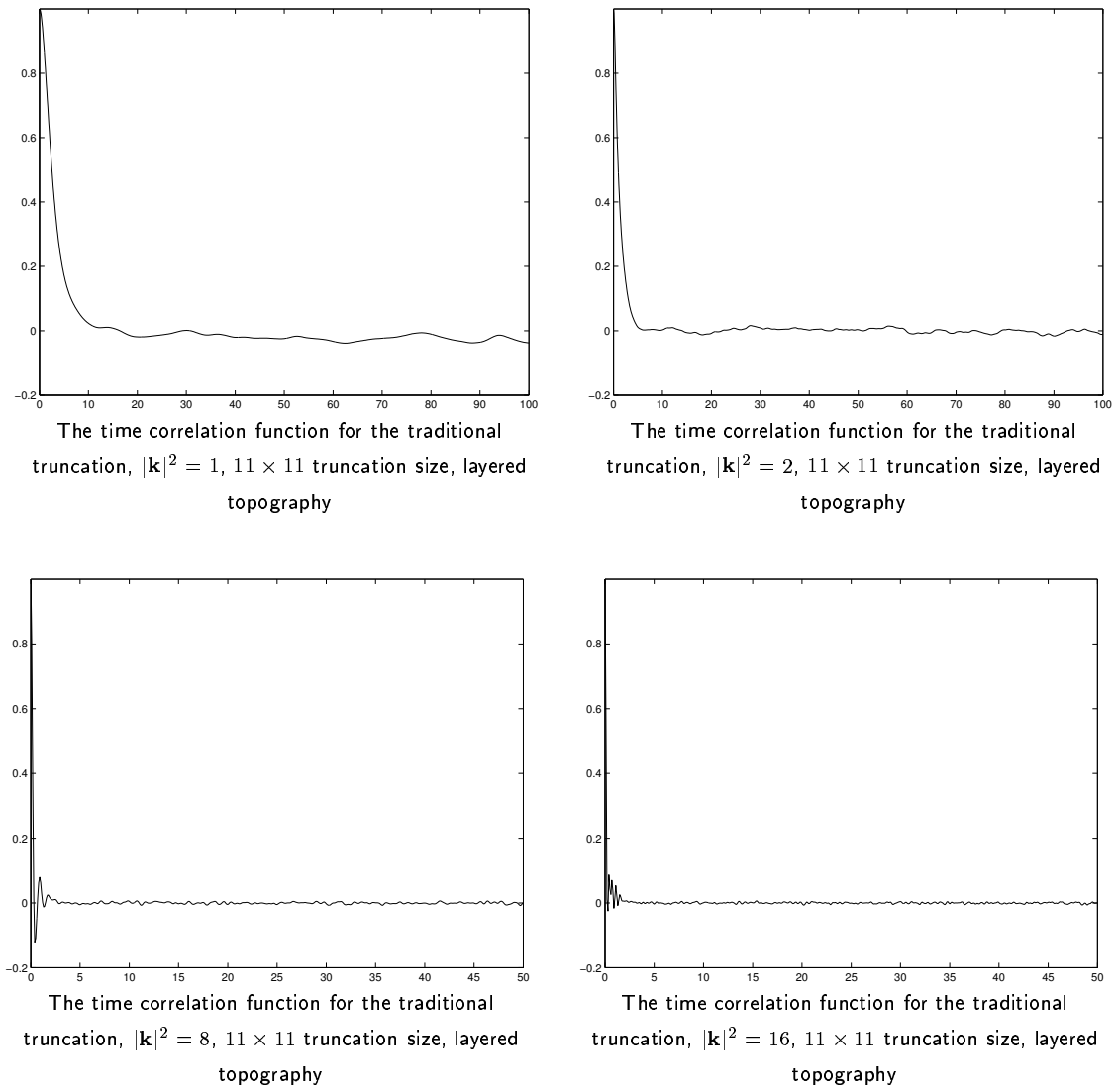

Figure 5.44: The time correlation functions for different Fourier modes for the 11×11 size traditional truncation, layered topography

pseudo-energy spectra, however this source was accounted for in the Section 5.1.2, and also Section 5.1.1, equation (5.9).

- **Collinearity of the mean state.** The collinearity of the predicted mean state for all three geophysical situations was confirmed by the Corr functions for both 11×11 and 23×23 traditional truncations (3.17) in Figures 5.8, 5.9, 5.24, 5.25, 5.40, and 5.41 in Sections 5.1.3, 5.2.3, and 5.3.3. We also confirmed the collinearity by plotting the scatterplots $\bar{q}$ vs $\bar{\psi}$ (Figures 5.10, 5.11, 5.26, 5.27, 5.42, and 5.43).

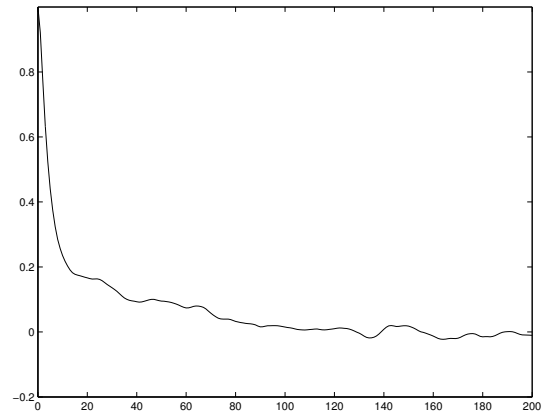

The time correlation function for the traditional truncation, $|\mathbf{k}|^2 = 1$, 23×23 truncation size, layered topography

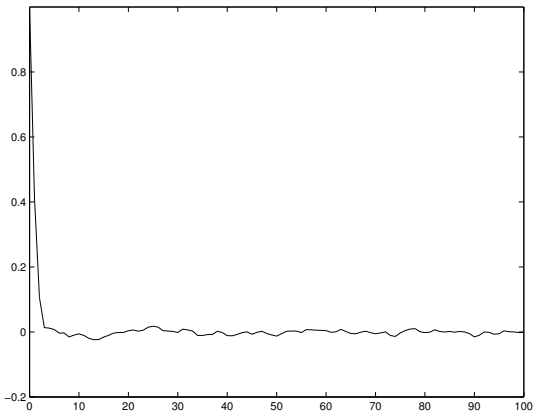

The time correlation function for the traditional truncation, $|\mathbf{k}|^2 = 2$, 23×23 truncation size, layered topography

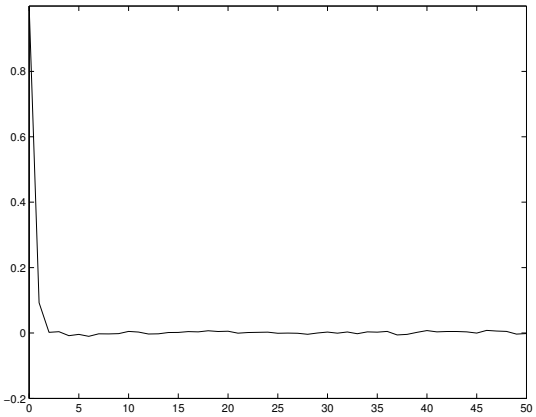

The time correlation function for the traditional truncation, $|\mathbf{k}|^2 = 8$, 23×23 truncation size, layered topography

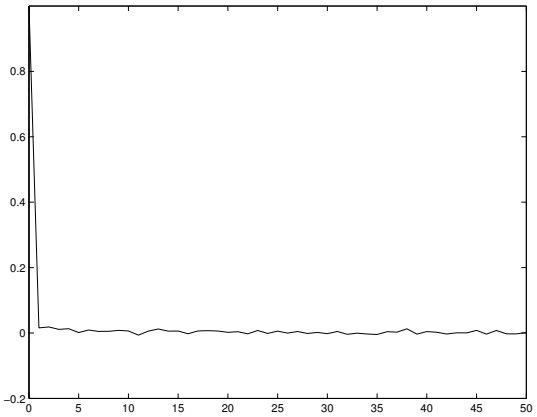

The time correlation function for the traditional truncation, $|\mathbf{k}|^2 = 16$, 23×23 truncation size, layered topography

Figure 5.45: The time correlation functions for different Fourier modes for the 23×23 size traditional truncation, layered topography

We have shown that the large scale mean flow (coarse-grained 5×5 grid of Fourier coefficients) is more collinear than the corresponding total mean flow (total 11×11 or 23×23 grid of Fourier coefficients) for all geophysical situations. We also discovered that in the case with non-zero topography on the first Fourier mode (geophysical situation with layered topography) the mean state exhibits much more collinearity than in any of the other geophysical cases (Figures 5.40, 5.41, 5.42, and 5.43).

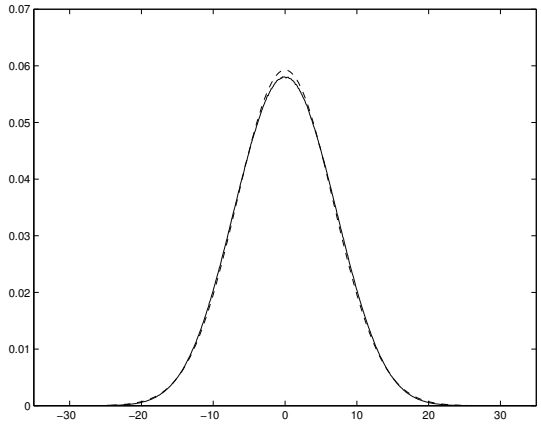

The PDF for the potential vorticity, 11×11 traditional truncation, layered topography, solid line - direct numerical simulation, dashed line - analytical Gaussian with the same variance

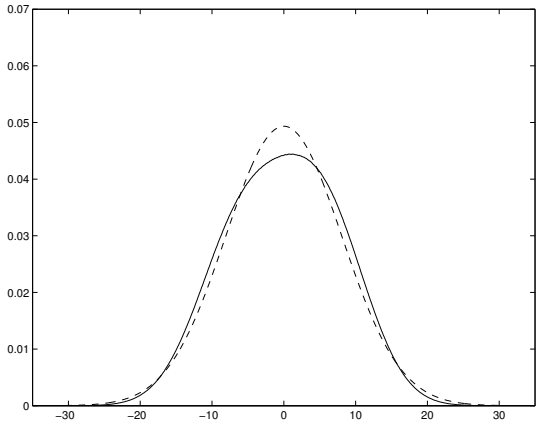

The PDF for the potential vorticity, 23×23 traditional truncation, layered topography, solid line - direct numerical simulation, dashed line - analytical Gaussian with the same variance

Figure 5.46: The spatially averaged probability density functions for the potential vorticity with removed mean, layered topography

- **Time correlation functions.** The time correlation functions (5.8) were observed for all three geophysical situations both for 11×11 and 23×23 traditional truncation (3.17) and shown in Figures 5.12, 5.13, 5.28, 5.29, 5.44, and 5.45. The decay rate of the correlation functions is slower for small wavenumbers (large scales), and faster for large wavenumbers (small scales), which is typical for actual weather systems. We also show that the rate of decay of the time correlation function for a particular wavenumber does not depend on the size of truncation, with the only exception at wavenumber $|\mathbf{k}|^2 = 1$ (first Fourier mode). For the first Fourier mode the time correlation function decays slower for larger truncation size.

- **Probability density functions.** We observed the probability density functions for the real parts of the Fourier modes for the potential vorticity, 23×23 traditional truncation (3.17), for all three geophysical situations, in Figures 5.15, 5.16, 5.17, 5.31, 5.32, 5.33, 5.47, 5.48, and 5.49, Sections 5.1.5, 5.2.5, and 5.3.5. The equilibrium statistical predictions for the most probable probability density (3.37), Chapter 3, were confirmed for all three geophysical cases with no topography, random topography, and layered topography. The majority of the PDF's has Gaussian shape, with only exceptions for large-scale modes with $|\mathbf{k}|^2 = 1$. We also looked at the averaged probability density functions for the potential vorticity with removed

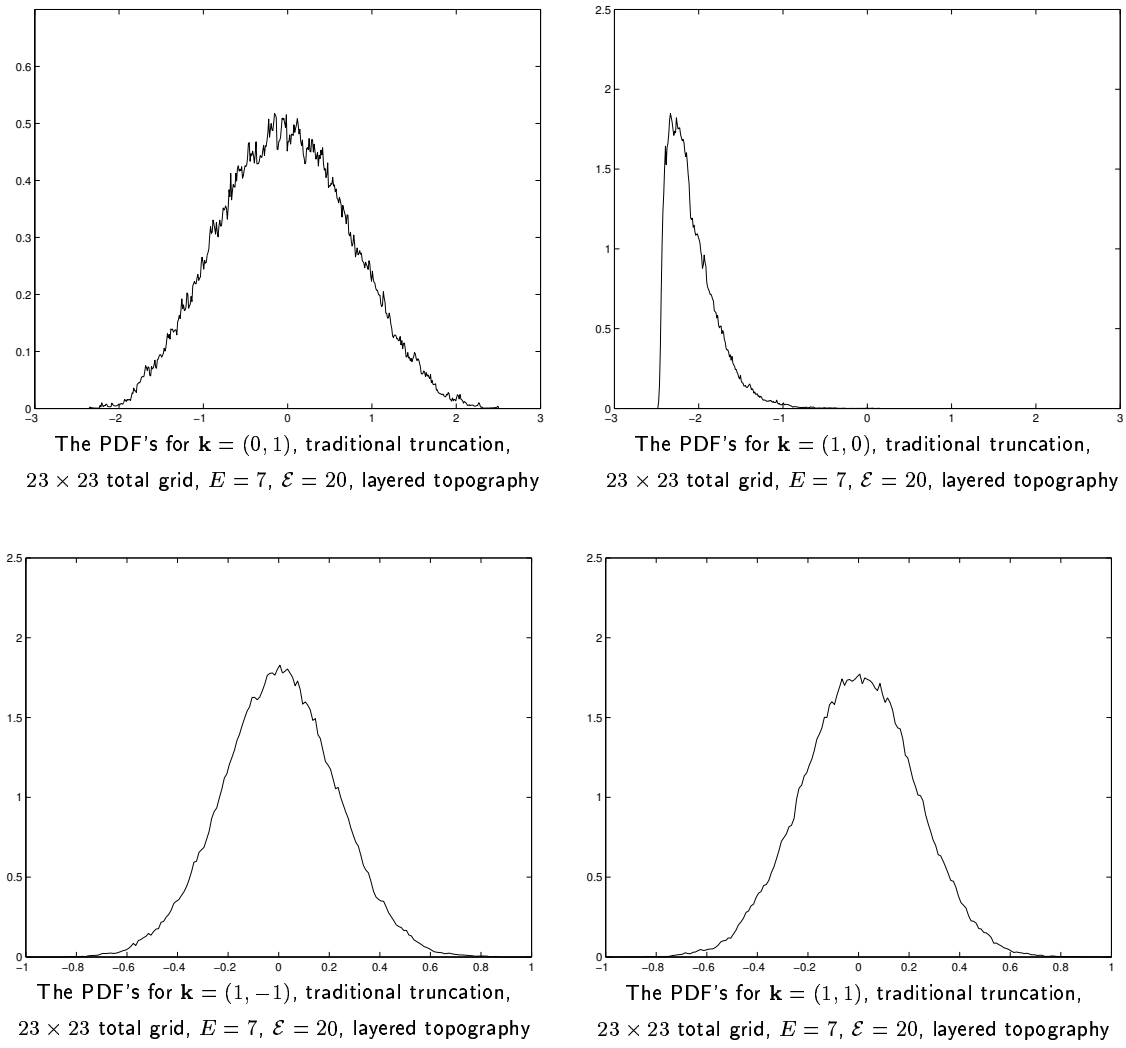

Figure 5.47: The probability density functions for the Fourier modes of the potential vorticity, wavenumbers $(0,1), (1,0), (1,-1), (1,1)$, 23×23 traditional truncation, layered topography

mean (algorithm is given in Section 5.0.3), and found that they also have Gaussian shape (Figures 5.14, 5.30, and 5.46) which is predicted by the equation (3.26).

Overall, the obtained numerical results are consistent with the equilibrium statistical theory presented in Chapter 3. In the next chapter we will compare the above results with similar direct simulations done with the sine-bracket truncation (4.1) with many additional conserved quantities, and thus quantify the influence of the additional conserved quantities on the equilibrium statistical predictions.

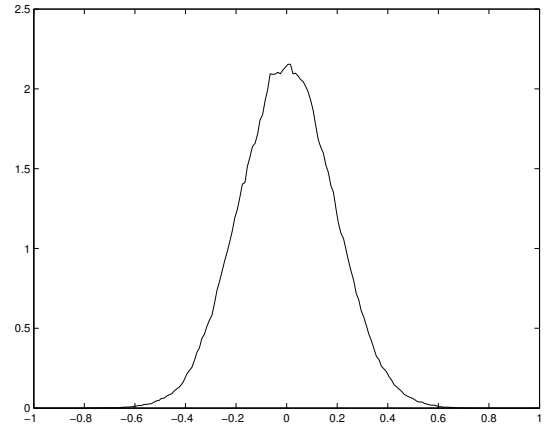

The PDF's for $\mathbf{k} = (0, 2)$, traditional truncation,
23×23 total grid, $E = 7$, $\mathcal{E} = 20$, layered topography

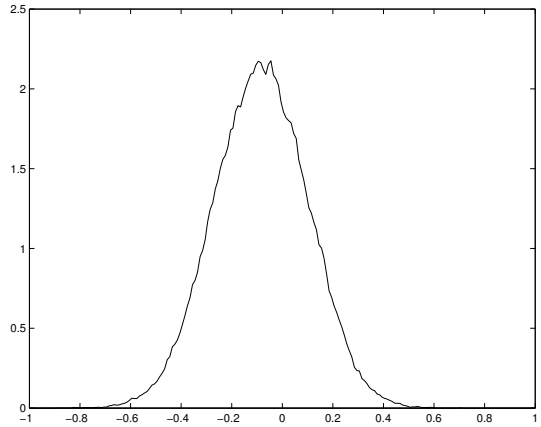

The PDF's for $\mathbf{k} = (2, 0)$, traditional truncation,
23×23 total grid, $E = 7$, $\mathcal{E} = 20$, layered topography

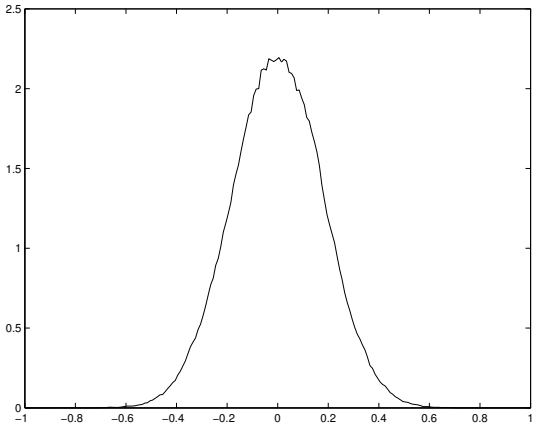

The PDF's for $\mathbf{k} = (1, -2)$, traditional truncation,
23×23 total grid, $E = 7$, $\mathcal{E} = 20$, layered topography

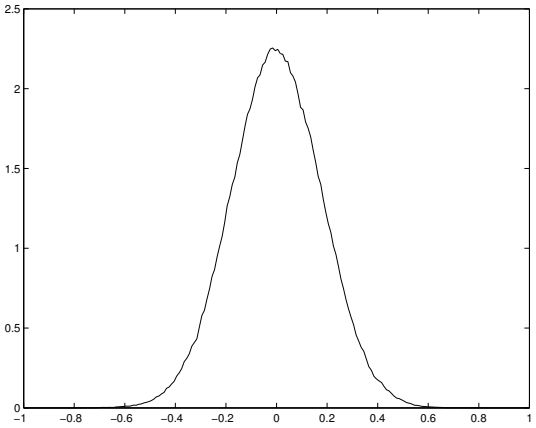

The PDF's for $\mathbf{k} = (1, 2)$, traditional truncation,
23×23 total grid, $E = 7$, $\mathcal{E} = 20$, layered topography

Figure 5.48: The probability density functions for the Fourier modes of the potential vorticity, wavenumbers $(0, 2), (2.0), (1, -2), (1, 2)$, 23×23 traditional truncation, layered topography

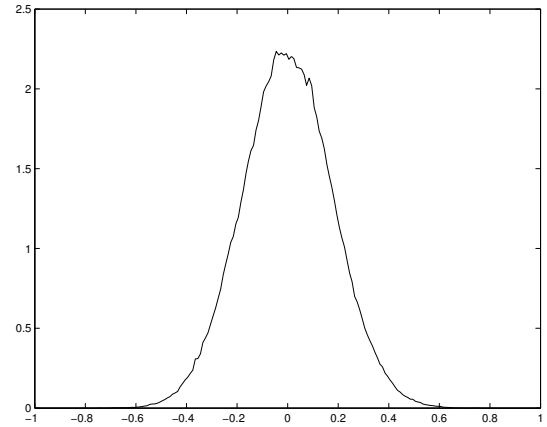

The PDF's for $\mathbf{k} = (2, -1)$, traditional truncation, 23×23 total grid, $E = 7$, $\mathcal{E} = 20$, layered topography

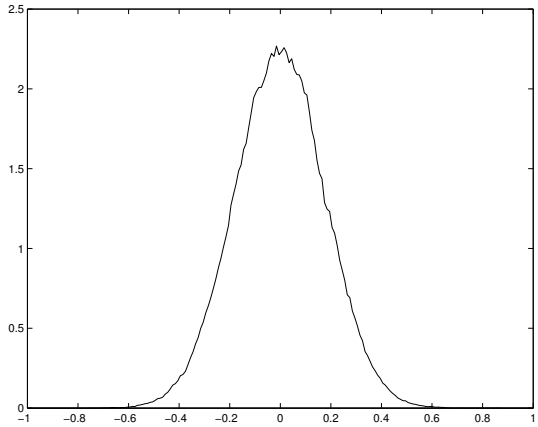

The PDF's for $\mathbf{k} = (2, 1)$, traditional truncation, 23×23 total grid, $E = 7$, $\mathcal{E} = 20$, layered topography

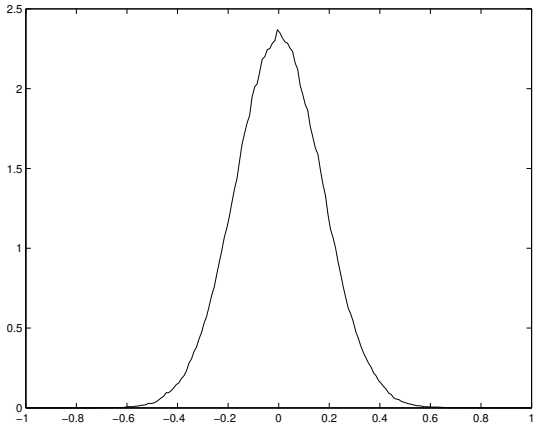

The PDF's for $\mathbf{k} = (2, -2)$, traditional truncation, 23×23 total grid, $E = 7$, $\mathcal{E} = 20$, layered topography

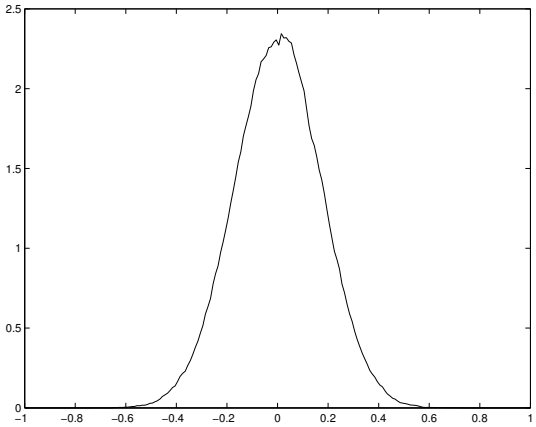

The PDF's for $\mathbf{k} = (2, 2)$, traditional truncation, 23×23 total grid, $E = 7$, $\mathcal{E} = 20$, layered topography

Figure 5.49: The probability density functions for the Fourier modes of the potential vorticity, wavenumbers $(2, -1), (2.1), (2, -2), (2, 2)$, 23×23 traditional truncation, layered topography

Fourier space PDF's		
Mode	Mean	Variance
$\mathbf{k} = (0, 1)$	$-2.810 \cdot 10^{-2}$	$6.003 \cdot 10^{-1}$
$\mathbf{k} = (1, 0)$	-2.075	$2.641 \cdot 10^{-1}$
$\mathbf{k} = (1, -1)$	$2.297 \cdot 10^{-3}$	$5.052 \cdot 10^{-2}$
$\mathbf{k} = (1, 1)$	$1.059 \cdot 10^{-3}$	$5.006 \cdot 10^{-2}$
$\mathbf{k} = (0, 2)$	$1.088 \cdot 10^{-3}$	$3.402 \cdot 10^{-2}$
$\mathbf{k} = (2, 0)$	$-8.457 \cdot 10^{-2}$	$3.415 \cdot 10^{-2}$
$\mathbf{k} = (1, -2)$	$-1.200 \cdot 10^{-3}$	$3.211 \cdot 10^{-2}$
$\mathbf{k} = (1, 2)$	$-4.804 \cdot 10^{-4}$	$3.179 \cdot 10^{-2}$
$\mathbf{k} = (2, -1)$	$-4.927 \cdot 10^{-4}$	$3.184 \cdot 10^{-2}$
$\mathbf{k} = (2, 1)$	$-2.105 \cdot 10^{-3}$	$3.154 \cdot 10^{-2}$
$\mathbf{k} = (2, -2)$	$7.210 \cdot 10^{-4}$	$2.951 \cdot 10^{-2}$
$\mathbf{k} = (2, 2)$	$1.501 \cdot 10^{-3}$	$2.907 \cdot 10^{-2}$

Table 5.12: The means and variances of the PDF's of the Fourier modes for the potential vorticity, 23×23 traditional truncation, layered topography

CHAPTER 6
NUMERICAL SIMULATIONS FOR STATISTICAL PREDICTIONS WITH THREE PROTOTYPE GEOPHYSICAL SITUATIONS, SINE-BRACKET TRUNCATION

In this chapter we introduce the simulations with the sine-bracket truncation (4.1). As we know, the sine-bracket truncation possesses many additional Casimir invariants of the form (4.4). First of all, for convenience we introduce the *normalized* Casimir invariants

$$\tilde{C}_N = \frac{C_N}{\mathcal{E}^{N/2}}, \tag{6.1}$$

i.e. we normalize all Casimir invariants with respect to the lowest order Casimir invariant, enstrophy (3.19).

We take the idea of relevant and irrelevant conserved quantities from the experience collected while working with the Burgers-Hopf truncation. Here we assume that the additional conserved quantities (6.1) may be relevant, and may be irrelevant, depending on their value. The number of additional conserved quantities depends on the size of the sine-bracket truncation, and, unfortunately, we can not trace all of them for the truncation of fair size. Instead, we employ the gradient descent algorithm, described in Section 4.3, to pre-define only three quantities – energy, enstrophy, and the normalized third Casimir invariant $\tilde{C}_3$. It is obvious that for the uniform distribution on the surface of constant enstrophy the mean value of $\tilde{C}_3$ will be zero, similar to what we saw in the TBH case. We expect statistically irrelevant values of $\tilde{C}_3$ to be concentrated around zero, and further check this fact with direct numerical simulations. Also we generate initial conditions for fixed energy, enstrophy, and the wide range of values of the normalized third Casimir invariant, and quantify the influence of the relevant $\tilde{C}_3$'s on the dynamics of sine-bracket truncation (4.1).

6.1 Simulations with no topography

In this section we represent the results obtained for the most simple geophysical case without topography. In the Section 5.1 of the Chapter 5 we presented the simulations with the traditional truncation (3.17) and no topography. To see the relevance of the 3rd Casimir invariant, we make the direct numerical simulations with the sine-bracket

11×11, total Fourier grid		
$\tilde{C}_3$	skewness	flatness
0	$4.885 \cdot 10^{-3}$	2.027
4	-0.7936	2.882
8	-1.161	3.821
11×11, coarse-grained grid		
$\tilde{C}_3$	skewness	flatness
0	$4.749 \cdot 10^{-3}$	2.021
4	-0.7912	2.847
8	-1.171	3.810

23×23, total Fourier grid		
$\tilde{C}_3$	skewness	flatness
0	$1.481 \cdot 10^{-3}$	2.027
4	-1.006	3.403
8	-0.8344	3.887
23×23, coarse-grained grid		
$\tilde{C}_3$	skewness	flatness
0	$1.461 \cdot 10^{-3}$	2.025
4	-1.001	3.357
8	-0.8088	3.921

Table 6.1: The spatially averaged skewness and flatness of the mean stream functions for 11×11 and 23×23 sine-bracket truncation, total and coarse-grained Fourier grids, no topography

truncation (4.1) for the same geophysical case with three values of $\tilde{C}_3$:

$$\tilde{C}_3 = 0, \quad \tilde{C}_3 = 4, \quad \tilde{C}_3 = 8,$$

where $\tilde{C}_3$ is defined by (6.1). We perform the simulations with two different sizes of sine-bracket truncation (4.1), 11×11 Fourier modes, and 23×23 Fourier modes. For the 11×11 and 23×23 sizes of truncation we represent the mean stream functions, and their moments, mean energy and pseudo-energy spectra, "Corr" functions, time correlation functions, and probability density functions.

6.1.1 Mean stream functions and their moments

Here we present the mean stream functions (5.2) and their moments (5.3) for the 23×23 size sine-bracket truncation (4.1). Our main purpose is to compare the results for the sine-bracket truncation with the with those for the traditional truncation (3.17) (Figures 5.2, 5.3, 5.4, 5.5, and Table 5.1) for the same geophysical case with no topography. The direct numerical simulations for the sine-bracket truncation were done for the set of initial conditions with energy $E = 7$, enstrophy $\mathcal{E} = 20$, and three different values of the normalized third Casimir invariant $\tilde{C}_3 = 0$, 4, and 8, where $\tilde{C}_3$ is defined by (6.1).

The total mean stream functions for the 11×11 and 23×23 sizes of the sine-bracket truncation (4.1) are presented in Figure 6.1 for $\tilde{C}_3 = 0$, Figure 6.2 for $\tilde{C}_3 = 4$, and Figure 6.3 for $\tilde{C}_3 = 8$. The most probable mean state is given by the statistical theory in (3.29), and is equal to zero in the absence of topography. In the Figure 6.1 we can see

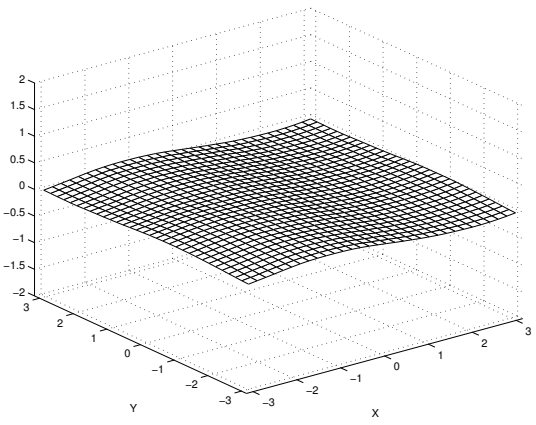

The stream function of the total mean flow for the sine-bracket truncation, 11×11 truncation size, $E = 7$, $\mathcal{E} = 20$, $\tilde{C}_3 = 0$

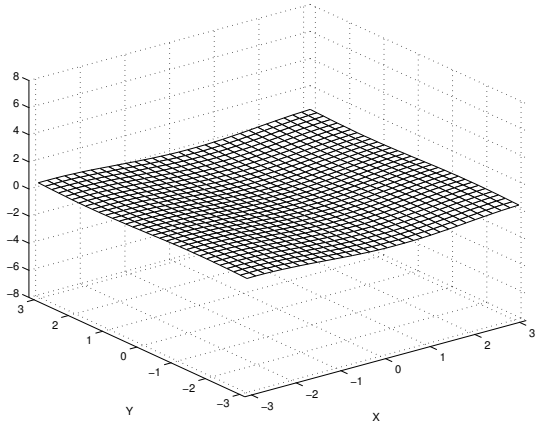

The stream function of the total mean flow for the sine-bracket truncation, 23×23 truncation size, $E = 7$, $\mathcal{E} = 20$, $\tilde{C}_3 = 0$

Figure 6.1: The total mean stream functions for the sine-bracket truncation, 11×11 and 23×23 truncation sizes, $\tilde{C}_3 = 0$, no topography

that the calculated mean stream function diverges from zero by at most ± 0.1 for 11×11 size, and ± 0.4 for 23×23 size of sine-bracket truncation, and thus the mean state, predicted by the theory and confirmed well by the direct numerical simulations with the traditional truncation (Figure 5.2), happens to be the same with the sine-bracket truncation and $\tilde{C}_3 = 0$. Thus, we conclude that $\tilde{C}_3 = 0$ is not relevant for the mean stream function. However, the mean stream functions for the sine-bracket truncation with $\tilde{C}_3 = 4$, which are shown in Figure 6.2, exhibit more distortions from zero, about ± 0.3 for 11×11 size, and ± 1.2 for 23×23 size of sine-bracket truncation. Thus, we conclude that $\tilde{C}_3 = 4$ is relevant for the mean stream function. Now let us look at the mean stream functions for the sine-bracket truncation with $\tilde{C}_3 = 8$, which are shown in Figure 6.3. We can see that the mean stream functions develop significant distortions for both 11×11 and 23×23 sizes of the sine-bracket truncation, with the divergence from zero within ± 2 for 11×11, and within ± 8 for 23×23 sizes of sine-bracket truncation. We conclude that $\tilde{C}_3 = 8$ is strongly relevant for the mean stream function. Note that the influence of $\tilde{C}_3$ depends also on the size of truncation: for larger size the influence is greater for the same value of $\tilde{C}_3$.

The variances of the stream functions for the 11×11 and 23×23 sizes of the sine-bracket truncation (4.1) are presented in Figure 6.4 for $\tilde{C}_3 = 0$, Figure 6.5 for $\tilde{C}_3 = 4$, and Figure 6.6 for $\tilde{C}_3 = 8$. The variances predicted by the theory in (3.30), confirmed by the

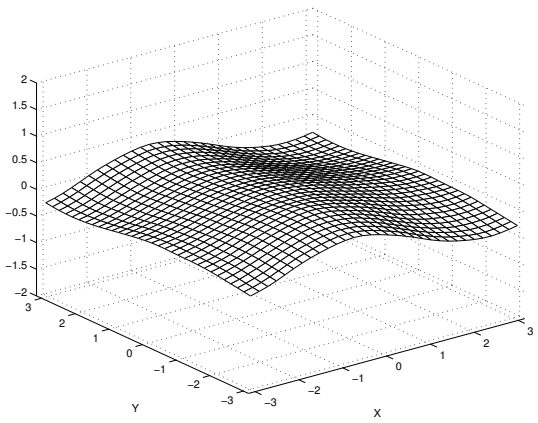

The stream function of the total mean flow for the sine-bracket truncation, 11×11 truncation size, $E = 7$, $\mathcal{E} = 20$, $\tilde{C}_3 = 4$

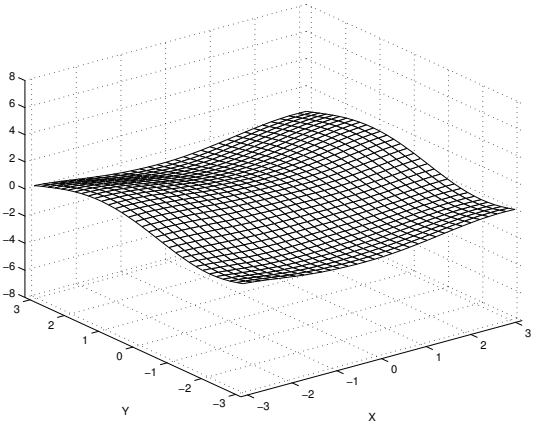

The stream function of the total mean flow for the sine-bracket truncation, 23×23 truncation size, $E = 7$, $\mathcal{E} = 20$, $\tilde{C}_3 = 4$

Figure 6.2: The total mean stream functions for the sine-bracket truncation, 11×11 and 23×23 truncation sizes, $\tilde{C}_3 = 4$, no topography

direct numerical simulations with the traditional truncation in Figure 5.3, and expected to be flat, are the same for the sine-bracket truncation with $\tilde{C}_3 = 0$, which is shown in Figure 6.4 for both 11×11 and 23×23 sine-bracket truncation. This again confirms that $\tilde{C}_3 = 0$ is irrelevant to the statistical predictions. However, the variances of the stream functions for the sine-bracket truncation with $\tilde{C}_3 = 4$, which are shown in Figure 6.5, exhibit more distortions from the test result for the traditional truncation (Figure 5.3), and in case with 23×23 size sine-bracket truncation the variance is not flat at all. Thus, we conclude that $\tilde{C}_3 = 4$ is relevant for the variance of the stream function. Now let us look at the variances of the stream functions for the sine-bracket truncation with $\tilde{C}_3 = 8$, which are shown in Figure 6.6. As we can see, the variances for $\tilde{C}_3 = 8$ exhibit huge distortions from the flat variance for the traditional truncation (Figure 5.3). We conclude that $\tilde{C}_3 = 8$ is strongly relevant for the variances of the stream function. Note that the influence of $\tilde{C}_3$ depends also on the size of truncation: for larger size the influence is greater for the same value of $\tilde{C}_3$.

The skewness of the stream functions for the 11×11 and 23×23 sizes of the sine-bracket truncation (4.1) are presented in Figure 6.7 for $\tilde{C}_3 = 0$, Figure 6.8 for $\tilde{C}_3 = 4$, and Figure 6.9 for $\tilde{C}_3 = 8$. The spatially averaged skewness for all simulations with the sine-bracket truncation and no topography is shown in Table 6.1. The skewness predicted by the theory in (3.26), confirmed by the direct numerical simulations with the

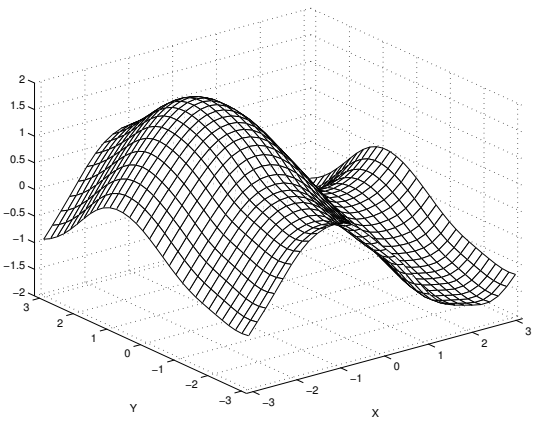

The stream function of the total mean flow for the sine-bracket truncation, 11×11 truncation size, $E = 7$, $\mathcal{E} = 20$, $\tilde{C}_3 = 8$

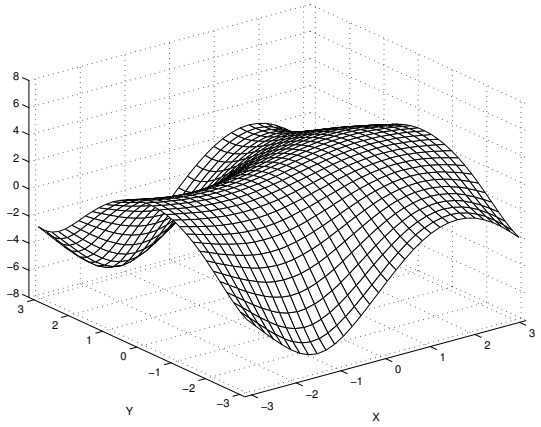

The stream function of the total mean flow for the sine-bracket truncation, 23×23 truncation size, $E = 7$, $\mathcal{E} = 20$, $\tilde{C}_3 = 8$

Figure 6.3: The total mean stream functions for the sine-bracket truncation, 11×11 and 23×23 truncation sizes, $\tilde{C}_3 = 8$, no topography

traditional truncation in Figure 5.4, and expected to be zero, is the same for the sine-bracket truncation with $\tilde{C}_3 = 0$, which is shown in Figure 6.7 for both 11×11 and 23×23 sine-bracket truncation, and in Table 6.1 its averaged value is $4.749 \cdot 10^{-3}$ for the 11×11 truncation size, and $1.461 \cdot 10^{-3}$ for the 23×23 truncation size. This again confirms that $\tilde{C}_3 = 0$ is irrelevant to the statistical predictions. However, the skewness of the stream functions for the sine-bracket truncation with $\tilde{C}_3 = 4$, which is shown in Figure 6.8, falls below zero, while retaining the flat shape, and its averaged value, shown in Table 6.1, -0.7936 for 11×11 truncation size, and -1.006 for 23×23 truncation size. Thus, we conclude that $\tilde{C}_3 = 4$ is relevant for the skewness of the stream function. Now let us look at the skewness of the stream function for the sine-bracket truncation with $\tilde{C}_3 = 8$, which is shown in Figure 6.9 for both 11×11 and 23×23 truncation sizes. As we can see, the skewness for $\tilde{C}_3 = 8$ does not retain the flat shape and is significantly distorted. We conclude that $\tilde{C}_3 = 8$ is strongly relevant for the skewness of the stream function. Note that the influence of $\tilde{C}_3$ depends also on the size of truncation: for larger size the influence is greater for the same value of $\tilde{C}_3$.

The flatness of the stream functions for the 11×11 and 23×23 sizes of the sine-bracket truncation (4.1) are presented in Figure 6.10 for $\tilde{C}_3 = 0$, Figure 6.11 for $\tilde{C}_3 = 4$, and Figure 6.12 for $\tilde{C}_3 = 8$. The spatially averaged flatness for all simulations with the sine-bracket truncation and no topography is shown in Table 6.1. The flatness obtained

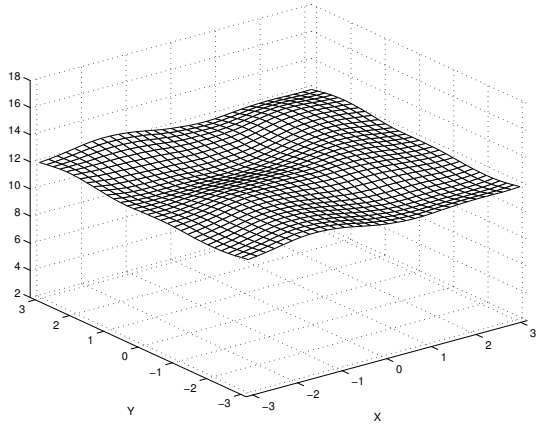

The variance of the stream function for the sine-bracket truncation, 11×11 truncation size, $E = 7$, $\mathcal{E} = 20$, $\tilde{C}_3 = 0$

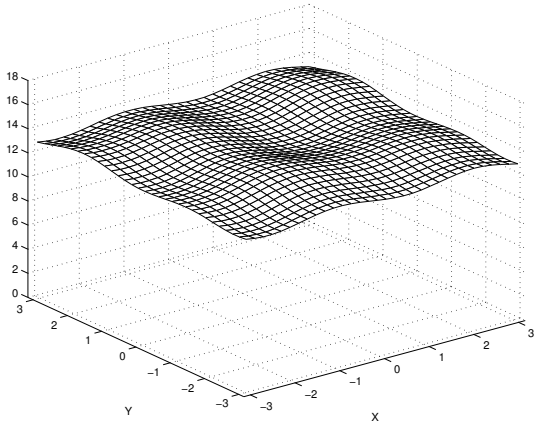

The variance of the stream function for the sine-bracket truncation, 23×23 truncation size, $E = 7$, $\mathcal{E} = 20$, $\tilde{C}_3 = 0$

Figure 6.4: The variances of the total mean stream functions for the sine-bracket truncation, 11×11 and 23×23 truncation sizes, $\tilde{C}_3 = 0$, no topography

by the direct numerical simulations with the traditional truncation in Figure 5.5 has a flat shape and is centered at 2. For the sine-bracket truncation with $\tilde{C}_3 = 0$, the flatness is also flat and centered at 2, which is shown in Figure 6.10 for both 11×11 and 23×23 sine-bracket truncation. Table 6.1 shows averaged values of flatness, which equals 2.027 for both 11×11 and 23×23 truncation sizes. This again confirms that $\tilde{C}_3 = 0$ is irrelevant to the statistical predictions. However, the flatness of the stream functions for the sine-bracket truncation with $\tilde{C}_3 = 4$, which is shown in Figure 6.11, is distorted for both 11×11 and 23×23 sizes of truncations, and we note that in case with 23×23 truncation size it is distorted much more than for 11×11 case. Thus, we conclude that $\tilde{C}_3 = 4$ is relevant for the skewness of the stream function. Now let us look at the flatness of the stream function for the sine-bracket truncation with $\tilde{C}_3 = 8$, which is shown in Figure 6.12 for both 11×11 and 23×23 truncation sizes. As we can see, the flatness for $\tilde{C}_3 = 8$ does not retain the flat shape and is significantly distorted. We conclude that $\tilde{C}_3 = 8$ is strongly relevant for the skewness of the stream function. Note that the influence of $\tilde{C}_3$ depends also on the size of truncation: for larger size the influence is greater for the same value of $\tilde{C}_3$.

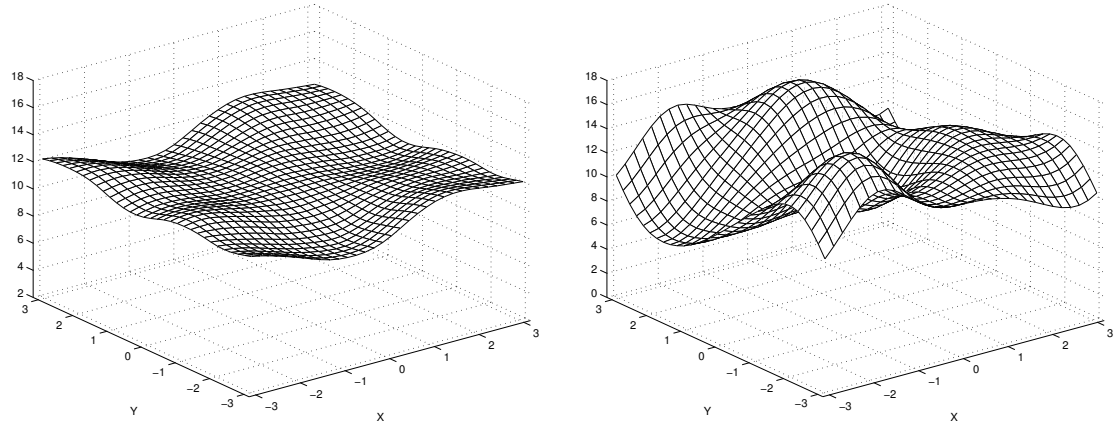

The variance of the stream function for the sine-bracket truncation, 11×11 truncation size, $E = 7$, $\mathcal{E} = 20$, $\tilde{C}_3 = 4$

The variance of the stream function for the sine-bracket truncation, 23×23 truncation size, $E = 7$, $\mathcal{E} = 20$, $\tilde{C}_3 = 4$

Figure 6.5: The variances of the total mean stream functions for the sine-bracket truncation, 11×11 and 23×23 truncation sizes, $\tilde{C}_3 = 4$, no topography

11×11			23×23		
$\tilde{C}_3$	μ	α	$\tilde{C}_3$	μ	α
0	-1.042	4.895	0	-1.001	20.51
4	-1.059	4.792	4	-1.095	20.38
8	-1.035	5.063	8	-1.237	21.53

Table 6.2: The numerically determined parameters μ and α for the sine-bracket truncation, no topography

6.1.2 The mean energy and pseudo-energy spectra

The pseudo-energy spectrum and energy of the mean spectrum calculated by the sine-bracket truncation (4.1) are presented in Figures 6.13 and 6.14 for the two sizes of truncations, 11×11 and 23×23 Fourier modes, and the values of the normalized third Casimir $\tilde{C}_3 = 0$, 4, and 8, where $\tilde{C}_3$ is given by (6.1). We use the equations (5.4) and (5.5) described in Section 5.0.3 to compute the mean energy and pseudo-energy spectra. In order to represent the result for the pseudo-energy in the pseudo-energy variables (3.48), we used the numerically calculated parameters μ and α which are shown in Table 6.2. According to the theoretical prediction in (3.50), the pseudo-energy should be equipartitioned in spectral space for the traditional truncation (3.17), and this is confirmed by the direct numerical simulations with the traditional truncation (3.17) in the Section 5.1.2

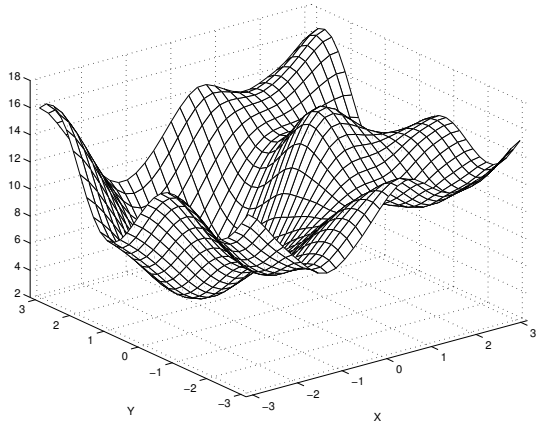

The variance of the stream function for the sine-bracket truncation, 11×11 truncation size, $E = 7$, $\mathcal{E} = 20$, $\tilde{C}_3 = 8$

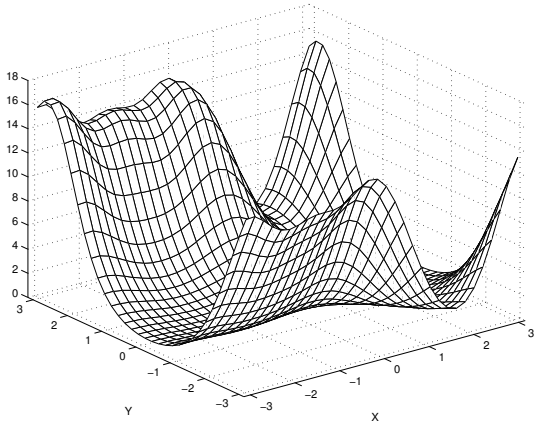

The variance of the stream function for the sine-bracket truncation, 23×23 truncation size, $E = 7$, $\mathcal{E} = 20$, $\tilde{C}_3 = 8$

Figure 6.6: The variances of the total mean stream functions for the sine-bracket truncation, 11×11 and 23×23 truncation sizes, $\tilde{C}_3 = 8$, no topography

in Figures 5.6 and 5.7. As we can see in Figures 6.13 and 6.14, the equipartition holds very well for the pseudo-energy in case with $\tilde{C}_3 = 0$ (solid line with circles) for both 11×11 and 23×23 truncation sizes. However, as $\tilde{C}_3$ increases, becoming relevant, the pseudo-energy spectrum is no more equipartitioned, and here we can see that the size of the sine-bracket truncation (4.1) makes difference. While the results for relevant values of $\tilde{C}_3 = 4$ and $\tilde{C}_3 = 8$ and 11×11 truncation size (dashed and dot-dashed lines in Figure 6.13) diverge up and down from the predicted horizontal line for different Fourier modes, the pseudo-energy spectra for the 23×23 exhibit different and well-quantifiable trend: they fall below predicted value except for a few large-scale modes (shown in Figure 6.14, dashed and dot-dashed lines). This systematic lowering of the pseudo-energy spectrum happens in Overall, we can see that for both 11×11 and 23×23 pseudo-energy spectra the non-uniform structure which is developed for $\tilde{C}_3 = 4$, is essentially amplified for $\tilde{C}_3 = 8$ (Figures 6.13 and 6.14).

As for the energy of the mean state, the statistical theory in (3.46a) states that in the absence of the topography it should be zero, and this is confirmed by the direct simulations with the traditional truncation (3.17) (Section 5.1.2, Figures 5.6 and 5.7). As shown in Figures 6.13 and 6.14, obtained with the sine-bracket truncation (4.1), for the statistically irrelevant value $\tilde{C}_3 = 0$ (solid line) the amount of energy in the Fourier mode

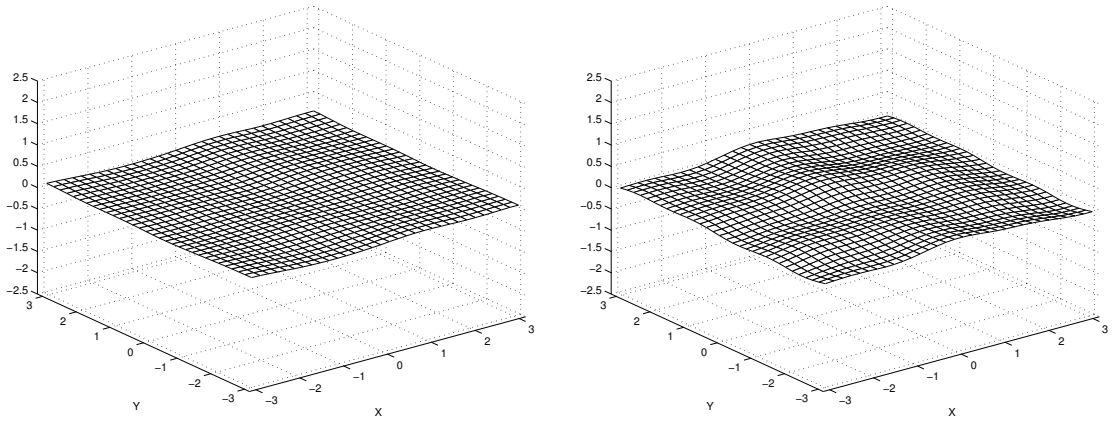

The skewness of the stream function for the sine-bracket truncation, 11×11 truncation size, $E = 7$, $\mathcal{E} = 20$, $\tilde{C}_3 = 0$

The skewness of the stream function for the sine-bracket truncation, 23×23 truncation size, $E = 7$, $\mathcal{E} = 20$, $\tilde{C}_3 = 0$

Figure 6.7: The skewness of the total mean stream functions for the sine-bracket truncation, 11×11 and 23×23 truncation sizes, $\tilde{C}_3 = 0$, no topography

$|\mathbf{k}|^2 = 1$ is very close to zero in comparison with the results for $\tilde{C}_3 = 4$ and $\tilde{C}_3 = 8$ (dashed and dot-dashed lines, respectively). Thus, we can see in Figures 6.13 and 6.14, that the statistically relevant value of $\tilde{C}_3$ creates the large-scale mean flow, and the larger the truncation size, the more energy is contained in the mean state. Overall, we conclude that $\tilde{C}_3 = 0$ is statistically irrelevant in pseudo-energy and mean energy predictions, and $\tilde{C}_3 = 4$, $\tilde{C}_3 = 8$ are statistically relevant.

6.1.3 Total and coarse-grained "Corr" functions and scatterplots

The total and coarse-grained Corr functions for the numerical simulations with the 11×11 and 23×23 sine-bracket truncations (4.1) for the values of the normalized third Casimir invariant $\tilde{C}_3 = 0$, 4, and 8 are shown in Figures 6.15 and 6.16. We use the equation (5.7) described in Section 5.0.3 to compute the Corr functions and associated scatterplots. The theoretical relation (3.28) predicts that the Corr functions must eventually converge to -1 for negative μ's, thus showing that the mean state is collinear. This is also confirmed by the direct simulations with the traditional truncation (3.17) in Section 5.1.3, Figures 5.8 and 5.9. Here we can see the differences in behavior between different sizes of truncations. For the 11×11 sine-bracket truncation (4.1), the collinearity in the mean state is essentially the same for all values of $\tilde{C}_3$, which is shown in Figure 6.15. However, for the 23×23 sine-bracket truncation the collinearity in the mean state depends

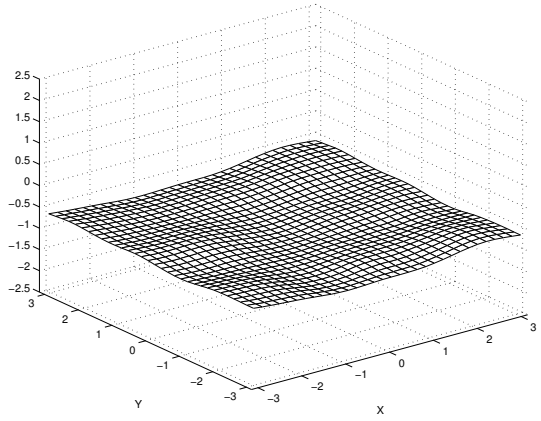

The skewness of the stream function for the sine-bracket truncation, 11×11 truncation size, $E = 7$, $\mathcal{E} = 20$, $\tilde{C}_3 = 4$

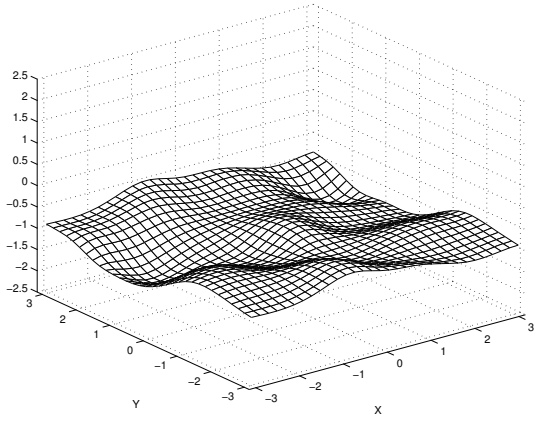

The skewness of the stream function for the sine-bracket truncation, 23×23 truncation size, $E = 7$, $\mathcal{E} = 20$, $\tilde{C}_3 = 4$

Figure 6.8: The skewness of the total mean stream functions for the sine-bracket truncation, 11×11 and 23×23 truncation sizes, $\tilde{C}_3 = 4$, no topography

strongly on the value of $\tilde{C}_3$, which is shown in Figure 6.16. We can see that for the statistically relevant values $\tilde{C}_3 = 4$ and $\tilde{C}_3 = 8$ the mean state loses collinearity as $\tilde{C}_3$ increases. Also Figure 6.16 shows that as $\tilde{C}_3$ becomes statistically relevant, the coarse-grained Corr functions are not more collinear than their total counterparts, unlike 11×11 sine-bracket truncation (Figure 6.15), or the traditional truncation (Figures 5.8 and 5.9).

As well as Corr functions, we present the scatterplots $\bar{q}$ vs $\bar{\psi}$ for all points in the physical space grid. The scatterplots for both 11×11 and 23×23 sizes of the sine-bracket truncation and $\tilde{C}_3 = 0$, 4, and 8 are shown in Figures 6.17, 6.18, 6.19, 6.20, 6.21, and 6.22. As we can see, the $\tilde{C}_3$ does not have much influence on the the scatterplots for 11×11 sine-bracket truncation, and the corresponding scatterplots show approximately the same amount of collinearity for all values of the normalized third Casimir (Figures 6.17, 6.18, and 6.19). However, the statistically relevant values $\tilde{C}_3 = 4$ and $\tilde{C}_3 = 8$ affect the collinearity in the mean state (Figures 6.20, 6.21, and 6.22). Note that the scatterplot in case with $\tilde{C}_3 = 8$, 23×23 sine-bracket truncation, is significantly bent (Figure 6.22).

Overall, we conclude that for the collinearity of the mean state, the values of $\tilde{C}_3$ away from zero are statistically irrelevant for the 11×11 sine-bracket truncation and they are statistically relevant for the 23×23 sine-bracket truncation.

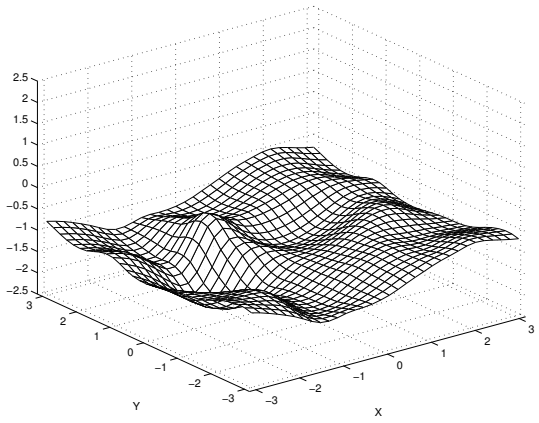

The skewness of the stream function for the sine-bracket truncation, 11×11 truncation size, $E = 7$, $\mathcal{E} = 20$, $\tilde{C}_3 = 8$

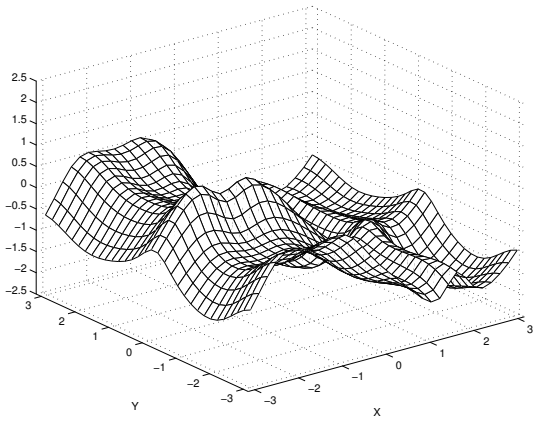

The skewness of the stream function for the sine-bracket truncation, 23×23 truncation size, $E = 7$, $\mathcal{E} = 20$, $\tilde{C}_3 = 8$

Figure 6.9: The skewness of the total mean stream functions for the sine-bracket truncation, 11×11 and 23×23 truncation sizes, $\tilde{C}_3 = 8$, no topography

6.1.4 Time correlation functions

The time correlation functions (5.8) for different Fourier modes for the two sine-bracket truncation sizes, 11×11 and 23×23, are shown in Figures 6.23 and 6.24. We use the equation (5.8) described in Section 5.0.3 to compute the time correlation functions. Here we show that the statistically relevant values of the normalized third Casimir invariant affect the time correlation functions in a very simple way. If we compare the correlation functions for the traditional truncation (3.17), which are shown in Figures 5.12 and 5.13, and the correlation functions for the sine-bracket truncation (4.1) which are shown in Figures 6.23 and 6.24, we can see that the statistically irrelevant value $\tilde{C}_3 = 0$ does not affect the correlation functions for both truncation sizes, but the statistically relevant values $\tilde{C}_3 = 4$ and $\tilde{C}_3 = 8$ slow down the decay rate of correlation functions, and, again, the 23×23 sine-bracket truncation is more sensitive to the influence of relevant $\tilde{C}_3$, than the 11×11 sine-bracket truncation. For the same values of $\tilde{C}_3$, the correlation functions for the 23×23 sine-bracket truncation de-correlate much slower (Figure 6.24), than those for the 11×11 sine-bracket truncation (Figure 6.24). We also note that for the case with 23×23 truncation, $\tilde{C}_3 = 8$ it is not clear whether the statistical results are valid due to the failure of ergodicity.

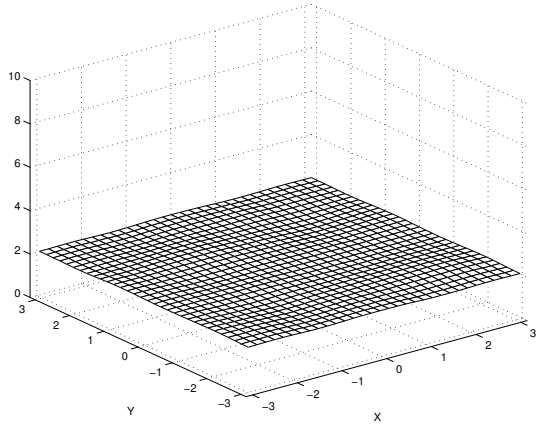

The flatness of the stream function for the sine-bracket truncation, 11×11 truncation size, $E = 7$, $\mathcal{E} = 20$, $\tilde{C}_3 = 0$

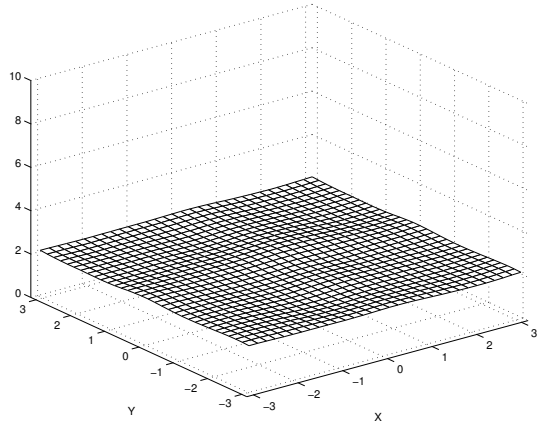

The flatness of the stream function for the sine-bracket truncation, 23×23 truncation size, $E = 7$, $\mathcal{E} = 20$, $\tilde{C}_3 = 0$

Figure 6.10: The flatness of the total mean stream functions for the sine-bracket truncation, 11×11 and 23×23 truncation sizes, $\tilde{C}_3 = 0$, no topography

6.1.5 Probability density functions

The probability density functions for the real parts of the Fourier modes of the potential vorticity obtained with the 23×23 sine-bracket truncation (4.1) for three values of the normalized third Casimir invariant $\tilde{C}_3 = 0$, 4, and 8, where $\tilde{C}_3$ is given by (6.1), are shown in Figures 6.25, 6.26, and 6.27. The numerical algorithm which was used in obtaining the PDF's is described in the Section 5.0.3. According to the statistical predictions (3.37), the shape of the PDF's should be Gaussian, which is confirmed by the direct numerical simulations with the traditional truncation (3.17), Figures 5.15, 5.16, and 5.17. In the Figures 6.25, 6.26, and 6.27 we can see how the statistically relevant values $\tilde{C}_3 = 4$ and $\tilde{C}_3 = 8$ affect the shapes of the probability density functions: the PDF's become bimodal, and the large scale PDF's are more sensitive to the influence of $\tilde{C}_3$. While the PDF's for the statistically irrelevant value $\tilde{C}_3 = 0$ are essentially Gaussian, for the statistically relevant value $\tilde{C}_3 = 4$ the bimodality of the probability density functions arises in the circle $|\mathbf{k}|^2 = 5$ (Figures 6.25 and 6.26, dashed line), and outside this circle the PDF's are unimodal (Figures 6.27, dashed line). However, for $\tilde{C}_3 = 8$ all the PDF's on the 5×5 coarse-grained grid are affected (Figures 6.25, 6.26, and 6.27, dot-dashed line).

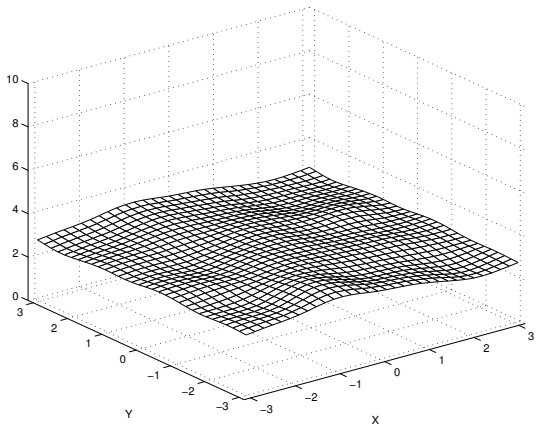

The flatness of the stream function for the sine-bracket truncation, 11×11 truncation size, $E = 7$, $\mathcal{E} = 20$, $\tilde{C}_3 = 4$

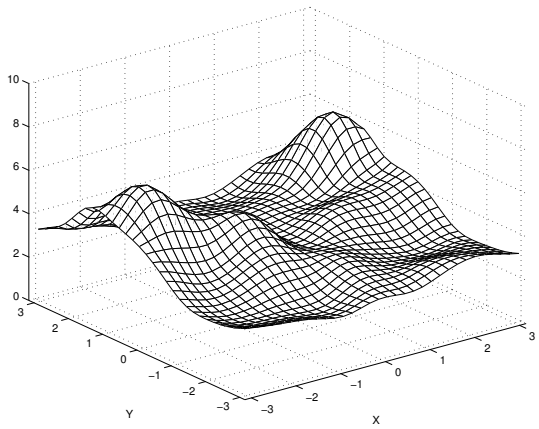

The flatness of the stream function for the sine-bracket truncation, 23×23 truncation size, $E = 7$, $\mathcal{E} = 20$, $\tilde{C}_3 = 4$

Figure 6.11: The flatness of the total mean stream functions for the sine-bracket truncation, 11×11 and 23×23 truncation sizes, $\tilde{C}_3 = 4$, no topography

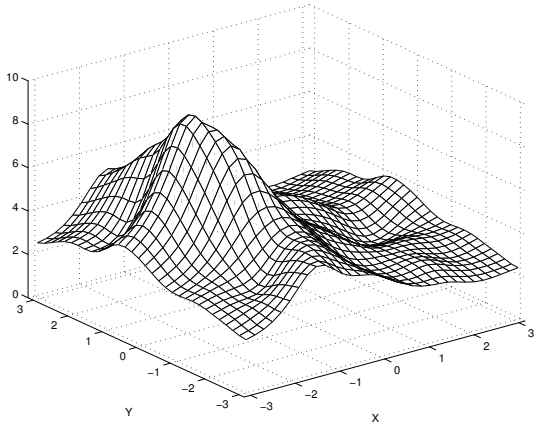

The flatness of the stream function for the sine-bracket truncation, 11×11 truncation size, $E = 7$, $\mathcal{E} = 20$, $\tilde{C}_3 = 8$

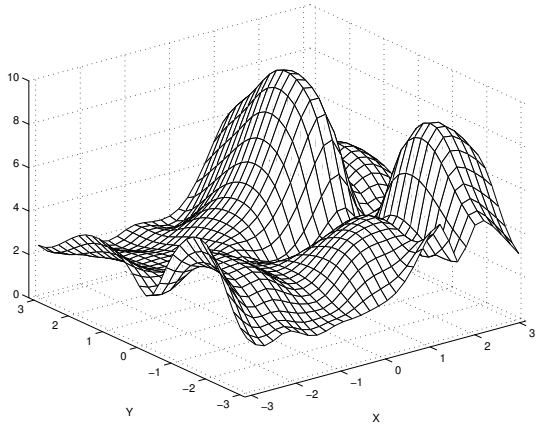

The flatness of the stream function for the sine-bracket truncation, 23×23 truncation size, $E = 7$, $\mathcal{E} = 20$, $\tilde{C}_3 = 8$

Figure 6.12: The flatness of the total mean stream functions for the sine-bracket truncation, 11×11 and 23×23 truncation sizes, $\tilde{C}_3 = 8$, no topography

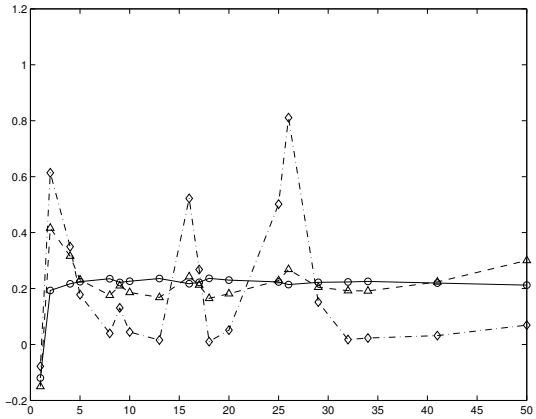

The pseudo-energy spectrum, sine-bracket truncation, 11×11 truncation size, $E = 7$, $\mathcal{E} = 20$, solid line with circles – $\tilde{C}_3 = 0$, dashed line with triangles – $\tilde{C}_3 = 4$, dot-dashed line with diamonds – $\tilde{C}_3 = 8$

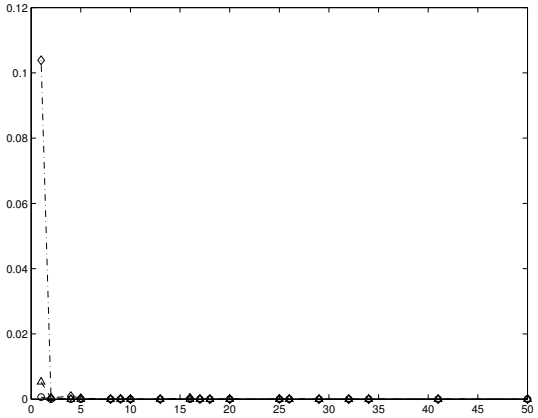

The energy of the mean flow spectrum, sine-bracket truncation, 11×11 truncation size, $E = 7$, $\mathcal{E} = 20$, solid line with circles – $\tilde{C}_3 = 0$, dashed line with triangles – $\tilde{C}_3 = 4$, dot-dashed line with diamonds – $\tilde{C}_3 = 8$

Figure 6.13: The pseudo-energy spectrum and the spectrum of energy of the mean, 11×11 sine-bracket truncation, no topography

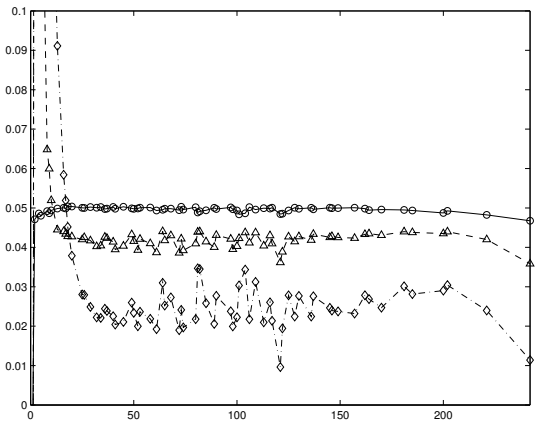

The pseudo-energy spectrum, sine-bracket truncation, 23×23 truncation size, $E = 7$, $\mathcal{E} = 20$, solid line with circles – $\tilde{C}_3 = 0$, dashed line with triangles – $\tilde{C}_3 = 4$, dot-dashed line with diamonds – $\tilde{C}_3 = 8$

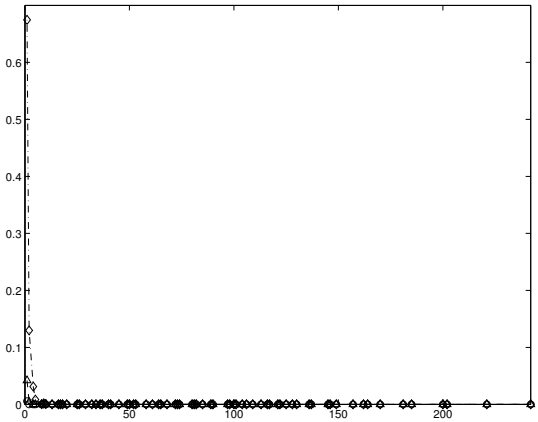

The energy of the mean flow spectrum, sine-bracket truncation, 23×23 truncation size, $E = 7$, $\mathcal{E} = 20$, solid line with circles – $\tilde{C}_3 = 0$, dashed line with triangles – $\tilde{C}_3 = 4$, dot-dashed line with diamonds – $\tilde{C}_3 = 8$

Figure 6.14: The pseudo-energy spectrum and the spectrum of energy of the mean, 23×23 sine-bracket truncation, no topography

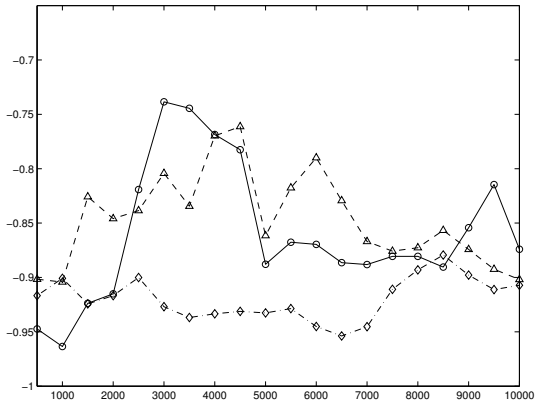

The Corr$[\langle\psi\rangle_\tau, \langle q\rangle_\tau](\tau)$ function for the sine-bracket truncation, 11×11 truncation size, $E = 7$, $\mathcal{E} = 20$, solid line with circles – $\tilde{C}_3 = 0$, dashed line with triangles – $\tilde{C}_3 = 4$, dot-dashed line with diamonds – $\tilde{C}_3 = 8$

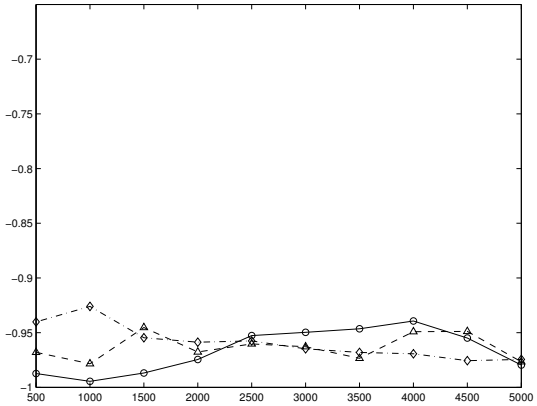

The coarse-grained Corr$[\langle\psi\rangle_\tau, \langle q\rangle_\tau](\tau)$ function for the sine-bracket truncation, 11×11 truncation size, $E = 7$, $\mathcal{E} = 20$, solid line with circles – $\tilde{C}_3 = 0$, dashed line with triangles – $\tilde{C}_3 = 4$, dot-dashed line with diamonds – $\tilde{C}_3 = 8$

Figure 6.15: The total and coarse-grained Corr functions for the sine-bracket truncation, 11×11 truncation size, $\tilde{C}_3 = 0, 4, 8$, no topography

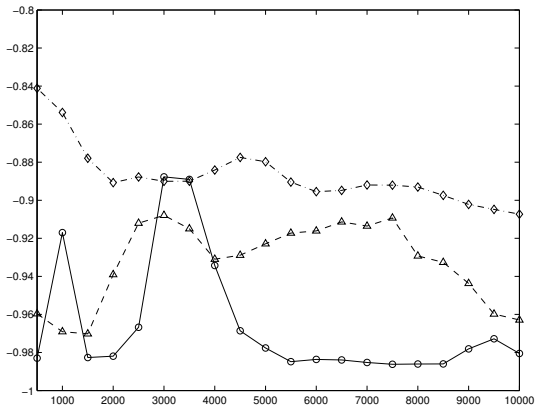

The Corr$[\langle\psi\rangle_\tau, \langle q\rangle_\tau](\tau)$ function for the sine-bracket truncation, 23×23 truncation size, $E = 7$, $\mathcal{E} = 20$, solid line with circles – $\tilde{C}_3 = 0$, dashed line with triangles – $\tilde{C}_3 = 4$, dot-dashed line with diamonds – $\tilde{C}_3 = 8$

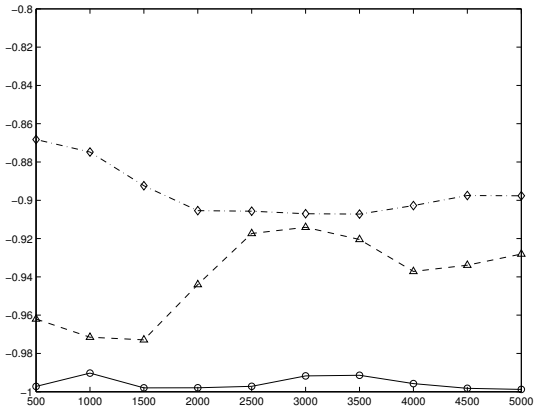

The coarse-grained Corr$[\langle\psi\rangle_\tau, \langle q\rangle_\tau](\tau)$ function for the sine-bracket truncation, 23×23 truncation size, $E = 7$, $\mathcal{E} = 20$, solid line with circles – $\tilde{C}_3 = 0$, dashed line with triangles – $\tilde{C}_3 = 4$, dot-dashed line with diamonds – $\tilde{C}_3 = 8$

Figure 6.16: The total and coarse-grained Corr functions for the sine-bracket truncation, 23×23 truncation size, $\tilde{C}_3 = 0, 4, 8$, no topography

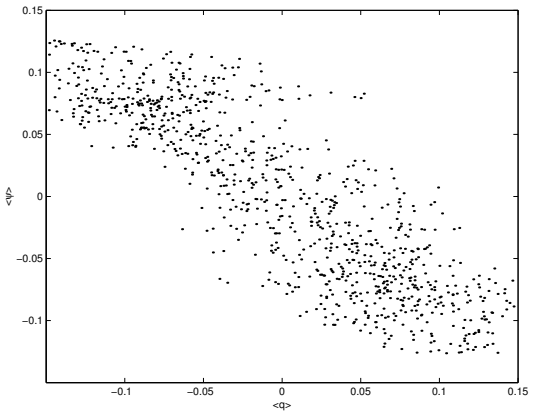

The scatterplot $\langle\psi\rangle_\tau$ vs $\langle q\rangle_\tau$, sine-bracket truncation, 11×11 truncation size, $E = 7$, $\mathcal{E} = 20$, $\tilde{C}_3 = 0$

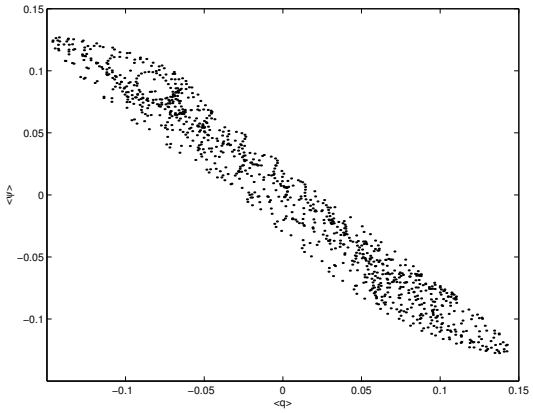

The coarse-grained scatterplot $\langle\psi\rangle_\tau$ vs $\langle q\rangle_\tau$, sine-bracket truncation, 11×11 truncation size, $E = 7$, $\mathcal{E} = 20$, $\tilde{C}_3 = 0$

Figure 6.17: The total and coarse-grained scatterplots $\bar{q}$ vs $\bar{\psi}$, 11×11 sine-bracket truncation, $\tilde{C}_3 = 0$, no topography

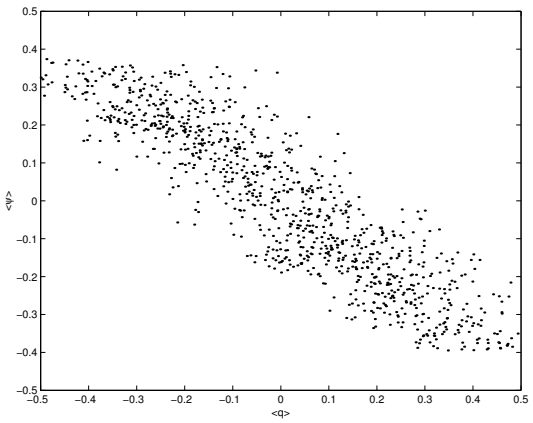

The scatterplot $\langle\psi\rangle_\tau$ vs $\langle q\rangle_\tau$, sine-bracket truncation, 11×11 truncation size, $E = 7$, $\mathcal{E} = 20$, $\tilde{C}_3 = 4$

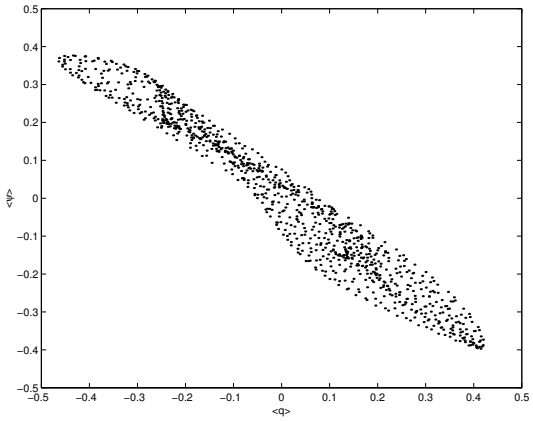

The coarse-grained scatterplot $\langle\psi\rangle_\tau$ vs $\langle q\rangle_\tau$, sine-bracket truncation, 11×11 truncation size, $E = 7$, $\mathcal{E} = 20$, $\tilde{C}_3 = 4$

Figure 6.18: The total and coarse-grained scatterplots $\bar{q}$ vs $\bar{\psi}$, 11×11 sine-bracket truncation, $\tilde{C}_3 = 4$, no topography

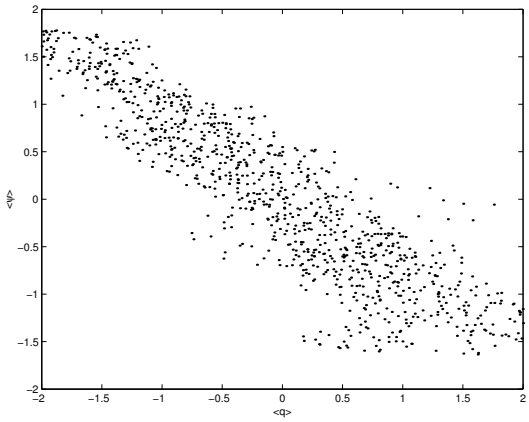

The scatterplot $\langle\psi\rangle_\tau$ vs $\langle q\rangle_\tau$, sine-bracket truncation, 11×11 truncation size, $E = 7$, $\mathcal{E} = 20$, $\tilde{C}_3 = 8$

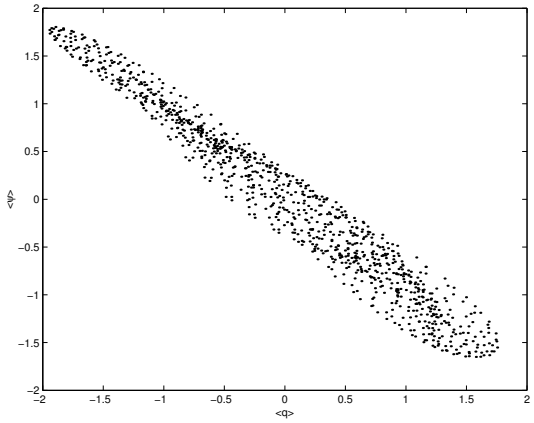

The coarse-grained scatterplot $\langle\psi\rangle_\tau$ vs $\langle q\rangle_\tau$, sine-bracket truncation, 11×11 truncation size, $E = 7$, $\mathcal{E} = 20$, $\tilde{C}_3 = 8$

Figure 6.19: The total and coarse-grained scatterplots $\bar{q}$ vs $\bar{\psi}$, 11×11 sine-bracket truncation, $\tilde{C}_3 = 8$, no topography

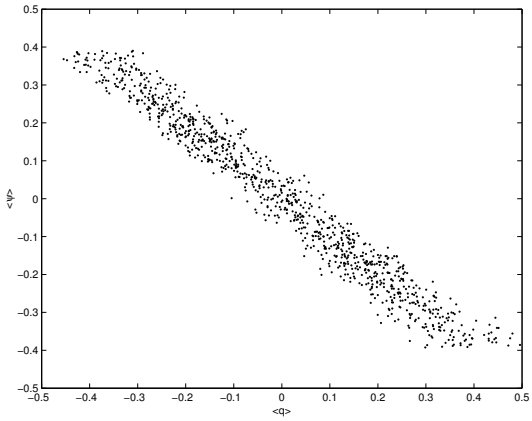

The scatterplot $\langle\psi\rangle_\tau$ vs $\langle q\rangle_\tau$, sine-bracket truncation, 23×23 truncation size, $E = 7$, $\mathcal{E} = 20$, $\tilde{C}_3 = 0$

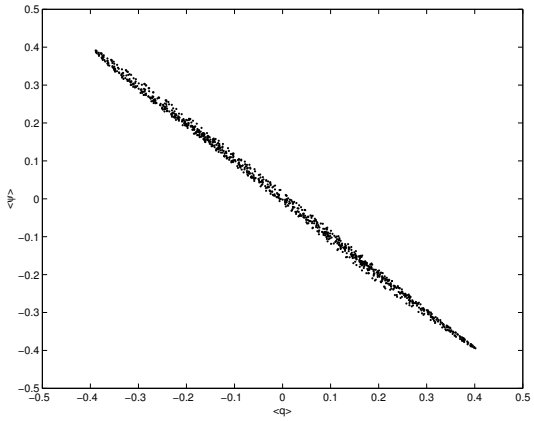

The coarse-grained scatterplot $\langle\psi\rangle_\tau$ vs $\langle q\rangle_\tau$, sine-bracket truncation, 23×23 truncation size, $E = 7$, $\mathcal{E} = 20$, $\tilde{C}_3 = 0$

Figure 6.20: The total and coarse-grained scatterplots $\bar{q}$ vs $\bar{\psi}$, 23×23 sine-bracket truncation, $\tilde{C}_3 = 0$, no topography

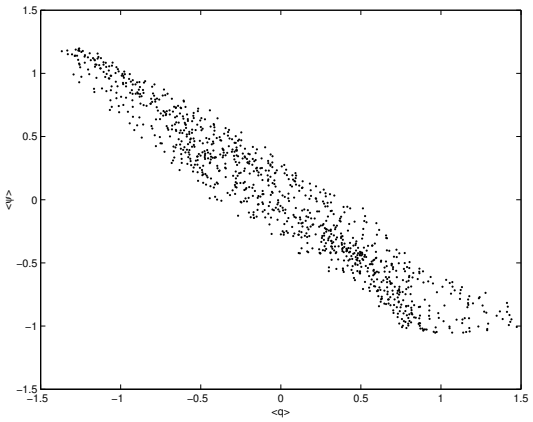

The scatterplot $\langle\psi\rangle_\tau$ vs $\langle q\rangle_\tau$, sine-bracket truncation, 23×23 truncation size, $E = 7$, $\mathcal{E} = 20$, $\tilde{C}_3 = 4$

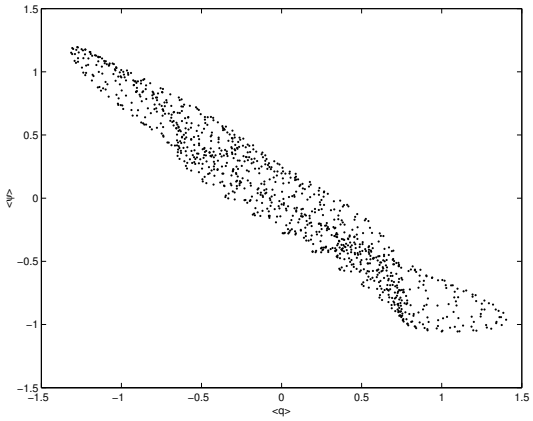

The coarse-grained scatterplot $\langle\psi\rangle_\tau$ vs $\langle q\rangle_\tau$, sine-bracket truncation, 23×23 truncation size, $E = 7$, $\mathcal{E} = 20$, $\tilde{C}_3 = 4$

Figure 6.21: The total and coarse-grained scatterplots $\bar{q}$ vs $\bar{\psi}$, 23×23 sine-bracket truncation, $\tilde{C}_3 = 4$, no topography

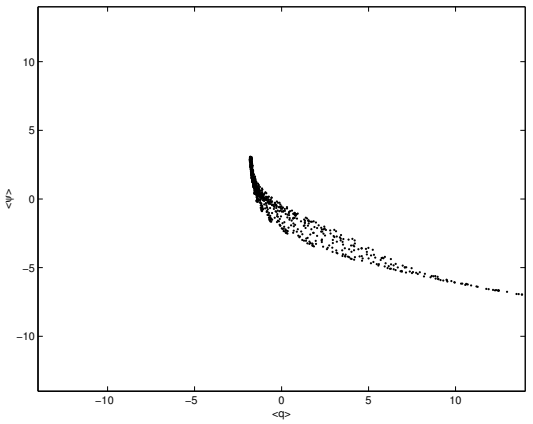

The scatterplot $\langle\psi\rangle_\tau$ vs $\langle q\rangle_\tau$, sine-bracket truncation, 23×23 truncation size, $E = 7$, $\mathcal{E} = 20$, $\tilde{C}_3 = 8$

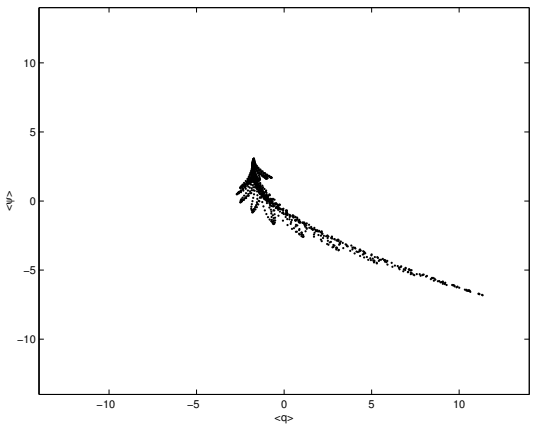

The coarse-grained scatterplot $\langle\psi\rangle_\tau$ vs $\langle q\rangle_\tau$, sine-bracket truncation, 23×23 truncation size, $E = 7$, $\mathcal{E} = 20$, $\tilde{C}_3 = 8$

Figure 6.22: The total and coarse-grained scatterplots $\bar{q}$ vs $\bar{\psi}$, 23×23 sine-bracket truncation, $\tilde{C}_3 = 8$, no topography

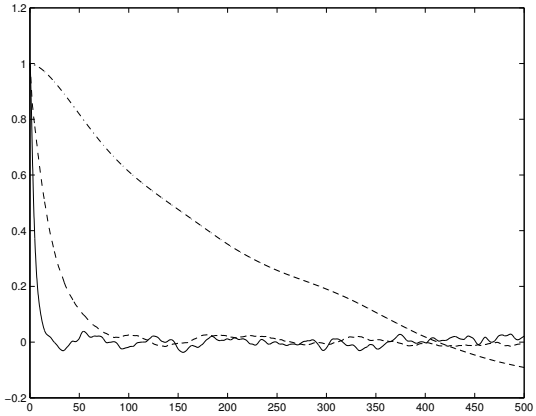

The time correlation functions for $|\mathbf{k}|^2 = 1$, sine-bracket truncation, 11×11 truncation size, $E = 7$, $\mathcal{E} = 20$, solid line – $\tilde{C}_3 = 0$, dashed line – $\tilde{C}_3 = 4$, dot-dashed line – $\tilde{C}_3 = 8$

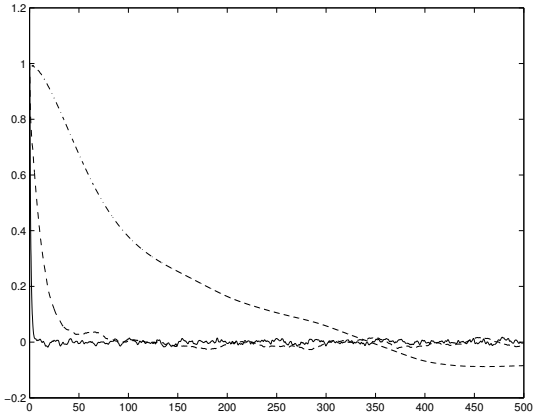

The time correlation functions for $|\mathbf{k}|^2 = 2$, sine-bracket truncation, 11×11 truncation size, $E = 7$, $\mathcal{E} = 20$, solid line – $\tilde{C}_3 = 0$, dashed line – $\tilde{C}_3 = 4$, dot-dashed line – $\tilde{C}_3 = 8$

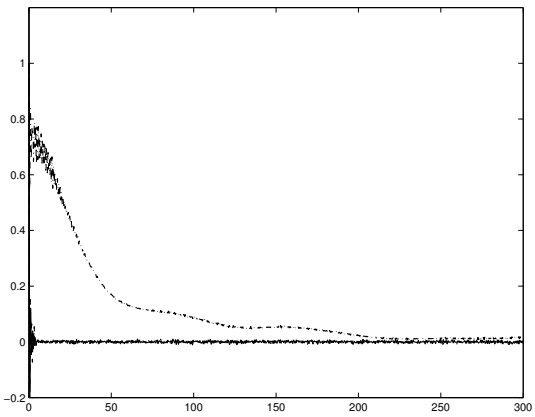

The time correlation functions for $|\mathbf{k}|^2 = 8$, sine-bracket truncation, 11×11 truncation size, $E = 7$, $\mathcal{E} = 20$, solid line – $\tilde{C}_3 = 0$, dashed line – $\tilde{C}_3 = 4$, dot-dashed line – $\tilde{C}_3 = 8$

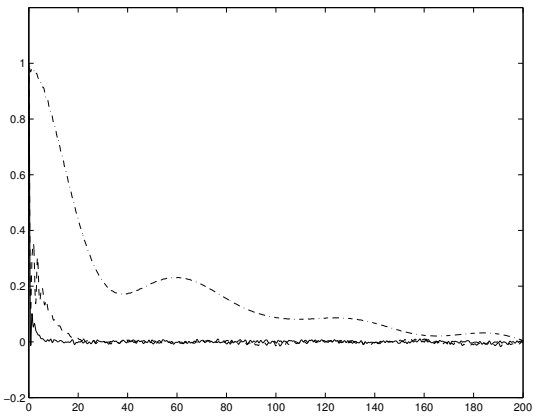

The time correlation functions for $|\mathbf{k}|^2 = 16$, sine-bracket truncation, 11×11 truncation size, $E = 7$, $\mathcal{E} = 20$, solid line – $\tilde{C}_3 = 0$, dashed line – $\tilde{C}_3 = 4$, dot-dashed line – $\tilde{C}_3 = 8$

Figure 6.23: The time correlation functions for the 11×11 sine-bracket truncation, no topography

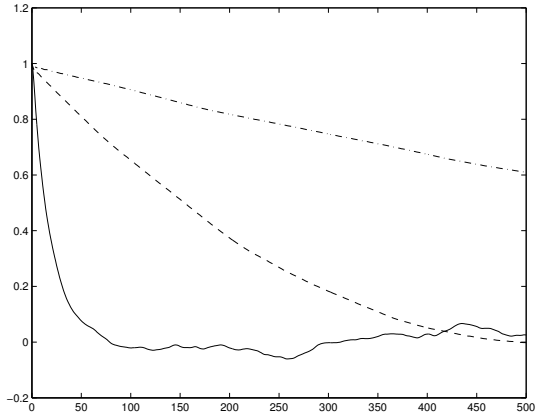

The time correlation functions for $|\mathbf{k}|^2 = 1$, sine-bracket truncation, 23×23 truncation size, $E = 7$, $\mathcal{E} = 20$, solid line – $\tilde{C}_3 = 0$, dashed line – $\tilde{C}_3 = 4$, dot-dashed line – $\tilde{C}_3 = 8$

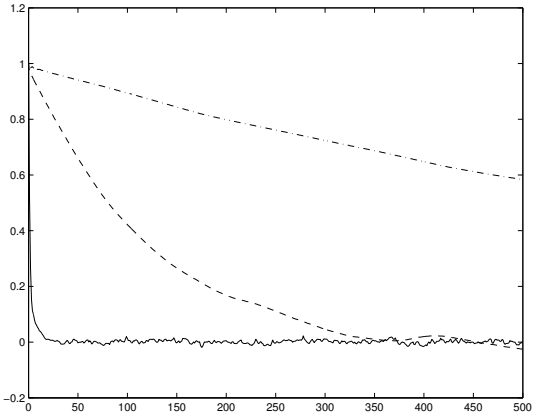

The time correlation functions for $|\mathbf{k}|^2 = 2$, sine-bracket truncation, 23×23 truncation size, $E = 7$, $\mathcal{E} = 20$, solid line – $\tilde{C}_3 = 0$, dashed line – $\tilde{C}_3 = 4$, dot-dashed line – $\tilde{C}_3 = 8$

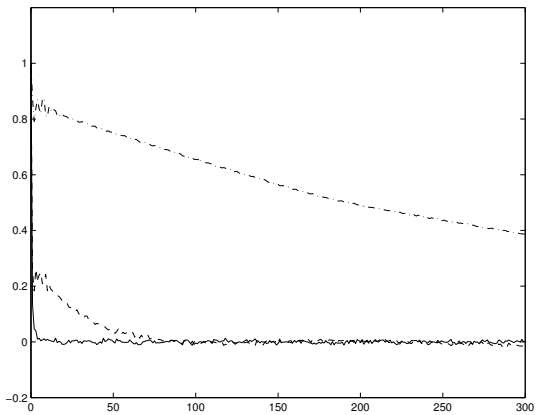

The time correlation functions for $|\mathbf{k}|^2 = 8$, sine-bracket truncation, 23×23 truncation size, $E = 7$, $\mathcal{E} = 20$, solid line – $\tilde{C}_3 = 0$, dashed line – $\tilde{C}_3 = 4$, dot-dashed line – $\tilde{C}_3 = 8$

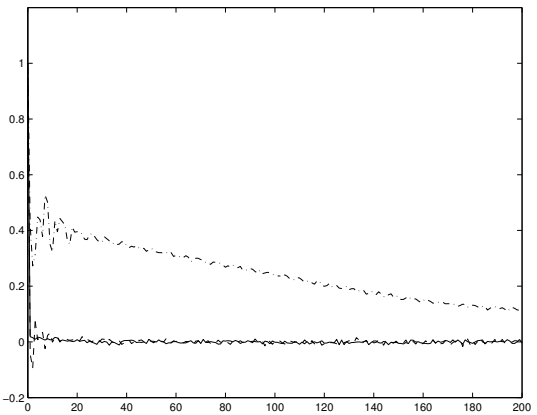

The time correlation functions for $|\mathbf{k}|^2 = 16$, sine-bracket truncation, 23×23 truncation size, $E = 7$, $\mathcal{E} = 20$, solid line – $\tilde{C}_3 = 0$, dashed line – $\tilde{C}_3 = 4$, dot-dashed line – $\tilde{C}_3 = 8$

Figure 6.24: The time correlation functions for the 23×23 sine-bracket truncation, no topography

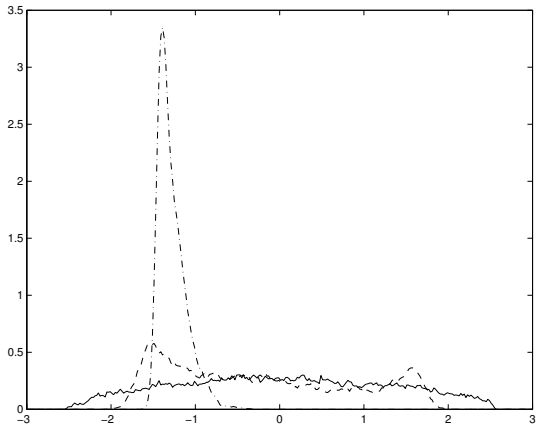

The PDF's for $\mathbf{k} = (1, 0)$, sine-bracket truncation, 23×23 total grid, $E = 7$, $\mathcal{E} = 20$, solid line – $\tilde{C}_3 = 0$, dashed line – $\tilde{C}_3 = 4$, dot-dashed line – $\tilde{C}_3 = 8$

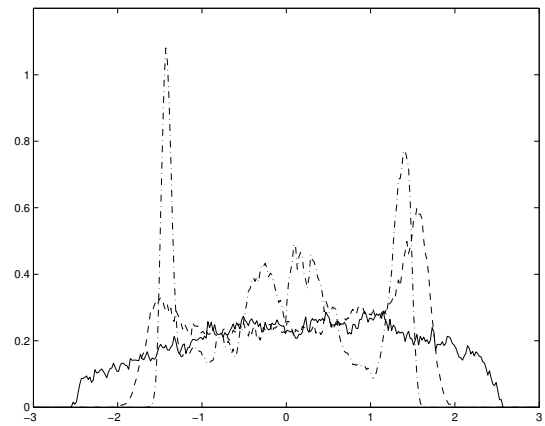

The PDF's for $\mathbf{k} = (0, 1)$, sine-bracket truncation, 23×23 total grid, $E = 7$, $\mathcal{E} = 20$, solid line – $\tilde{C}_3 = 0$, dashed line – $\tilde{C}_3 = 4$, dot-dashed line – $\tilde{C}_3 = 8$

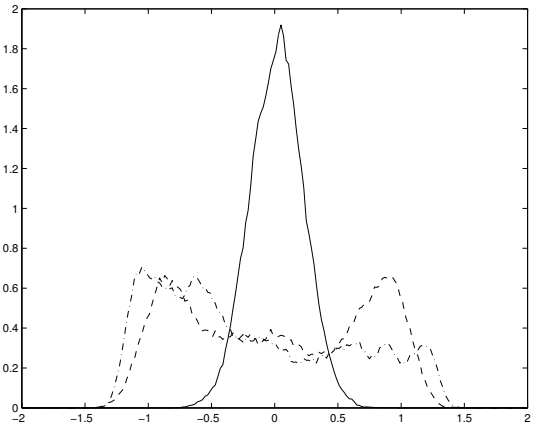

The PDF's for $\mathbf{k} = (-1, 1)$, sine-bracket truncation, 23×23 total grid, $E = 7$, $\mathcal{E} = 20$, solid line – $\tilde{C}_3 = 0$, dashed line – $\tilde{C}_3 = 4$, dot-dashed line – $\tilde{C}_3 = 8$

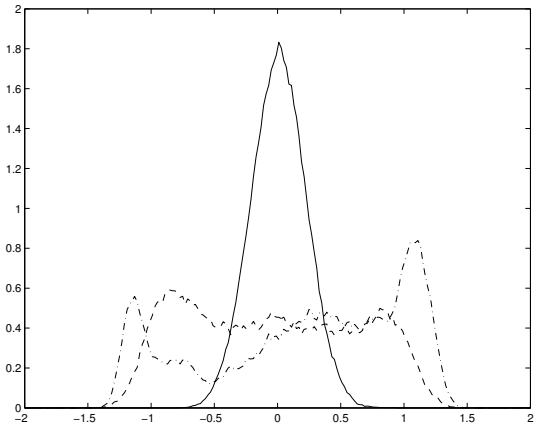

The PDF's for $\mathbf{k} = (1, 1)$, sine-bracket truncation, 23×23 total grid, $E = 7$, $\mathcal{E} = 20$, solid line – $\tilde{C}_3 = 0$, dashed line – $\tilde{C}_3 = 4$, dot-dashed line – $\tilde{C}_3 = 8$

Figure 6.25: The probability density functions for the Fourier modes of the potential vorticity, wavenumbers $(0, 1), (1.0), (-1, 1), (1, 1)$, 23×23 sine-bracket truncation, $\tilde{C}_3 = 0$, 4, and 8, no topography

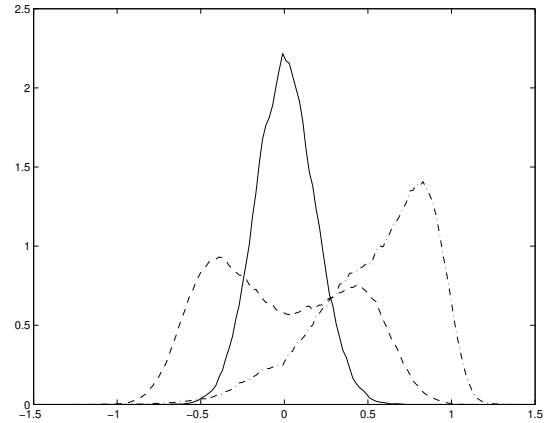

The PDF's for $\mathbf{k} = (2, 0)$, sine-bracket truncation, 23×23 total grid, $E = 7$, $\mathcal{E} = 20$, solid line – $\tilde{C}_3 = 0$, dashed line – $\tilde{C}_3 = 4$, dot-dashed line – $\tilde{C}_3 = 8$

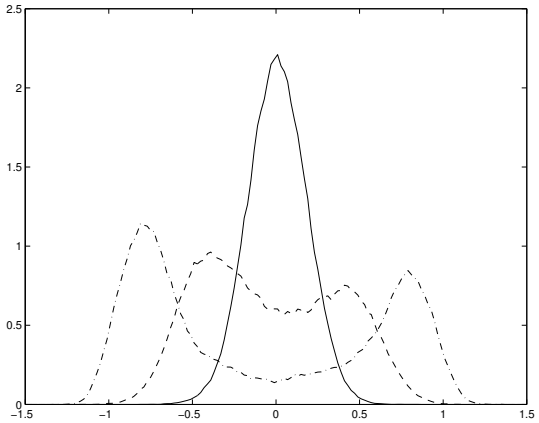

The PDF's for $\mathbf{k} = (0, 2)$, sine-bracket truncation, 23×23 total grid, $E = 7$, $\mathcal{E} = 20$, solid line – $\tilde{C}_3 = 0$, dashed line – $\tilde{C}_3 = 4$, dot-dashed line – $\tilde{C}_3 = 8$

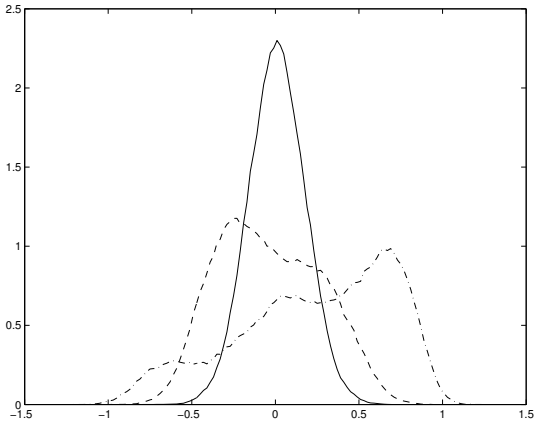

The PDF's for $\mathbf{k} = (-2, 1)$, sine-bracket truncation, 23×23 total grid, $E = 7$, $\mathcal{E} = 20$, solid line – $\tilde{C}_3 = 0$, dashed line – $\tilde{C}_3 = 4$, dot-dashed line – $\tilde{C}_3 = 8$

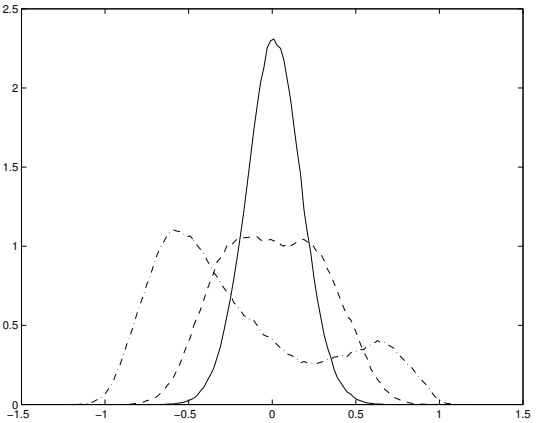

The PDF's for $\mathbf{k} = (2, 1)$, sine-bracket truncation, 23×23 total grid, $E = 7$, $\mathcal{E} = 20$, solid line – $\tilde{C}_3 = 0$, dashed line – $\tilde{C}_3 = 4$, dot-dashed line – $\tilde{C}_3 = 8$

Figure 6.26: The probability density functions for the Fourier modes of the potential vorticity, wavenumbers $(2, 0), (0, 2), (-2, 1), (2, 1)$, 23×23 sine-bracket truncation, $\tilde{C}_3 = 0$, 4, and 8, no topography

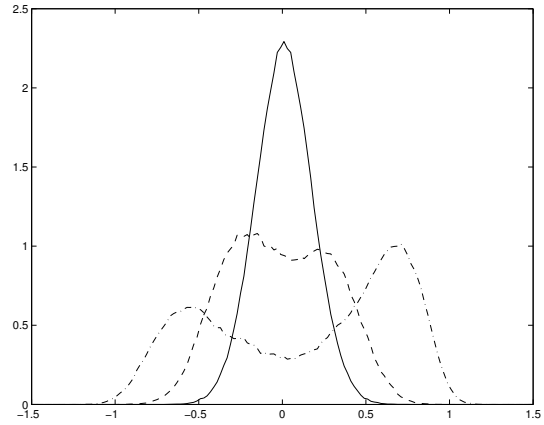

The PDF's for $\mathbf{k} = (-1, 2)$, sine-bracket truncation, 23×23 total grid, $E = 7$, $\mathcal{E} = 20$, solid line – $\tilde{C}_3 = 0$, dashed line – $\tilde{C}_3 = 4$, dot-dashed line – $\tilde{C}_3 = 8$

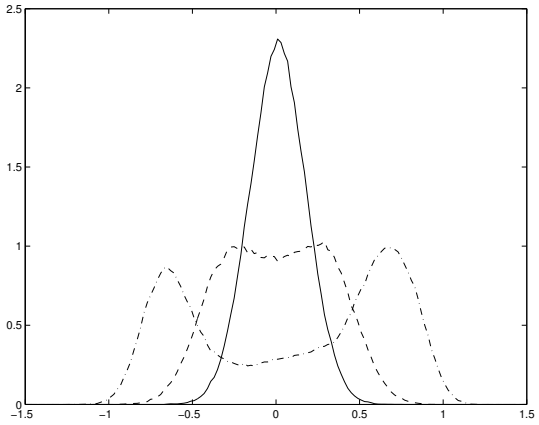

The PDF's for $\mathbf{k} = (1, 2)$, sine-bracket truncation, 23×23 total grid, $E = 7$, $\mathcal{E} = 20$, solid line – $\tilde{C}_3 = 0$, dashed line – $\tilde{C}_3 = 4$, dot-dashed line – $\tilde{C}_3 = 8$

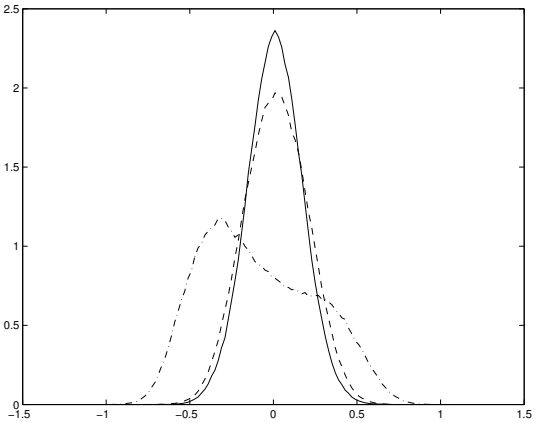

The PDF's for $\mathbf{k} = (-2, 2)$, sine-bracket truncation, 23×23 total grid, $E = 7$, $\mathcal{E} = 20$, solid line – $\tilde{C}_3 = 0$, dashed line – $\tilde{C}_3 = 4$, dot-dashed line – $\tilde{C}_3 = 8$

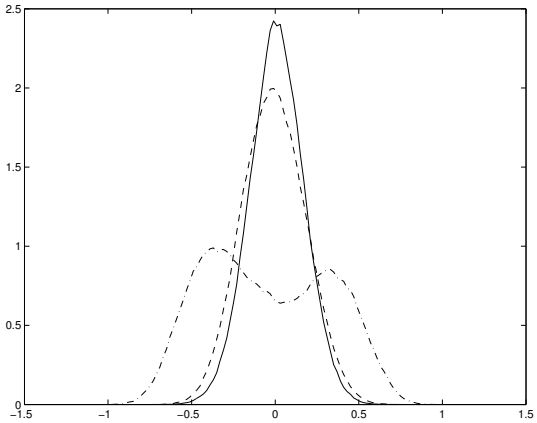

The PDF's for $\mathbf{k} = (2, 2)$, sine-bracket truncation, 23×23 total grid, $E = 7$, $\mathcal{E} = 20$, solid line – $\tilde{C}_3 = 0$, dashed line – $\tilde{C}_3 = 4$, dot-dashed line – $\tilde{C}_3 = 8$

Figure 6.27: The probability density functions for the Fourier modes of the potential vorticity, wavenumbers $(-1, 2), (1, 2), (-2, 2), (2, 2)$, 23×23 sine-bracket truncation, $\tilde{C}_3 = 0$, 4, and 8, no topography

11×11, total Fourier grid		
$\tilde{C}_3$	skewness	flatness
0	$8.454 \cdot 10^{-3}$	2.118
4	-0.9657	3.195
8	-1.321	4.979
11×11, coarse-grained grid		
$\tilde{C}_3$	skewness	flatness
0	$8.552 \cdot 10^{-3}$	2.106
4	-0.9504	3.141
8	-1.336	4.989

23×23, total Fourier grid		
$\tilde{C}_3$	skewness	flatness
0	$1.616 \cdot 10^{-2}$	2.109
4	-0.9495	3.514
8	-1.737	10.04
23×23, coarse-grained grid		
$\tilde{C}_3$	skewness	flatness
0	$1.616 \cdot 10^{-2}$	2.105
4	-0.9503	3.502
8	-1.816	10.76

Table 6.3: The spatially averaged skewness and flatness of the mean stream functions for 11×11 and 23×23 sine-bracket truncation, total and coarse-grained Fourier grids, random topography

6.2 Simulations with random topography

In this section we represent the results obtained for the geophysical case with random topography, which is shown in Figure 5.1. To see the relevance of the 3rd Casimir invariant, we make the direct numerical simulations with three values of $\tilde{C}_3$:

$$\tilde{C}_3 = 0, \quad \tilde{C}_3 = 4, \quad \tilde{C}_3 = 8.$$

We perform the simulations with two different sizes of truncations. For the 11×11 size of truncation we represent the pseudo-energy spectra, "Corr" functions, and correlation functions. For the 23×23 truncation size, in addition to the above, we present the mean stream functions, their variances, skewnesses and flatnesses.

6.2.1 Mean stream functions and their moments

Here we present the mean stream functions (5.2) and their moments (5.3) for the 11×11 and 23×23 size sine-bracket truncation (4.1). Our main purpose is to compare the results for the sine-bracket truncation with the with those for the traditional truncation (3.17) (Figures 5.18, 5.19, 5.20, 5.21, and Table 5.5) for the same geophysical case with random topography. The direct numerical simulations for the sine-bracket truncation were done for the set of initial conditions with energy $E = 7$, enstrophy $\mathcal{E} = 20$, and three different values of the normalized third Casimir invariant $\tilde{C}_3 = 0$, 4, and 8, where $\tilde{C}_3$ is defined by (6.1).

The total mean stream functions for the 11×11 and 23×23 sizes of the sine-bracket truncation (4.1) are presented in Figure 6.28 for $\tilde{C}_3 = 0$, Figure 6.29 for $\tilde{C}_3 = 4$,

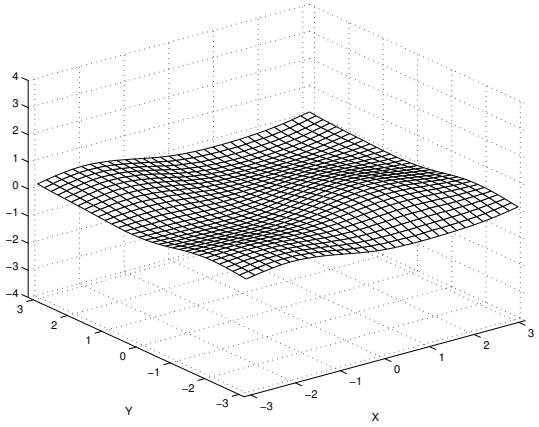

The stream function of the total mean flow for the sine-bracket truncation, 11×11 truncation size, $E = 7$, $\mathcal{E} = 20$, $\tilde{C}_3 = 0$

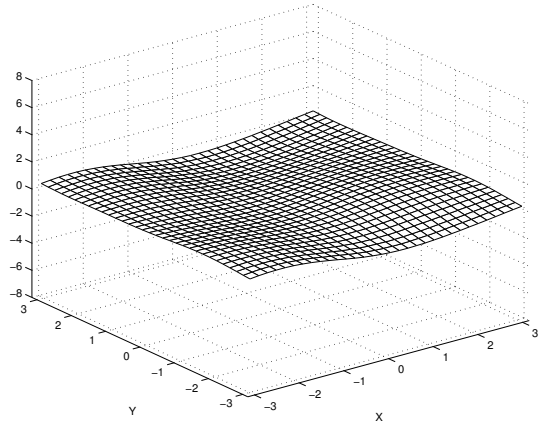

The stream function of the total mean flow for the sine-bracket truncation, 23×23 truncation size, $E = 7$, $\mathcal{E} = 20$, $\tilde{C}_3 = 0$

Figure 6.28: The total mean stream functions for the sine-bracket truncation, 11×11 and 23×23 truncation sizes, $\tilde{C}_3 = 0$, random topography

and Figure 6.30 for $\tilde{C}_3 = 8$. The most probable mean state is given by the statistical theory in (3.29), and is confirmed by the direct simulations with the sine-bracket truncation (3.17), Section 5.2.1, Figures 5.18, 5.19, 5.20, 5.21. This mean state happens to be the same with the sine-bracket truncation and $\tilde{C}_3 = 0$, which is shown in Figure 6.28. Thus, we conclude that $\tilde{C}_3 = 0$ is not relevant for the mean stream function. However, the mean stream functions for the sine-bracket truncation with $\tilde{C}_3 = 4$, which are shown in Figure 6.29, exhibit significant distortions from the mean state for both 11×11 and 23×23 sizes of the sine-bracket truncation. Also we note that the statistically relevant $\tilde{C}_3 = 4$ affects the 23×23 sine-bracket truncation stronger than 11×11 sine-bracket truncation. Thus, we conclude that $\tilde{C}_3 = 4$ is relevant for the mean stream function. Now let us look at the mean stream functions for the sine-bracket truncation with $\tilde{C}_3 = 8$, which are shown in Figure 6.30. We can see that the mean stream functions develop significant distortions for both 11×11 and 23×23 sizes of the sine-bracket truncation, and again statistically relevant $\tilde{C}_3 = 8$ affects the 23×23 sine-bracket truncation stronger than 11×11 sine-bracket truncation. We conclude that $\tilde{C}_3 = 8$ is strongly relevant for the mean stream function. Note that the influence of $\tilde{C}_3$ depends also on the size of truncation: for larger size the influence is greater for the same value of $\tilde{C}_3$.

The variances of the stream functions for the 11×11 and 23×23 sizes of the sine-bracket truncation (4.1) are presented in Figure 6.31 for $\tilde{C}_3 = 0$, Figure 6.32 for $\tilde{C}_3 = 4$,

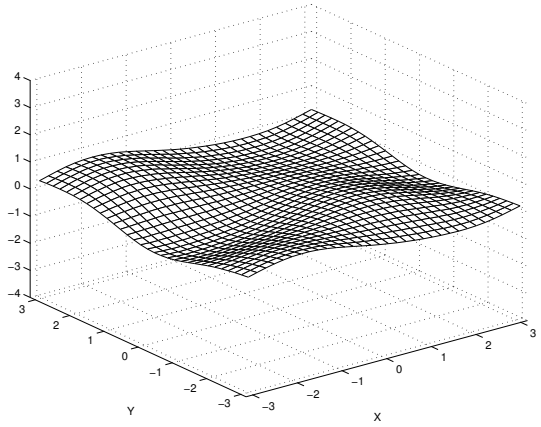

The stream function of the total mean flow for the sine-bracket truncation, 11×11 truncation size, $E = 7$, $\mathcal{E} = 20$, $\tilde{C}_3 = 4$

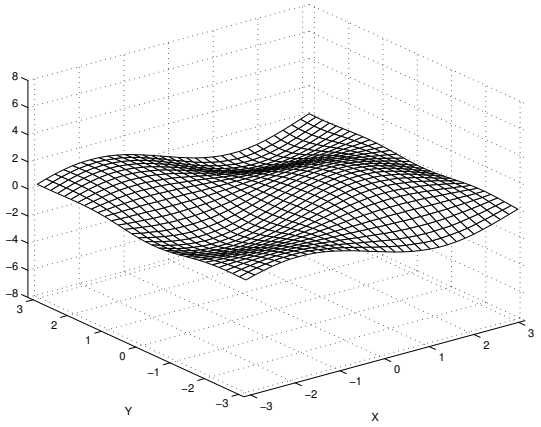

The stream function of the total mean flow for the sine-bracket truncation, 23×23 truncation size, $E = 7$, $\mathcal{E} = 20$, $\tilde{C}_3 = 4$

Figure 6.29: The total mean stream functions for the sine-bracket truncation, 11×11 and 23×23 truncation sizes, $\tilde{C}_3 = 4$, random topography

and Figure 6.33 for $\tilde{C}_3 = 8$. The variances predicted by the theory in (3.30), confirmed by the direct numerical simulations with the traditional truncation in Figure 5.19, and expected to be flat, are the same for the sine-bracket truncation with $\tilde{C}_3 = 0$, which is shown in Figure 6.31 for both 11×11 and 23×23 sine-bracket truncation. This again confirms that $\tilde{C}_3 = 0$ is irrelevant to the statistical predictions. However, the variances of the stream functions for the sine-bracket truncation with $\tilde{C}_3 = 4$, which are shown in Figure 6.32, exhibit more distortions from the test result for the traditional truncation (Figure 5.19), and in case with 23×23 size sine-bracket truncation the variance is not flat at all. Thus, we conclude that $\tilde{C}_3 = 4$ is relevant for the variance of the stream function. Now let us look at the variances of the stream functions for the sine-bracket truncation with $\tilde{C}_3 = 8$, which are shown in Figure 6.33. As we can see, the variances for $\tilde{C}_3 = 8$ exhibit huge distortions from the flat variance for the traditional truncation (Figure 5.19). We conclude that $\tilde{C}_3 = 8$ is strongly relevant for the variances of the stream function. Note that the influence of $\tilde{C}_3$ depends also on the size of truncation: for larger size the influence is greater for the same value of $\tilde{C}_3$.

The skewness of the stream functions for the 11×11 and 23×23 sizes of the sine-bracket truncation (4.1) are presented in Figure 6.34 for $\tilde{C}_3 = 0$, Figure 6.35 for $\tilde{C}_3 = 4$, and Figure 6.36 for $\tilde{C}_3 = 8$. The spatially averaged skewness for all simulations with the sine-bracket truncation and no topography is shown in Table 6.3. The skewness

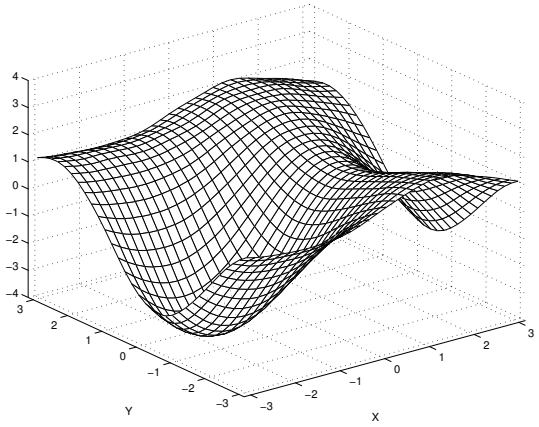

The stream function of the total mean flow for the sine-bracket truncation, 11×11 truncation size, $E = 7$, $\mathcal{E} = 20$, $\tilde{C}_3 = 8$

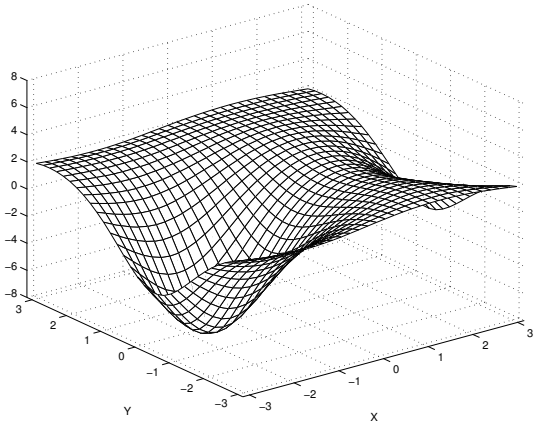

The stream function of the total mean flow for the sine-bracket truncation, 23×23 truncation size, $E = 7$, $\mathcal{E} = 20$, $\tilde{C}_3 = 8$

Figure 6.30: The total mean stream functions for the sine-bracket truncation, 11×11 and 23×23 truncation sizes, $\tilde{C}_3 = 8$, random topography

predicted by the theory in (3.26), confirmed by the direct numerical simulations with the traditional truncation in Figure 5.20, and expected to be zero, is the same for the sine-bracket truncation with $\tilde{C}_3 = 0$, which is shown in Figure 6.34 for both 11×11 and 23×23 sine-bracket truncation, and in Table 6.3 its averaged value is $8.454 \cdot 10^{-3}$ for the 11×11 truncation size, and $1.616 \cdot 10^{-2}$ for the 23×23 truncation size. This again confirms that $\tilde{C}_3 = 0$ is irrelevant to the statistical predictions. However, the skewness of the stream functions for the sine-bracket truncation with $\tilde{C}_3 = 4$, which is shown in Figure 6.35, falls below zero, while retaining the flat shape, and its averaged value, shown in Table 6.3, -0.9495 for 11×11 truncation size, and -0.9504 for 23×23 truncation size. Thus, we conclude that $\tilde{C}_3 = 4$ is relevant for the skewness of the stream function. Now let us look at the skewness of the stream function for the sine-bracket truncation with $\tilde{C}_3 = 8$, which is shown in Figure 6.36 for both 11×11 and 23×23 truncation sizes. As we can see, the skewness for $\tilde{C}_3 = 8$ does not retain the flat shape and is significantly distorted. We conclude that $\tilde{C}_3 = 8$ is strongly relevant for the skewness of the stream function. Note that the influence of $\tilde{C}_3$ depends also on the size of truncation: for larger size the influence is greater for the same value of $\tilde{C}_3$.

The flatness of the stream functions for the 11×11 and 23×23 sizes of the sine-bracket truncation (4.1) are presented in Figure 6.37 for $\tilde{C}_3 = 0$, Figure 6.38 for $\tilde{C}_3 = 4$, and Figure 6.39 for $\tilde{C}_3 = 8$. The spatially averaged flatness for all simulations with the

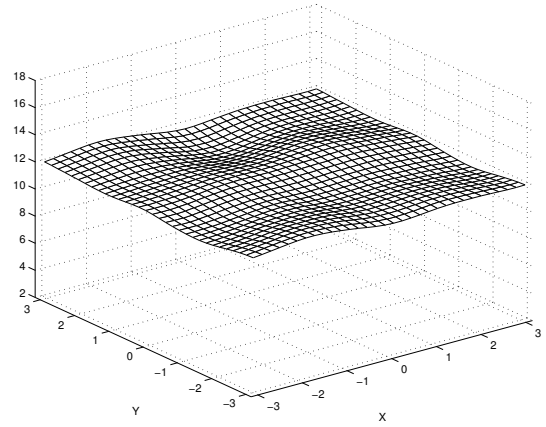

The variance of the stream function for the sine-bracket truncation, 11×11 truncation size, $E = 7$, $\mathcal{E} = 20$, $\tilde{C}_3 = 0$

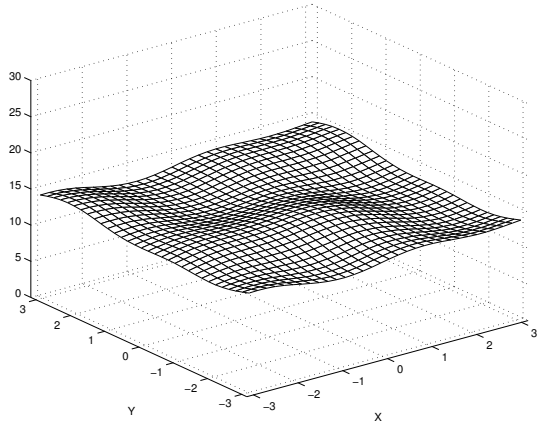

The variance of the stream function for the sine-bracket truncation, 23×23 truncation size, $E = 7$, $\mathcal{E} = 20$, $\tilde{C}_3 = 0$

Figure 6.31: The variances of the total mean stream functions for the sine-bracket truncation, 11×11 and 23×23 truncation sizes, $\tilde{C}_3 = 0$, random topography

sine-bracket truncation and no topography is shown in Table 6.3. The flatness obtained by the direct numerical simulations with the traditional truncation in Figure 5.21 has a flat shape and is centered at 2. For the sine-bracket truncation with $\tilde{C}_3 = 0$, the flatness is also flat and centered at 2, which is shown in Figure 6.37 for both 11×11 and 23×23 sine-bracket truncation. Table 6.3 shows averaged values of flatness, which equals 2.118 for 11×11 and 2.109 for 23×23 truncation sizes. This again confirms that $\tilde{C}_3 = 0$ is irrelevant to the statistical predictions. However, the flatness of the stream functions for the sine-bracket truncation with $\tilde{C}_3 = 4$, which is shown in Figure 6.38, is distorted for both 11×11 and 23×23 sizes of truncations, and we note that in case with 23×23 truncation size it is distorted much more than for 11×11 case. Thus, we conclude that $\tilde{C}_3 = 4$ is relevant for the skewness of the stream function. Now let us look at the flatness of the stream function for the sine-bracket truncation with $\tilde{C}_3 = 8$, which is shown in Figure 6.39 for both 11×11 and 23×23 truncation sizes. As we can see, the flatness for $\tilde{C}_3 = 8$ does not retain the flat shape and is significantly distorted. We conclude that $\tilde{C}_3 = 8$ is strongly relevant for the skewness of the stream function. Note that the influence of $\tilde{C}_3$ depends also on the size of truncation: for larger size the influence is greater for the same value of $\tilde{C}_3$.

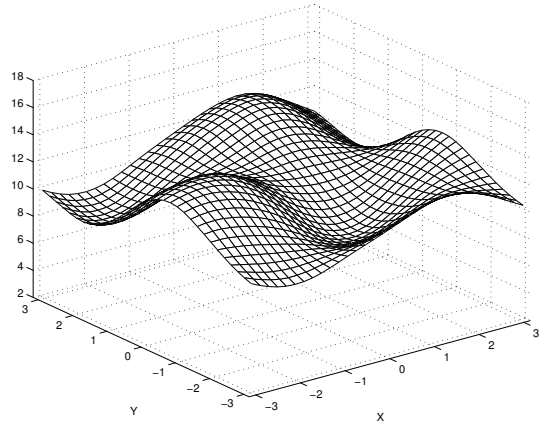

The variance of the stream function for the sine-bracket truncation, 11×11 truncation size, $E = 7$, $\mathcal{E} = 20$, $\tilde{C}_3 = 4$

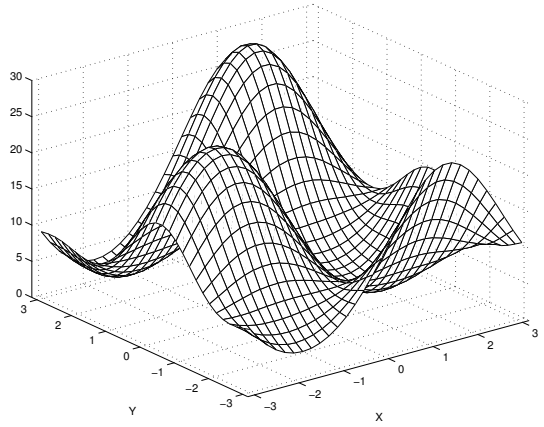

The variance of the stream function for the sine-bracket truncation, 23×23 truncation size, $E = 7$, $\mathcal{E} = 20$, $\tilde{C}_3 = 4$

Figure 6.32: The variances of the total mean stream functions for the sine-bracket truncation, 11×11 and 23×23 truncation sizes, $\tilde{C}_3 = 4$, random topography

11×11			23×23		
$\tilde{C}_3$	μ	α	$\tilde{C}_3$	μ	α
0	-0.9613	4.567	0	-0.9969	20.37
4	-1.209	5.373	4	-1.783	23.56
8	-1.092	4.634	8	-1.365	25.57

Table 6.4: The numerically determined parameters μ and α for the sine-bracket truncation, random topography

6.2.2 The mean energy and pseudo-energy spectra

The pseudo-energy spectrum and energy of the mean spectrum calculated by the sine-bracket truncation (4.1) are presented in Figures 6.40 and 6.41 for the two sizes of truncations, 11×11 and 23×23 Fourier modes, and the values of the normalized third Casimir $\tilde{C}_3 = 0$, 4, and 8, where $\tilde{C}_3$ is given by (6.1). We use the equations (5.4) and (5.5) described in Section 5.0.3 to compute the mean energy and pseudo-energy spectra. In order to represent the result for the pseudo-energy in the pseudo-energy variables (3.48), we used the numerically calculated parameters μ and α which are shown in Table 6.4. According to the theoretical prediction in (3.50), the pseudo-energy should be equipartitioned in spectral space, and this is confirmed by the direct numerical simulations with the traditional truncation (3.17) in the Section 5.2.2 in Figures 5.22 and 5.23. As we can

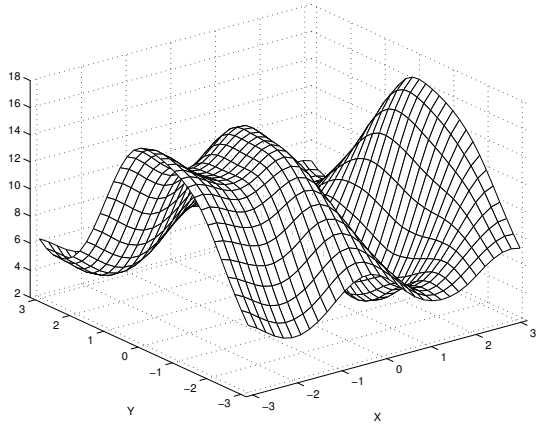

The variance of the stream function for the sine-bracket truncation, 11×11 truncation size, $E = 7$, $\mathcal{E} = 20$, $\tilde{C}_3 = 8$

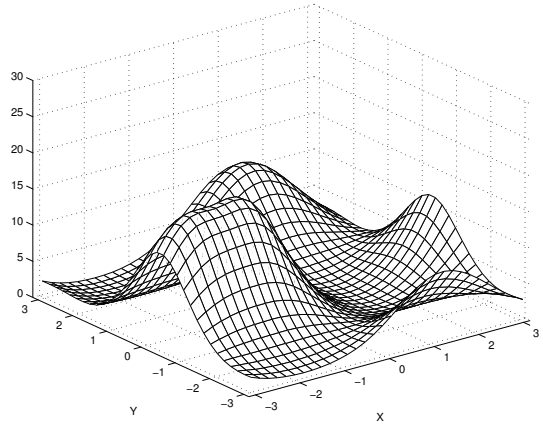

The variance of the stream function for the sine-bracket truncation, 23×23 truncation size, $E = 7$, $\mathcal{E} = 20$, $\tilde{C}_3 = 8$

Figure 6.33: The variances of the total mean stream functions for the sine-bracket truncation, 11×11 and 23×23 truncation sizes, $\tilde{C}_3 = 8$, random topography

see in Figures 6.40 and 6.41, the equipartition holds very well for the pseudo-energy in case with $\tilde{C}_3 = 0$ (solid line with circles) for both 11×11 and 23×23 truncation sizes. However, as $\tilde{C}_3$ increases, becoming relevant, the pseudo-energy spectrum is no more equipartitioned, and here we can see that the size of the sine-bracket truncation (4.1) makes difference. While the results for relevant values of $\tilde{C}_3 = 4$ and $\tilde{C}_3 = 8$ and 11×11 truncation size (dashed and dot-dashed lines in Figure 6.40) diverge up and down from the predicted horizontal line for different Fourier modes, the pseudo-energy spectra for the 23×23 sine-bracket truncation fall below predicted value except for a few large-scale modes (shown in Figure 6.41, dashed and dot-dashed lines). Overall, we can see that for 23×23 pseudo-energy spectrum the non-uniform structure which is developed for $\tilde{C}_3 = 4$, is essentially amplified for $\tilde{C}_3 = 8$ (Figure 6.41).

As for the energy of the mean state, the statistical theory in (3.46a) states that it should be zero on those Fourier modes where the topography is not present, and this is confirmed by the direct simulations with the traditional truncation (3.17) (Section 5.2.2, Figures 5.22 and 5.23). As shown in Figures 6.40 and 6.41, obtained with the sine-bracket truncation (4.1), for the statistically irrelevant value $\tilde{C}_3 = 0$ (solid line) the amount of energy in the Fourier mode $|\mathbf{k}|^2 = 1$ is very close to zero in comparison with the result for $\tilde{C}_3 = 8$ (dot-dashed line). Thus, we can see in Figures 6.40 and 6.41, that the statistically

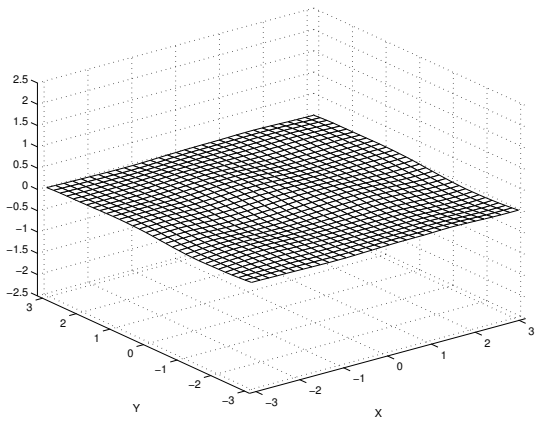

The skewness of the stream function for the sine-bracket truncation, 11×11 truncation size, $E = 7$, $\mathcal{E} = 20$, $\tilde{C}_3 = 0$

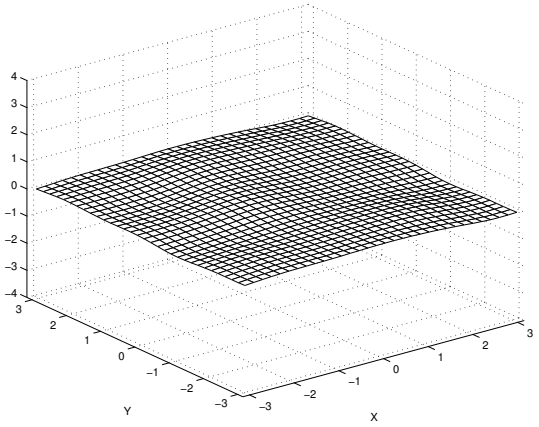

The skewness of the stream function for the sine-bracket truncation, 23×23 truncation size, $E = 7$, $\mathcal{E} = 20$, $\tilde{C}_3 = 0$

Figure 6.34: The skewness of the total mean stream functions for the sine-bracket truncation, 11×11 and 23×23 truncation sizes, $\tilde{C}_3 = 0$, random topography

relevant value of $\tilde{C}_3$ creates the large-scale mean flow, and the larger the truncation size, the more energy is contained in the mean state. Overall, we conclude that $\tilde{C}_3 = 0$ is statistically irrelevant in pseudo-energy and mean energy predictions, and $\tilde{C}_3 = 4$, $\tilde{C}_3 = 8$ are statistically relevant.

6.2.3 Total and coarse-grained "Corr" functions and scatterplots

The total and coarse-grained Corr functions for the numerical simulations with the 11×11 and 23×23 sine-bracket truncations (4.1) for the values of the normalized third Casimir invariant $\tilde{C}_3 = 0$, 4, and 8 are shown in Figures 6.42 and 6.43. We use the equation (5.7) described in Section 5.0.3 to compute the Corr functions and associated scatterplots. The theoretical relation (3.28) predicts that the Corr functions must eventually converge to -1 for negative μ's, thus showing that the mean state is collinear. This is also confirmed by the direct simulations with the traditional truncation (3.17) in Section 5.2.3, Figures 5.24 and 5.25. Here we can see the differences in behavior between different sizes of truncations. For the 11×11 sine-bracket truncation (4.1), the collinearity in the mean state is essentially the same for all values of $\tilde{C}_3$, which is shown in Figure 6.42. However, for the 23×23 sine-bracket truncation the collinearity in the mean state depends strongly on the value of $\tilde{C}_3$, which is shown in Figure 6.43. We can see that for the statis-

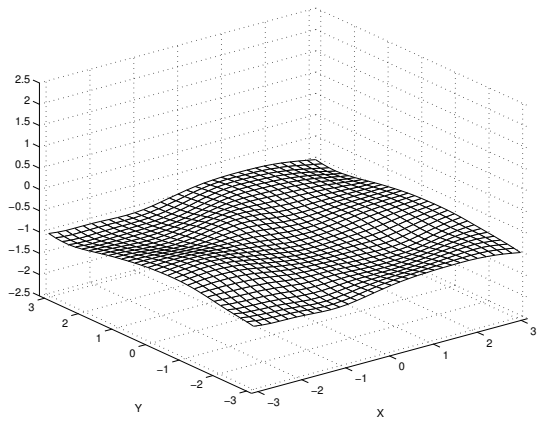

The skewness of the stream function for the sine-bracket truncation, 11×11 truncation size, $E = 7$, $\mathcal{E} = 20$, $\tilde{C}_3 = 4$

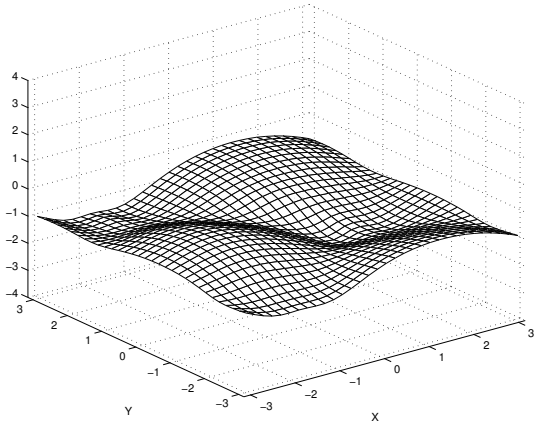

The skewness of the stream function for the sine-bracket truncation, 23×23 truncation size, $E = 7$, $\mathcal{E} = 20$, $\tilde{C}_3 = 4$

Figure 6.35: The skewness of the total mean stream functions for the sine-bracket truncation, 11×11 and 23×23 truncation sizes, $\tilde{C}_3 = 4$, random topography

tically relevant values $\tilde{C}_3 = 4$ and $\tilde{C}_3 = 8$ the mean state loses collinearity as $\tilde{C}_3$ increases. Also Figure 6.43 shows that as $\tilde{C}_3$ becomes statistically relevant, the coarse-grained Corr functions are not more collinear than their total counterparts, unlike 11×11 sine-bracket truncation (Figure 6.42), or the traditional truncation (Figures 5.24 and 5.25).

As well as Corr functions, we present the scatterplots $\bar{q}$ vs $\bar{\psi}$ for all points in the physical space grid. The scatterplots for both 11×11 and 23×23 sizes of the sine-bracket truncation and $\tilde{C}_3 = 0$, 4, and 8 are shown in Figures 6.44, 6.45, 6.46, 6.47, 6.48, and 6.49. As we can see, the statistically relevant values of $\tilde{C}_3$ have different kinds of influence for different truncation sizes. Thus, for 11×11 sine-bracket truncation the relevant $\tilde{C}_3$'s make the scatterplots more blurred (Figures 6.44, 6.45, and 6.46). However, for 23×23 sine-bracket truncation, the scatterplots become bent (Figures 6.47, 6.48, and 6.49). Overall, we conclude that for the collinearity of the mean state, the values of $\tilde{C}_3$ away from zero are statistically irrelevant for the 11×11 sine-bracket truncation and they are statistically relevant for the 23×23 sine-bracket truncation.

6.2.4 Time correlation functions

The time correlation functions (5.8) for different Fourier modes for the two sine-bracket truncation sizes, 11×11 and 23×23, are shown in Figures 6.50 and 6.51. We use the

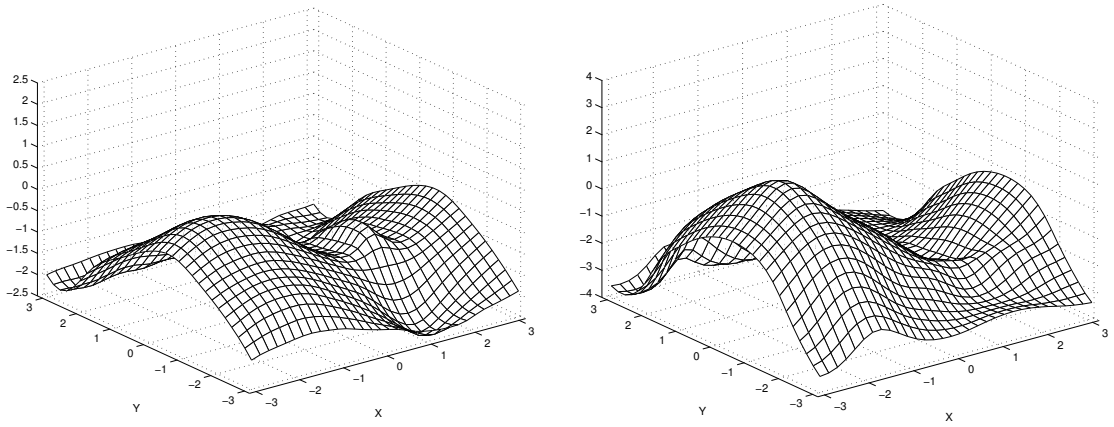

The skewness of the stream function for the sine-bracket truncation, 11×11 truncation size, $E = 7$, $\mathcal{E} = 20$, $\tilde{C}_3 = 8$

The skewness of the stream function for the sine-bracket truncation, 23×23 truncation size, $E = 7$, $\mathcal{E} = 20$, $\tilde{C}_3 = 8$

Figure 6.36: The skewness of the total mean stream functions for the sine-bracket truncation, 11×11 and 23×23 truncation sizes, $\tilde{C}_3 = 8$, random topography

equation (5.8) described in Section 5.0.3 to compute the time correlation functions. Here we show that the statistically relevant values of the normalized third Casimir invariant affect the time correlation functions in a very simple way. If we compare the correlation functions for the traditional truncation (3.17), which are shown in Figures 5.28 and 5.29, and the correlation functions for the sine-bracket truncation (4.1) which are shown in Figures 6.50 and 6.51, we can see that the statistically irrelevant value $\tilde{C}_3 = 0$ does not affect the correlation functions for both truncation sizes, but the statistically relevant values $\tilde{C}_3 = 4$ and $\tilde{C}_3 = 8$ slow down the decay rate of correlation functions, and, again, the 23×23 sine-bracket truncation is more sensitive to the influence of relevant $\tilde{C}_3$ than the 11×11 sine-bracket truncation. For the same values of $\tilde{C}_3$, the correlation functions for the 23×23 sine-bracket truncation de-correlate much slower (Figure 6.51), than those for the 11×11 sine-bracket truncation (Figure 6.51). We also note that the correlation functions exhibit more oscillations than those for the situation with no topography (Figures 6.23 and 6.24).

6.3 Simulations with layered topography

In this section we represent the results obtained for the geophysical case with layered topography (5.1). This time, however, we present only the simulations with the 23×23 size

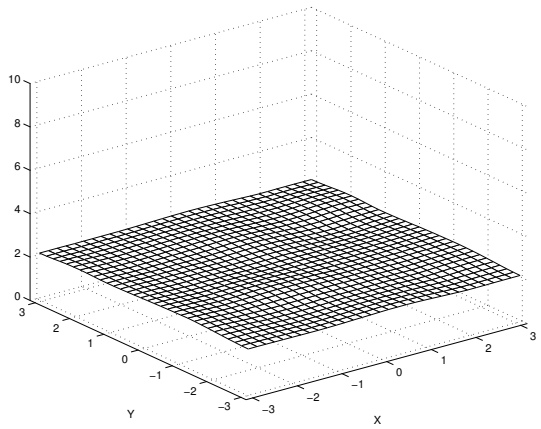

The flatness of the stream function for the sine-bracket truncation, 11×11 truncation size, $E = 7$, $\mathcal{E} = 20$, $\tilde{C}_3 = 0$

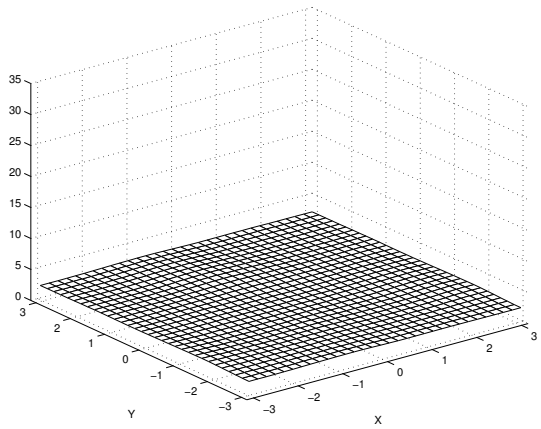

The flatness of the stream function for the sine-bracket truncation, 23×23 truncation size, $E = 7$, $\mathcal{E} = 20$, $\tilde{C}_3 = 0$

Figure 6.37: The flatness of the total mean stream functions for the sine-bracket truncation, 11×11 and 23×23 truncation sizes, $\tilde{C}_3 = 0$, random topography

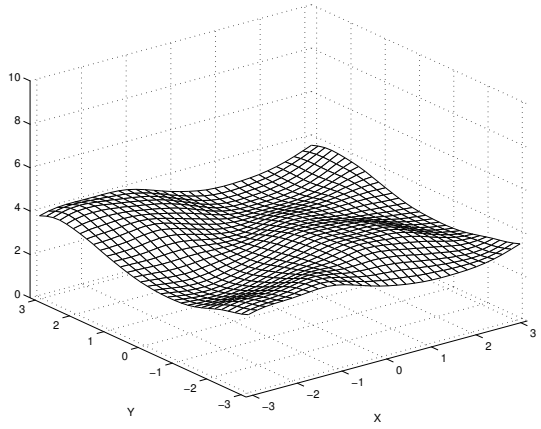

The flatness of the stream function for the sine-bracket truncation, 11×11 truncation size, $E = 7$, $\mathcal{E} = 20$, $\tilde{C}_3 = 4$

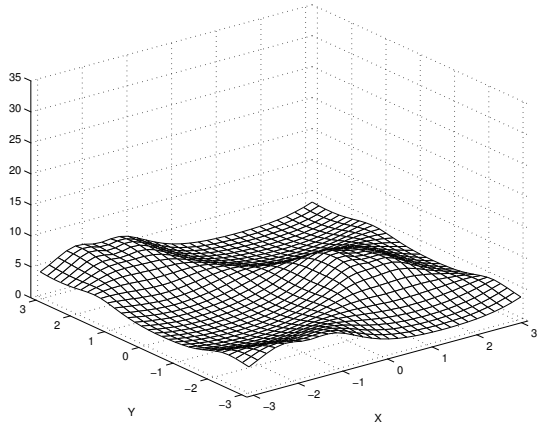

The flatness of the stream function for the sine-bracket truncation, 23×23 truncation size, $E = 7$, $\mathcal{E} = 20$, $\tilde{C}_3 = 4$

Figure 6.38: The flatness of the total mean stream functions for the sine-bracket truncation, 11×11 and 23×23 truncation sizes, $\tilde{C}_3 = 4$, random topography

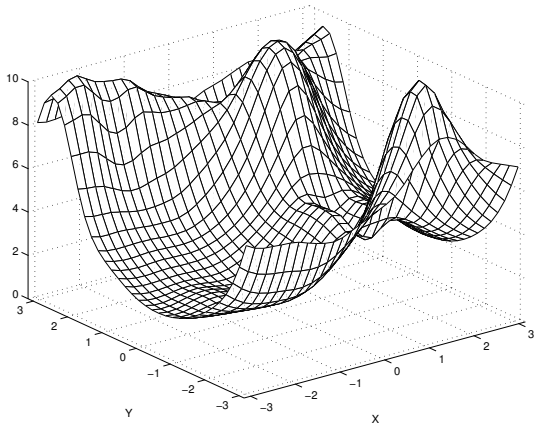

The flatness of the stream function for the sine-bracket truncation, 11×11 truncation size, $E = 7$, $\mathcal{E} = 20$, $\tilde{C}_3 = 8$

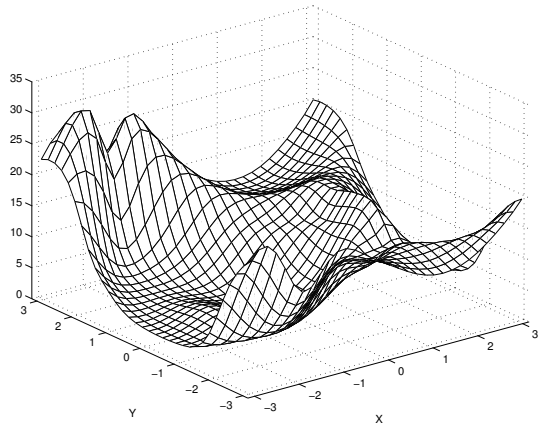

The flatness of the stream function for the sine-bracket truncation, 23×23 truncation size, $E = 7$, $\mathcal{E} = 20$, $\tilde{C}_3 = 8$

Figure 6.39: The flatness of the total mean stream functions for the sine-bracket truncation, 11×11 and 23×23 truncation sizes, $\tilde{C}_3 = 8$, random topography

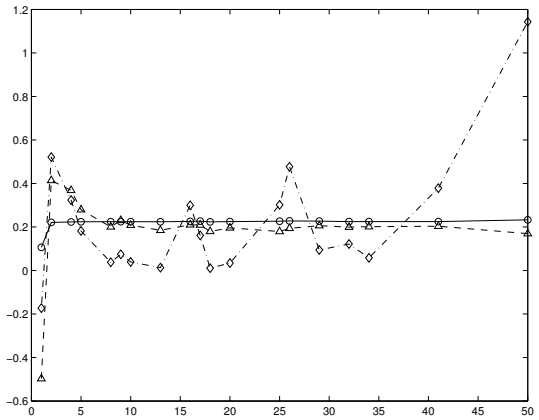

The pseudo-energy spectrum, sine-bracket truncation, 11×11 truncation size, $E = 7$, $\mathcal{E} = 20$, solid line with circles – $\tilde{C}_3 = 0$, dashed line with triangles – $\tilde{C}_3 = 4$, dot-dashed line with diamonds – $\tilde{C}_3 = 8$

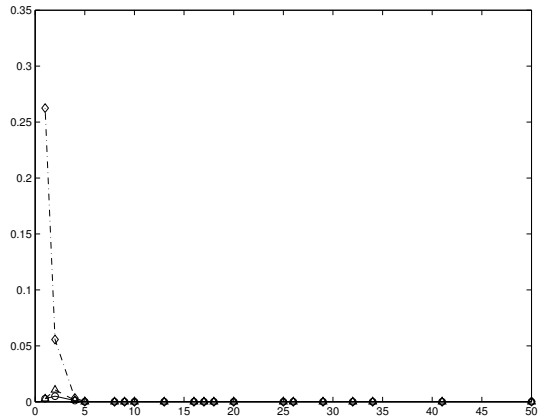

The energy of the mean flow spectrum, sine-bracket truncation, 11×11 truncation size, $E = 7$, $\mathcal{E} = 20$, solid line with circles – $\tilde{C}_3 = 0$, dashed line with triangles – $\tilde{C}_3 = 4$, dot-dashed line with diamonds – $\tilde{C}_3 = 8$

Figure 6.40: The pseudo-energy spectrum and the spectrum of energy of the mean, 11×11 sine-bracket truncation, random topography

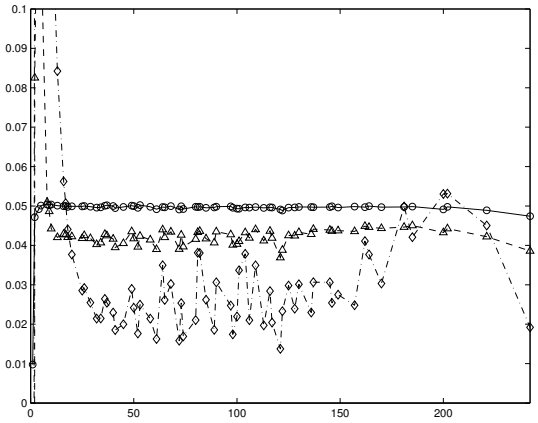

The pseudo-energy spectrum, sine-bracket truncation, 23×23 truncation size, $E = 7$, $\mathcal{E} = 20$, solid line with circles – $\tilde{C}_3 = 0$, dashed line with triangles – $\tilde{C}_3 = 4$, dot-dashed line with diamonds – $\tilde{C}_3 = 8$

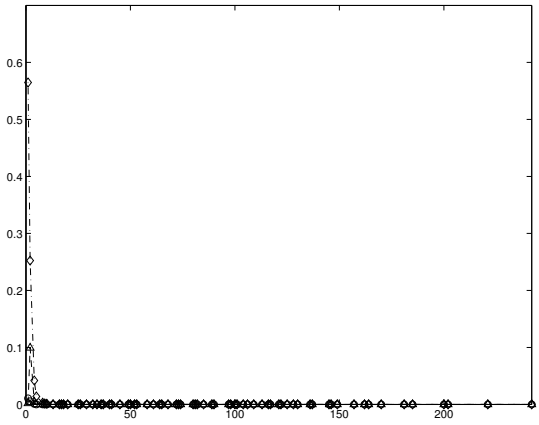

The energy of the mean flow spectrum, sine-bracket truncation, 23×23 truncation size, $E = 7$, $\mathcal{E} = 20$, solid line with circles – $\tilde{C}_3 = 0$, dashed line with triangles – $\tilde{C}_3 = 4$, dot-dashed line with diamonds – $\tilde{C}_3 = 8$

Figure 6.41: The pseudo-energy spectrum and the spectrum of energy of the mean, 23×23 sine-bracket truncation, random topography

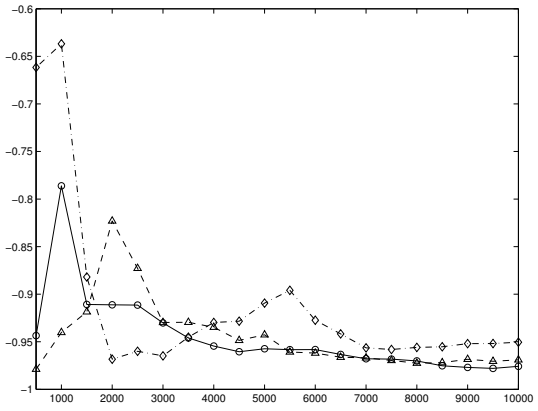

The Corr$[\langle\psi\rangle_\tau, \langle q\rangle_\tau](\tau)$ function for the sine-bracket truncation, 11×11 truncation size, $E = 7$, $\mathcal{E} = 20$, solid line with circles – $\tilde{C}_3 = 0$, dashed line with triangles – $\tilde{C}_3 = 4$, dot-dashed line with diamonds – $\tilde{C}_3 = 8$

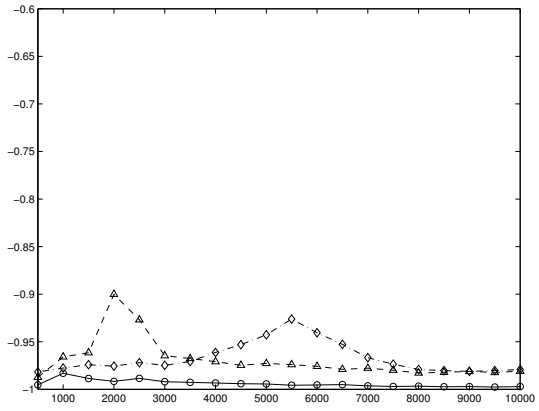

The coarse-grained Corr$[\langle\psi\rangle_\tau, \langle q\rangle_\tau](\tau)$ function for the sine-bracket truncation, 11×11 truncation size, $E = 7$, $\mathcal{E} = 20$, solid line with circles – $\tilde{C}_3 = 0$, dashed line with triangles – $\tilde{C}_3 = 4$, dot-dashed line with diamonds – $\tilde{C}_3 = 8$

Figure 6.42: The total and coarse-grained Corr functions for the sine-bracket truncation, 11×11 truncation size, $\tilde{C}_3 = 0, 4, 8$, random topography

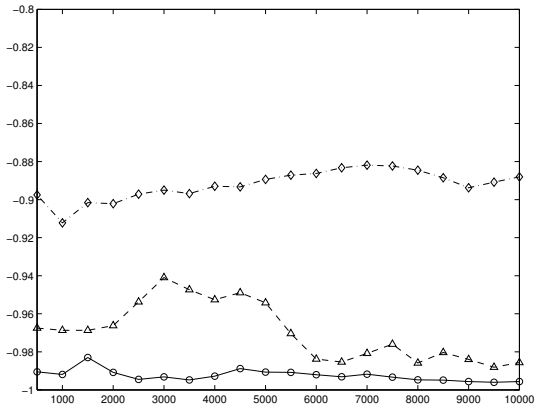

The Corr$[\langle\psi\rangle_\tau, \langle q\rangle_\tau](\tau)$ function for the sine-bracket truncation, 23×23 truncation size, $E = 7$, $\mathcal{E} = 20$, solid line with circles – $\tilde{C}_3 = 0$, dashed line with triangles – $\tilde{C}_3 = 4$, dot-dashed line with diamonds – $\tilde{C}_3 = 8$

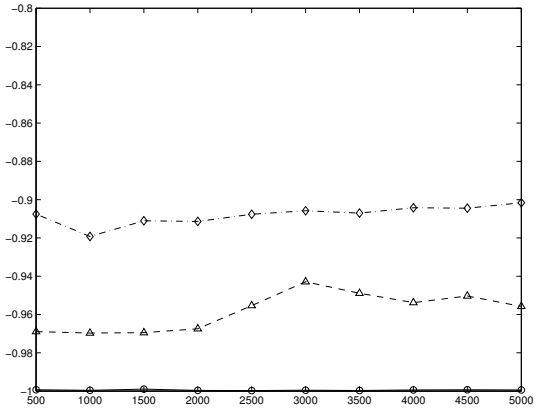

The coarse-grained Corr$[\langle\psi\rangle_\tau, \langle q\rangle_\tau](\tau)$ function for the sine-bracket truncation, 23×23 truncation size, $E = 7$, $\mathcal{E} = 20$, solid line with circles – $\tilde{C}_3 = 0$, dashed line with triangles – $\tilde{C}_3 = 4$, dot-dashed line with diamonds – $\tilde{C}_3 = 8$

Figure 6.43: The total and coarse-grained Corr functions for the sine-bracket truncation, 23×23 truncation size, $\tilde{C}_3 = 0, 4, 8$, random topography

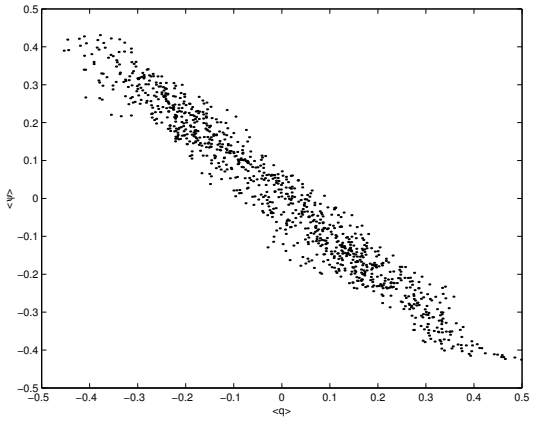

The scatterplot $\langle\psi\rangle_\tau$ vs $\langle q\rangle_\tau$, sine-bracket truncation, 11×11 truncation size, $E = 7$, $\mathcal{E} = 20$, $\tilde{C}_3 = 0$

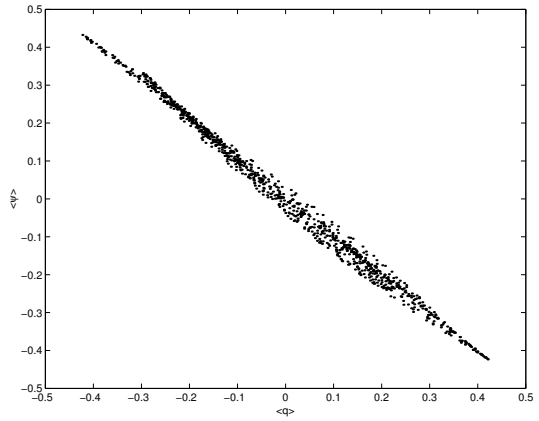

The coarse-grained scatterplot $\langle\psi\rangle_\tau$ vs $\langle q\rangle_\tau$, sine-bracket truncation, 11×11 truncation size, $E = 7$, $\mathcal{E} = 20$, $\tilde{C}_3 = 0$

Figure 6.44: The total and coarse-grained scatterplots $\bar{q}$ vs $\bar{\psi}$, 11×11 sine-bracket truncation, $\tilde{C}_3 = 0$, random topography

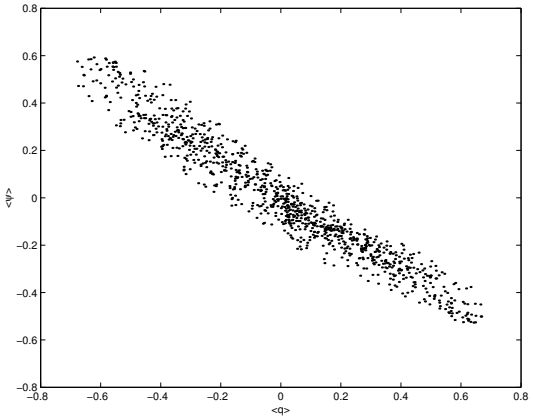

The scatterplot $\langle\psi\rangle_\tau$ vs $\langle q\rangle_\tau$, sine-bracket truncation, 11×11 truncation size, $E = 7$, $\mathcal{E} = 20$, $\tilde{C}_3 = 4$

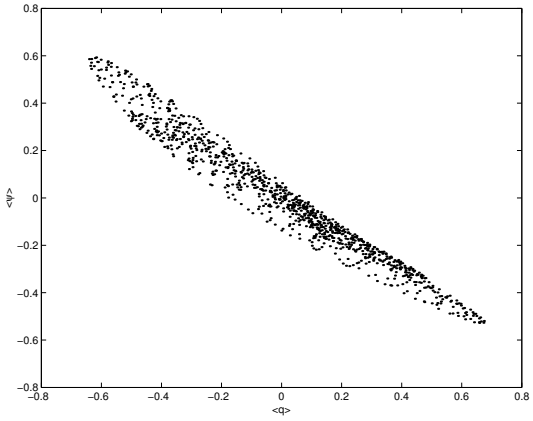

The coarse-grained scatterplot $\langle\psi\rangle_\tau$ vs $\langle q\rangle_\tau$, sine-bracket truncation, 11×11 truncation size, $E = 7$, $\mathcal{E} = 20$, $\tilde{C}_3 = 4$

Figure 6.45: The total and coarse-grained scatterplots $\bar{q}$ vs $\bar{\psi}$, 11×11 sine-bracket truncation, $\tilde{C}_3 = 4$, random topography

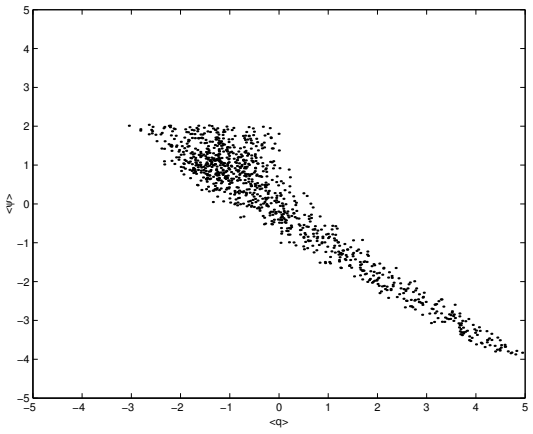

The scatterplot $\langle\psi\rangle_\tau$ vs $\langle q\rangle_\tau$, sine-bracket truncation, 11×11 truncation size, $E = 7$, $\mathcal{E} = 20$, $\tilde{C}_3 = 8$

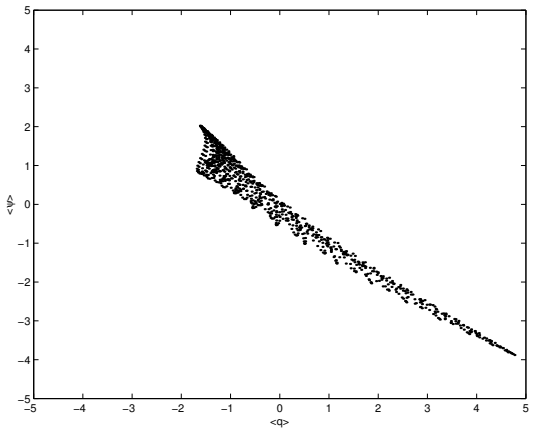

The coarse-grained scatterplot $\langle\psi\rangle_\tau$ vs $\langle q\rangle_\tau$, sine-bracket truncation, 11×11 truncation size, $E = 7$, $\mathcal{E} = 20$, $\tilde{C}_3 = 8$

Figure 6.46: The total and coarse-grained scatterplots $\bar{q}$ vs $\bar{\psi}$, 11×11 sine-bracket truncation, $\tilde{C}_3 = 8$, random topography

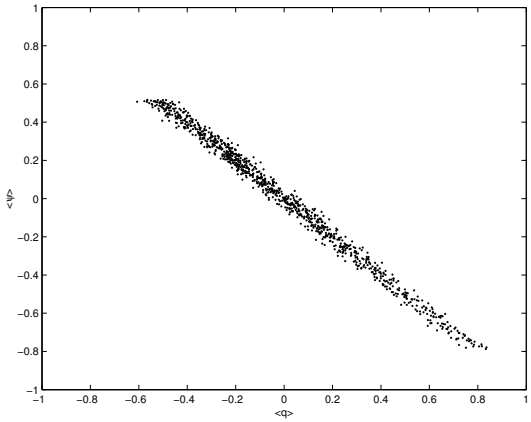

The scatterplot $\langle\psi\rangle_\tau$ vs $\langle q\rangle_\tau$, sine-bracket truncation, 23×23 truncation size, $E = 7$, $\mathcal{E} = 20$, $\tilde{C}_3 = 0$

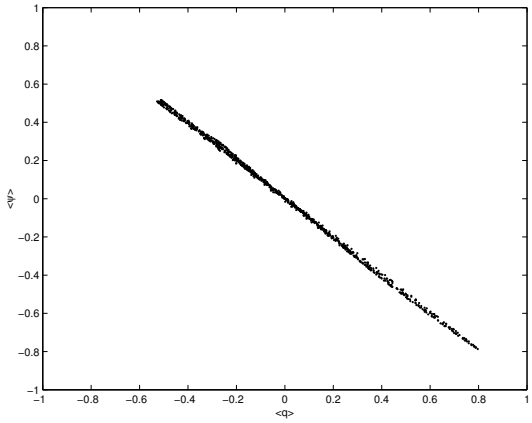

The coarse-grained scatterplot $\langle\psi\rangle_\tau$ vs $\langle q\rangle_\tau$, sine-bracket truncation, 23×23 truncation size, $E = 7$, $\mathcal{E} = 20$, $\tilde{C}_3 = 0$

Figure 6.47: The total and coarse-grained scatterplots $\bar{q}$ vs $\bar{\psi}$, 23×23 sine-bracket truncation, $\tilde{C}_3 = 0$, random topography

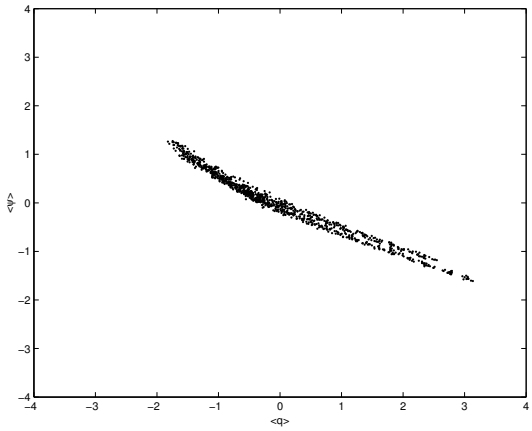

The scatterplot $\langle\psi\rangle_\tau$ vs $\langle q\rangle_\tau$, sine-bracket truncation, 23×23 truncation size, $E = 7$, $\mathcal{E} = 20$, $\tilde{C}_3 = 4$

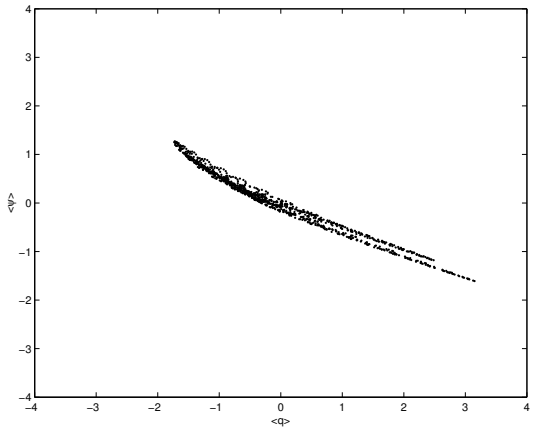

The coarse-grained scatterplot $\langle\psi\rangle_\tau$ vs $\langle q\rangle_\tau$, sine-bracket truncation, 23×23 truncation size, $E = 7$, $\mathcal{E} = 20$, $\tilde{C}_3 = 4$

Figure 6.48: The total and coarse-grained scatterplots $\bar{q}$ vs $\bar{\psi}$, 23×23 sine-bracket truncation, $\tilde{C}_3 = 4$, random topography

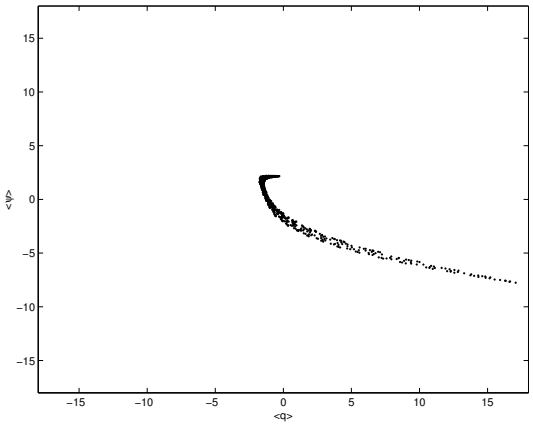

The scatterplot $\langle\psi\rangle_\tau$ vs $\langle q\rangle_\tau$, sine-bracket truncation, 23×23 truncation size, $E = 7$, $\mathcal{E} = 20$, $\tilde{C}_3 = 8$

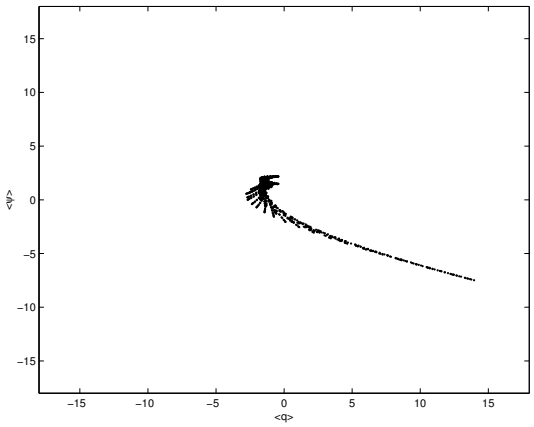

The coarse-grained scatterplot $\langle\psi\rangle_\tau$ vs $\langle q\rangle_\tau$, sine-bracket truncation, 23×23 truncation size, $E = 7$, $\mathcal{E} = 20$, $\tilde{C}_3 = 8$

Figure 6.49: The total and coarse-grained scatterplots $\bar{q}$ vs $\bar{\psi}$, 23×23 sine-bracket truncation, $\tilde{C}_3 = 8$, random topography

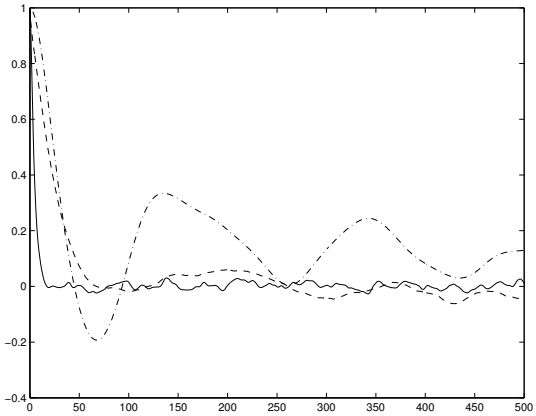

The time correlation functions for $|\mathbf{k}|^2 = 1$, sine-bracket truncation, 11×11 truncation size, $E = 7$, $\mathcal{E} = 20$, solid line – $\tilde{C}_3 = 0$, dashed line – $\tilde{C}_3 = 4$, dot-dashed line – $\tilde{C}_3 = 8$

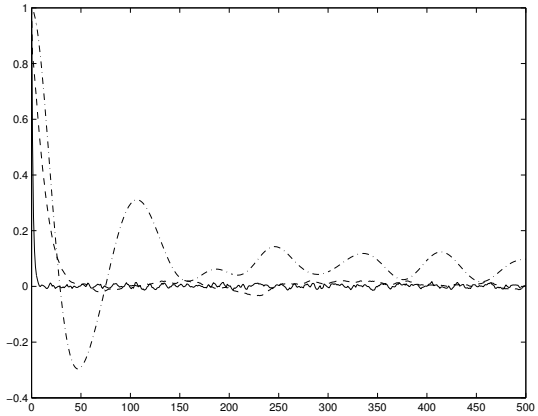

The time correlation functions for $|\mathbf{k}|^2 = 2$, sine-bracket truncation, 11×11 truncation size, $E = 7$, $\mathcal{E} = 20$, solid line – $\tilde{C}_3 = 0$, dashed line – $\tilde{C}_3 = 4$, dot-dashed line – $\tilde{C}_3 = 8$

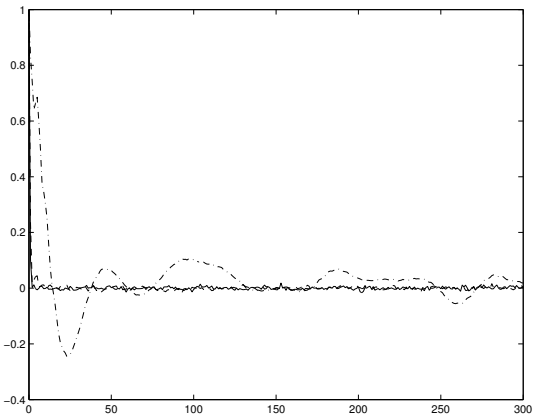

The time correlation functions for $|\mathbf{k}|^2 = 8$, sine-bracket truncation, 11×11 truncation size, $E = 7$, $\mathcal{E} = 20$, solid line – $\tilde{C}_3 = 0$, dashed line – $\tilde{C}_3 = 4$, dot-dashed line – $\tilde{C}_3 = 8$

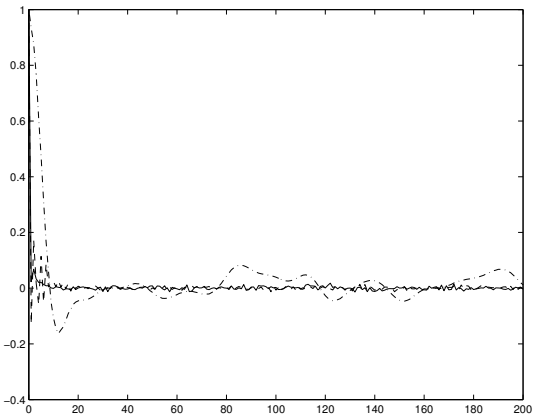

The time correlation functions for $|\mathbf{k}|^2 = 16$, sine-bracket truncation, 11×11 truncation size, $E = 7$, $\mathcal{E} = 20$, solid line – $\tilde{C}_3 = 0$, dashed line – $\tilde{C}_3 = 4$, dot-dashed line – $\tilde{C}_3 = 8$

Figure 6.50: The time correlation functions for the 11×11 sine-bracket truncation, random topography

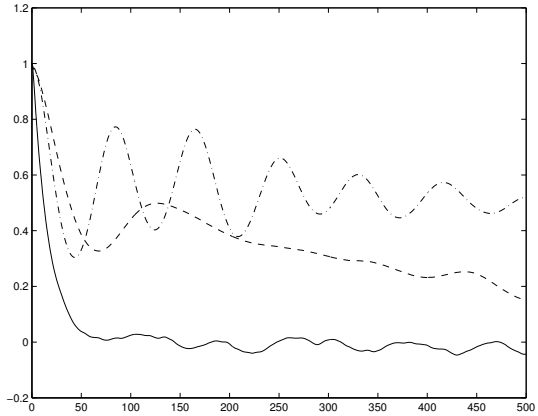

The time correlation functions for $|\mathbf{k}|^2 = 1$, sine-bracket truncation, 23×23 truncation size, $E = 7$, $\mathcal{E} = 20$, solid line – $\tilde{C}_3 = 0$, dashed line – $\tilde{C}_3 = 4$, dot-dashed line – $\tilde{C}_3 = 8$

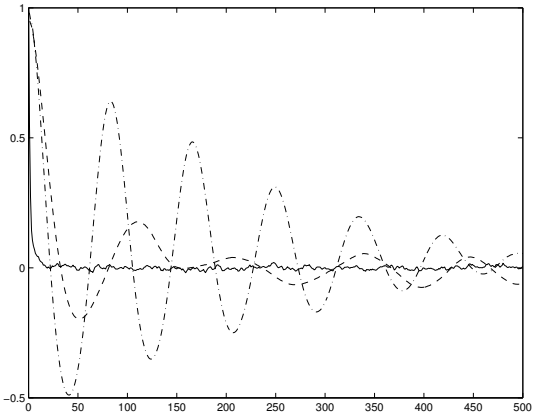

The time correlation functions for $|\mathbf{k}|^2 = 2$, sine-bracket truncation, 23×23 truncation size, $E = 7$, $\mathcal{E} = 20$, solid line – $\tilde{C}_3 = 0$, dashed line – $\tilde{C}_3 = 4$, dot-dashed line – $\tilde{C}_3 = 8$

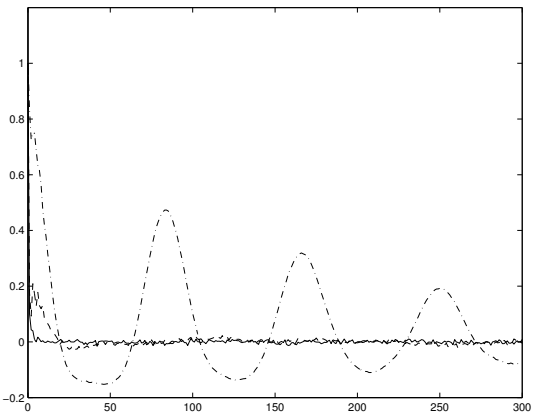

The time correlation functions for $|\mathbf{k}|^2 = 8$, sine-bracket truncation, 23×23 truncation size, $E = 7$, $\mathcal{E} = 20$, solid line – $\tilde{C}_3 = 0$, dashed line – $\tilde{C}_3 = 4$, dot-dashed line – $\tilde{C}_3 = 8$

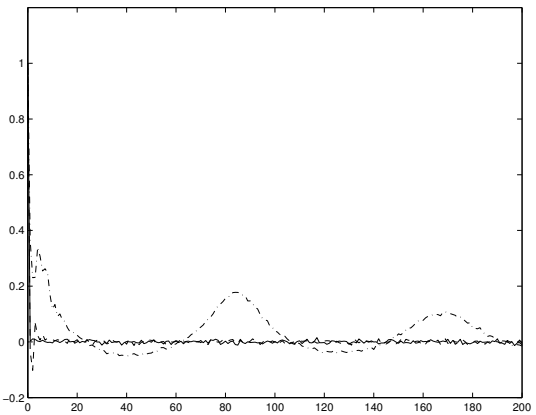

The time correlation functions for $|\mathbf{k}|^2 = 16$, sine-bracket truncation, 23×23 truncation size, $E = 7$, $\mathcal{E} = 20$, solid line – $\tilde{C}_3 = 0$, dashed line – $\tilde{C}_3 = 4$, dot-dashed line – $\tilde{C}_3 = 8$

Figure 6.51: The time correlation functions for the 23×23 sine-bracket truncation, random topography

23×23, total Fourier grid			23×23, coarse-grained grid		
$\tilde{C}_3$	skewness	flatness	$\tilde{C}_3$	skewness	flatness
0	$2.048 \cdot 10^{-3}$	2.879	0	$1.470 \cdot 10^{-3}$	2.878
2	-0.4061	2.557	2	-0.4047	2.5499
4	-0.7913	3.332	4	-0.7844	3.311
6	-1.112	4.249	6	-1.099	4.219

Table 6.5: The spatially averaged skewness and flatness of the mean stream functions for 23×23 sine-bracket truncation, total and coarse-grained Fourier grids, layered topography

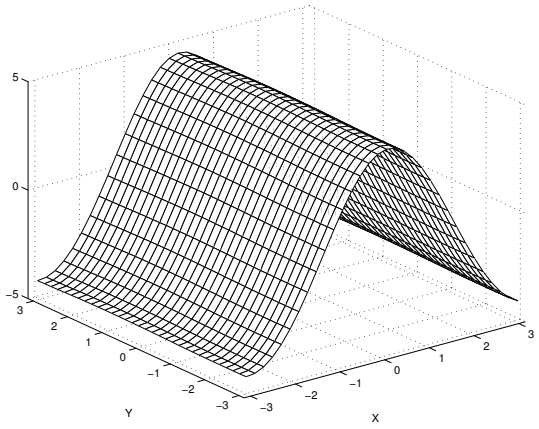

The stream function of the total mean flow for the sine-bracket truncation, 23×23 truncation size, $E = 7$, $\mathcal{E} = 20$, $\tilde{C}_3 = 0$

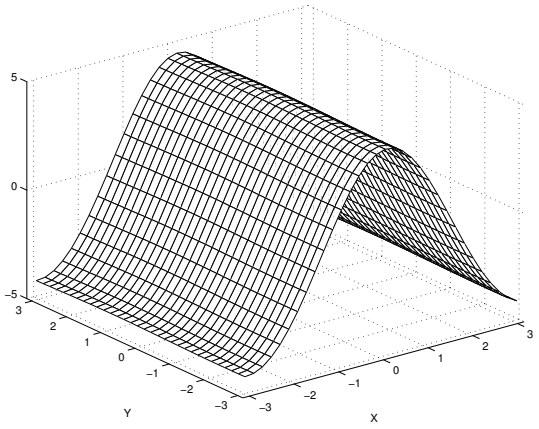

The stream function of the coarse-grained mean flow for the sine-bracket truncation, 23×23 truncation size, $E = 7$, $\mathcal{E} = 20$, $\tilde{C}_3 = 0$

Figure 6.52: The total and coarse-grained mean stream functions for the sine-bracket truncation, 23×23 truncation size, $\tilde{C}_3 = 0$, layered topography

of the sine-bracket truncation. The two previous cases, with no topography and random topography, show that the statistical results for the two truncation sizes differ significantly from each other, and we conclude that 11×11 size is not enough to reflect the actual statistical situation due to the lack of small scale resolution. For the case with layered topography (5.1), we present the simulations with 23×23 sine-bracket truncation (4.1) for the values of the normalized third Casimir invariant $\tilde{C}_3 = 0$, 2, 4, and 6, where $\tilde{C}_3$ is given by (6.1).

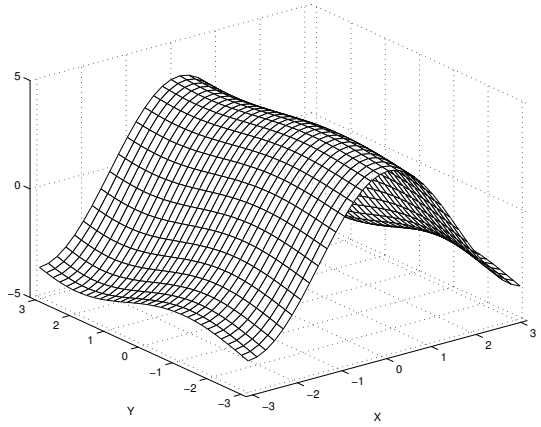

The stream function of the total mean flow for the sine-bracket truncation, 23×23 truncation size, $E = 7$, $\mathcal{E} = 20$, $\tilde{C}_3 = 2$

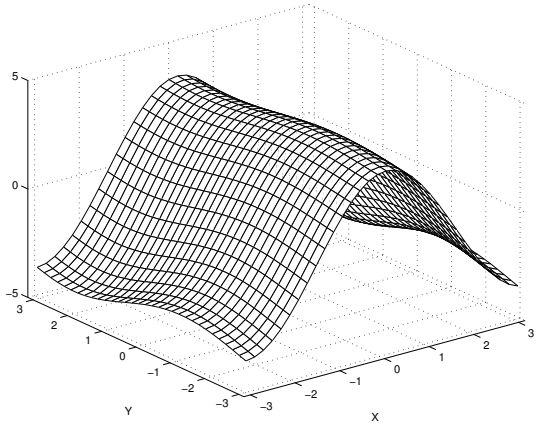

The stream function of the coarse-grained mean flow for the sine-bracket truncation, 23×23 truncation size, $E = 7$, $\mathcal{E} = 20$, $\tilde{C}_3 = 2$

Figure 6.53: The total and coarse-grained mean stream functions for the sine-bracket truncation, 23×23 truncation size, $\tilde{C}_3 = 2$, layered topography

6.3.1 Mean stream functions and their moments

We represent the total and coarse-grained mean stream functions in Figures 6.52, 6.53, 6.54, and 6.55. Both total and coarse-grained mean stream functions have essentially cosine shape (as they should for our choice of topography) with minor discrepancies for relevant $\tilde{C}_3$'s

Here we present the mean stream functions (5.2) and their moments (5.3) for the 23×23 size sine-bracket truncation (4.1). Our main purpose is to compare the results for the sine-bracket truncation with the with those for the traditional truncation (3.17) (Figures 5.34, 5.35, 5.36, 5.37, and Table 5.9) for the same geophysical case with layered topography (5.1). The direct numerical simulations for the sine-bracket truncation were done for the set of initial conditions with energy $E = 7$, enstrophy $\mathcal{E} = 20$, and four different values of the normalized third Casimir invariant $\tilde{C}_3 = 0$, 2, 4, and 6, where $\tilde{C}_3$ is defined by (6.1).

The total and coarse-grained mean stream functions for the 23×23 size of the sine-bracket truncation (4.1) are presented in Figure 6.52 for $\tilde{C}_3 = 0$, Figure 6.53 for $\tilde{C}_3 = 2$, Figure 6.54 for $\tilde{C}_3 = 4$, and Figure 6.55 for $\tilde{C}_3 = 6$. The most probable mean state for the layered topography (5.1), given by the statistical theory in (3.29), is expected to have the cosine shape in x-direction, and be layered in y-direction. Direct numerical simula-

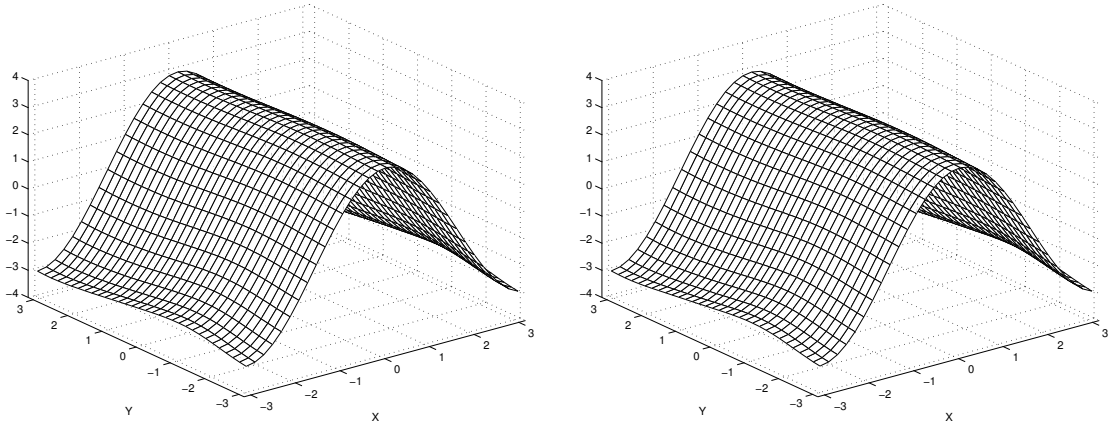

The stream function of the total mean flow for the sine-bracket truncation, 23×23 truncation size, $E = 7$, $\mathcal{E} = 20$, $\tilde{C}_3 = 4$

The stream function of the coarse-grained mean flow for the sine-bracket truncation, 23×23 truncation size, $E = 7$, $\mathcal{E} = 20$, $\tilde{C}_3 = 4$

Figure 6.54: The total and coarse-grained mean stream functions for the sine-bracket truncation, 23×23 truncation size, $\tilde{C}_3 = 4$, layered topography

tions with the traditional truncation (3.17), and with the layered topography, confirm the statistical predictions (Section 5.3.1), Figure 5.34). This mean state happens to be the same with the sine-bracket truncation and $\tilde{C}_3 = 0$, which is shown in Figure 6.52. Thus, we conclude that $\tilde{C}_3 = 0$ is not relevant for the mean stream function. The total and coarse-grained mean stream functions for 23×23 sine-bracket truncation with $\tilde{C}_3 = 2$, which are shown in Figure 6.53, exhibit significant distortions from the mean state for both total and coarse-grained mean stream functions for 23×23 sine-bracket truncation. $\tilde{C}_3 = 2$ has two major types of influence on the mean flow: first, it reduces the overall amplitude of the mean stream function (compare Figures 6.53 and 6.52), and, second, it changes the shape of the mean in y-direction. Thus, we conclude that $\tilde{C}_3 = 2$ is relevant for the mean stream function. The total and coarse-grained mean stream functions for 23×23 sine-bracket truncation with $\tilde{C}_3 = 4$, which are shown in Figure 6.54, exhibit distortions from the mean state for both total and coarse-grained mean stream functions for 23×23 sine-bracket truncation. Unlike the case with $\tilde{C}_3 = 2$, $\tilde{C}_3 = 4$ mainly reduces the overall amplitude of the mean (compare Figures 6.54 and 6.52), and does not cause any major distortions of the original shape of the mean. Thus, we conclude that $\tilde{C}_3 = 4$ is statistically relevant for the mean stream function. The total and coarse-grained mean stream functions for 23×23 sine-bracket truncation with $\tilde{C}_3 = 6$, which are shown in

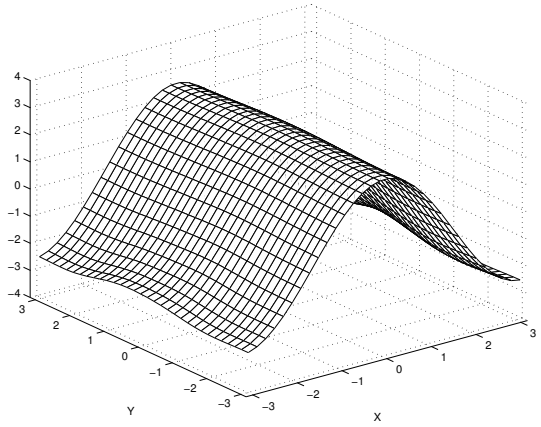

The stream function of the total mean flow for the sine-bracket truncation, 23×23 truncation size, $E = 7$, $\mathcal{E} = 20$, $\tilde{C}_3 = 6$

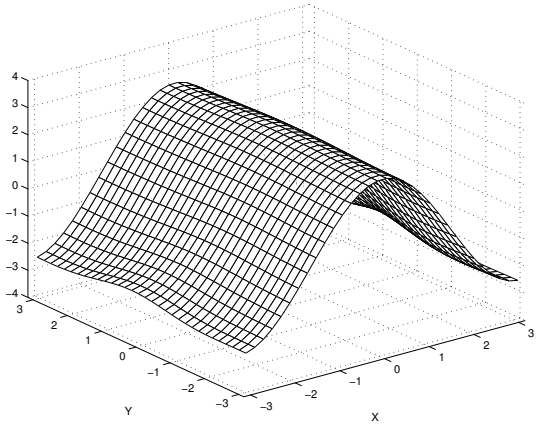

The stream function of the coarse-grained mean flow for the sine-bracket truncation, 23×23 truncation size, $E = 7$, $\mathcal{E} = 20$, $\tilde{C}_3 = 6$

Figure 6.55: The total and coarse-grained mean stream functions for the sine-bracket truncation, 23×23 truncation size, $\tilde{C}_3 = 6$, layered topography

Figure 6.55, exhibit distortions from the mean state for both total and coarse-grained mean stream functions for 23×23 sine-bracket truncation. The influence of $\tilde{C}_3 = 6$ is very similar to the influence of the statistically relevant $\tilde{C}_3 = 4$ (reduces amplitude yet more, compare Figures 6.55, 6.54, and 6.52), and, again, does not cause any major distortions of the original shape of the mean. Thus, we conclude that $\tilde{C}_3 = 6$ is statistically relevant for the mean stream function.

The variances of the total and coarse-grained stream functions for the 23×23 size of the sine-bracket truncation (4.1) are presented in Figure 6.56 for $\tilde{C}_3 = 0$, Figure 6.57 for $\tilde{C}_3 = 2$, Figure 6.58 for $\tilde{C}_3 = 4$, and Figure 6.59 for $\tilde{C}_3 = 6$. The variances predicted by the theory in (3.30) are not quite confirmed by the direct numerical simulations with the traditional truncation in Figure 5.35. However, if we compare Figures 6.56 and 5.35, we can see that the variances for the simulations with sine-bracket truncation (4.1) are identical with those with the traditional truncation (3.17). This again confirms that $\tilde{C}_3 = 0$ is irrelevant to the statistical predictions. The variances of the stream functions for the sine-bracket truncation with $\tilde{C}_3 = 2$, shown in Figure 6.57, differ significantly from the test result for the traditional truncation (Figure 5.35) and the result for the sine-bracket truncation with $\tilde{C}_3 = 0$ (Figure 6.56), having completely different shape for both total and coarse-grained variances. Thus, we conclude that $\tilde{C}_3 = 2$ is relevant for the variance of the

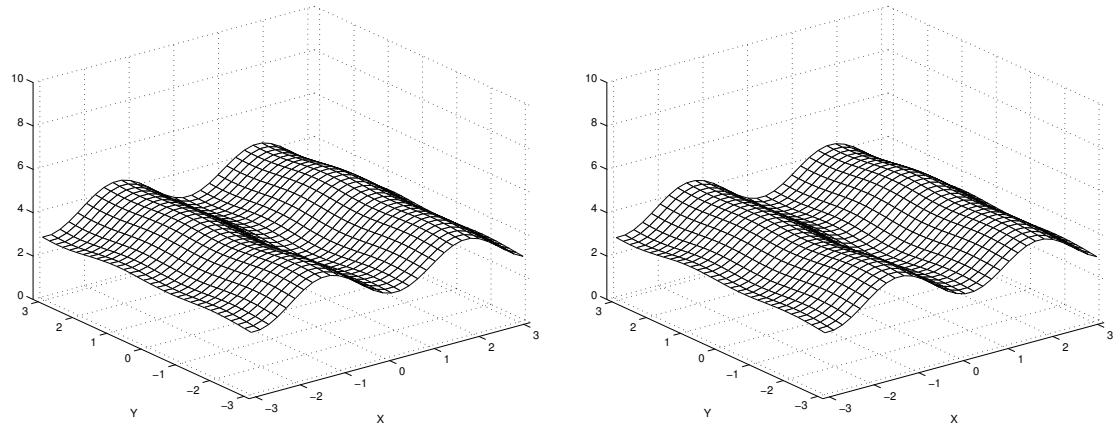

The variance of the total stream function for the sine-bracket truncation, 23×23 truncation size, $E = 7$, $\mathcal{E} = 20$, $\tilde{C}_3 = 0$

The variance of the coarse-grained stream function for the sine-bracket truncation, 23×23 truncation size, $E = 7$, $\mathcal{E} = 20$, $\tilde{C}_3 = 0$

Figure 6.56: The variances of the total and coarse-grained mean stream functions for the sine-bracket truncation, 23×23 truncation size, $\tilde{C}_3 = 0$, layered topography

stream function. The variances of the stream functions for the sine-bracket truncation with $\tilde{C}_3 = 4$, shown in Figure 6.58, have a shape very similar to those for $\tilde{C}_3 = 2$ (Figure 6.57), however the overall amplitude of the plot is increased. We can observe the same trend as we increase the value of $\tilde{C}_3$, setting it to $\tilde{C}_3 = 6$ (see Figure 6.59). The shape of the variance of the mean stream function is the same as for $\tilde{C}_3 = 2$ (Figure 6.57), and $\tilde{C}_3 = 4$ (Figure 6.58). We conclude that $\tilde{C}_3 = 6$ is statistically relevant for the variances of the stream function. Note that the breaking point (major shape change) happens at relatively small value $\tilde{C}_3 = 2$, and further $\tilde{C}_3$ increase affects only the amplitude, and not the shape.

The skewness of the total and coarse-grained stream functions for 23×23 size of the sine-bracket truncation (4.1) are presented in Figure 6.60 for $\tilde{C}_3 = 0$, Figure 6.61 for $\tilde{C}_3 = 2$, and Figure 6.62 for $\tilde{C}_3 = 4$, and Figure 6.63 for $\tilde{C}_3 = 6$. The spatially averaged skewness for all simulations with the sine-bracket truncation and random topography is shown in Table 6.5. The skewness predicted by the theory in (3.26), is expected to be zero. The direct numerical simulations with the traditional truncation in Figure 5.36, however, do not confirm this prediction. Nonetheless, the direct numerical simulation with the sine-bracket truncation and $\tilde{C}_3 = 0$, which is shown in Figure 6.60 for both total and coarse-grained grid, coincides with the result for the traditional truncation (compare Figures 6.60 and 5.36). Also Table 6.5 shows that the averaged value of skewness for this

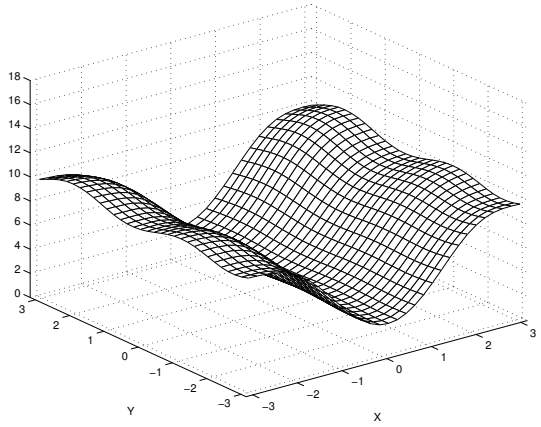

The variance of the total stream function for the sine-bracket truncation, 23×23 truncation size, $E = 7$, $\mathcal{E} = 20$, $\tilde{C}_3 = 2$

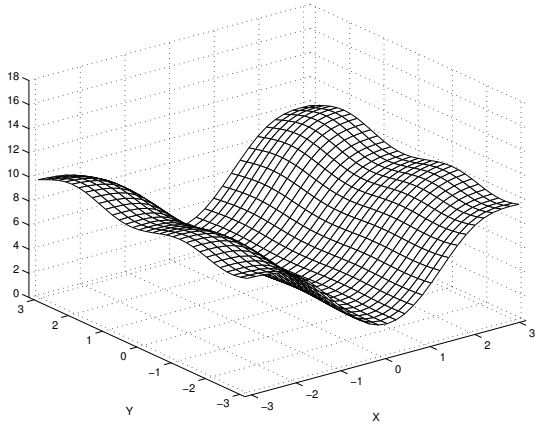

The variance of the coarse-grained stream function for the sine-bracket truncation, 23×23 truncation size, $E = 7$, $\mathcal{E} = 20$, $\tilde{C}_3 = 2$

Figure 6.57: The variances of the total and coarse-grained mean stream functions for the sine-bracket truncation, 23×23 truncation size, $\tilde{C}_3 = 2$, layered topography

case is $2.048 \cdot 10^{-3}$, which is quite close to zero. This confirms that $\tilde{C}_3 = 0$ is irrelevant to the statistical predictions. The skewness of the stream functions for the sine-bracket truncation with $\tilde{C}_3 = 2$, which is shown in Figure 6.61, falls below zero, and also gains a small bump centered at $y = 0$ and layered in y-direction. The averages value of the skewness for $\tilde{C}_3 = 2$ is -0.4061 (see Table 6.5). Thus, we conclude that $\tilde{C}_3 = 2$ is relevant for the skewness of the stream function. The trend in influence of larger values of $\tilde{C}_3$ on skewness is very similar to that on the variance: there is no major changes in shape in comparison with $\tilde{C}_2$ (see Figure 6.62 for $\tilde{C}_3 = 4$, and Figure 6.63 for $\tilde{C}_3 = 6$), however the amplitude of the plots increases as well as the depth below zero (averaged skewness values are -0.7913 for $\tilde{C}_3 = 4$ and -1.112 for $\tilde{C}_3 = 6$, see Table 6.5). Thus, $\tilde{C}_3 = 4$ and $\tilde{C}_3 = 6$ are statistically relevant.

The flatness of the total and coarse-grained stream functions for 23×23 size of the sine-bracket truncation (4.1) are presented in Figure 6.64 for $\tilde{C}_3 = 0$, Figure 6.65 for $\tilde{C}_3 = 2$, Figure 6.66 for $\tilde{C}_3 = 4$, and Figure 6.67 for $\tilde{C}_3 = 6$. The spatially averaged flatness for all simulations with the sine-bracket truncation and layered topography is shown in Table 6.5. The flatness predicted by the statistical theory in (3.26), is expected to be 3, and this is confirmed by the direct numerical simulations with the traditional truncation (3.17) in Figure 5.37. For the sine-bracket truncation with $\tilde{C}_3 = 0$, the flatness

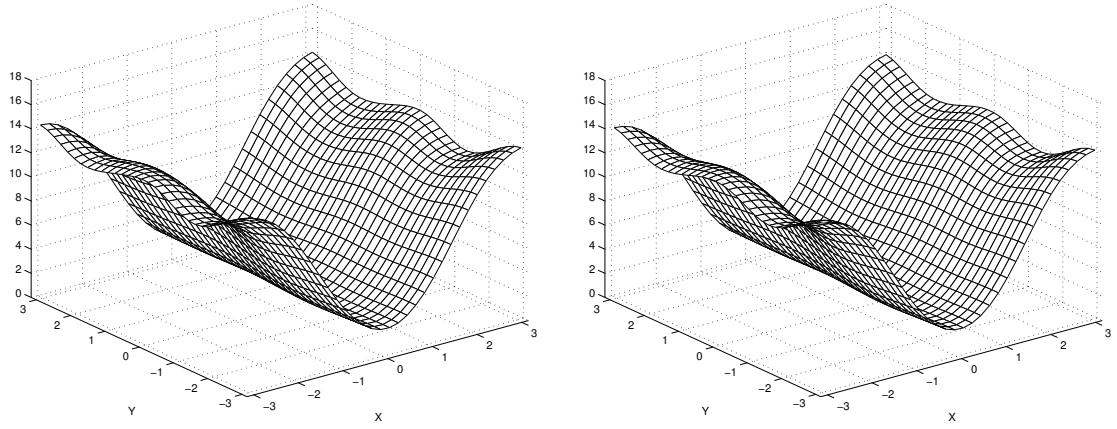

The variance of the total stream function for the sine-bracket truncation, 23×23 truncation size, $E = 7$, $\mathcal{E} = 20$, $\tilde{C}_3 = 4$

The variance of the coarse-grained stream function for the sine-bracket truncation, 23×23 truncation size, $E = 7$, $\mathcal{E} = 20$, $\tilde{C}_3 = 4$

Figure 6.58: The variances of the total and coarse-grained mean stream functions for the sine-bracket truncation, 23×23 truncation size, $\tilde{C}_3 = 4$, layered topography

has the same shape, and is also centered at 3, which is shown in Figure 6.64 for both 11×11 and 23×23 sine-bracket truncation. Table 6.5 shows averaged values of flatness, which equals 2.879. This is a confirmation that $\tilde{C}_3 = 0$ is irrelevant to the statistical predictions. The flatness of the stream functions for the sine-bracket truncation with $\tilde{C}_3 = 2$, which is shown in Figure 6.65, is significantly distorted in comparison with $\tilde{C}_3 = 0$ (Figure 6.64). The averages value of the flatness for $\tilde{C}_3 = 2$ is 2.557 (see Table 6.5). Thus, we conclude that $\tilde{C}_3 = 2$ is relevant for the flatness of the stream function. The trend in influence of larger values of $\tilde{C}_3$ on flatness is very similar to that on the variance and skewness: there is no major changes in shape in comparison with $\tilde{C}_2$ (see Figure 6.66 for $\tilde{C}_3 = 4$, and Figure 6.67 for $\tilde{C}_3 = 6$), however the amplitude of the plots increases as well as the averaged flatness (averaged flatness values are 3.332 for $\tilde{C}_3 = 4$ and 4.249 for $\tilde{C}_3 = 6$, see Table 6.5). Thus, $\tilde{C}_3 = 4$ and $\tilde{C}_3 = 6$ are statistically relevant for the flatness of the stream function.

6.3.2 The mean energy and pseudo-energy spectra

The pseudo-energy spectrum and energy of the mean spectrum calculated by the sine-bracket truncation (4.1) are presented in the Figures 6.68 for 23×23 sine-bracket truncation, and the values of the normalized third Casimir $\tilde{C}_3 = 0$,, 2, 4, and 6, where

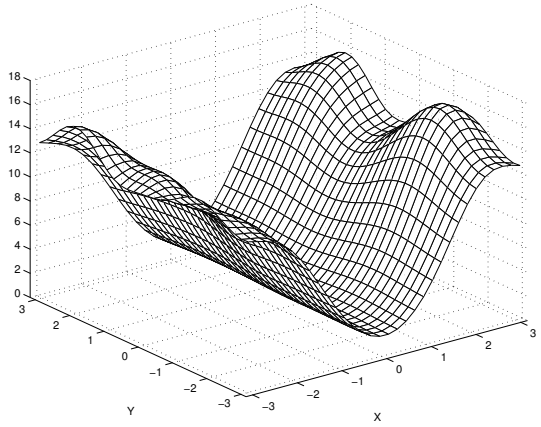

The variance of the total stream function for the sine-bracket truncation, 23×23 truncation size, $E = 7$, $\mathcal{E} = 20$, $\tilde{C}_3 = 6$

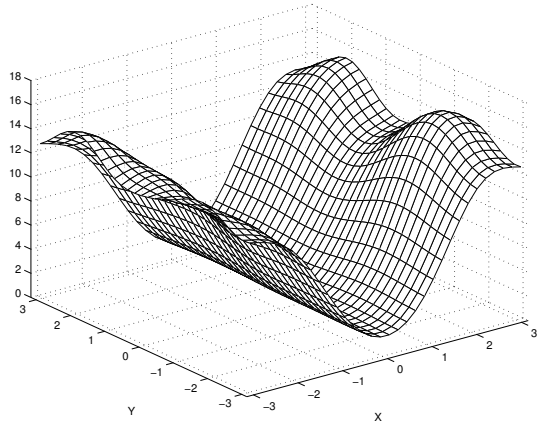

The variance of the coarse-grained stream function for the sine-bracket truncation, 23×23 truncation size, $E = 7$, $\mathcal{E} = 20$, $\tilde{C}_3 = 6$

Figure 6.59: The variances of the total and coarse-grained mean stream functions for the sine-bracket truncation, 23×23 truncation size, $\tilde{C}_3 = 6$, layered topography

23×23		
$\tilde{C}_3$	μ	α
0	-0.9546	19.18
2	-0.9498	19.82
4	-0.9442	19.99
6	-0.9397	19.46

Table 6.6: The numerically determined parameters μ and α for the sine-bracket truncation, layered topography

$\tilde{C}_3$ is given by (6.1). We use the equations (5.4) and (5.5) described in Section 5.0.3 to compute the mean energy and pseudo-energy spectra. In order to represent the result for the pseudo-energy in the pseudo-energy variables (3.48), we used the numerically calculated parameters μ and α which are shown in Table 6.6. According to the theoretical prediction in (3.50), the pseudo-energy should be equipartitioned in spectral space, and this is confirmed by the direct numerical simulations with the traditional truncation (3.17) in the Section 5.3.2 in Figures 5.38 and 5.39. As we can see in Figure 6.68, the equipartition holds very well for the pseudo-energy in case with $\tilde{C}_3 = 0$ (solid line with circles) for the 23×23 sine-bracket truncation, and that means that $\tilde{C}_3 = 0$ is statistically irrelevant. However, as $\tilde{C}_3$ increases, becoming relevant, the pseudo-energy spectrum is no more equipartitioned. The pseudo-energy spectra for the 23×23 sine-bracket truncation and

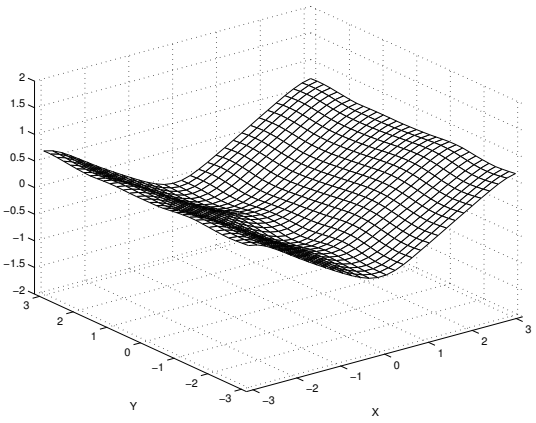

The skewness of the total stream function for the sine-bracket truncation, 23×23 truncation size, $E = 7$, $\mathcal{E} = 20$, $\tilde{C}_3 = 0$

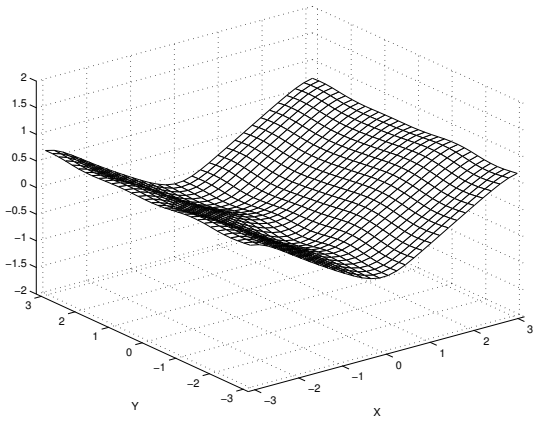

The skewness of the coarse-grained stream function for the sine-bracket truncation, 23×23 truncation size, $E = 7$, $\mathcal{E} = 20$, $\tilde{C}_3 = 0$

Figure 6.60: The skewness of the total and coarse-grained mean stream functions for the sine-bracket truncation, 23×23 truncation size, $\tilde{C}_3 = 0$, layered topography

statistically relevant values $\tilde{C}_3 = 2$, 4, and 6, fall below predicted value except for a few large-scale modes (shown in Figure 6.68, dotted, dashed, and dot-dashed lines for $\tilde{C}_3 = 2$, 4, and 6, respectively). Overall, we can see that the non-uniform spectrum structure, developed for $\tilde{C}_3 = 2$, is essentially amplified for $\tilde{C}_3 = 4$ and 6.

As for the energy of the mean state, the statistical theory in (3.46a) states that it should be non-zero only in the Fourier modes where the topography in present, and this is confirmed by the direct simulations with the traditional truncation (3.17) (Section 5.3.2, Figures 5.38 and 5.39). As shown in Figure 6.68, obtained with the sine-bracket truncation (4.1), for the statistically irrelevant value $\tilde{C}_3 = 0$ (solid line) the amount of energy in the Fourier mode $|\mathbf{k}|^2 = 1$ (marked by circle in Figure 6.68) is the same as that for the traditional truncation (Figure 5.39), which means that $\tilde{C}_3 = 0$ is statistically irrelevant. However, as we increase the value of $\tilde{C}_3$, the amount of energy in the first Fourier mode decreases, while the rest of the mean energy spectra stays unchanged (Figure 6.68, marked by square, triangle, and diamond, for $\tilde{C}_3 = 2$, 4, and 6, respectively), which means that the values of $\tilde{C}_3 = 2$, 4, and 6 are statistically relevant.

6.3.3 Total and coarse-grained "Corr" functions and scatterplots

The total and coarse-grained Corr functions for the numerical simulations with the 23×23 sine-bracket truncation (4.1) for the values of the normalized third Casimir

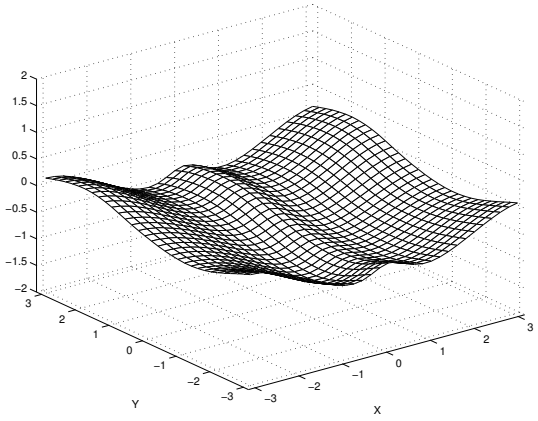

The skewness of the total stream function for the sine-bracket truncation, 23×23 truncation size, $E = 7$, $\mathcal{E} = 20$, $\tilde{C}_3 = 2$

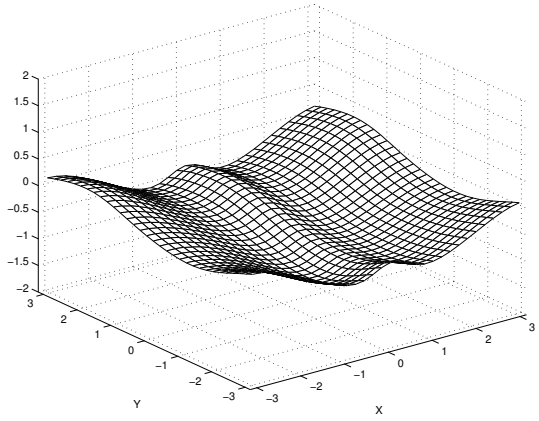

The skewness of the coarse-grained stream function for the sine-bracket truncation, 23×23 truncation size, $E = 7$, $\mathcal{E} = 20$, $\tilde{C}_3 = 2$

Figure 6.61: The skewness of the total and coarse-grained mean stream functions for the sine-bracket truncation, 23×23 truncation size, $\tilde{C}_3 = 2$, layered topography

invariant $\tilde{C}_3 = 0$, 2, 4, and 6 are shown in Figure 6.69. We use the equation (5.7) described in Section 5.0.3 to compute the Corr functions and associated scatterplots. The theoretical relation (3.28) predicts that the Corr functions must eventually converge to -1 for negative μ's, thus showing that the mean state is collinear. This is also confirmed by the direct simulations with the traditional truncation (3.17) in Section 5.3.3, Figures 5.40 and 5.41. For the direct simulation with the 23×23 sine-bracket truncation and $\tilde{C}_3 = 0$ we can see that the mean state is perfectly collinear both for total and coarse-grained Corr functions (Figure 6.69, solid line), which means that $\tilde{C}_3 = 0$ is statistically irrelevant. However, as we increase the value of $\tilde{C}_3$, the mean state loses collinearity. We can see that the larger the value of $\tilde{C}_3$, the less collinearity is present in the mean state, and it is true for both total and coarse-grained Corr functions (Figure 6.69, dotted, dashed, and dot-dashed lines for $\tilde{C}_3 = 2$, 4, and 6, respectively). Statistically relevant values of the normalized third Casimir $\tilde{C}_3$ affect the collinearity of the mean state.

As well as Corr functions, we present the scatterplots $\bar{q}$ vs $\bar{\psi}$ for all points in the physical space grid. Both total and coarse-grained scatterplots for 23×23 sine-bracket truncation and $\tilde{C}_3 = 0$, 2, 4, and 6 are shown in Figures 6.70, 6.71, 6.72, and 6.73. Both total and coarse-grained scatterplots for $\tilde{C}_3 = 0$ (Figure 6.70) are absolutely collinear, and look identical to the corresponding scatterplots for the traditional truncation (Fig-

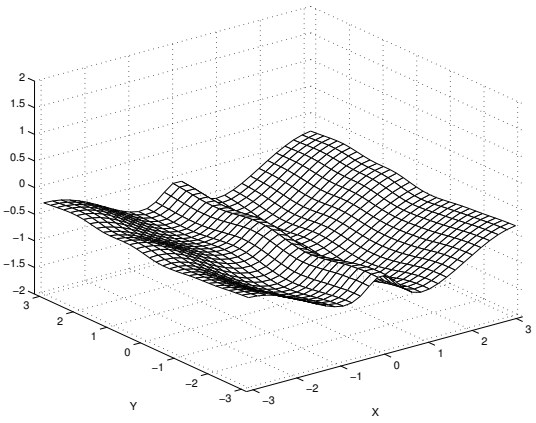

The skewness of the total stream function for the sine-bracket truncation, 23×23 truncation size, $E = 7$, $\mathcal{E} = 20$, $\tilde{C}_3 = 4$

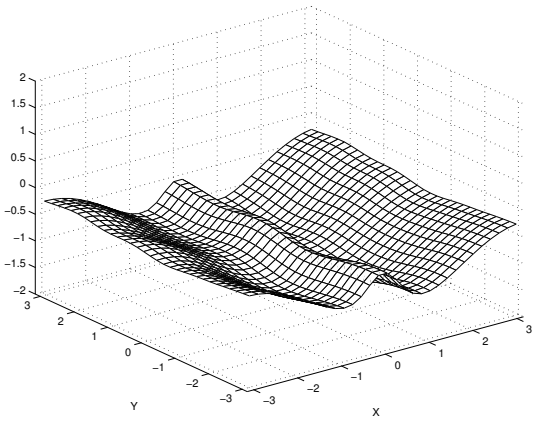

The skewness of the coarse-grained stream function for the sine-bracket truncation, 23×23 truncation size, $E = 7$, $\mathcal{E} = 20$, $\tilde{C}_3 = 4$

Figure 6.62: The skewness of the total and coarse-grained mean stream functions for the sine-bracket truncation, 23×23 truncation size, $\tilde{C}_3 = 4$, layered topography

ure 5.43), thus confirming that the value $\tilde{C}_3 = 0$ is statistically irrelevant. However, as we increase the $\tilde{C}_3$, the scatterplots become bent, and the curvature of scatterplots clearly increases with increasing values of $\tilde{C}_3$ (Figure 6.71 for $\tilde{C}_3 = 2$, Figure 6.72 for $\tilde{C}_3 = 4$, and Figure 6.73 for $\tilde{C}_3 = 6$).

6.3.4 Time correlation functions

The time correlation functions (5.8) for different Fourier modes of the 23×23 sine-bracket truncation (4.1), are shown in Figures 6.74. We use the equation (5.8) described in Section 5.0.3 to compute the time correlation functions. Here we show that the statistically relevant values of the normalized third Casimir invariant affect the time correlation functions in a very simple way. If we compare the correlation functions for the traditional truncation (3.17), which are shown in Figure 5.45, and the correlation functions for the sine-bracket truncation (4.1) which are shown in Figure 6.74, we can see that the statistically irrelevant value $\tilde{C}_3 = 0$ does not affect the correlation functions for both truncation sizes, but the statistically relevant values $\tilde{C}_3 = 2$, $\tilde{C}_3 = 4$ and $\tilde{C}_3 = 8$ slow down the decay rate of correlation functions. However, we note that, unlike the cases with no topography (Figure 6.24), and random topography (Figure 6.51), in this case with layered topography the correlation functions decay fast enough to admit that the statistical calculations are valid for all values $\tilde{C}_3 = 0$, 2, 4, and 6.

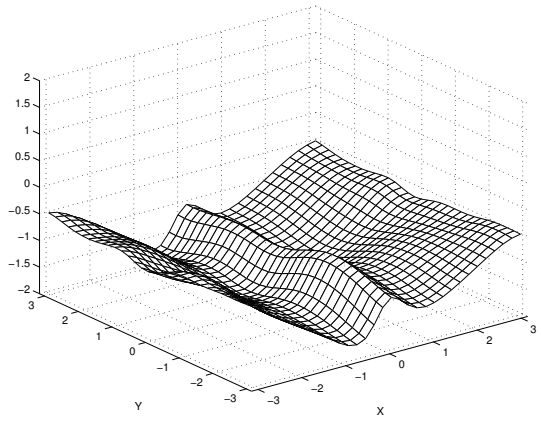

The skewness of the total stream function for the sine-bracket truncation, 23×23 truncation size, $E = 7$, $\mathcal{E} = 20$, $\tilde{C}_3 = 6$

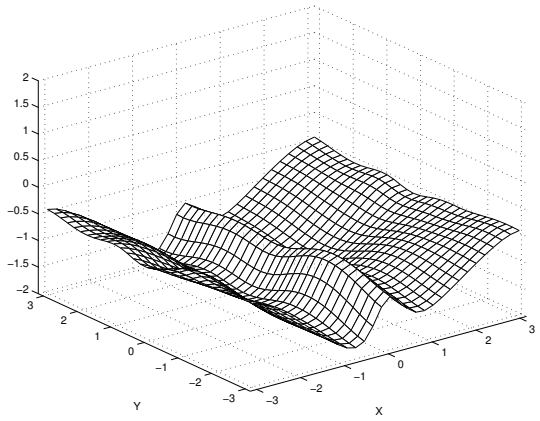

The skewness of the coarse-grained stream function for the sine-bracket truncation, 23×23 truncation size, $E = 7$, $\mathcal{E} = 20$, $\tilde{C}_3 = 6$

Figure 6.63: The skewness of the total and coarse-grained mean stream functions for the sine-bracket truncation, 23×23 truncation size, $\tilde{C}_3 = 6$, layered topography

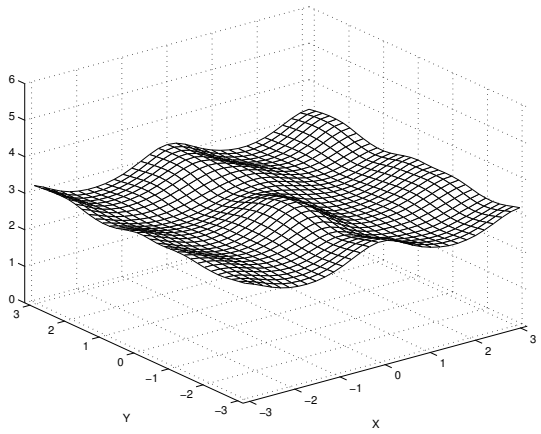

The flatness of the total stream function for the sine-bracket truncation, 23×23 truncation size, $E = 7$, $\mathcal{E} = 20$, $\tilde{C}_3 = 0$

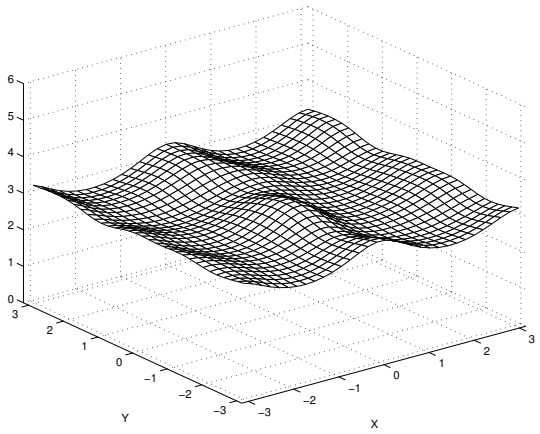

The flatness of the coarse-grained stream function for the sine-bracket truncation, 23×23 truncation size, $E = 7$, $\mathcal{E} = 20$, $\tilde{C}_3 = 0$

Figure 6.64: The flatness of the total and coarse-grained mean stream functions for the sine-bracket truncation, 23×23 truncation size, $\tilde{C}_3 = 0$, layered topography

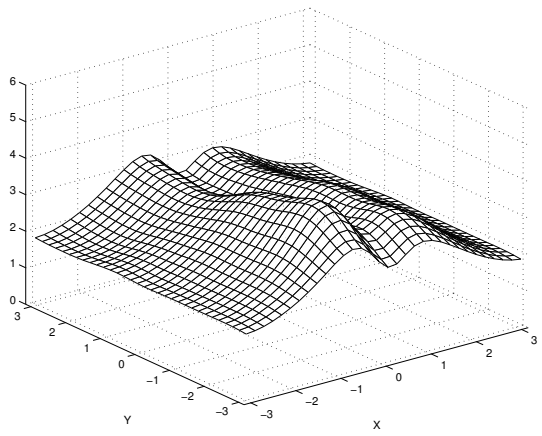

The flatness of the total stream function for the sine-bracket truncation, 23×23 truncation size, $E = 7$, $\mathcal{E} = 20$, $\tilde{C}_3 = 2$

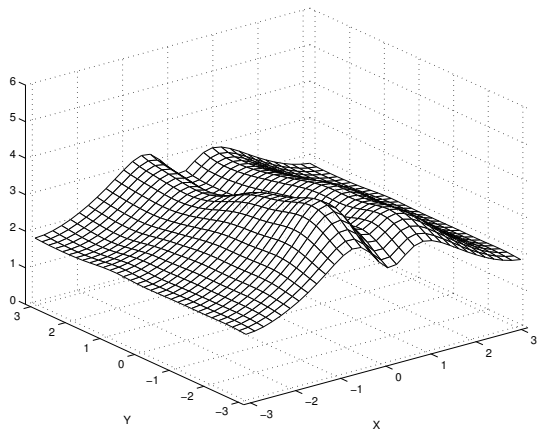

The flatness of the coarse-grained stream function for the sine-bracket truncation, 23×23 truncation size, $E = 7$, $\mathcal{E} = 20$, $\tilde{C}_3 = 2$

Figure 6.65: The flatness of the total and coarse-grained mean stream functions for the sine-bracket truncation, 23×23 truncation size, $\tilde{C}_3 = 2$, layered topography

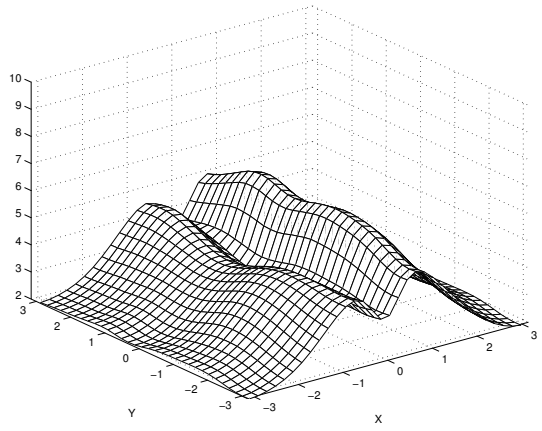

The flatness of the total stream function for the sine-bracket truncation, 23×23 truncation size, $E = 7$, $\mathcal{E} = 20$, $\tilde{C}_3 = 4$

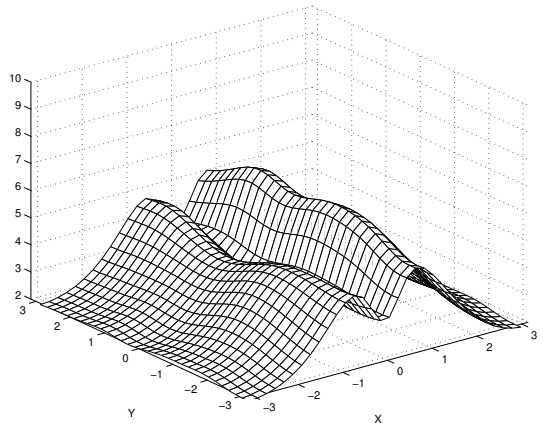

The flatness of the coarse-grained stream function for the sine-bracket truncation, 23×23 truncation size, $E = 7$, $\mathcal{E} = 20$, $\tilde{C}_3 = 4$

Figure 6.66: The flatness of the total and coarse-grained mean stream functions for the sine-bracket truncation, 23×23 truncation size, $\tilde{C}_3 = 4$, layered topography

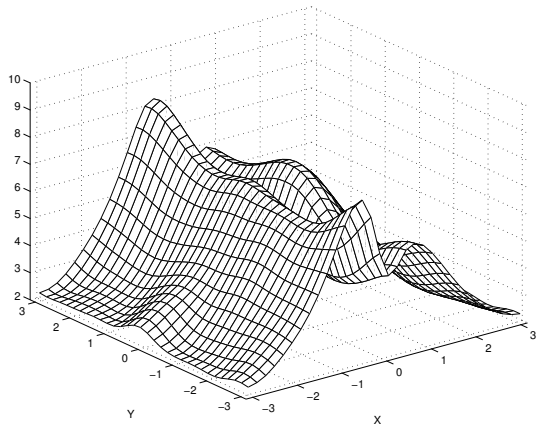

The flatness of the total stream function for the sine-bracket truncation, 23×23 truncation size, $E = 7$, $\mathcal{E} = 20$, $\tilde{C}_3 = 6$

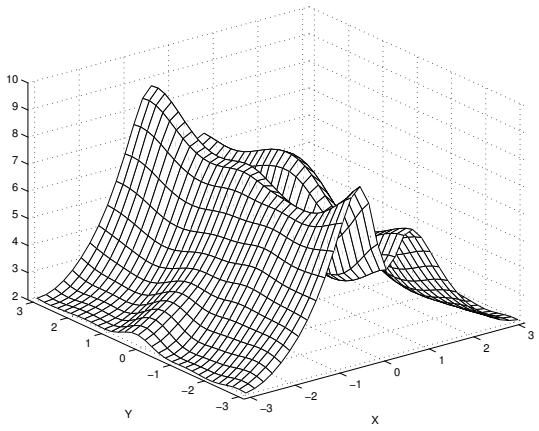

The flatness of the coarse-grained stream function for the sine-bracket truncation, 23×23 truncation size, $E = 7$, $\mathcal{E} = 20$, $\tilde{C}_3 = 6$

Figure 6.67: The flatness of the total and coarse-grained mean stream functions for the sine-bracket truncation, 23×23 truncation size, $\tilde{C}_3 = 6$, layered topography

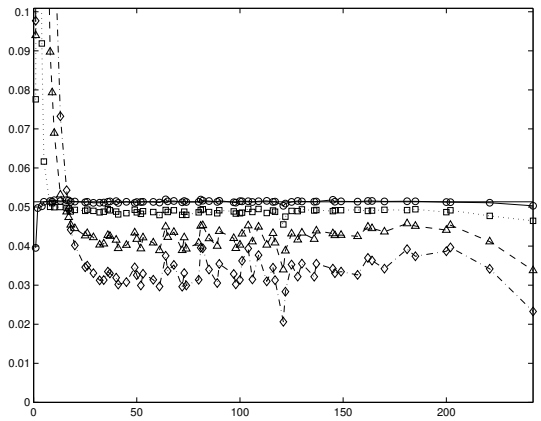

The pseudo-energy spectrum, sine-bracket truncation, 23×23 truncation size, $E = 7$, $\mathcal{E} = 20$, solid line with circles – $\tilde{C}_3 = 0$, dotted line with squares – $\tilde{C}_3 = 2$, dashed line with triangles – $\tilde{C}_3 = 4$, dot-dashed line with diamonds – $\tilde{C}_3 = 6$

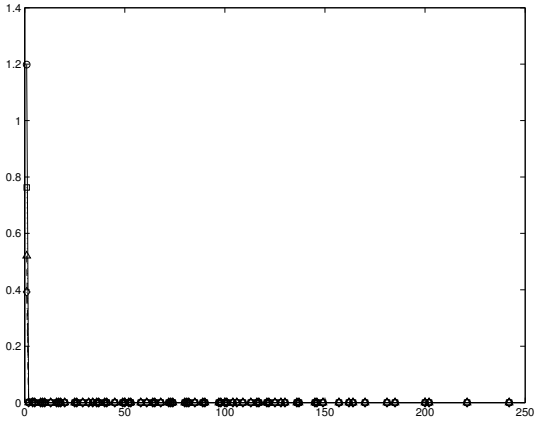

The energy of the mean flow spectrum, sine-bracket truncation, 23×23 truncation size, $E = 7$, $\mathcal{E} = 20$, solid line with circles – $\tilde{C}_3 = 0$, dotted line with squares – $\tilde{C}_3 = 2$, dashed line with triangles – $\tilde{C}_3 = 4$, dot-dashed line with diamonds – $\tilde{C}_3 = 6$

Figure 6.68: The pseudo-energy spectrum and the spectrum of energy of the mean, 23×23 sine-bracket truncation, layered topography

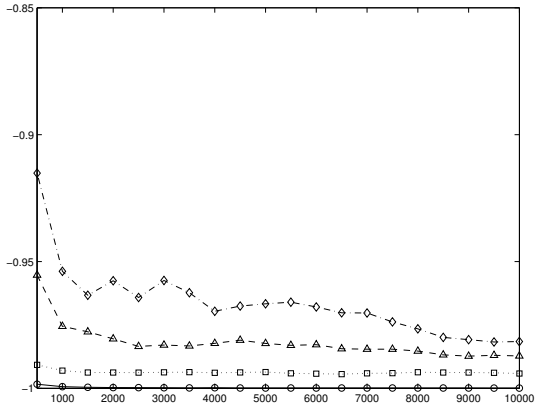

The total Corr$[\langle\psi\rangle_\tau, \langle q\rangle_\tau](\tau)$ function for the sine-bracket truncation, 23×23 truncation size, $E = 7$, $\mathcal{E} = 20$, solid line with circles – $\tilde{C}_3 = 0$, dotted line with squares – $\tilde{C}_3 = 2$, dashed line with triangles – $\tilde{C}_3 = 4$, dot-dashed line with diamonds – $\tilde{C}_3 = 6$

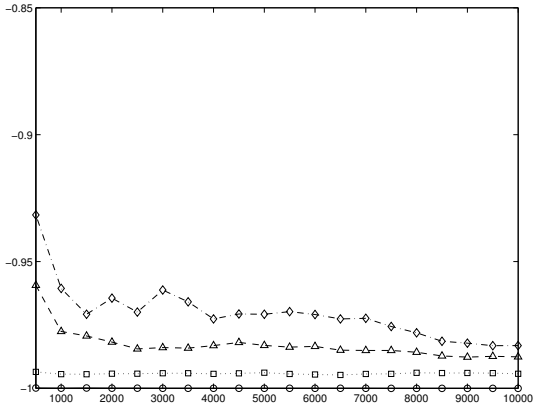

The coarse-grained Corr$[\langle\psi\rangle_\tau, \langle q\rangle_\tau](\tau)$ function for the sine-bracket truncation, 23×23 truncation size, $E = 7$, $\mathcal{E} = 20$, solid line with circles – $\tilde{C}_3 = 0$, dotted line with squares – $\tilde{C}_3 = 2$, dashed line with triangles – $\tilde{C}_3 = 4$, dot-dashed line with diamonds – $\tilde{C}_3 = 6$

Figure 6.69: The total and coarse-grained Corr functions for the sine-bracket truncation, 23×23 truncation size, $\tilde{C}_3 = 0$, 2, 4, and 6, layered topography

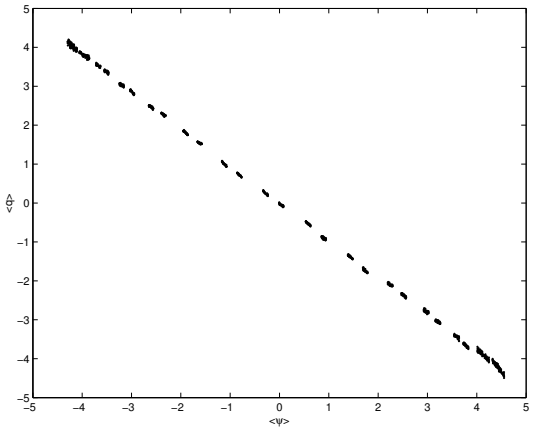

The scatterplot $\langle\psi\rangle_\tau$ vs $\langle q\rangle_\tau$, sine-bracket truncation, 23×23 truncation size, $E = 7$, $\mathcal{E} = 20$, $\tilde{C}_3 = 0$

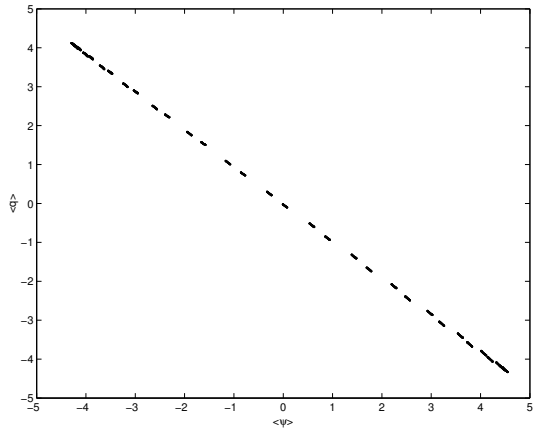

The coarse-grained scatterplot $\langle\psi\rangle_\tau$ vs $\langle q\rangle_\tau$, sine-bracket truncation, 23×23 truncation size, $E = 7$, $\mathcal{E} = 20$, $\tilde{C}_3 = 0$

Figure 6.70: The total and coarse-grained scatterplots $\bar{q}$ vs $\bar{\psi}$, 23×23 sine-bracket truncation, $\tilde{C}_3 = 0$, layered topography

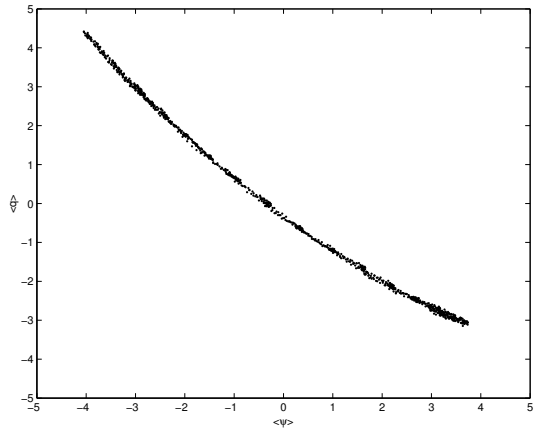

The scatterplot $\langle\psi\rangle_\tau$ vs $\langle q\rangle_\tau$, sine-bracket truncation, 23×23 truncation size, $E = 7$, $\mathcal{E} = 20$, $\tilde{C}_3 = 2$

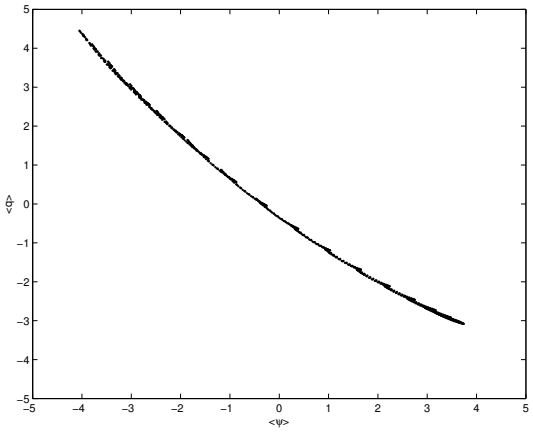

The coarse-grained scatterplot $\langle\psi\rangle_\tau$ vs $\langle q\rangle_\tau$, sine-bracket truncation, 23×23 truncation size, $E = 7$, $\mathcal{E} = 20$, $\tilde{C}_3 = 2$

Figure 6.71: The total and coarse-grained scatterplots $\bar{q}$ vs $\bar{\psi}$, 23×23 sine-bracket truncation, $\tilde{C}_3 = 2$, layered topography

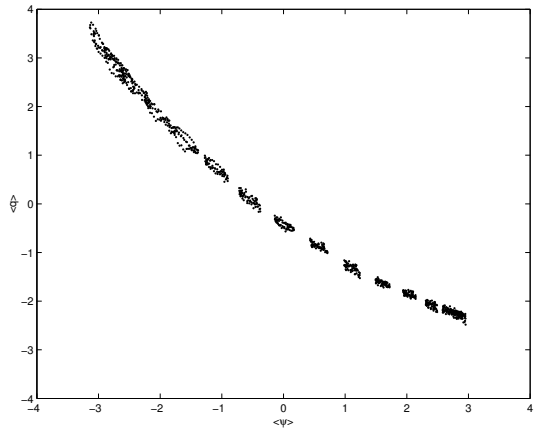

The scatterplot $\langle\psi\rangle_\tau$ vs $\langle q\rangle_\tau$, sine-bracket truncation, 23×23 truncation size, $E = 7$, $\mathcal{E} = 20$, $\tilde{C}_3 = 4$

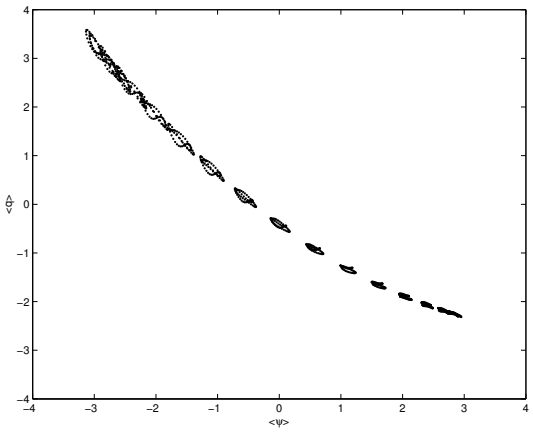

The coarse-grained scatterplot $\langle\psi\rangle_\tau$ vs $\langle q\rangle_\tau$, sine-bracket truncation, 23×23 truncation size, $E = 7$, $\mathcal{E} = 20$, $\tilde{C}_3 = 4$

Figure 6.72: The total and coarse-grained scatterplots $\bar{q}$ vs $\bar{\psi}$, 23×23 sine-bracket truncation, $\tilde{C}_3 = 4$, layered topography

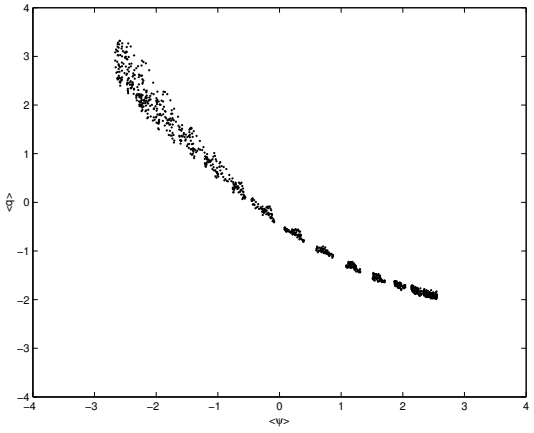

The scatterplot $\langle\psi\rangle_\tau$ vs $\langle q\rangle_\tau$, sine-bracket truncation, 23×23 truncation size, $E = 7$, $\mathcal{E} = 20$, $\tilde{C}_3 = 6$

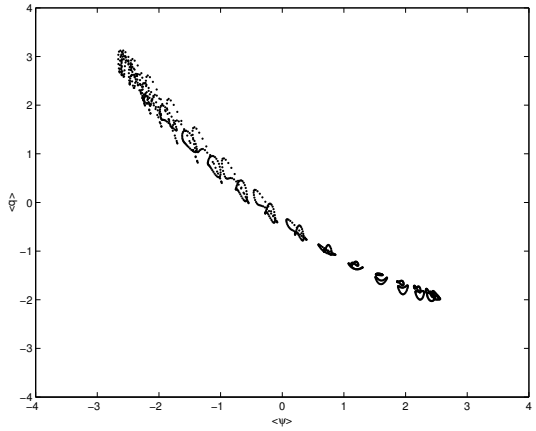

The coarse-grained scatterplot $\langle\psi\rangle_\tau$ vs $\langle q\rangle_\tau$, sine-bracket truncation, 23×23 truncation size, $E = 7$, $\mathcal{E} = 20$, $\tilde{C}_3 = 6$

Figure 6.73: The total and coarse-grained scatterplots $\bar{q}$ vs $\bar{\psi}$, 23×23 sine-bracket truncation, $\tilde{C}_3 = 6$, layered topography

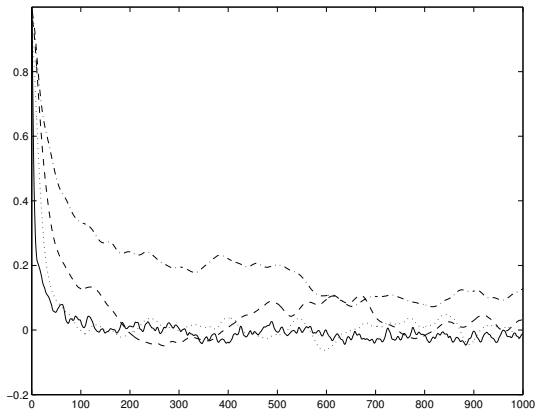

The time correlation functions for $|\mathbf{k}|^2 = 1$, sine-bracket truncation, 23×23 truncation size, $E = 7$, $\mathcal{E} = 20$, solid line – $\tilde{C}_3 = 0$, dotted line – $\tilde{C}_3 = 2$, dashed line – $\tilde{C}_3 = 4$, dot-dashed line – $\tilde{C}_3 = 6$

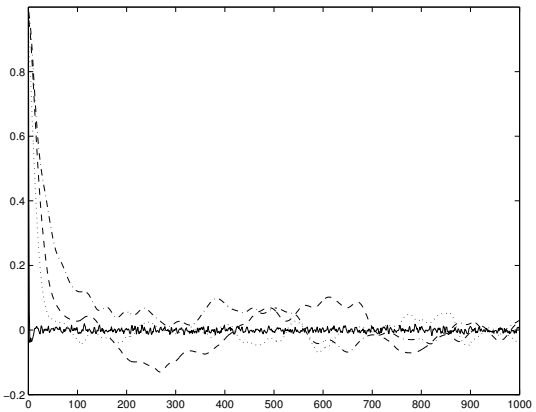

The time correlation functions for $|\mathbf{k}|^2 = 2$, sine-bracket truncation, 23×23 truncation size, $E = 7$, $\mathcal{E} = 20$, solid line – $\tilde{C}_3 = 0$, dotted line – $\tilde{C}_3 = 2$, dashed line – $\tilde{C}_3 = 4$, dot-dashed line – $\tilde{C}_3 = 6$

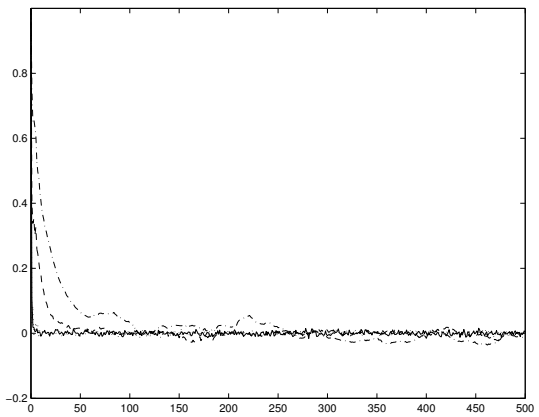

The time correlation functions for $|\mathbf{k}|^2 = 8$, sine-bracket truncation, 23×23 truncation size, $E = 7$, $\mathcal{E} = 20$, solid line – $\tilde{C}_3 = 0$, dotted line – $\tilde{C}_3 = 2$, dashed line – $\tilde{C}_3 = 4$, dot-dashed line – $\tilde{C}_3 = 6$

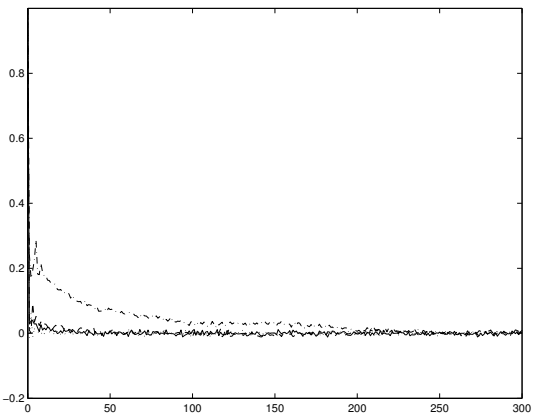

The time correlation functions for $|\mathbf{k}|^2 = 16$, sine-bracket truncation, 23×23 truncation size, $E = 7$, $\mathcal{E} = 20$, solid line – $\tilde{C}_3 = 0$, dotted line – $\tilde{C}_3 = 2$, dashed line – $\tilde{C}_3 = 4$, dot-dashed line – $\tilde{C}_3 = 6$

Figure 6.74: The time correlation functions for the 23×23 sine-bracket truncation, layered topography

$\tilde{C}_3$	Variance	Skewness
0	65.67	$-1.37 \cdot 10^{-2}$
2	56.14	0.3114
4	50.82	0.7752
6	48.08	1.441

Table 6.7: The variance and skewness of spatially averaged probability density functions for the potential vorticity, 23×23 sine-bracket truncation, layered topography

Fourier space PDF's		
Mode	Mean	Variance
$\mathbf{k} = (0,1)$	$-1.932 \cdot 10^{-2}$	$5.868 \cdot 10^{-1}$
$\mathbf{k} = (1,0)$	-2.089	$2.691 \cdot 10^{-1}$
$\mathbf{k} = (1,-1)$	$-3.688 \cdot 10^{-3}$	$4.722 \cdot 10^{-2}$
$\mathbf{k} = (1,1)$	$-4.293 \cdot 10^{-3}$	$4.743 \cdot 10^{-2}$
$\mathbf{k} = (0,2)$	$9.112 \cdot 10^{-4}$	$3.358 \cdot 10^{-2}$
$\mathbf{k} = (2,0)$	$-4.787 \cdot 10^{-2}$	$3.189 \cdot 10^{-2}$
$\mathbf{k} = (1,-2)$	$-3.975 \cdot 10^{-4}$	$3.168 \cdot 10^{-2}$
$\mathbf{k} = (1,2)$	$-9.594 \cdot 10^{-5}$	$3.193 \cdot 10^{-2}$
$\mathbf{k} = (2,-1)$	$-5.959 \cdot 10^{-4}$	$3.169 \cdot 10^{-2}$
$\mathbf{k} = (2,1)$	$1.270 \cdot 10^{-6}$	$3.165 \cdot 10^{-2}$
$\mathbf{k} = (2,-2)$	$-3.876 \cdot 10^{-4}$	$2.914 \cdot 10^{-2}$
$\mathbf{k} = (2,2)$	$1.539 \cdot 10^{-3}$	$2.924 \cdot 10^{-2}$

Table 6.8: The means and variances of the PDF's of the Fourier modes for the potential vorticity, 23×23 sine-bracket truncation, $\tilde{C}_3 = 0$, layered topography

6.3.5 Probability density functions

In this section we represent the numerically computed probability density functions of the two kinds: the PDF's for the real parts of the Fourier modes of the potential vorticity, and the spatially averaged probability density functions for the potential vorticity with removed mean.

6.3.5.1 Probability density functions for the potential vorticity

We present the spatially averaged PDF with removed mean for the potential vorticity in physical space, computed with 23×23 sine-bracket truncation truncation (4.1) for the values $\tilde{C}_3 = 0$, 2, 4, and 6. The numerical algorithm which was used in obtaining the PDF's in described in the Section 5.0.3. Thus obtained probability density functions for the potential vorticity are represented in Figure 6.75, and their variances and skewnesses

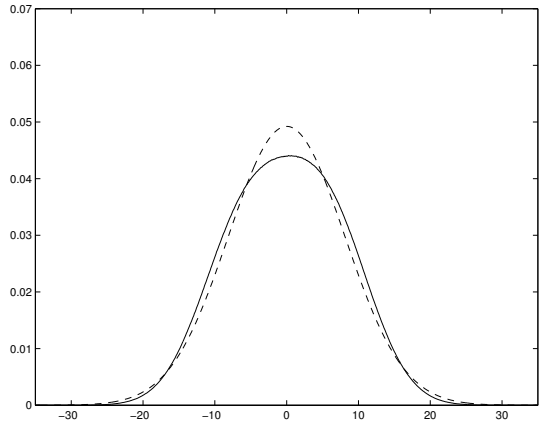

The PDF for the potential vorticity, 23×23 sine-bracket truncation, $\tilde{C}_3 = 0$, layered topography, solid line - direct numerical simulation, dashed line - analytical Gaussian with the same variance

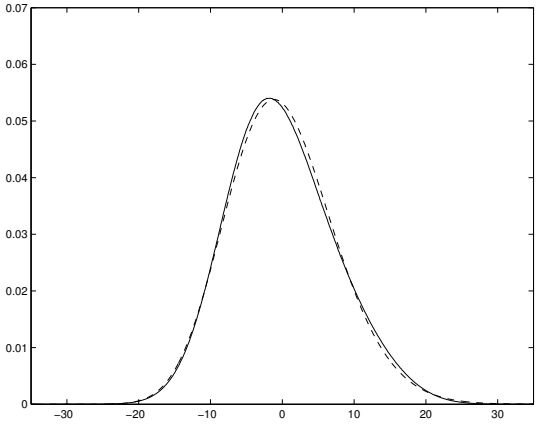

The PDF for the potential vorticity, 23×23 sine-bracket truncation, $\tilde{C}_3 = 2$, layered topography, solid line - direct numerical simulation, dashed line - analytical Gamma distribution with the same variance and skewness

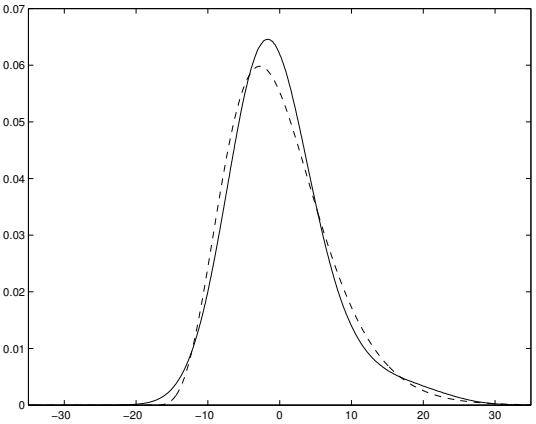

The PDF for the potential vorticity, 23×23 sine-bracket truncation, $\tilde{C}_3 = 4$, layered topography, solid line - direct numerical simulation, dashed line - analytical Gamma-distribution with the same variance and skewness

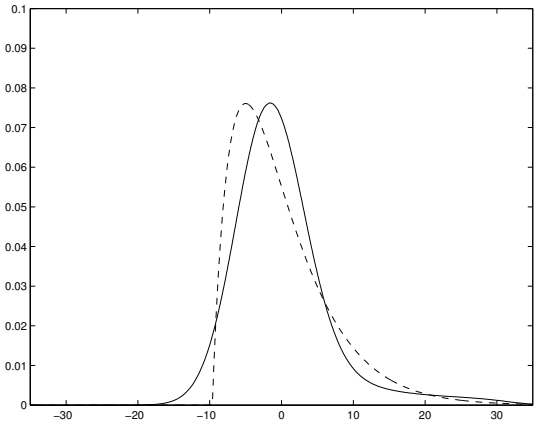

The PDF for the potential vorticity, 23×23 sine-bracket truncation, $\tilde{C}_3 = 6$, layered topography, solid line - direct numerical simulation, dashed line - analytical Gamma-distribution with the same variance and skewness

Figure 6.75: The spatially averaged probability density function for the potential vorticity with removed mean, $\tilde{C}_3 = 0$, 2, 4, and 6, layered topography

Fourier space PDF's		
Mode	Mean	Variance
$\mathbf{k} = (0,1)$	$-6.696 \cdot 10^{-2}$	1.137
$\mathbf{k} = (1,0)$	-1.635	$3.531 \cdot 10^{-1}$
$\mathbf{k} = (1,-1)$	$2.499 \cdot 10^{-2}$	$2.305 \cdot 10^{-1}$
$\mathbf{k} = (1,1)$	$1.634 \cdot 10^{-2}$	$2.261 \cdot 10^{-1}$
$\mathbf{k} = (0,2)$	$-1.435 \cdot 10^{-2}$	$5.677 \cdot 10^{-2}$
$\mathbf{k} = (2,0)$	$1.536 \cdot 10^{-1}$	$5.163 \cdot 10^{-2}$
$\mathbf{k} = (1,-2)$	$6.187 \cdot 10^{-3}$	$3.701 \cdot 10^{-2}$
$\mathbf{k} = (1,2)$	$7.382 \cdot 10^{-3}$	$3.692 \cdot 10^{-2}$
$\mathbf{k} = (2,-1)$	$-3.026 \cdot 10^{-3}$	$3.958 \cdot 10^{-2}$
$\mathbf{k} = (2,1)$	$-2.546 \cdot 10^{-3}$	$3.887 \cdot 10^{-2}$
$\mathbf{k} = (2,-2)$	$-4.975 \cdot 10^{-4}$	$2.849 \cdot 10^{-2}$
$\mathbf{k} = (2,2)$	$-1.294 \cdot 10^{-3}$	$2.805 \cdot 10^{-2}$

Table 6.9: The means and variances of the PDF's of the Fourier modes for the potential vorticity, 23×23 sine-bracket truncation, $\tilde{C}_3 = 2$, layered topography

Fourier space PDF's		
Mode	Mean	Variance
$\mathbf{k} = (0,1)$	$-4.304 \cdot 10^{-2}$	1.293
$\mathbf{k} = (1,0)$	-1.342	$9.072 \cdot 10^{-1}$
$\mathbf{k} = (1,-1)$	$1.412 \cdot 10^{-2}$	$5.035 \cdot 10^{-1}$
$\mathbf{k} = (1,1)$	$4.370 \cdot 10^{-2}$	$4.832 \cdot 10^{-1}$
$\mathbf{k} = (0,2)$	$2.960 \cdot 10^{-2}$	$1.693 \cdot 10^{-1}$
$\mathbf{k} = (2,0)$	$2.090 \cdot 10^{-1}$	$1.323 \cdot 10^{-1}$
$\mathbf{k} = (1,-2)$	$-2.689 \cdot 10^{-2}$	$1.098 \cdot 10^{-1}$
$\mathbf{k} = (1,2)$	$-1.636 \cdot 10^{-2}$	$1.102 \cdot 10^{-1}$
$\mathbf{k} = (2,-1)$	$-4.315 \cdot 10^{-3}$	$1.210 \cdot 10^{-1}$
$\mathbf{k} = (2,1)$	$-2.273 \cdot 10^{-2}$	$1.155 \cdot 10^{-1}$
$\mathbf{k} = (2,-2)$	$1.447 \cdot 10^{-2}$	$4.991 \cdot 10^{-2}$
$\mathbf{k} = (2,2)$	$6.004 \cdot 10^{-3}$	$5.103 \cdot 10^{-2}$

Table 6.10: The means and variances of the PDF's of the Fourier modes for the potential vorticity, 23×23 sine-bracket truncation, $\tilde{C}_3 = 4$, layered topography

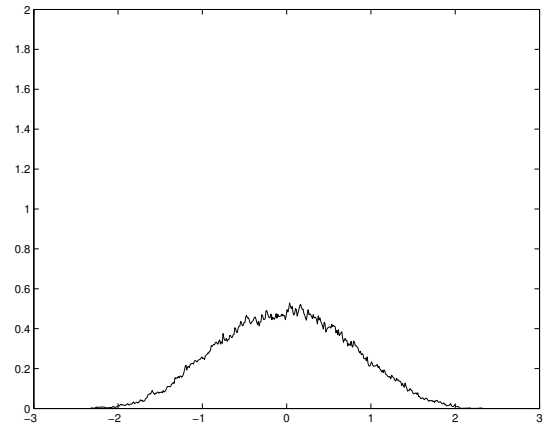

The PDF's for $\mathbf{k} = (0, 1)$, sine-bracket truncation, $\tilde{C}_3 = 0$, 23×23 total grid, $E = 7$, $\mathcal{E} = 20$, layered topography

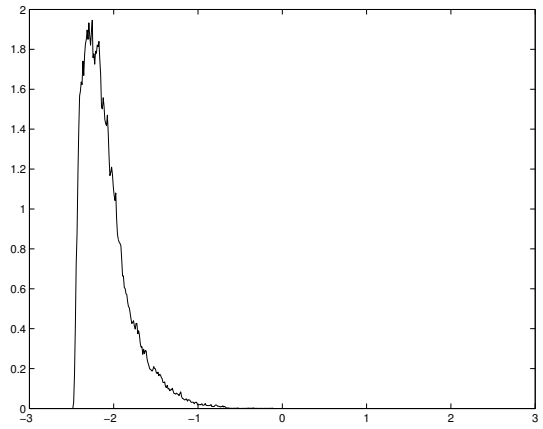

The PDF's for $\mathbf{k} = (1, 0)$, sine-bracket truncation, $\tilde{C}_3 = 0$, 23×23 total grid, $E = 7$, $\mathcal{E} = 20$, layered topography

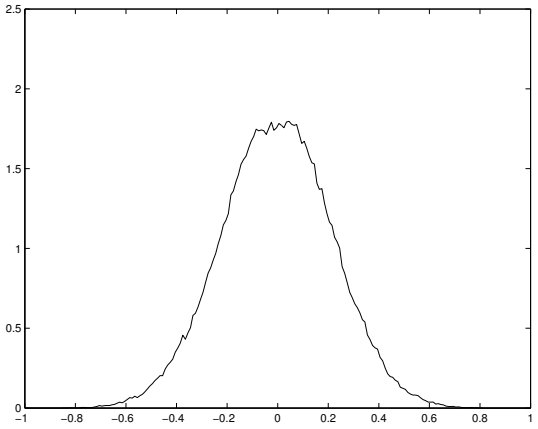

The PDF's for $\mathbf{k} = (1, -1)$, sine-bracket truncation, $\tilde{C}_3 = 0$, 23×23 total grid, $E = 7$, $\mathcal{E} = 20$, layered topography

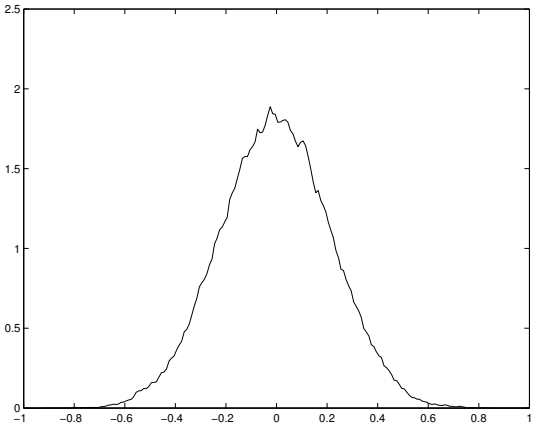

The PDF's for $\mathbf{k} = (1, 1)$, sine-bracket truncation, $\tilde{C}_3 = 0$, 23×23 total grid, $E = 7$, $\mathcal{E} = 20$, layered topography

Figure 6.76: The probability density functions for the Fourier modes of the potential vorticity, wavenumbers $(0, 1), (1.0), (1, -1), (1, 1)$, 23×23 sine-bracket truncation, $\tilde{C}_3 = 0$, layered topography

are provided in Table 6.7. The results for the traditional truncation (3.17) (Figure 5.46) and the sine-bracket truncation with $\tilde{C}_3 = 0$ (Figure 6.75) are identical, though not quite Gaussian. Nonetheless, this identity of the results for the traditional and sine-bracket truncations means that $\tilde{C}_3 = 0$ is statistically irrelevant. However, the PDF obtained for the direct numerical simulations with 23×23 sine-bracket truncation and $\tilde{C}_3 = 2$, exhibit significant amount of skewness (Figure 6.75). We fit the PDF for $\tilde{C}_3 = 2$ with the standard Gamma-distribution with the same variance and skewness (given in Table 6.7,

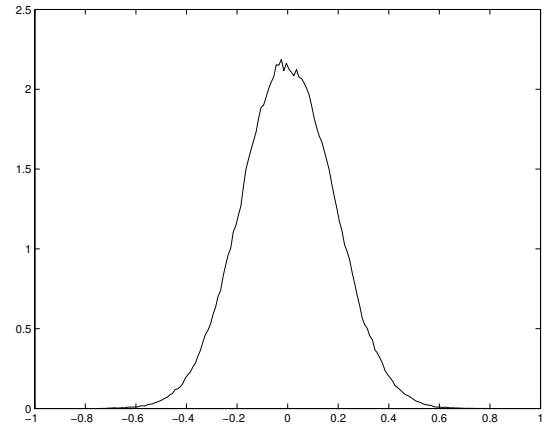

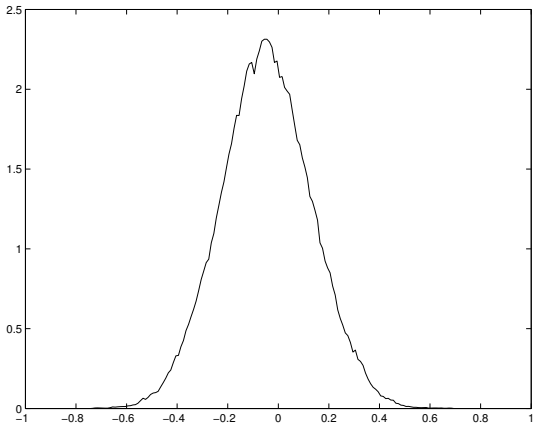

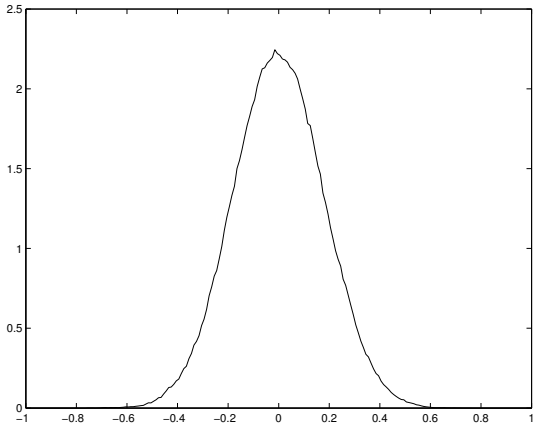

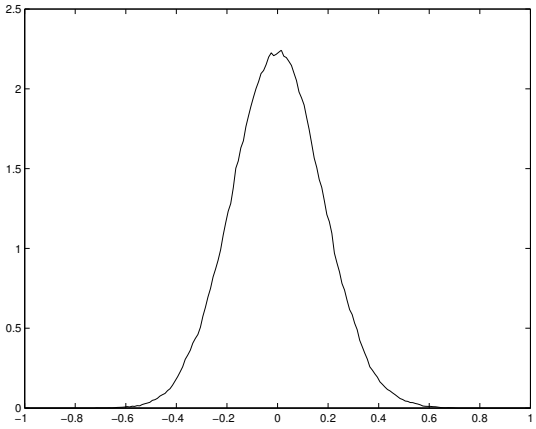

Figure 6.77: The probability density functions for the Fourier modes of the potential vorticity, wavenumbers $(0, 2), (2.0), (1, -2), (1, 2)$, 23×23 sine-bracket truncation, $\tilde{C}_3 = 0$, layered topography

skewness – 0.3114), and it fits very well (shown in Figure 6.75 as a dashed line). The PDF obtained for the direct numerical simulations with 23×23 sine-bracket truncation and $\tilde{C}_3 = 4$ exhibits twice as much of skewness (0.7752), which is also shown in Figure 6.75. This time, however, the Gamma-distribution fit fails to reproduce the original with same precision as before. The PDF obtained for the direct numerical simulations with 23×23 sine-bracket truncation and $\tilde{C}_3 = 6$ exhibits yet twice as much of skewness (1.441), which is also shown in Figure 6.75. However, for this value of $\tilde{C}_3$ the Gamma-distribution is not

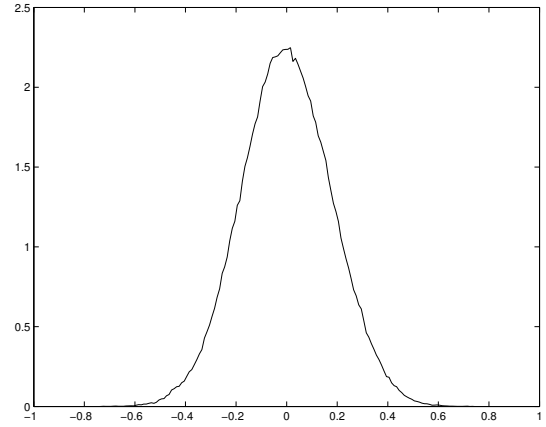

The PDF's for $\mathbf{k} = (2, -1)$, sine-bracket truncation, $\tilde{C}_3 = 0$, 23×23 total grid, $E = 7$, $\mathcal{E} = 20$, layered topography

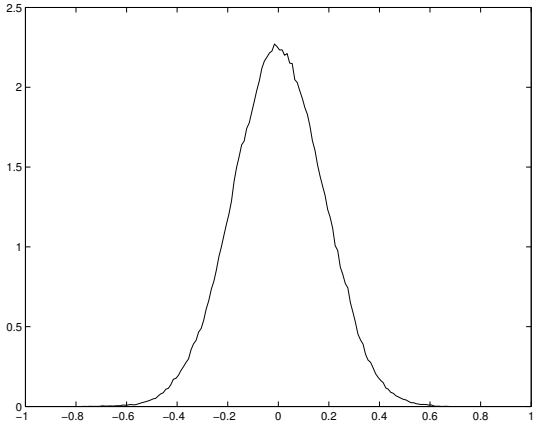

The PDF's for $\mathbf{k} = (2, 1)$, sine-bracket truncation, $\tilde{C}_3 = 0$, 23×23 total grid, $E = 7$, $\mathcal{E} = 20$, layered topography

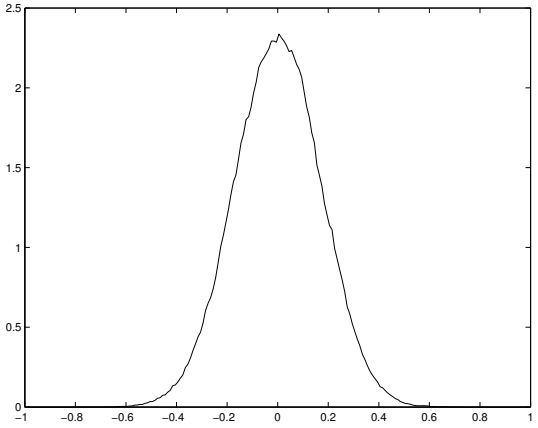

The PDF's for $\mathbf{k} = (2, -2)$, sine-bracket truncation, $\tilde{C}_3 = 0$, 23×23 total grid, $E = 7$, $\mathcal{E} = 20$, layered topography

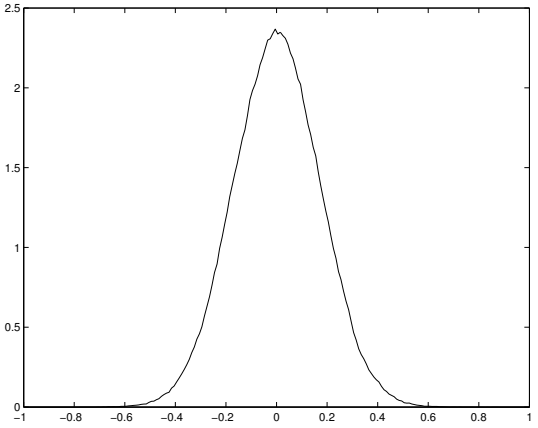

The PDF's for $\mathbf{k} = (2, 2)$, sine-bracket truncation, $\tilde{C}_3 = 0$, 23×23 total grid, $E = 7$, $\mathcal{E} = 20$, layered topography

Figure 6.78: The probability density functions for the Fourier modes of the potential vorticity, wavenumbers $(2, -1), (2.1), (2, -2), (2, 2)$, 23×23 sine-bracket truncation, $\tilde{C}_3 = 0$, layered topography

a good fit for the numerical result. Overall, $\tilde{C}_3 = 0$ is the statistically irrelevant values of the normalized third Casimir invariant, whereas $\tilde{C}_3 = 2$, 4, and 6 are statistically relevant.

6.3.5.2 PDF's for the Fourier modes of the potential vorticity

Here we present the probability density functions for the real parts of the Fourier modes of the potential vorticity obtained with the 23×23 sine-bracket truncation (4.1) for the values of the normalized third Casimir invariant $\tilde{C}_3 = 0$, 2, 4, and 6, where $\tilde{C}_3$ is given

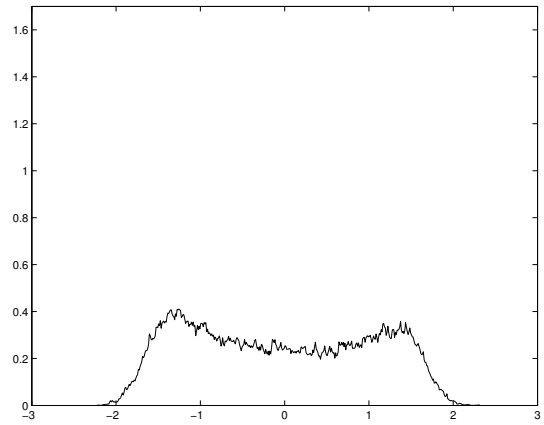

The PDF's for $\mathbf{k} = (0, 1)$, sine-bracket truncation, $\tilde{C}_3 = 2$, 23×23 total grid, $E = 7$, $\mathcal{E} = 20$, layered topography

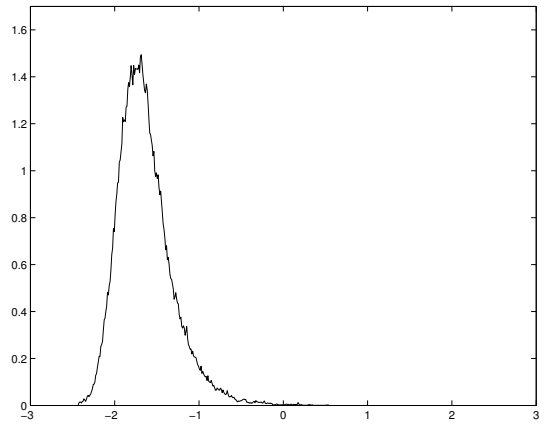

The PDF's for $\mathbf{k} = (1, 0)$, sine-bracket truncation, $\tilde{C}_3 = 2$, 23×23 total grid, $E = 7$, $\mathcal{E} = 20$, layered topography

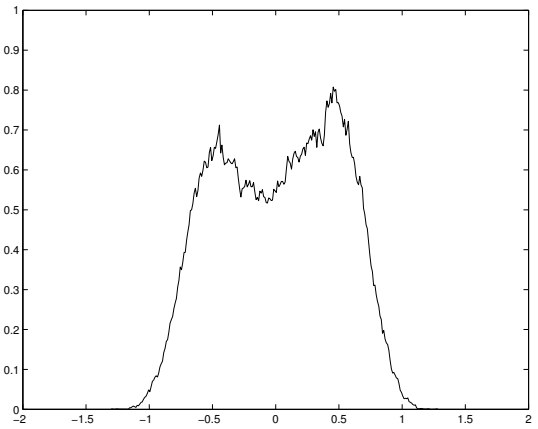

The PDF's for $\mathbf{k} = (1, -1)$, sine-bracket truncation, $\tilde{C}_3 = 2$, 23×23 total grid, $E = 7$, $\mathcal{E} = 20$, layered topography

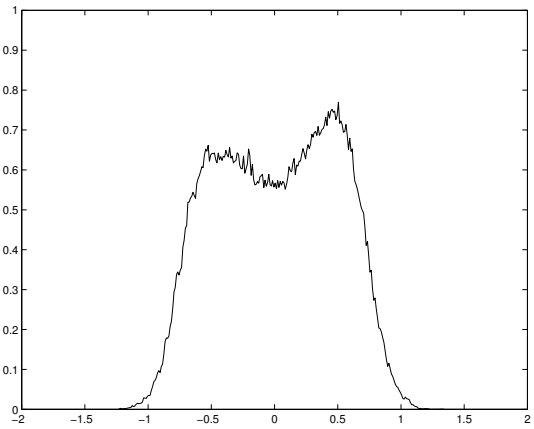

The PDF's for $\mathbf{k} = (1, 1)$, sine-bracket truncation, $\tilde{C}_3 = 2$, 23×23 total grid, $E = 7$, $\mathcal{E} = 20$, layered topography

Figure 6.79: The probability density functions for the Fourier modes of the potential vorticity, wavenumbers $(0, 1), (1.0), (1, -1), (1, 1)$, 23×23 sine-bracket truncation, $\tilde{C}_3 = 2$, layered topography

by (6.1). The numerical algorithm which was used in obtaining the PDF's is described in the Section 5.0.3. According to the statistical predictions (3.37), the shape of the PDF's should be Gaussian, which is confirmed by the direct numerical simulations with the traditional truncation (3.17), Figures 5.47, 5.48, and 5.49. The probability density functions for 23×23 sine-bracket truncation with $\tilde{C}_3 = 0$ are shown in Figures 6.76, 6.77, and 6.78. The means and variances for PDF's of the Fourier modes for the potential vorticity are shown in Table 6.8. As we can see, the PDF's for the sine-bracket truncation with $\tilde{C}_3 = 0$

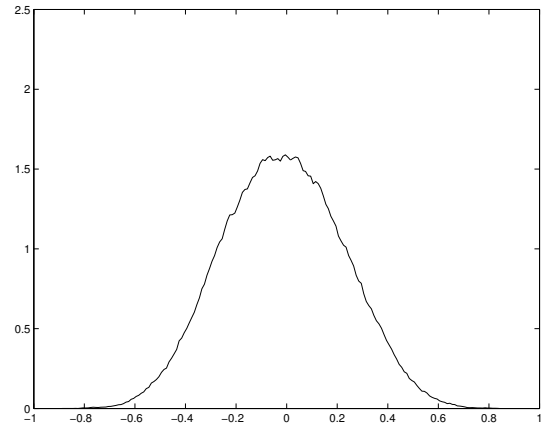

The PDF's for $\mathbf{k} = (0, 2)$, sine-bracket truncation, $\tilde{C}_3 = 2$, 23×23 total grid, $E = 7$, $\mathcal{E} = 20$, layered topography

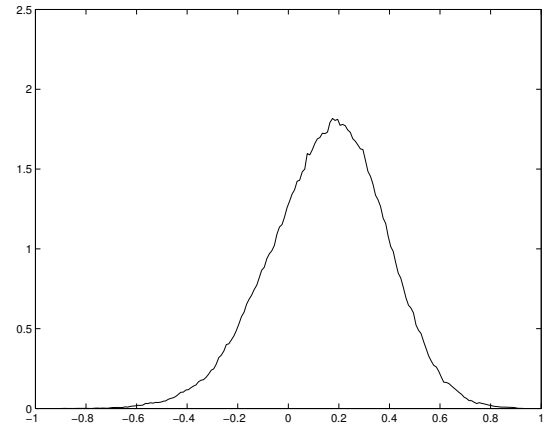

The PDF's for $\mathbf{k} = (2, 0)$, sine-bracket truncation, $\tilde{C}_3 = 2$, 23×23 total grid, $E = 7$, $\mathcal{E} = 20$, layered topography

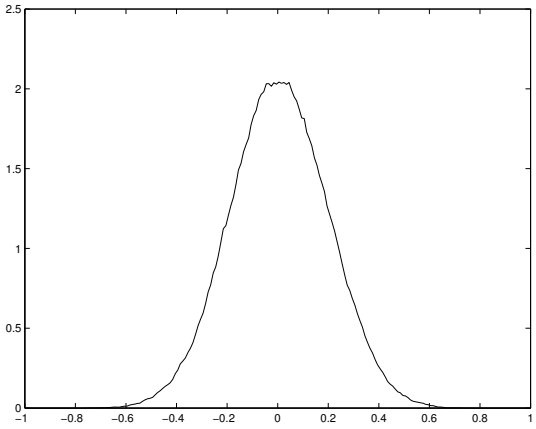

The PDF's for $\mathbf{k} = (1, -2)$, sine-bracket truncation, $\tilde{C}_3 = 2$, 23×23 total grid, $E = 7$, $\mathcal{E} = 20$, layered topography

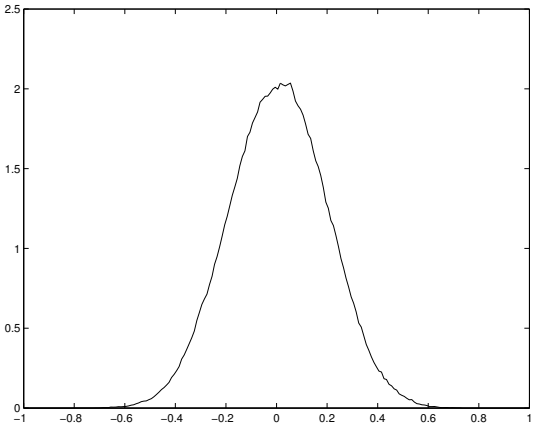

The PDF's for $\mathbf{k} = (1, 2)$, sine-bracket truncation, $\tilde{C}_3 = 2$, 23×23 total grid, $E = 7$, $\mathcal{E} = 20$, layered topography

Figure 6.80: The probability density functions for the Fourier modes of the potential vorticity, wavenumbers $(0, 2), (2.0), (1, -2), (1, 2)$, 23×23 sine-bracket truncation, $\tilde{C}_3 = 2$, layered topography

coincide with the corresponding PDF's for the traditional truncation (Figures 5.47, 5.48, and 5.49). Again, as in the case with the traditional truncation, we can see that essentially all PDF's have Gaussian shape, except for the PDF of mode $\mathbf{k} = (1, 0)$, which is shifted to the left from zero, and this is probably caused by the non-zero topography on that mode. The value $\tilde{C}_3 = 0$ is clearly irrelevant to the statistics since the results with $\tilde{C}_3 = 0$ coincide with those for the traditional truncation. The probability density functions for 23×23 sine-bracket truncation with $\tilde{C}_3 = 2$ are shown in Figures 6.79, 6.80, and 6.81, and

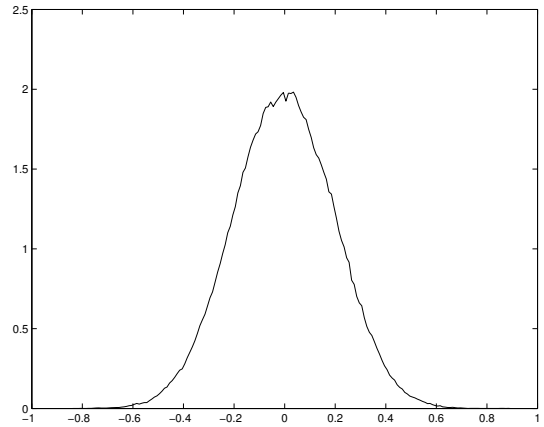

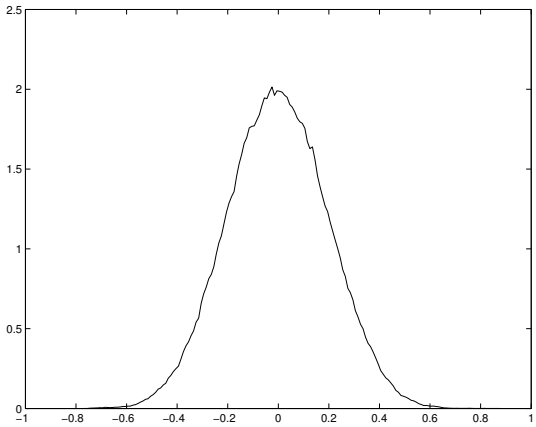

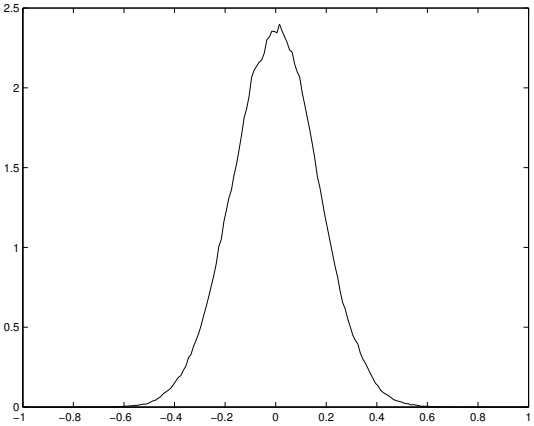

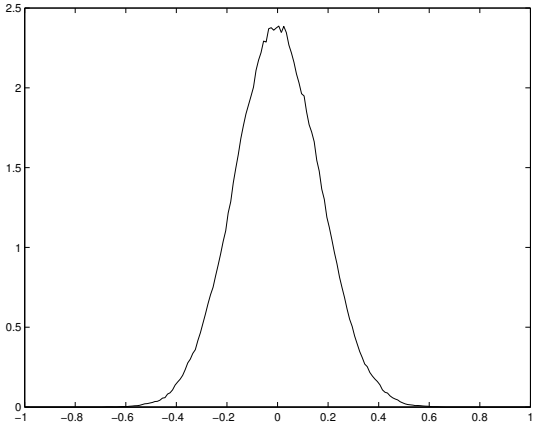

Figure 6.81: The probability density functions for the Fourier modes of the potential vorticity, wavenumbers $(2, -1), (2.1), (2, -2), (2, 2)$, 23×23 sine-bracket truncation, $\tilde{C}_3 = 2$, layered topography

the means and variances for these PDF's are shown in Table 6.9. The influence of statistically relevant Casimir invariant expands on the modes with $\mathbf{k} = (0, 1), (1, 0), (1, -1), (1, 1)$, (Figure 6.79), where the probability density functions are bimodal. The rest of the PDF's have Gaussian shape, except for the PDF for $\mathbf{k} = (2, 0)$, which is significantly skewed due to non-zero topography present on that mode (Figure 6.80). The probability density functions for 23×23 sine-bracket truncation with $\tilde{C}_3 = 4$ are shown in Figures 6.82, 6.83, and 6.84. The means and variances for these PDF's are shown in Table 6.10. The influence

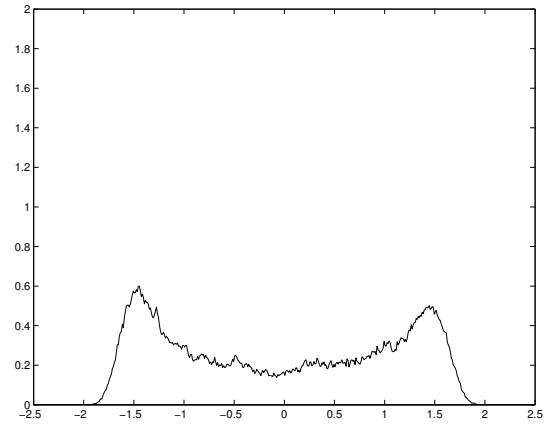

The PDF's for $\mathbf{k} = (0, 1)$, sine-bracket truncation, $\tilde{C}_3 = 4$, 23×23 total grid, $E = 7$, $\mathcal{E} = 20$, layered topography

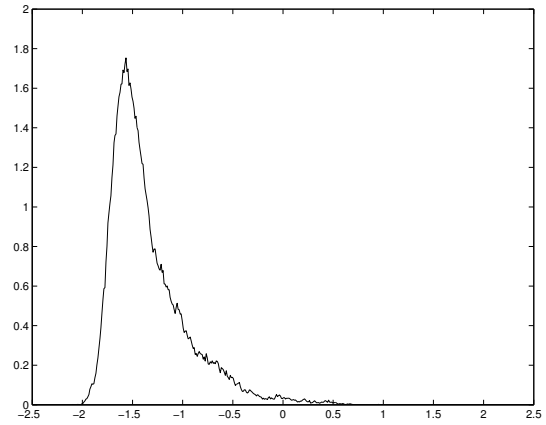

The PDF's for $\mathbf{k} = (1, 0)$, sine-bracket truncation, $\tilde{C}_3 = 4$, 23×23 total grid, $E = 7$, $\mathcal{E} = 20$, layered topography

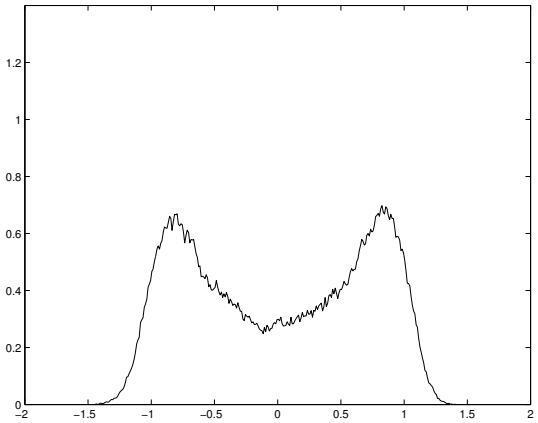

The PDF's for $\mathbf{k} = (1, -1)$, sine-bracket truncation, $\tilde{C}_3 = 4$, 23×23 total grid, $E = 7$, $\mathcal{E} = 20$, layered topography

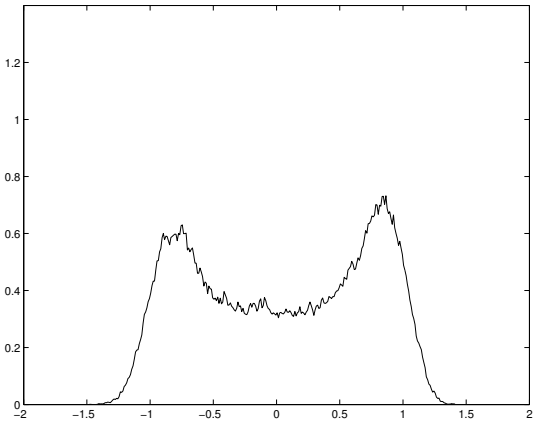

The PDF's for $\mathbf{k} = (1, 1)$, sine-bracket truncation, $\tilde{C}_3 = 4$, 23×23 total grid, $E = 7$, $\mathcal{E} = 20$, layered topography

Figure 6.82: The probability density functions for the Fourier modes of the potential vorticity, wavenumbers $(0, 1), (1.0), (1, -1), (1, 1)$, 23×23 sine-bracket truncation, $\tilde{C}_3 = 4$, layered topography

of statistically relevant Casimir invariant expands on all modes within the 5×5 coarse-grained grid except for those with $\mathbf{k} = (2, -2), (2, 2)$, (Figures 6.82, 6.83, and 6.84), where the probability density functions are bimodal. The PDF's for the modes with $\mathbf{k} = (1, 0)$ and $\mathbf{k} = (2, 0)$ are unimodal, but significantly skewed due to the presence of non-zero topography on those modes (Figures 6.82, and 6.83). The probability density functions for 23×23 sine-bracket truncation with $\tilde{C}_3 = 6$ are shown in Figures 6.85, 6.86, and 6.87. The means and variances for these PDF's are shown in Table 6.11. Here the influence of

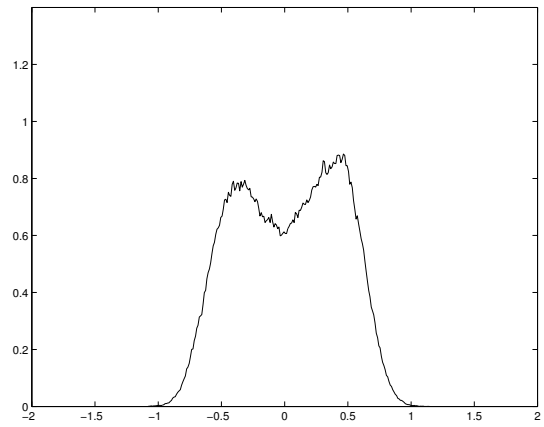

The PDF's for $\mathbf{k} = (0, 2)$, sine-bracket truncation, $\tilde{C}_3 = 4$, 23×23 total grid, $E = 7$, $\mathcal{E} = 20$, layered topography

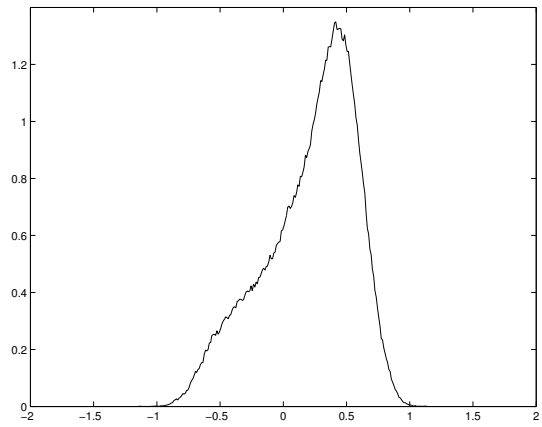

The PDF's for $\mathbf{k} = (2, 0)$, sine-bracket truncation, $\tilde{C}_3 = 4$, 23×23 total grid, $E = 7$, $\mathcal{E} = 20$, layered topography

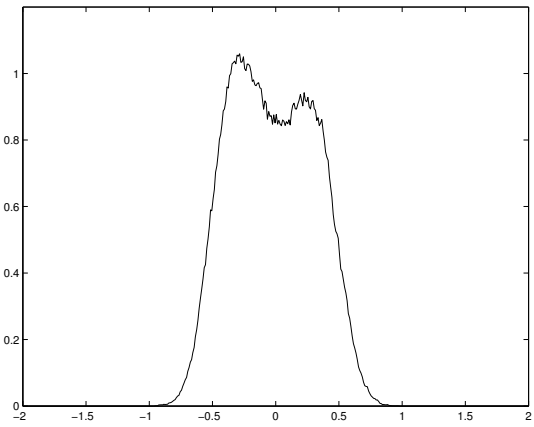

The PDF's for $\mathbf{k} = (1, -2)$, sine-bracket truncation, $\tilde{C}_3 = 4$, 23×23 total grid, $E = 7$, $\mathcal{E} = 20$, layered topography

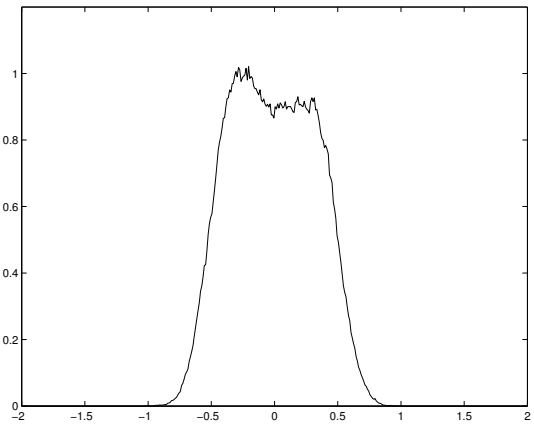

The PDF's for $\mathbf{k} = (1, 2)$, sine-bracket truncation, $\tilde{C}_3 = 4$, 23×23 total grid, $E = 7$, $\mathcal{E} = 20$, layered topography

Figure 6.83: The probability density functions for the Fourier modes of the potential vorticity, wavenumbers $(0, 2), (2.0), (1, -2), (1, 2)$, 23×23 sine-bracket truncation, $\tilde{C}_3 = 4$, layered topography

the statistically relevant $\tilde{C}_3 = 6$ expands on all the modes within the 5×5 coarse-grained grid. The majority of the PDF's are bimodal, except for those at $\mathbf{k} = (1, 0)$ (Figure 6.85), and $\mathbf{k} = (2, 0)$ (Figure 6.86), which are significantly skewed due to the presence of non-zero topography on those modes.

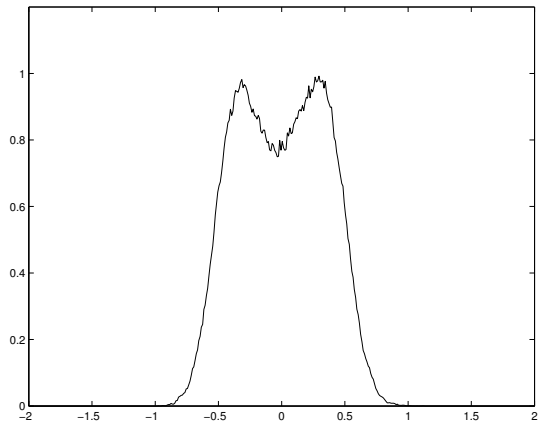

The PDF's for $\mathbf{k} = (2, -1)$, sine-bracket truncation, $\tilde{C}_3 = 4$, 23×23 total grid, $E = 7$, $\mathcal{E} = 20$, layered topography

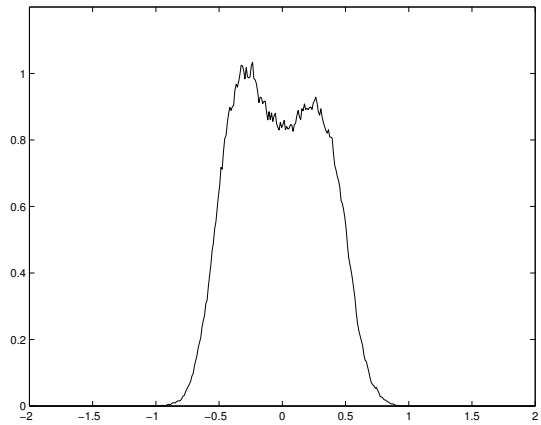

The PDF's for $\mathbf{k} = (2, 1)$, sine-bracket truncation, $\tilde{C}_3 = 4$, 23×23 total grid, $E = 7$, $\mathcal{E} = 20$, layered topography

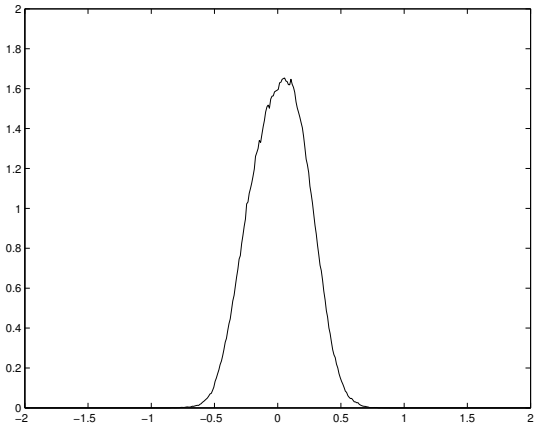

The PDF's for $\mathbf{k} = (2, -2)$, sine-bracket truncation, $\tilde{C}_3 = 4$, 23×23 total grid, $E = 7$, $\mathcal{E} = 20$, layered topography

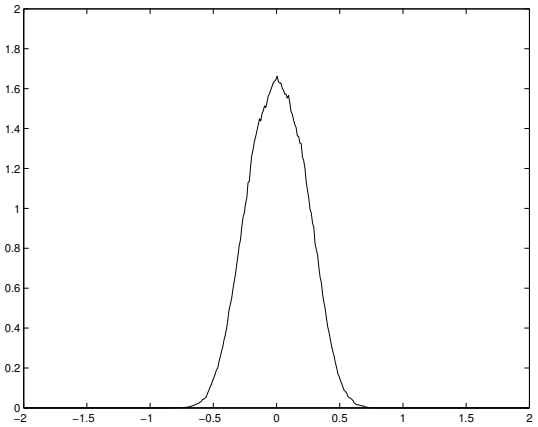

The PDF's for $\mathbf{k} = (2, 2)$, sine-bracket truncation, $\tilde{C}_3 = 4$, 23×23 total grid, $E = 7$, $\mathcal{E} = 20$, layered topography

Figure 6.84: The probability density functions for the Fourier modes of the potential vorticity, wavenumbers $(2, -1), (2.1), (2, -2), (2, 2)$, 23×23 sine-bracket truncation, $\tilde{C}_3 = 4$, layered topography

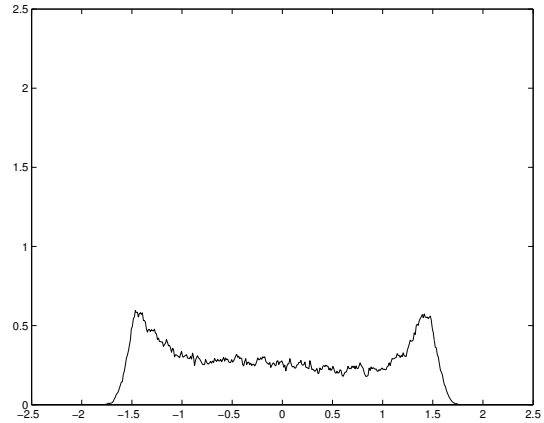

The PDF's for $\mathbf{k} = (0, 1)$, sine-bracket truncation, $\tilde{C}_3 = 6$, 23×23 total grid, $E = 7$, $\mathcal{E} = 20$, layered topography

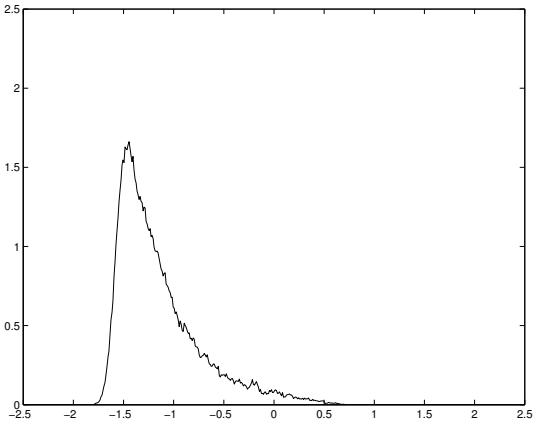

The PDF's for $\mathbf{k} = (1, 0)$, sine-bracket truncation, $\tilde{C}_3 = 6$, 23×23 total grid, $E = 7$, $\mathcal{E} = 20$, layered topography

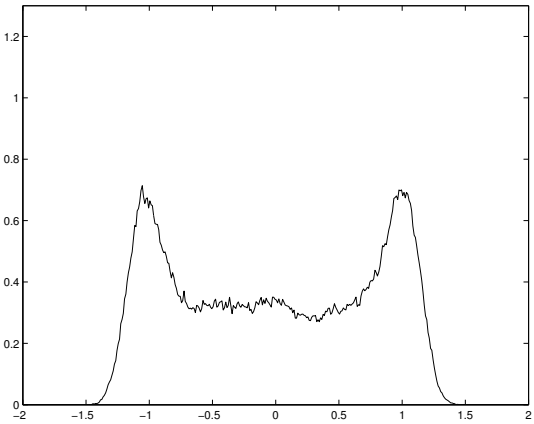

The PDF's for $\mathbf{k} = (1, -1)$, sine-bracket truncation, $\tilde{C}_3 = 6$, 23×23 total grid, $E = 7$, $\mathcal{E} = 20$, layered topography

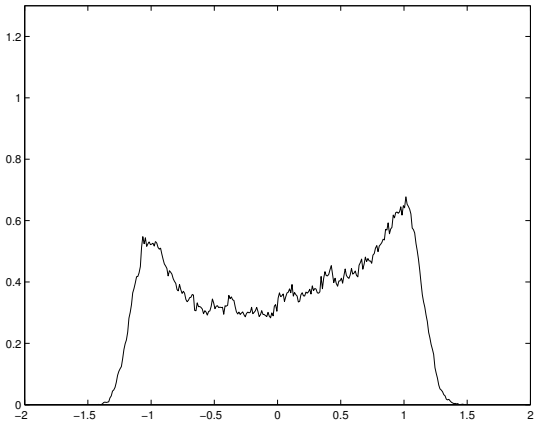

The PDF's for $\mathbf{k} = (1, 1)$, sine-bracket truncation, $\tilde{C}_3 = 6$, 23×23 total grid, $E = 7$, $\mathcal{E} = 20$, layered topography

Figure 6.85: The probability density functions for the Fourier modes of the potential vorticity, wavenumbers $(0, 1), (1.0), (1, -1), (1, 1)$, 23×23 sine-bracket truncation, $\tilde{C}_3 = 6$, layered topography

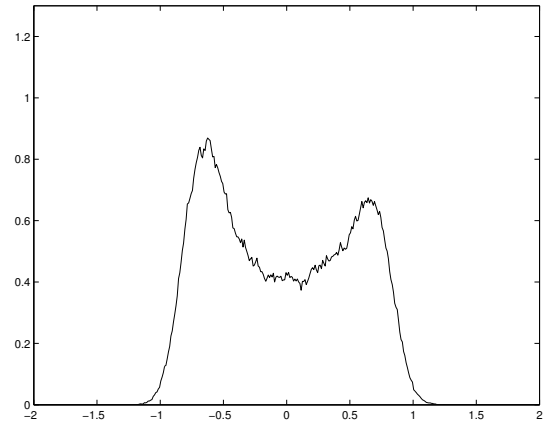

The PDF's for $\mathbf{k} = (0, 2)$, sine-bracket truncation, $\tilde{C}_3 = 6$, 23×23 total grid, $E = 7$, $\mathcal{E} = 20$, layered topography

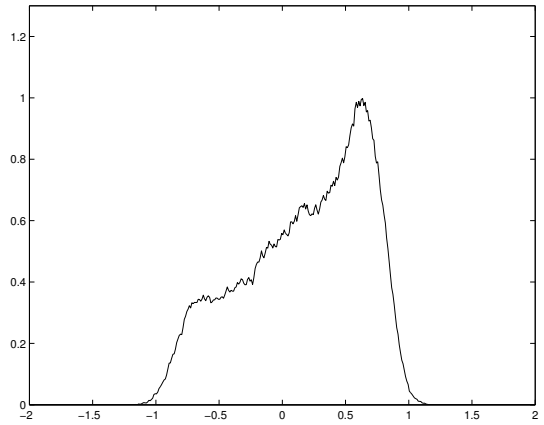

The PDF's for $\mathbf{k} = (2, 0)$, sine-bracket truncation, $\tilde{C}_3 = 6$, 23×23 total grid, $E = 7$, $\mathcal{E} = 20$, layered topography

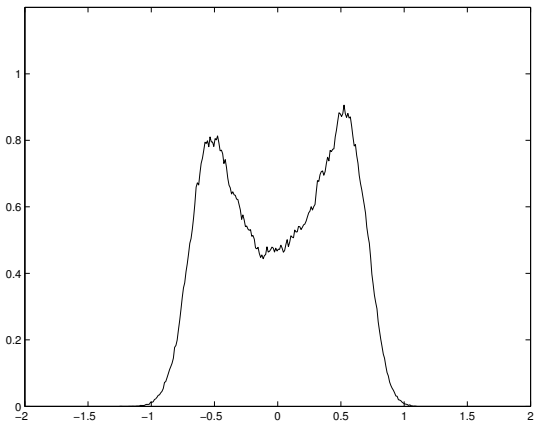

The PDF's for $\mathbf{k} = (1, -2)$, sine-bracket truncation, $\tilde{C}_3 = 6$, 23×23 total grid, $E = 7$, $\mathcal{E} = 20$, layered topography

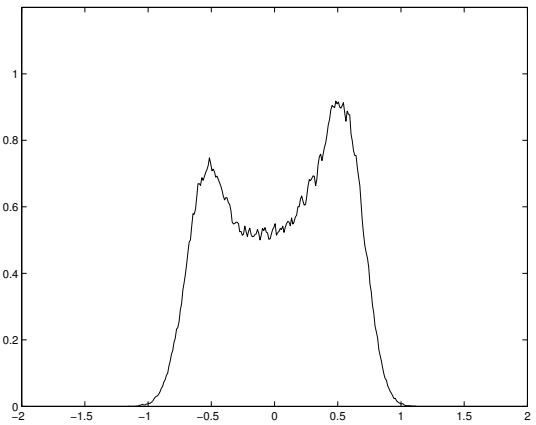

The PDF's for $\mathbf{k} = (1, 2)$, sine-bracket truncation, $\tilde{C}_3 = 6$, 23×23 total grid, $E = 7$, $\mathcal{E} = 20$, layered topography

Figure 6.86: The probability density functions for the Fourier modes of the potential vorticity, wavenumbers $(0, 2), (2.0), (1, -2), (1, 2)$, 23×23 sine-bracket truncation, $\tilde{C}_3 = 6$, layered topography

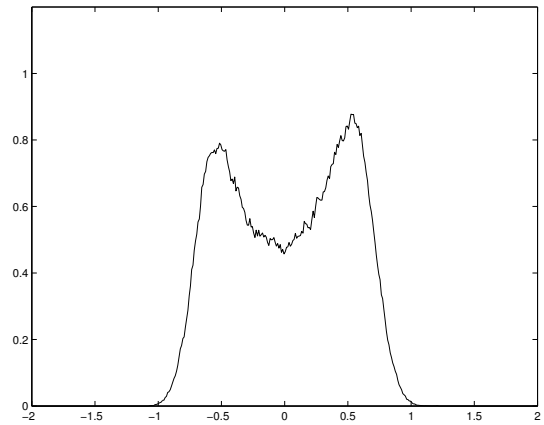

The PDF's for $\mathbf{k} = (2, -1)$, sine-bracket truncation, $\tilde{C}_3 = 6$, 23×23 total grid, $E = 7$, $\mathcal{E} = 20$, layered topography

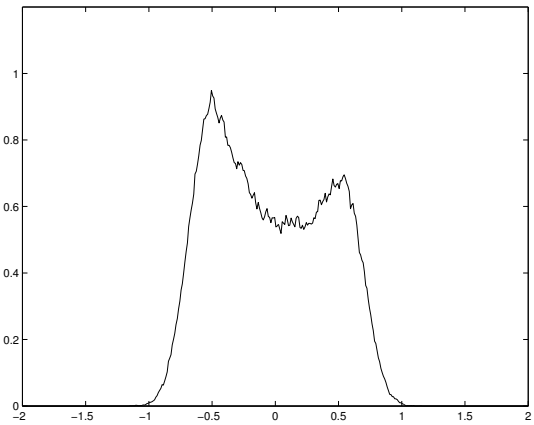

The PDF's for $\mathbf{k} = (2, 1)$, sine-bracket truncation, $\tilde{C}_3 = 6$, 23×23 total grid, $E = 7$, $\mathcal{E} = 20$, layered topography

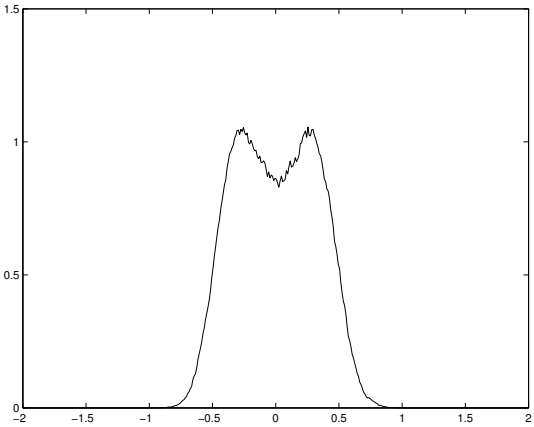

The PDF's for $\mathbf{k} = (2, -2)$, sine-bracket truncation, $\tilde{C}_3 = 6$, 23×23 total grid, $E = 7$, $\mathcal{E} = 20$, layered topography

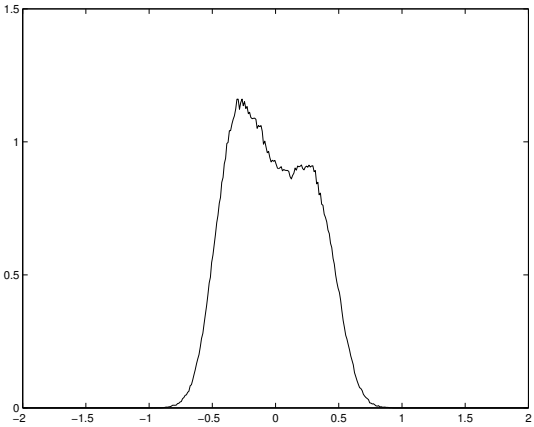

The PDF's for $\mathbf{k} = (2, 2)$, sine-bracket truncation, $\tilde{C}_3 = 6$, 23×23 total grid, $E = 7$, $\mathcal{E} = 20$, layered topography

Figure 6.87: The probability density functions for the Fourier modes of the potential vorticity, wavenumbers $(2, -1), (2.1), (2, -2), (2, 2)$, 23×23 sine-bracket truncation, $\tilde{C}_3 = 6$, layered topography

Fourier space PDF's		
Mode	Mean	Variance
$\mathbf{k} = (0,1)$	$-5.599 \cdot 10^{-2}$	1.046
$\mathbf{k} = (1,0)$	-1.148	$5.639 \cdot 10^{-1}$
$\mathbf{k} = (1,-1)$	$-6.665 \cdot 10^{-3}$	$6.217 \cdot 10^{-1}$
$\mathbf{k} = (1,1)$	$6.896 \cdot 10^{-2}$	$5.589 \cdot 10^{-1}$
$\mathbf{k} = (0,2)$	$-4.385 \cdot 10^{-2}$	$3.071 \cdot 10^{-1}$
$\mathbf{k} = (2,0)$	$1.749 \cdot 10^{-1}$	$2.378 \cdot 10^{-1}$
$\mathbf{k} = (1,-2)$	$2.042 \cdot 10^{-2}$	$2.274 \cdot 10^{-1}$
$\mathbf{k} = (1,2)$	$4.863 \cdot 10^{-2}$	$2.161 \cdot 10^{-1}$
$\mathbf{k} = (2,-1)$	$2.074 \cdot 10^{-2}$	$2.274 \cdot 10^{-1}$
$\mathbf{k} = (2,1)$	$-4.512 \cdot 10^{-2}$	$2.065 \cdot 10^{-1}$
$\mathbf{k} = (2,-2)$	$1.651 \cdot 10^{-3}$	$1.036 \cdot 10^{-1}$
$\mathbf{k} = (2,2)$	$-3.038 \cdot 10^{-2}$	$9.887 \cdot 10^{-2}$

Table 6.11: The means and variances of the PDF's of the Fourier modes for the potential vorticity, 23×23 sine-bracket truncation, $\tilde{C}_3 = 6$, layered topography

CHAPTER 7
STATISTICALLY RELEVANT AND IRRELEVANT CONSERVED QUANTITIES

In the Chapters 5 and 6 we presented various numerical simulations with the two truncations of the equations for barotropic flow: traditional truncation (3.17), and the sine-bracket truncation (4.1), respectively, where the sine-bracket truncation preserves many additional conserved quantities (4.4). Three geophysical situations were considered: no topography, random topography (Figure 5.1), and layered topography (5.1). Employing the numerical algorithm, developed in Chapter 4, Section 4.3, we have generated the set of initial conditions with pre-defined energy, enstrophy, and different values of the normalized third Casimir invariant $\tilde{C}_3$, which is defined in (6.1). In this chapter we analyze the numerical results from Chapters 5 and 6, quantify the statistical behavior and trends of various statistical parameters, arising from the influence of the additional statistically relevant conserved quantities, triggered by the normalized third Casimir invariant $\tilde{C}_3$. The statistical parameters we observed during our study (described in Section 5.0.3) are:

- Mean stream function (5.2) and its moments (5.3);
- Mean energy (5.4) and pseudo-energy (5.5) spectra;
- The Corr functions (5.7) and the mean state scatterplots;
- Correlation functions (5.8) for the Fourier modes of the potential vorticity;
- Probability density functions for the potential vorticity.

In the current work, however, we do not present the exact analytical explanations of the observed phenomena. Our purpose here is to show the results of the numerical experiments confirming the relevance or irrelevance of the additional conserved quantities on the system, and try to classify the statistical trends empirically.

7.1 Ergodicity and mixing

Our statistical simulations throughout the thesis are based on the assumption that the solution of the numerical scheme shows mixing and ergodicity. This assumption allows us to perform the long-time time averaging with the single numerical solution rather

then do an ensemble averaging with lots of initial conditions on a microcanonical energy-enstrophy surface. The time correlation functions (5.8), described in the Section 5.0.3, help us to obtain the numerical evidence of ergodicity and mixing. The rate of correlation decay shows the amount of mixing in the system, and in some sense gives us a clue about the suitable length of time averaging window. On the other hand, it is also highly desirable to study the influence of the relevant additional conserved quantities on the correlation decay rate. First we looked at the time correlation functions for the 11×11 and 23×23 traditional truncations in the Chapter 5; Figures 5.12 and 5.13 in the Section 5.1.4 for no topography, Figures 5.28 and 5.29 in Section 5.2.4 for layered topography, and Figures 5.44 and 5.45 in Section 5.3.4 for layered topography. We note that the correlation decay rate does not depend on the geophysical case, i.e. the time correlation functions for the same wavenumber and truncation size are almost identical regardless of the topography type. Also we can see, that the expansion of the truncation size to 23×23 affects the rate of decay in the mode $|\mathbf{k}|^2 = 1$ only (it decays slower for 23×23 size of traditional truncation).

The direct simulations with the sine-bracket truncation (4.1) show that statistically relevant values of $\tilde{C}_3$ affect the rate of correlation decay, in particular, they slow it down. This can be seen in the Figures 6.23 and 6.24 for no topography case, Figures 6.50 and 6.51 for random topography, and Figure 6.74 for layered topography. The first trend we observe is that for larger values of $\tilde{C}_3$ the correlation decay rate is slower. This holds for any type of topography. Second, we observe that the correlation rate slow-down is significantly more substantial for larger truncation size, 23×23 sine-bracket truncation. This can be explained as follows: 11×11 truncation has, apart from circulation, energy, and enstrophy, 8 more additional conserved quantities, whereas 23×23 sine-bracket truncation possesses 20 more additional Casimir invariants, and due to the increased amount of constraints in the system the correlation functions for 23×23 sine-bracket truncation decay slower.

Slow correlation decay rate questions the validity of the statistical results for the cases with $\tilde{C}_3 = 8$, 23×23 sine-bracket truncation, no topography and random topography (Figures 6.24 and 6.51). However, in the case with layered topography we still have acceptable correlation decay rate (Figure 6.74) for all values $\tilde{C}_3 = 0$, 2, 4, and 6, and for this case the statistical validity of the results is not in question.

11×11, total Fourier grid		
$\tilde{C}_3$	skewness	flatness
0	$4.885 \cdot 10^{-3}$	2.027
4	-0.7936	2.882
8	-1.161	3.821
11×11, coarse-grained grid		
$\tilde{C}_3$	skewness	flatness
0	$4.749 \cdot 10^{-3}$	2.021
4	-0.7912	2.847
8	-1.171	3.810

23×23, total Fourier grid		
$\tilde{C}_3$	skewness	flatness
0	$1.481 \cdot 10^{-3}$	2.027
4	-1.006	3.403
8	-0.8344	3.887
23×23, coarse-grained grid		
$\tilde{C}_3$	skewness	flatness
0	$1.461 \cdot 10^{-3}$	2.025
4	-1.001	3.357
8	-0.8088	3.921

Table 7.1: The spatially averaged skewness and flatness of the mean stream functions for 11×11 and 23×23 sine-bracket truncation, total and coarse-grained Fourier grids, no topography. Note the systematic lowering of skewness as $\tilde{C}_3$ increases.

11×11, total Fourier grid		
$\tilde{C}_3$	skewness	flatness
0	$8.454 \cdot 10^{-3}$	2.118
4	-0.9657	3.195
8	-1.321	4.979
11×11, coarse-grained grid		
$\tilde{C}_3$	skewness	flatness
0	$8.552 \cdot 10^{-3}$	2.106
4	-0.9504	3.141
8	-1.336	4.989

23×23, total Fourier grid		
$\tilde{C}_3$	skewness	flatness
0	$1.616 \cdot 10^{-2}$	2.109
4	-0.9495	3.514
8	-1.737	10.04
23×23, coarse-grained grid		
$\tilde{C}_3$	skewness	flatness
0	$1.616 \cdot 10^{-2}$	2.105
4	-0.9503	3.502
8	-1.816	10.76

Table 7.2: The spatially averaged skewness and flatness of the mean stream functions for 11×11 and 23×23 sine-bracket truncation, total and coarse-grained Fourier grids, random topography. Note the systematic lowering of skewness as $\tilde{C}_3$ increases.

7.2 Mean stream functions and their moments

The energy-enstrophy statistical theory, developed in Chapter 3, establishes the most probable mean state (3.29) for the two-dimensional vorticity equation with topography (3.1). It happens that the most probable probability density (3.26), predicted by the energy-enstrophy statistical theory, is Gaussian with the mean (3.29). We confirm the equilibrium statistical predictions of the Chapter 3 with the traditional truncation (3.17) in the Chapter 5, Sections 5.1.1, 5.2.1, and 5.3.1, and study the influence of the additional conserved quantity $\tilde{C}_3$ in sine-bracket truncation, given by (6.1), in the Chapter 6, Sections 6.1.1, 6.2.1, and 6.3.1. In this section we summarize the statistical trends and be-

23×23, total Fourier grid			23×23, coarse-grained grid		
$\tilde{C}_3$	skewness	flatness	$\tilde{C}_3$	skewness	flatness
0	$2.048 \cdot 10^{-3}$	2.879	0	$1.470 \cdot 10^{-3}$	2.878
2	-0.4061	2.557	2	-0.4047	2.5499
4	-0.7913	3.332	4	-0.7844	3.311
6	-1.112	4.249	6	-1.099	4.219

Table 7.3: The spatially averaged skewness and flatness of the mean stream functions for 23×23 sine-bracket truncation, total and coarse-grained Fourier grids, layered topography. Note the systematic lowering of skewness as $\tilde{C}_3$ increases.

Energy of the mean state Layered topography		
$\tilde{C}_3$	First mode	Total
0	4.793	4.808
2	3.052	3.059
4	2.082	2.085
6	1.571	1.578

Table 7.4: The energy of the mean in the first Fourier mode and the total energy of the mean, $\tilde{C}_3 = 0$, 2, 4, and 6, layered topography. Note that the energy in both columns systematically decreases with increasing $\tilde{C}_3$.

havior of the mean stream functions (5.2) and their moments (5.3) for statistically relevant and irrelevant normalized third Casimir invariant $\tilde{C}_3$.

- Mean stream functions.
  - For the statistically irrelevant value $\tilde{C}_3 = 0$ the equilibrium statistical predictions in (3.29) are well satisfied. Experiments with the traditional truncation (3.17) in the Chapter 5, Sections 5.1.1, 5.2.1, and 5.3.1 confirm the statistical predictions for three geophysical cases: no topography, random topography (Figure 5.1), and layered topography (5.1), and the results are shown in Figures 5.2, 5.18, and 5.34. The direct simulations with the sine-bracket truncation (4.1), presented in the Chapter 6, Sections 6.1.1, 6.2.1, and 6.3.1 also confirm the statistical predictions for the statistically irrelevant $\tilde{C}_3 = 0$ for all geophysical cases. The results are shown in Figures 6.1, 6.28, and 6.52.
  - For the statistically relevant values $\tilde{C}_3 = 2$, 4, 6, and 8, sine-bracket truncation (4.1), the mean stream functions (5.2) exhibit significant distortions, which

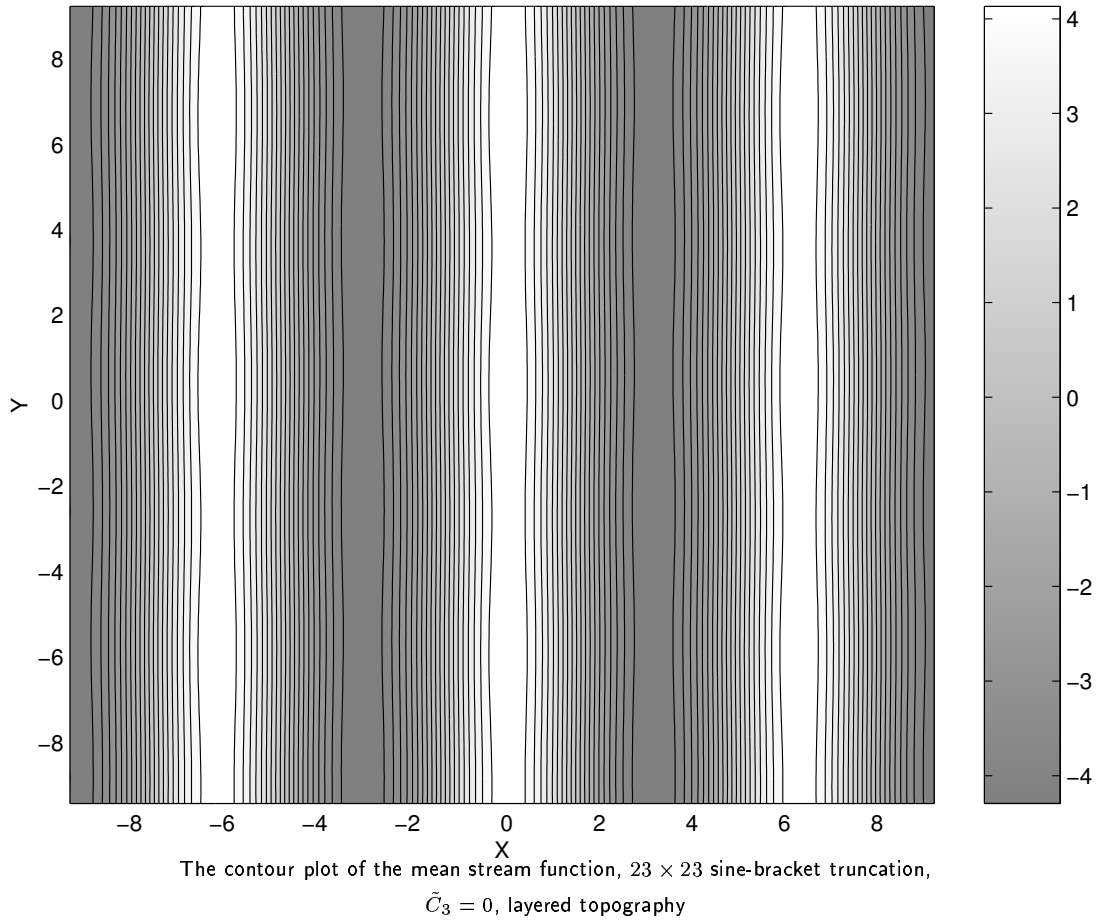

Figure 7.1: The 3-periodic contour plot of the mean stream function, 23×23 sine-bracket truncation, layered topography, $\tilde{C}_3 = 0$. Here we observed the zonal jet flow, no vortices.

are presented and quantified in the Chapter 6, Sections 6.1.1, 6.2.1, and 6.3.1, in Figures 6.2, 6.3, 6.29, 6.30, 6.53, 6.54, and 6.55. The general trend for the statistically relevant $\tilde{C}_3$'s is that for larger values the distortions of the mean stream functions are more significant. For the layered topography, it is also interesting to see whether the statistically relevant $\tilde{C}_3$'s create vortices in the flow. For this purpose we present the 3-periodic contour plots of the stream functions in the Figures 7.1, 7.2, 7.3, and 7.4. In a contour plot, vortices are designated by the closed level curves of a stream function. As we can see in Figure 7.1, the flow for $\tilde{C}_3 = 0$ contains no vortices (no closed curves). However, the flow for $\tilde{C}_3 = 2$, shown in Figure 7.2, clearly contains at least two vortices, rotating in opposite directions. As $\tilde{C}_3$ increases, the flow loses the

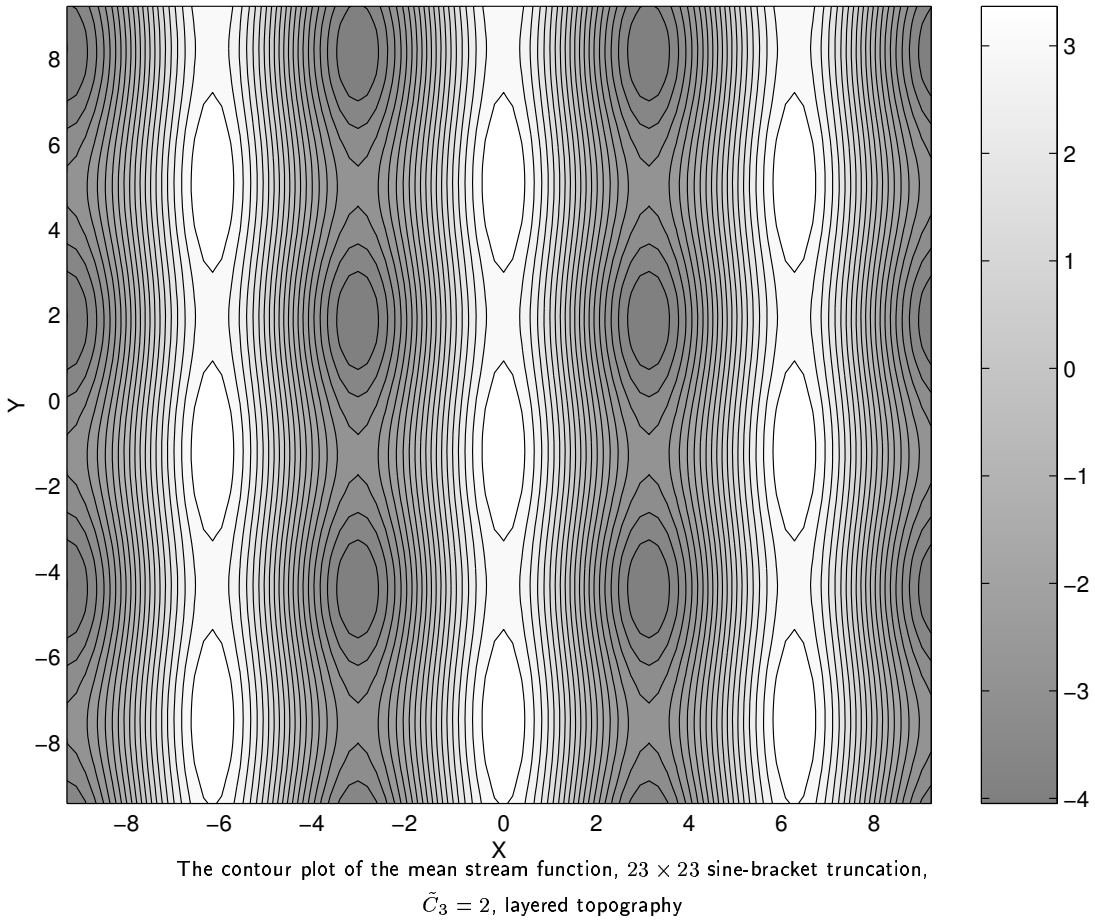

Figure 7.2: The 3-periodic contour plot of the mean stream function, 23×23 sine-bracket truncation, layered topography, $\tilde{C}_3 = 2$. We observe two vortices rotating in opposite directions.

vortex which rotates clockwise, while retaining the counter-clockwise rotating vortex (Figure 7.3 for $\tilde{C}_3 = 4$, and Figure 7.4 for $\tilde{C}_3 = 6$). Also note that the amplitude of the mean stream function decreases (look at the color bars in the Figures 7.1, 7.2, 7.3, and 7.4) with increasing $\tilde{C}_3$, as does the vortex. To confirm the mean state amplitude decrease, we present the energy of the mean state for different $\tilde{C}_3$'s in the Table 7.4. The first column of the Table 7.4 contains the values of $\tilde{C}_3$, second – the amount of energy in the first Fourier mode of the mean state, and the third – the overall amount of energy in the mean state. In the Table 7.4 we can see the systematic decrease of the energy of the mean as $\tilde{C}_3$ increases, from 4.808 for $\tilde{C}_3 = 0$, to 1.578 for $\tilde{C}_3 = 6$.

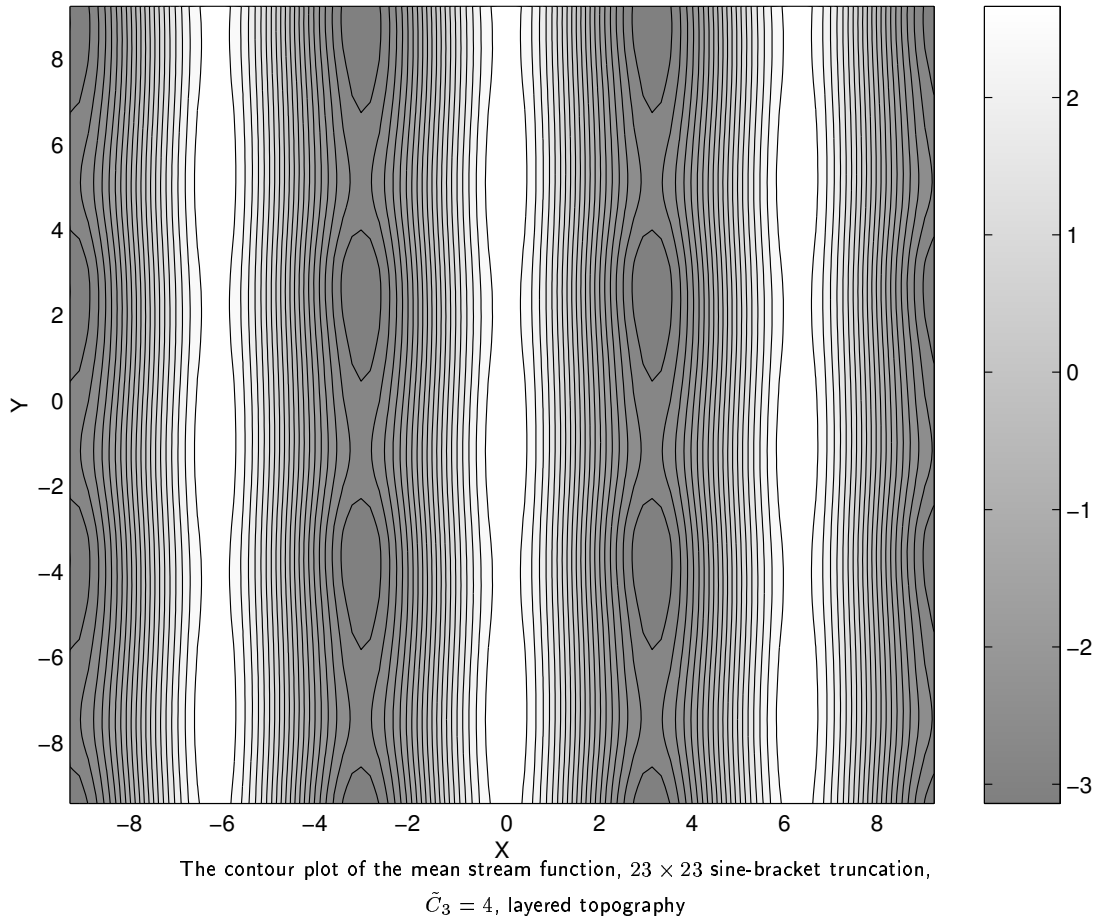

Figure 7.3: The 3-periodic contour plot of the mean stream function, 23×23 sine-bracket truncation, layered topography, $\tilde{C}_3 = 4$. We observed one vortex, rotating counter-clockwise.

- Variance of the stream function.

  - The experiments with the traditional truncation (3.17) in the Chapter 5, Sections 5.1.1, 5.2.1, and 5.3.1 confirm the statistical predictions of the variances for the stream functions for three geophysical cases: no topography, random topography (Figure 5.1), and layered topography (5.1), and the results are shown in Figures 5.3, 5.19, and 5.35. The direct simulations with the sine-bracket truncation (4.1), presented in the Chapter 6, Sections 6.1.1, 6.2.1, and 6.3.1 also confirm the statistical predictions for the statistically irrelevant $\tilde{C}_3 = 0$ for all geophysical cases. The results are shown in Figures 6.4, 6.31, and 6.56.
  - For the statistically relevant values $\tilde{C}_3 = 2$, 4, 6, and 8, sine-bracket trun-

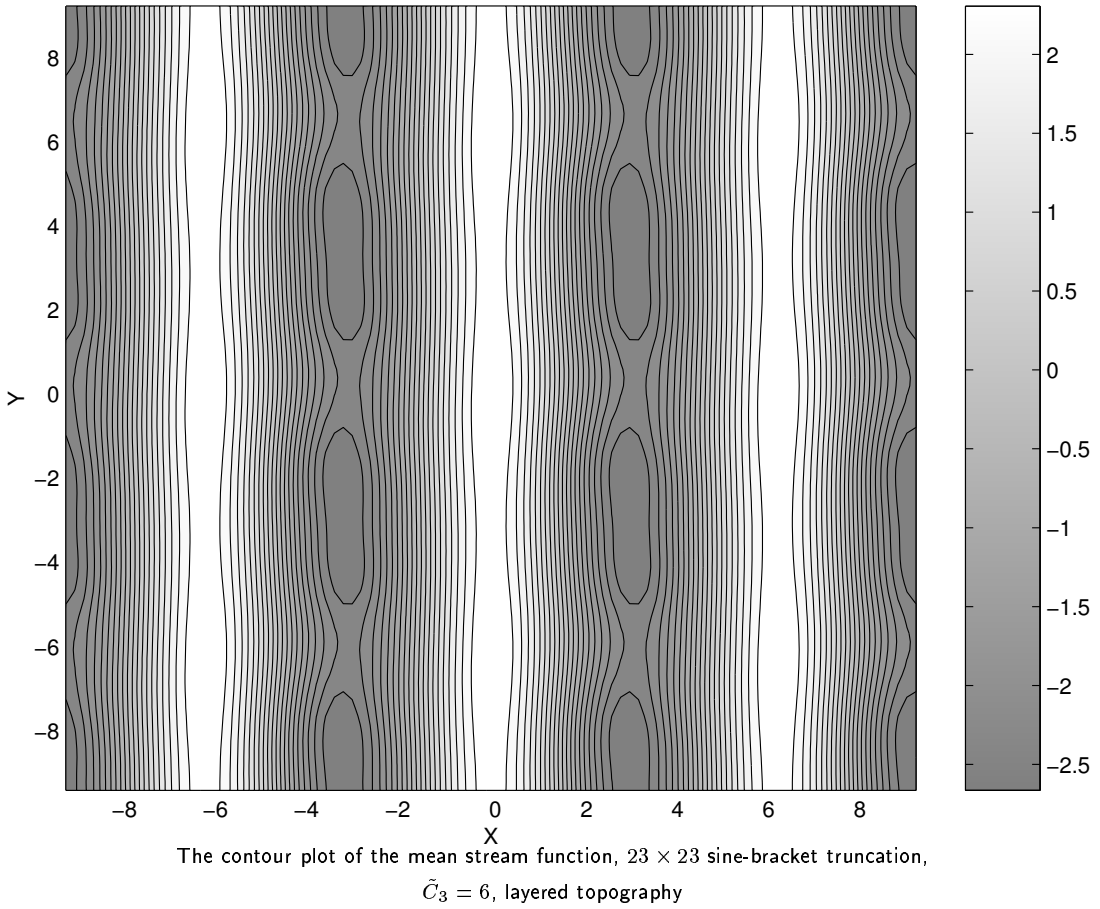

Figure 7.4: The 3-periodic contour plot of the mean stream function, 23×23 sine-bracket truncation, layered topography, $\tilde{C}_3 = 6$. We observed one vortex, rotating counter-clockwise.

cation (4.1), the variances of the mean stream functions exhibit significant distortions from the original shape, which are presented and quantified in the Chapter 6, Sections 6.1.1, 6.2.1, and 6.3.1, in Figures 6.5, 6.6, 6.32, 6.33, 6.57, 6.58, and 6.59. The general trend for the statistically relevant $\tilde{C}_3$'s is that for larger values the distortions of variances of the mean stream functions are more significant.

- Skewness of the stream function.

  – The equilibrium energy-enstrophy statistical theory, presented in the Chapter 3, predicts that the most probable statistical state is defined by the canonical Gibbs measure with the Gaussian distribution (3.26). As we know, the skew-

ness for the Gaussian distribution should be identically zero. This prediction is confirmed very well by the traditional truncation (3.17) for the cases with no topography and random topography (Sections 5.1.1 and 5.2.1). For the case with layered topography (5.1), the skewness obtained with the traditional truncation is not identically zero, however, its spatial average is zero. (Section 5.3.1, Table 5.9). The results are shown in Figures 5.4, 5.20, and 5.36. The direct numerical simulations with the sine-bracket truncation (4.1) and statistically irrelevant $\tilde{C}_3 = 0$, presented in Sections 6.1.1, 6.2.1, and 6.3.1, confirm the statistical predictions and the numerical results for the traditional truncation. The results are shown in Figures 6.7, 6.34, and 6.60.

- For the statistically relevant values $\tilde{C}_3 = 2$, 4, 6, and 8, sine-bracket truncation (4.1), the skewness of the mean stream functions exhibit significant distortions from the original shape, which are presented and quantified in the Chapter 6, Sections 6.1.1, 6.2.1, and 6.3.1, in Figures 6.8, 6.9, 6.35, 6.36, 6.61, 6.62, and 6.63. The general trend for the statistically relevant values of $\tilde{C}_3$ is that the skewness shifts downwards, becoming negative, under the influence of the additional conserved quantity. This trend is observed in all geophysical situations, for all statistically relevant values $\tilde{C}_3 = 2$, 4, 6, and 8, and for the larger values of $\tilde{C}_3$ the skewness is farther away from zero, which we repeat here in Tables 7.1, 7.2, and 7.3.

- Flatness of the stream function.

  - The equilibrium energy-enstrophy statistical theory, presented in the Chapter 3, predicts that the most probable statistical state is defined by the canonical Gibbs measure with the Gaussian distribution (3.26). As we know, the flatness for the Gaussian distribution should be 3. This prediction is confirmed very well by the traditional truncation (3.17) for the case with layered topography (Section 5.2.1). For the case with no topography and random topography, the skewness obtained with the traditional truncation is centered at 2 (Sections 5.1.1, 5.2.1). The results are shown in Figures 5.5, 5.21, and 5.37. The results of the direct numerical simulations with the sine-bracket truncation (4.1) and statistically irrelevant $\tilde{C}_3 = 0$, presented in Sections 6.1.1, 6.2.1, and 6.3.1, coincide with the corresponding results for the traditional truncation,

with confirms that $\tilde{C}_3 = 0$ is statistically irrelevant. The results are shown in Figures 6.10, 6.37, and 6.64.

– For the statistically relevant values $\tilde{C}_3 = 2$, 4, 6, and 8, sine-bracket truncation (4.1), the flatness of the mean stream functions exhibit significant distortions from the original shape, which are presented and quantified in the Chapter 6, Sections 6.1.1, 6.2.1, and 6.3.1, in Figures 6.11, 6.12, 6.38, 6.39, 6.65, 6.66, and 6.67. However, no quantifiable general trend for the flatness was found, apart from the observed fact that it is distorted under the influence of statistically relevant $\tilde{C}_3$. We should also recall that the test of the flatness does not show much if skewness is already non-zero.

7.3 Mean energy and pseudo-energy spectra

The equilibrium energy-enstrophy statistical theory, developed in Chapter 3, predicts the most probable mean energy spectrum, which is shown in (3.46a). The theory predicts that the energy in the mean state is present only in those Fourier modes which possess non-zero topography. Direct numerical simulations in the Chapter 5, Sections 5.1.2, 5.2.2, and 5.3.2 confirm the statistical predictions for the traditional truncation (3.17). According to the energy-enstrophy statistical theory, in the geophysical case with no topography, the mean state should not possess any energy, which is confirmed by the traditional truncation in Section 5.1.2, Figures 5.6 and 5.7. There we can see that the amount of energy in the single Fourier mode of the mean state in the worst case never exceeds $2.5 \cdot 10^{-3}$, which is negligible when compared to the total energy $E = 7$. For the layered topography (5.1), the theory predicts that the mean energy should be present only in the Fourier modes $|\mathbf{k}|^2 = 1$ and $|\mathbf{k}|^2 = 4$, and this prediction is confirmed by the direct numerical simulations with the traditional truncation in Chapter 5, Section 5.1.2, Figures 5.38 and 5.39.

The direct numerical simulations with the sine-bracket truncation (4.1) and statistically irrelevant normalized third Casimir invariant $\tilde{C}_3 = 0$, presented in Sections 6.1.2, 6.2.2, and 6.3.2, also confirm the equilibrium statistical predictions, being identical with the corresponding simulations with the traditional truncation. However, the direct numerical simulations with statistically relevant values $\tilde{C}_3 = 2$, 4, 6, and 8 show that the mean energy is affected by the additional conserved quantity. Depending on the type of topography, the influence of relevant $\tilde{C}_3$'s on the mean energy spectrum is different. For no topography and random topography cases, presented in Sections 6.1.2 and 6.2.2 of

the Chapter 5, we observe the increased amount of energy in the large-scale modes of the mean state, (Figures 6.13 and 6.14 for no topography, and Figures 6.40 and 6.41 for random topography). In the case with the layered topography (5.1) the statistical trend is different. According to the theory in (3.46a), the first Fourier mode $|\mathbf{k}|^2 = 1$ should contain a lot of energy, which is confirmed by the direct numerical simulations with the traditional truncation. However, the statistically relevant Casimir invariants $\tilde{C}_3 = 2$, 4, and 6 *decrease* the amount of energy contained in the large-scale first Fourier mode, as shown in Table 7.4. The table shows that the energy content in the first Fourier mode systematically decreases as $\tilde{C}_3$ increases, from 4.793 for $\tilde{C}_3 = 0$, to 1.571 for $\tilde{C}_3 = 6$.

The energy-enstrophy statistical theory in Chapter 3 predicts the Fourier space equipartition of the pseudo-energy (3.47) in the predicted statistical state (3.50). The direct numerical simulations with the traditional truncation (3.17), presented in the Chapter 5, Sections 5.1.2, 5.2.2, and 5.3.2, confirm the statistical predictions of the Chapter 3 for all geophysical situations (Figures 6.13 and 6.14 for no topography, Figures 6.40 and 6.41 for random topography, and Figure 6.68 for layered topography). The significant discrepancy of the pseudo-energy in the first Fourier mode is caused by the fact that in all cases $\mu \approx -1$ (Tables 5.2, 5.6, and 5.10), and therefore the first Fourier mode is very sensitive to the numerical errors in μ according to (3.47) and discussion in Section 5.1.2.

The direct numerical simulations with the sine-bracket truncation (4.1) and statistically irrelevant normalized third Casimir invariant $\tilde{C}_3 = 0$, presented in the Chapter 6, Sections 6.1.2, 6.2.2, and 6.3.2, Figures 6.13, 6.14, 6.40, 6.41, and 6.68, confirm the statistical predictions of the Chapter 3 and are identical with the corresponding simulations with the traditional truncation. However, the direct numerical simulations with the sine-bracket truncation and statistically relevant values $\tilde{C}_3 = 2$, 4, 6, and 8 show that the pseudo-energy equipartition is affected by the additional conserved quantity. We observe that the influence of statistically relevant $\tilde{C}_3$ depends on the size of the sine-bracket truncation. For the 11×11 truncation size the resulting pseudo-energy partition lacks any noticeable trends, being chaotic among different Fourier modes (Figures 6.13 and 6.40). This happens due to the lack of small-scale resolution, because for the 23×23 sine-bracket truncation the situation is different. In the Figures 6.14, 6.41, and 6.68 we can see that under the influence of statistically relevant $\tilde{C}_3$'s the pseudo-energy spectrum dives under the predicted equipartition, and the pseudo-energy transfer to the large-scale modes can be clearly observed. We also note the interesting fact, that is, the "de-equipartition" of

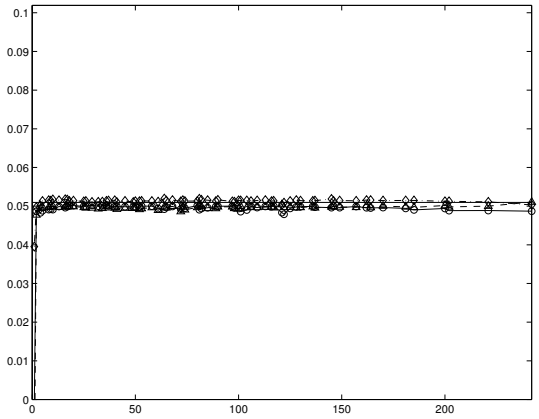

The pseudo-energy spectrum, sine-bracket truncation, 23×23 total grid, $E = 7$, $\mathcal{E} = 20$, $\tilde{C}_3 = 0$, solid line with circles – no topography, dashed line with triangles – random topography, dot-dashed line with diamonds – layered topography, horizontal solid line - analytical prediction

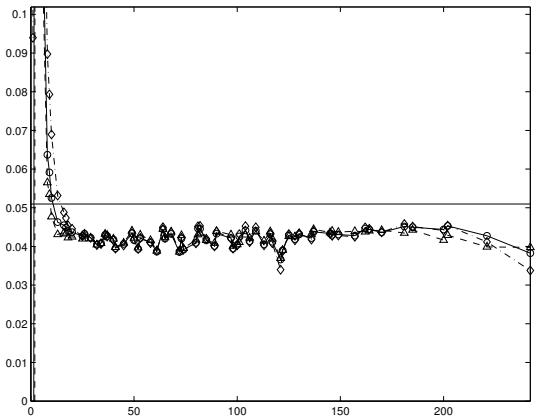

The pseudo-energy spectrum, sine-bracket truncation, 23×23 total grid, $E = 7$, $\mathcal{E} = 20$, $\tilde{C}_3 = 4$, solid line with circles – no topography, dashed line with triangles – random topography, dot-dashed line with diamonds – layered topography, horizontal solid line - analytical prediction

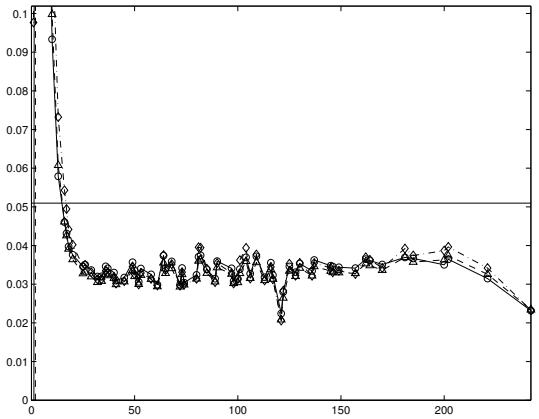

The pseudo-energy spectrum, sine-bracket truncation, 23×23 total grid, $E = 7$, $\mathcal{E} = 20$, $\tilde{C}_3 = 6$, solid line with circles – no topography, dashed line with triangles – random topography, dot-dashed line with diamonds – layered topography, horizontal solid line - analytical prediction

Figure 7.5: The pseudo-energy spectrum, 23×23 sine-bracket truncation, statistically relevant $\tilde{C}_3 = 0$, 4, and 6, different topographies. The deviation of the pseudo-energy spectrum from the predicted equipartition does not depend on the topography.

the pseudo-energy under the influence of $\tilde{C}_3$ occurs independently of the topography type. In order to better see this, we show the pseudo-energy spectrum for the fixed value of $\tilde{C}_3$ and different topographies in a single plot. Three such plots for $\tilde{C}_3 = 0$, 4 and 6 are shown in Figure 7.5. Clearly the shape of the pseudo-energy partition does not depend on the topography type, and depends only on the value of $\tilde{C}_3$. This observation suggests that, despite the changes in the mean flow, the pseudo-energy remains the perturbation around that mean flow, regardless of how the mean flow changed. This assumption, however, is entirely based on the above observation and lacks any analytical explanation.

7.4 Collinearity of the mean state

The statistical theories presented in Chapter 3 show that the most probable mean state should be collinear:

$$\bar{q} = \mu\bar{\psi}. \tag{7.1}$$

One can find the above statement in (3.28) and (3.40), Chapter 3. In the Sections 5.1.3, 5.2.3, and 5.3.3 of Chapter 5 we check the collinearity of the mean state (7.1) for the traditional truncation (3.17) with all kinds of topographies via the Corr functions (5.7) and scatterplots $\bar{q}$ vs $\bar{\psi}$. Let us recall that the Corr function $\mathrm{Corr}(x, y)$ outputs 1 or -1 iff $x = \alpha y$, depending on the sign of α. As we can see in Figures 5.9, 5.25, and 5.41, the Corr functions show a lot of collinearity between the $\bar{q}$ and $\bar{\psi}$ for all types of topography (the values of the coarse-grained Corr function are about -0.997 for no topography, -0.999 for random topography, and -1 for layered topography, 23×23 traditional truncation, 5×5 coarse-grained grid). Thus the theoretical prediction (7.1) is confirmed very well by the Corr functions for the traditional truncation. We also observe that the Corr functions for the 11×11 traditional truncation (Figures 5.8, 5.24, and 5.40) exhibit less collinearity than those for the 23×23 traditional truncation, which happens due to the lack of small-scale resolution, and further we will be referring only to the results for 23×23 truncation.

The direct numerical simulations with the sine-bracket truncation (4.1) with the statistically irrelevant value $\tilde{C}_3 = 0$ show the same amount of collinearity in the large-scale mean flow (Chapter 6; Figure 6.16 in Section 6.1.3 for no topography, Figure 6.43 in Section 6.2.3 for random topography, and Figure 6.69 in Section 6.3.3 for layered topography, solid lines) as the simulations with the traditional truncation do, so the collinearity of the large-scale mean flow is not affected by $\tilde{C}_3 = 0$. As $\tilde{C}_3$ increases, becoming statis-

tically relevant, the influence of additional conserved quantity depends on the type of the topography we employ. For the case with no topography (Figure 6.16, Section 6.1.3) we can see that the presence of statistically relevant $\tilde{C}_3$ significantly reduces collinearity of the mean state. In Figure 6.16, coarse-grained plot, we can see that for $\tilde{C}_3 = 4$ the value of the Corr function is -0.93 (compare to -0.997 for $\tilde{C}_3 = 0$), and -0.9 for the simulation with $\tilde{C}_3 = 8$. For the case with the random topography (Figure 6.43, Section 6.2.3) the changes in collinearity are as considerable as for the case with no topography. In Figure 6.43, coarse-grained plot, we can see that for $\tilde{C}_3 = 4$ the value of the Corr function is -0.96 (compare to -0.999 for $\tilde{C}_3 = 0$), and -0.9 for the simulation with $\tilde{C}_3 = 8$. For the simulations with layered topography (Figure 6.69, Section 6.3.3), however, the influence of the statistically relevant $\tilde{C}_3$ on the collinearity of the mean state is less substantial. In Figure 6.69, coarse-grained plot, we can see that for $\tilde{C}_3 = 2$ the value of the Corr function is -0.99, for $\tilde{C}_3 = 4$ the value of the Corr function is -0.97, and for $\tilde{C}_3 = 6$ the value of the Corr function is -0.96. Thus, we conclude that topography with non-zero first Fourier mode somehow relieves the statistical effects of relevant $\tilde{C}_3$.

As well as the Corr functions, we check the collinearity (7.1) of the mean flow via scatterplots $\bar{q}$ vs $\bar{\psi}$. If the mean state is collinear, the scatterplot $\bar{q}$ vs $\bar{\psi}$ should look like a straight line. In the Sections 5.1.3, 5.2.3, and 5.3.3 of Chapter 5 we check the collinearity of the mean state (7.1) for the traditional truncation (3.17) with all kinds of topographies via the scatterplots $\bar{q}$ vs $\bar{\psi}$. As we can see in Figures 5.11, 5.27, and 5.43, which were obtained with the 23×23 traditional truncation (3.17), the amount of the collinearity in the mean state depends on the topography. The coarse-grained scatterplot $\bar{q}$ vs $\bar{\psi}$ for the case with no topography looks like a significantly scattered straight line (Figure 5.11). However, the scale of the scatterplot is small (± 0.3 in both $\bar{q}$ and $\bar{\psi}$), and therefore the width of the scatterplot is significant due to the visually amplified numerical errors (Note that according to the theory the mean state should be identically zero in the absence of topography, and the scatterplot should represent a dot at the origin). The coarse-grained scatterplot $\bar{q}$ vs $\bar{\psi}$ for the case with random topography looks like a less scattered straight line (Figure 5.27). The scale of the plot is ± 0.8 in both $\bar{q}$ and $\bar{\psi}$ directions, and therefore the numerical errors (width of the plot) are less noticeable. The coarse-grained scatterplot $\bar{q}$ vs $\bar{\psi}$ for the case with layered topography (5.1) is a completely straight line (Figure 5.43). Here the scale of the plot is ± 5 in both $\bar{q}$ and $\bar{\psi}$ directions, and therefore the width of the scatterplot is very small. Overall, the statistical predictions of collinearity of the mean

state are confirmed by the simulations with the traditional truncation.

The direct numerical simulations with the sine-bracket truncation (4.1) with the statistically irrelevant value $\tilde{C}_3 = 0$ show the same amount of collinearity in the large-scale mean flow (Chapter 6; Figure 6.20 in Section 6.1.3 for no topography, Figure 6.47 in Section 6.2.3 for random topography, and Figure 6.70 in Section 6.3.3 for layered topography) as the results for the traditional truncation, and that means that $\tilde{C}_3 = 0$ does not affect the collinearity of the mean state. As $\tilde{C}_3$ increases, however, the situation changes, and the trends depend on the topography type. For the geophysical situation with no topography, $\tilde{C}_3 = 4$ makes the plot $\bar{q}$ vs $\bar{\psi}$ more scattered (Figure 6.21), and for $\tilde{C}_3 = 8$ the scatterplot, shown in Figure 6.22 is clearly non-linear. For the geophysical situation with random topography, $\tilde{C}_3 = 4$ makes the scatterplot $\bar{q}$ vs $\bar{\psi}$ slightly bent in the upper-left part of the plot, and forked in the lower-right part of the scatterplot (shown in Figure 6.48, note the two branches in the lower-left part of the plot). $\tilde{C}_3 = 8$ makes the scatterplot for the random topography completely non-linear (Figure 6.49).

We would like to emphasize the results obtained with the sine-bracket truncation (4.1) for the case with layered topography (5.1). Here in this section we show the Figure 7.6, where we combine together the total scatterplots for the 23×23 sine-bracket truncation, $\tilde{C}_3 = 0$, 2, 4, and 6. On the Figure 7.6 we observe that the scatterplots $\bar{q}$ vs $\bar{\psi}$ are bent by the statistically relevant $\tilde{C}_3$'s, and the amount of curvature in the plots increases with increasing $\tilde{C}_3$. The statistical trend in this case is easily quantifiable, on the contrary to the cases with no topography and random topography, and therefore we make it stand-alone, trying to attract reader's attention. Further in this chapter we will show another set of results for the same case with layered topography and different $\tilde{C}_3$'s, which is also easily quantifiable and we hope to find the connection between the content of the current section and the results we will show further.

7.5 Probability density functions

The energy-enstrophy statistical theory presented in the Chapter 3 provides us with the most probable probability density (3.37) for the Fourier modes of the potential vorticity, and the most probable probability density (3.26) for the potential vorticity itself. It is very interesting to check whether the traditional truncation confirms those predictions, and also check the influence of the statistically relevant Casimir invariants in the sine-bracket truncation.

$\tilde{C}_3$	Variance	Skewness	Flatness
0	65.67	$-1.37 \cdot 10^{-2}$	2.559
2	56.14	0.3114	2.937
4	50.82	0.7752	4.167
6	48.08	1.441	6.785

Table 7.5: The variance, skewness, and flatness of spatially averaged probability density functions for the potential vorticity, 23×23 sine-bracket truncation, layered topography. Note the increasing skewness as $\tilde{C}_3$ increases.

First we looked at the probability densities of the Fourier modes $\hat{q}_k$ of the potential vorticity for the traditional truncation (3.17). The simulations were done with three geophysical cases: no topography, random topography (Figure 5.1), and the layered topography (5.1). The results are represented in the Section 5.1.5 for no topography case, Section 5.2.5 for random topography, and Section 5.3.5 for layered topography. In the case with no topography (Section 5.1.5, Figures 5.15, 5.16, and 5.17) we observed that all the PDF's, except for the largest scale $|\mathbf{k}|^2 = 1$ have Gaussian shape, which is predicted by the theory in (3.37). In the case with random topography (Section 5.2.5, Figures 5.31, 5.32, and 5.33) we also observed that all the PDF's, except for the largest scale $|\mathbf{k}|^2 = 1$ have Gaussian shape, which is predicted by the theory in (3.37). In the case with layered topography (Section 5.3.5, Figures 5.47, 5.48, and 5.49) we can see that all the PDF's have Gaussian shape, except for the mode $\mathbf{k} = (1, 0)$, where the PDF has non-trivial mean and is significantly skewed (Figure 5.47). We conclude that the mode $\mathbf{k} = (1, 0)$ is special because it contains non-zero topography ($h = 0.2\cos(x) + 0.4\cos(2x)$). Overall, the results with the traditional truncation confirm the theory in (3.37).

Direct numerical simulations with the sine-bracket truncation confirm the fact that $\tilde{C}_3 = 0$ is statistically irrelevant for the dynamics of the system. For the case with no topography (Section 6.1.5, Figures 6.25, 6.26, and 6.27), we can see that the Fourier modes for the statistically irrelevant $\tilde{C}_3 = 0$ have the same shape as the PDF's for the traditional truncation. However for statistically relevant $\tilde{C}_3 = 4$ and 8 the PDF's lose original shape, becoming bimodal. The area of the Fourier grid, which is affected by statistically relevant $\tilde{C}_3$, is centered at zero Fourier coefficient and spreads radially outwards as $\tilde{C}_3$ increases. The same trend is also true for the case with layered topography, Section 6.3.5 (Figures 6.76, 6.77, 6.78, 6.79, 6.80, 6.81, 6.82, 6.83, 6.84, 6.85, 6.86, and 6.87).

We also observed the probability density functions for the potential vorticity in

the physical space. According to the theory predictions, the most probable probability density for the potential vorticity should be Gaussian. Direct numerical simulations with the traditional truncation (3.17) confirm this prediction for the three types of geophysical situations. The results for the traditional truncation with no topography were presented in the Section 5.1.5, Figure 5.14. On the Figure we can see that the probability density functions both for 11×11 and 23×23 traditional truncations have Gaussian shape, which is confirmed by the Gaussian fit with the same variance in each plot. We can observe the same situation for the traditional truncation with random topography (Section 5.2.5, Figure 5.30). The results of the direct numerical simulations with layered topography, traditional truncation, were a bit of surprise (Section 5.1.5, Figure 5.46), because the PDF for the 11×11 traditional truncation fits analytical Gaussian better than the PDF for the 23×23 traditional truncation, which is really strange and we do not know yet how to explain it.

We performed the direct numerical simulations for the physical space PDF's with the sine-bracket truncation (4.1) and layered topography. The results have very simple trend for statistically relevant $\tilde{C}_3$'s, which we present in the Figure 7.7 and Table 7.5, where we combined the results of the direct numerical simulations with layered topography, 23×23 sine-bracket truncation, $\tilde{C}_3 = 0$, 2, 4, and 6. As we can see, the value $\tilde{C}_3 = 0$ is statistically irrelevant. However, as we increase $\tilde{C}_3$, the PDF's gain non-trivial skewness. As we know, the standard Gamma-distribution is the most simple distribution with non-trivial skewness, and therefore on the Figure 7.7 we fitted the numerical results for $\tilde{C}_3 = 2$, 4, and 6 with the Gamma-distribution (shown as a dashed line), which has the same variance and skewness as numerical PDF's do, taken from Table 7.5. We can see that the Gamma-distribution fits the numerical result for $\tilde{C}_3 = 2$ very well. However, however, for larger values of $\tilde{C}_3$ the Gamma-fit is obviously not a best choice, which is shown in Figure 7.7. Nonetheless, here we can clearly see how statistically relevant $\tilde{C}_3$'s affect the probability density function for the potential vorticity – the PDF gains skewness and loses variance (see Table 7.5) as $\tilde{C}_3$ becomes statistically relevant. Due to this simple statistical trend, we think that these results are very important, and can be studied together with the results for the scatterplots $\bar{q}$ vs $\bar{\psi}$ (presented earlier in this section in Figure 7.6) to establish a connection between the shape of PDF and the shape of scatterplot.

7.6 Statistical predictions of the non-linear structure of the mean state

In the previous section we demonstrated, for the case with the layered topography (5.1), that the scatterplots $\bar{q}$ vs $\bar{\psi}$, shown in Figure 7.6, are bent for the statistically relevant values of the third Casimir invariant. Also in the Figure 7.7 we observed that the probability density functions for the potential vorticity exhibit systematic increase of skewness with increasing $\tilde{C}_3$. In this section we connect these two observations in a sense of the statistical mechanical framework described in the paper by Majda, Turkington, Haven, and DiBattista [16].

Let us look at the barotropic flow with two constraints: energy

$$E = \frac{1}{8\pi^2} \int |\nabla \psi|^2 \, \mathrm{d}x \, \mathrm{d}y, \tag{7.2}$$

and circulation

$$M = \frac{1}{4\pi^2} \int q \, \mathrm{d}x \, \mathrm{d}y, \tag{7.3}$$

where ψ is the stream function, and q is the potential vorticity. In other words, let us proclaim the enstrophy to be an additional conserved quantity, like all other Casimir invariants. Later we will see that by using the method described below we still take into account the enstrophy and all other Casimir invariants in a very elegant way, by using the concept of the maximum entropy principle with a given prior distribution, described in the Chapter 3, Section 3.2, equations (3.22) and (3.23), where the known prior distribution will be the suitable analytical approximation to the numerical PDF's for the potential vorticity, shown in the Figure 7.7.

Repeating the usual steps for the maximum entropy principle (3.22), for the variational derivatives of energy and circulation we obtain

$$\frac{\delta \bar{E}}{\delta \rho} = -\frac{1}{4\pi^2} \bar{\psi} \lambda,$$

$$\frac{\delta \bar{M}}{\delta \rho} = \frac{1}{4\pi^2} \lambda.$$

The solution to the maximum entropy principle equation (3.22) with a prior distribution is the canonical Gibbs distribution:

$$\rho^*(\vec{x},\lambda) = \frac{\exp\left[\frac{1}{4\pi^2}(\theta\bar{\psi}^* - \gamma)\lambda\right]\Pi(\vec{x},\lambda)}{\int \exp\left[\frac{1}{4\pi^2}(\theta\bar{\psi}^* - \gamma)\lambda\right]\Pi(\vec{x},\lambda)\,\mathrm{d}\lambda}, \tag{7.4}$$

where $\bar{\psi}^*$ is the mean stream function given by the most probable statistical state, and $\Pi(\vec{x},\lambda)$ is the known prior distribution, which, in general, may depend on the spatial coordinates $\vec{x}$. The above given probability density satisfies the Definition 2 for the probability density of the potential vorticity.

As we can see from (7.4), ρ^* is normalized. The parameters θ and γ are the Lagrange multipliers for energy and circulation, respectively. Further we assume that $\Pi(\vec{x},\lambda) = \Pi(\lambda)$, i.e. Π is spatially homogeneous. Given the form of (7.4), one can introduce the moment generating function

$$G(s) = \ln \int \exp(s\lambda)\Pi(\lambda)\,\mathrm{d}\lambda. \tag{7.5}$$

Given the moment generating function, it is very easy to determine mean, variance, and skewness of Π:

$$\mathrm{Mean}(\Pi) = G'(0) = \int \lambda\Pi(\lambda)\,\mathrm{d}\lambda, \tag{7.6a}$$

$$\mathrm{Var}(\Pi) = G''(0) = \int (\lambda - \mathrm{Mean}(\Pi))^2\Pi(\lambda)\,\mathrm{d}\lambda, \tag{7.6b}$$

$$\mathrm{Skew}(\Pi)\left[\mathrm{Var}(\Pi)^{\frac{3}{2}}\right] = G'''(0) = \int (\lambda - \mathrm{Mean}(\Pi))^3\Pi(\lambda)\,\mathrm{d}\lambda. \tag{7.6c}$$

According to the notation (7.5), the equation for the most probable mean state is

$$\bar{q}^* = G'\left[\frac{1}{4\pi^2}(\theta\bar{\psi}^* - \gamma)\right]. \tag{7.7}$$

For some certain choices of the prior distribution, we can derive the analytical answer to (7.7). We observe in the Figure 7.7, where the numerically obtained PDF's for the potential vorticity are fitted with the Gamma distributions with the same variance and skewness, that the standard Gamma distribution is a suitable analytical approximation for the prior distribution. In fact, Majda, Turkington, Haven, and DiBattista in [16] used the Gamma distribution as the prior distribution with skewness for statistical predictions of the Great Red Spot on Jupiter. The standard Gamma distribution is defined as

$\tilde{C}_3$	θ	γ
0	$-5.724 \cdot 10^{-1}$	$7.658 \cdot 10^{-8}$
2	$-6.908 \cdot 10^{-1}$	$1.938 \cdot 10^{-1}$
4	$-7.382 \cdot 10^{-1}$	$3.126 \cdot 10^{-1}$
6	$-7.816 \cdot 10^{-1}$	$4.658 \cdot 10^{-1}$

Table 7.6: The Lagrange multipliers for energy and circulation, determined by the least squares fit (7.10) to the scatterplots shown in the Figure 7.6 for layered topography.

$$R(\lambda, \alpha) = \frac{1}{\Gamma(\alpha)} \lambda^{\alpha-1} e^{-\lambda}. \tag{7.8}$$

However, we would like to scale Π in such a way that it would have zero mean, and predefined variance and skewness. Taking this into account, we choose the following Π:

$$\Pi(\lambda, \sigma, 2\varepsilon) = \frac{1}{|\varepsilon|\sqrt{\sigma}\,\Gamma(\varepsilon^{-2})} \left[\varepsilon^{-2}\left(1 + \lambda\varepsilon\sigma^{-1/2}\right)\right]^{\varepsilon^{-2}-1} \exp\left[-\varepsilon^{-2}(1 + \lambda\varepsilon\sigma^{-1/2})\right]. \tag{7.9}$$

The above distribution (7.9) has zero mean, σ variance, and 2ε skewness. Now we substitute (7.9) into (7.7) as a prior distribution, and after a straightforward calculation we obtain the following equation for the mean flow (technical details are omitted):

$$\bar{q}^* = \frac{\sigma(\theta\bar{\psi}^* - \gamma)}{4\pi^2 - \varepsilon\sigma^{1/2}(\theta\bar{\psi}^* - \gamma)}. \tag{7.10}$$

We have obtained the analytical relation between the mean stream function and the mean potential vorticity, under the assumption of the Gamma prior distribution. As we can see, the parameters in the equation (7.10) are the variance and skewness of the prior distribution, and the Lagrange multipliers for energy and circulation. Now we take the variance and skewness for the prior Gamma distribution from the Table 7.5, and determine the Lagrange multipliers θ and γ from the least squares fit of the relation (7.10) to the scatterplots shown in the Figure 7.6. The numerically determined θ and γ are shown in the Table 7.6, and the corresponding analytical fits are shown in the Figure 7.8. The Table 7.6 shows that the Lagrange multipliers for the energy are negative, i.e. the system is in the negative temperature regime. The analytical approximations (7.10) in the Figure 7.8 fit the numerically obtained scatterplots very well, and, in fact, reconstruct the curvature of the numerically obtained scatterplots. This means that given the suitable analytical

approximation, which in our case is Gamma distribution (7.9), to the actual prior distribution, which is presented in the Figure 7.7, *we are able to predict the non-linear structure of the mean flow by using the maximum entropy principle (3.22) and (3.23)*, and this is shown in the Figure 7.8. Note that, though in (7.4) we explicitly take into account energy and circulation only, the influence of the enstrophy and higher order Casimir invariants is hidden in the prior distribution.

7.7 Concluding discussion

As the end of the chapter we would like to summarize the results obtained for the simulations with the traditional and the sine-bracket truncations for the equations for barotropic flow. The framework of our research was oriented on the "atmospheric" behavior of the model (enstrophy is concentrated in high Fourier modes, μ close to -1). Three different geophysical situations were considered: no topography, the random topography with no Fourier components at the large-scale modes, and the y-layered topography $h = 0.2\cos(x) + 0.4\cos(2x)$. In each geophysical case, the energy-enstrophy based energy-enstrophy statistical theory, presented in the Chapter 3, was confirmed by the direct numerical simulations with the traditional truncation (3.17) in the Chapter 5. For the sine-bracket truncation (4.1), for each of three geophysical cases, in the Chapter 6 we presented the direct numerical simulations with varying values of the normalized third Casimir invariant $\tilde{C}_3$. Similar to the case with the truncated Burgers-Hopf equation, which is presented in the Chapter 2, the statistically irrelevant values of $\tilde{C}_3$ accumulate near the origin, and, to our surprise, for the statistically irrelevant values of $\tilde{C}_3$ the results for the sine-bracket truncation are identical with those for the traditional truncation. However, for the statistically relevant values of $\tilde{C}_3$, which are located away from zero, we observed various trends in behavior of all statistical quantities we considered. The most interesting trends are (as $\tilde{C}_3$ becomes more and more relevant): appearance of vortices in the mean flow, systematic drifting of the skewness of the stream function towards negative values, systematic lowering of the pseudo-energy spectrum, systematic bending of the scatterplots mean stream function vs mean potential vorticity, the time correlation decay slowdown, and the systematic increase of skewness of the probability density functions for the potential vorticity. In the Section 7.6 we show that one can predict the non-linear structure of the mean state by using the direct connection between the curvature of the scatterplots of the mean flow, and the skewness in the probability density of the potential vorticity. Our

future work on this project will be centered at more precise quantification of the aforementioned method and will be published by Majda and the author elsewhere. Another direction of the research one might also consider is to check the statistical relevance and irrelevance of the additional conserved quantities for the different dynamical regimes of the truncated equations. The "oceanographic" regime (low enstrophy, $\mu > 0$, distinct nontrivial topography) is very important in the studies of the equilibrium statistical predictions for the ocean. However, the variety of cases which can be studied with the sine-bracket truncation is somewhat limited due to the fact, that the unique Hamiltonian structure of the sine-bracket truncation can be lost in cases with dissipation and forcing, and with no dissipation or forcing but with different type of domain (non-periodic). Nonetheless, we have learned a lot about the statistical influence of additional conserved quantities by studying this relatively simple (in comparison with actual weather systems) model, which hopefully will help in future studies of more sophisticated models.

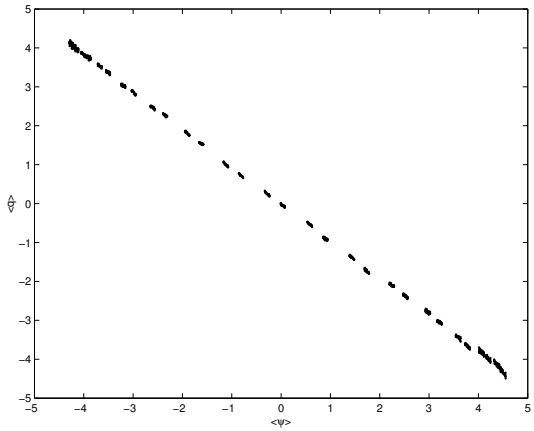

The total scatterplot $\langle\psi\rangle_\tau$ vs $\langle q\rangle_\tau$, sine-bracket truncation, 23×23 truncation size, $E = 7$, $\mathcal{E} = 20$, $\tilde{C}_3 = 0$

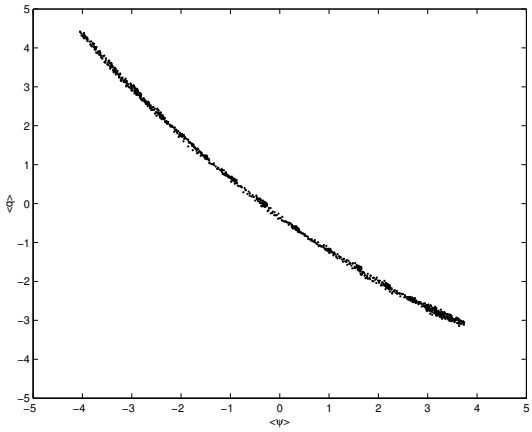

The total scatterplot $\langle\psi\rangle_\tau$ vs $\langle q\rangle_\tau$, sine-bracket truncation, 23×23 truncation size, $E = 7$, $\mathcal{E} = 20$, $\tilde{C}_3 = 2$

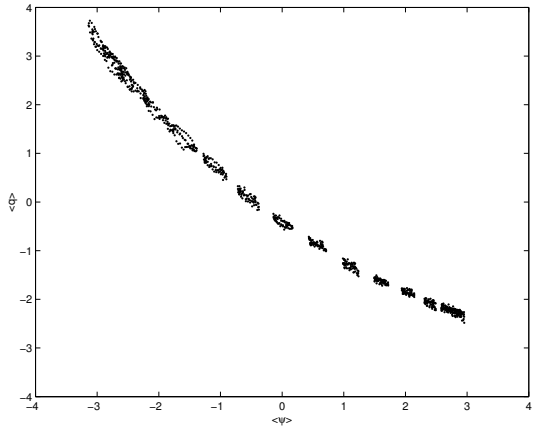

The total scatterplot $\langle\psi\rangle_\tau$ vs $\langle q\rangle_\tau$, sine-bracket truncation, 23×23 truncation size, $E = 7$, $\mathcal{E} = 20$, $\tilde{C}_3 = 4$

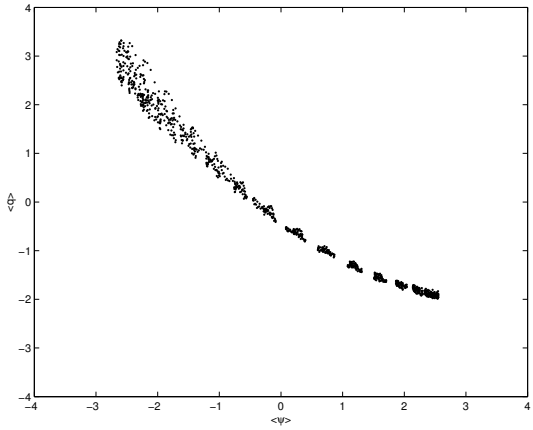

The total scatterplot $\langle\psi\rangle_\tau$ vs $\langle q\rangle_\tau$, sine-bracket truncation, 23×23 truncation size, $E = 7$, $\mathcal{E} = 20$, $\tilde{C}_3 = 6$

Figure 7.6: The total scatterplots $\bar{q}$ vs $\bar{\psi}$ for the 23×23 sine-bracket truncation, layered topography, $\tilde{C}_3 = 0$, 2, 4, and 6. Note that the scatterplots are bent, and the curvature of the scatterplots increases with increasing $\tilde{C}_3$.

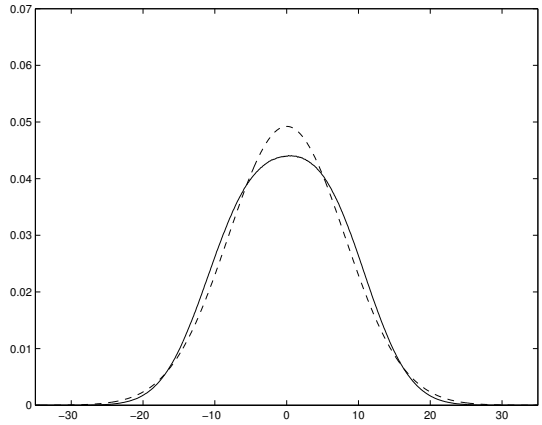

The PDF for the potential vorticity, 23×23 sine-bracket truncation, $\tilde{C}_3 = 0$, layered topography, solid line - direct numerical simulation, dashed line - analytical Gaussian with the same variance

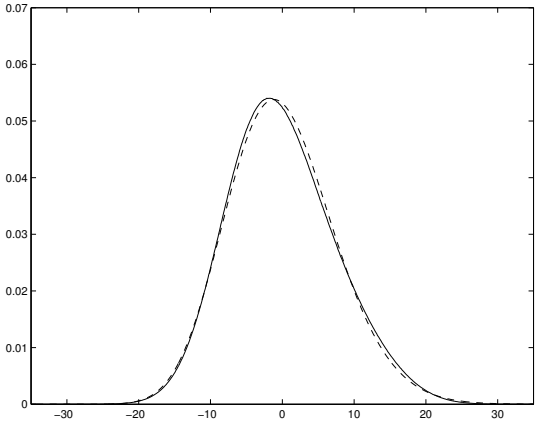

The PDF for the potential vorticity, 23×23 sine-bracket truncation, $\tilde{C}_3 = 2$, layered topography, solid line - direct numerical simulation, dashed line - analytical Gamma distribution with the same variance and skewness

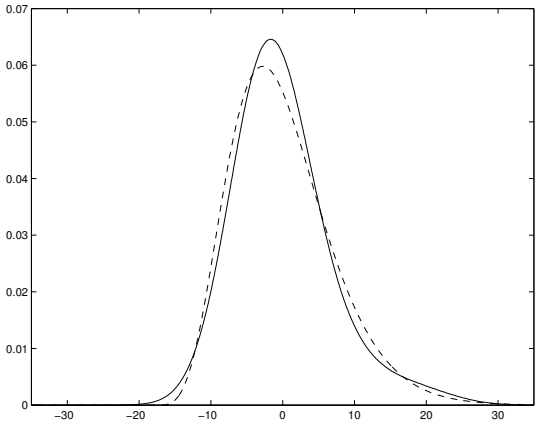

The PDF for the potential vorticity, 23×23 sine-bracket truncation, $\tilde{C}_3 = 4$, layered topography, solid line - direct numerical simulation, dashed line - analytical Gamma-distribution with the same variance and skewness

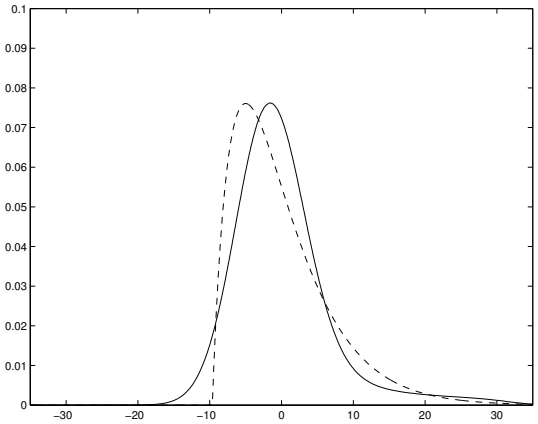

The PDF for the potential vorticity, 23×23 sine-bracket truncation, $\tilde{C}_3 = 6$, layered topography, solid line - direct numerical simulation, dashed line - analytical Gamma-distribution with the same variance and skewness

Figure 7.7: The spatially averaged probability density function for the potential vorticity with removed mean, $\tilde{C}_3 = 0$, 2, 4, and 6, layered topography. Note the increasing skewness in the PDF's.

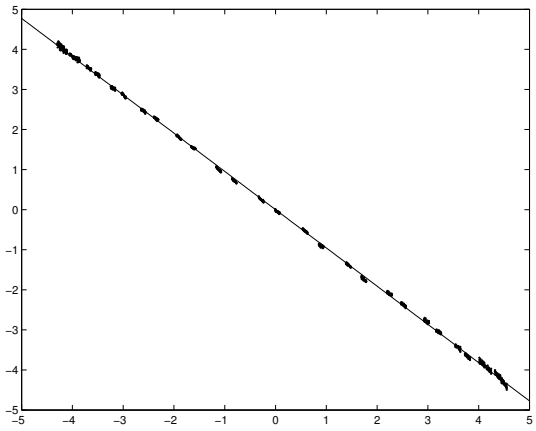

The total scatterplot $\langle\psi\rangle_\tau$ vs $\langle q\rangle_\tau$, sine-bracket truncation, 23×23 truncation size, $E = 7$, $\mathcal{E} = 20$, $\tilde{C}_3 = 0$. Analytical fit is represented by the solid line

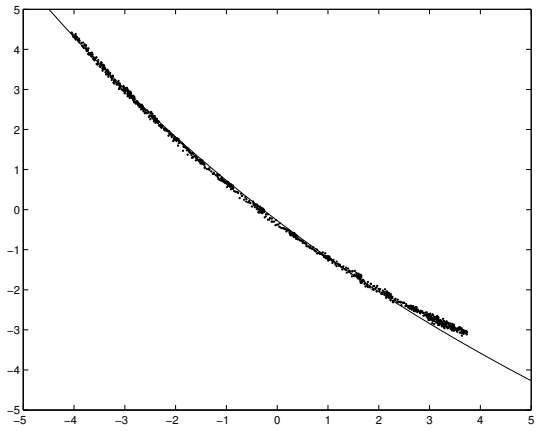

The total scatterplot $\langle\psi\rangle_\tau$ vs $\langle q\rangle_\tau$, sine-bracket truncation, 23×23 truncation size, $E = 7$, $\mathcal{E} = 20$, $\tilde{C}_3 = 2$. Analytical fit is represented by the solid line

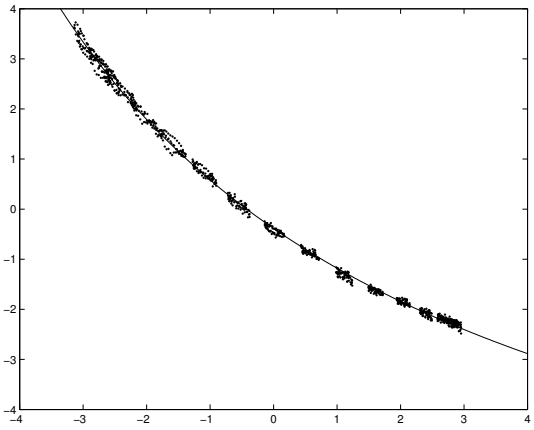

The total scatterplot $\langle\psi\rangle_\tau$ vs $\langle q\rangle_\tau$, sine-bracket truncation, 23×23 truncation size, $E = 7$, $\mathcal{E} = 20$, $\tilde{C}_3 = 4$. Analytical fit is represented by the solid line

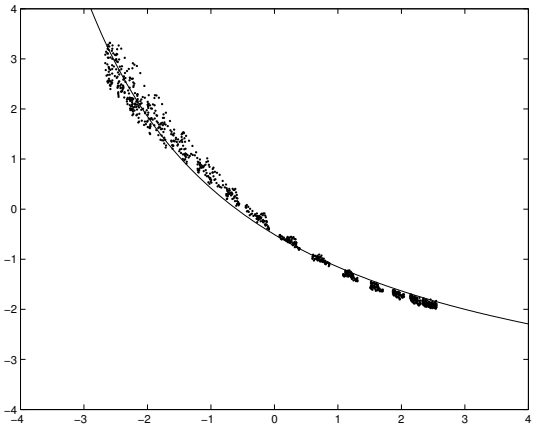

The total scatterplot $\langle\psi\rangle_\tau$ vs $\langle q\rangle_\tau$, sine-bracket truncation, 23×23 truncation size, $E = 7$, $\mathcal{E} = 20$, $\tilde{C}_3 = 6$. Analytical fit is represented by the solid line

Figure 7.8: The total scatterplots $\bar{q}$ vs $\bar{\psi}$ for the 23×23 sine-bracket truncation, layered topography, $\tilde{C}_3 = 0$, 2, 4, and 6. The curvature of the scatterplots is reconstructed by the analytical fits.

LIST OF TABLES

LIST OF FIGURES

BIBLIOGRAPHY

[1] R. Abraham and J. E. Marsden. *Foundations of Mechanics.* Addison-Wesley Publishing Co. Inc., Redwood City, CA, second edition edition, 1985.

[2] R. Abramov, G. Kovačič, and A. Majda. Hamiltonian Structure and Statistically Relevant Conserved Quantities for the Truncated Burgers-Hopf Equation. *Comm. Pure Appl. Math.*, 2001.

[3] V. I. Arnold. *Mathematical methods of classical mechanics.* Springer-Verlag, New York, Heidelberg, Berlin, 1989.

[4] Uri M. Ascher and Linda R. Petzold. *Computer Methods for Ordinary Differential Equations and Differential-Algebraic Equations.* SIAM, Philadelphia, 1998.

[5] G. F. Carnevale and J. S. Frederiksen. Nonlinear stability and statistical mechanics of flow over topography. *Journal of Fluid Mechanics*, 175:153–181, 1987.

[6] C. S. Gardner. The Korteweg–deVries equation and generalizations. IV. the Korteweg–deVries equation as a Hamiltonian system. *J. Math. Phys.*, 12:1548–1551, 1971.

[7] G. Holloway. Eddies, waves, circulation, and mixing: Statistical geofluid mechanics. *Annu. Rev. Fluid Mech.*, 18:49–65, 1986.

[8] E. Jaynes. Information theory and statistical mechanics. *Phys. Rev.*, 106:620–630, 1957.

[9] R. Kleeman, A. Majda, and I. Timofeyev. Quantifying predictability in a model with statistical features of the atmosphere. Submitted July 2001 and in press for Physica D.

[10] John Lamperti. *Probability: a Survey of the Mathematical Theory.* W. A. Benjamin, Inc., New York, Amsterdam, 1966.

[11] A. Lasota and M. Mackey. Chaos, fractals, and noise. *Applied Math. Sciences*, 97, 1994.

[12] A. Majda and A. Bertozzi. *Vorticity and Incompressible Flow.* Cambrige University Press, 2002.

[13] A. Majda and M. Holen. Dissipation, topography, and statistical theories for large-scale coherent structure. *Comm. Pure Appl. Math.*, L:1183–1234, 1997.

[14] A. Majda, I. Timofeyev, and E. Vanden Eijnden. Apriori tests of a stochastic mode elimination strategy. Submitted November 2001 to Physica D.

[15] A. Majda, I. Timofeyev, and E. Vanden Eijnden. A mathematical framework for stochastic climate models. *Comm. Pure Appl. Math.*, LIV(0891-0974), 2001.

[16] A. Majda, B. Turkington, K. Haven, and M. DiBattista. Statistical equilibrium predictions of jets and spots on Jupiter. *Proc. Natl. Acad. Sci.*, 98:12346–12350, 2001.

[17] A. Majda and X. Wang. Nonlinear dynamics and statistical theories for basic geophysical flow. Book in preparation based on Majda's lectures at Courant Institute, 1997,1999,2001-2002.

[18] A. J. Majda and I. Timofeyev. Remarkable statistical behavior for truncated Burgers-Hopf dynamics. *Proc. Natl. Acad. Sci. USA*, 97(23):12413–12417, 2000.

[19] A. J. Majda and I. Timofeyev. Statistical mechanics for truncations of the Burgers-Hopf equation: a model for intrinsic stochastic behavior with scaling. Submitted on 9/15/00, accepted 10/15/00, and to appear in the first issue of Milan Journal of Mathematics, Spring 2002.

[20] R. I. McLachlan. Explicit Lie-Poisson integration and the Euler equations. *Phys. Rev. Lett.*, 71:3043–3046, 1993.

[21] J. Miller, P. Weichman, and M.C. Cross. Statistical mechanics, Euler's equations, and Jupiter's Red Spot. *Phys. Rev.*, A45:2328–2359, 1992.

[22] P. J. Morrison. Hamiltonian description of the ideal fluid. *Reviews of Modern Physics*, 70:467–521, April 1998.

[23] R. Salmon. *Lectures on Geophysical Fluid Dynamics.* Oxford Press, New York, 1998.

[24] C. Shannon and W. Weaver. *Mathematical Theory of Communication.* Univ. Illinois Press, Urbana, 1949.

[25] V. Zeitlin. Finite-mode analogues of 2D ideal hydrodynamics: Coadjoint orbits and local canonical structure. *Physica D*, 49:353–362, 1991.